

UNIVERSITY OF OKLAHOMA

GRADUATE COLLEGE

COMBINED EXPERIMENTAL AND COMPUTATIONAL STUDIES OF
MODEL COMPOUNDS TO GAIN UNDERSTANDING OF
CATALYTIC UPGRADING OF BIO-OILS

A DISSERTATION

SUBMITTED TO THE GRADUATE FACULTY

in partial fulfillment of the requirements for the

Degree of

DOCTOR OF PHILOSOPHY

By

TEERAWIT PRASOMSRI

Norman, Oklahoma

2011

COMBINED EXPERIMENTAL AND COMPUTATIONAL STUDIES OF
MODEL COMPOUNDS TO GAIN UNDERSTANDING OF
CATALYTIC UPGRADING OF BIO-OILS

A DISSERTATION APPROVED FOR THE
SCHOOL OF CHEMICAL, BIOLOGICAL & MATERIALS ENGINEERING

BY

Dr. Daniel E. Resasco, Chair

Dr. Richard G. Mallinson

Dr. Lance L. Lobban

Dr. Walter E. Alvarez

Dr. Kenneth M. Nicholas

ACKNOWLEDGEMENTS

First, I would like to record my sincerest gratitude to my Ph.D. thesis advisor, Dr. Daniel Resasco, for his guidance, encouragement, and patience. I would also like to thank him for being very inspirational, giving me this opportunity and allowing me the independence in designing the framework of the research work. It is a great pleasure working in his group, and will always be my best memory and treasure in my future career.

I would like to express my appreciation to my M.S. thesis advisor, Dr. Siriporn Jongpatiwut at the Petroleum and Petrochemical College, for introducing and giving me an opportunity to carry out the research work at OU during my Master's program. It is truly considered as the first important stepping stone to my future achievement.

I wish to express my gratefulness to Dr. Tawan Sooknoi at the King Mongkut's Institute of Technology Ladkrabang for being very flexible and understanding some tough situations that I faced during my time at the beginning here. Without his personal and academic supports, I could not have made it this far.

I would like to thank Dr. Walter Alvarez and Dr. Steven Crossley for their useful comments on this work. I enjoy very much the knowledge and wisdom of industrial practice that they have given me as well as the supportive opportunities.

I want to thank Dr. Sanwu Wang at the University of Tulsa for his hospitality during my visit to the University of Tulsa, where I can learn how to use VASP from scratch. Without this collaboration and the use of his computer programs and facilities, this work could not have been completed.

I am grateful to Dr. Kenneth Nicholas for serving as my dissertation committee.

I feel greatly privileged to work at OU in this group at this time. The helpful discussions and insights arose by all of the outstanding professors in our group meetings have extremely helped me in my advancement. I would especially like to thank Dr. Richard Mallinson, Dr. Lance Lobban, Dr. Roberto Galiasso, Dr. Friederike Jentoft, and Dr. Rolf Jentoft for bringing various fields of expertise into our scientific conversation. It has been an enjoyable experience as being a part of such a very exciting and powerful group.

I would like to thank all of my fellow students and post-docs which I have met and worked with during my time at OU. First and foremost, I would like to thank my previous officemates, Steven and Phuong. Not only the work space has been shared between us, but also the interesting discussions on research have been exchanged constantly. I would also like to thank Brian Morrow for first showing how to perform the Density Functional Theory calculation by using the GAUSSIAN software, which has turned out to be essential for our research. Moreover, I want to thank Dr. Wei An for his computational expertise and help in my calculation improvement. There are many other bright students and post-docs who I am happy to have known over

the years, many whom I have been privileged to work with. They are Kyu, Sunya, On, Bokie, Tu, Anh, Lei, Dachuan, Miguel, Amalia, Jimmy, Santiago, Xinli, Anirudhan, Kyle, Paula, Cristina, Sarah, Matt, Kassie, Hernando, Andrew, Tanate, Trung (Hoang), Trung (Pham), Veronica, Pilar, Shaolong, Min, Jonathan, Wes, Yanger, Michael, Julien, Jeab, Meaow, Pak, Martina, Stefano, Federico, Quincy, Hui, Lyon, Tan, Nok, Sergio, and Ariela. I would like to thank for their warm support and friendship through different phases of my graduate study.

I would also like to thank the people who help keep everything moving. They are Kelly, Terri, Donna, Vernita and Alan from the Chemical Engineering Department; and Dr. Henry Neeman, Brandon George, Brett Zimmerman and Joshua Alexander from the OU Supercomputing Center for Education & Research. Thank you very much for all of the help you have given me.

Most of all, I really want to express my great thankfulness to my parents, grandparents and brother for their endless love, support and encouragement.

TABLE OF CONTENTS

1.	Introduction	1
1.1	Chemical composition of wood	2
1.2	Pyrolysis of biomass	5
1.3	Properties of bio-oils	6
1.4	Compositions of bio-oils	9
1.5	Review of bio-oil upgrading	12
1.6	Outline	15
2.	Computational Background	21
2.1	Introduction to quantum mechanics	21
2.2	Schrödinger equation and Born-Oppenheimer approximation	22
2.3	Quantum mechanical methods	23
2.4	Exchange-correlation functionals	24
2.5	Basis functions	29
2.6	Basis sets	30
2.7	Quantum mechanical calculations	31
2.8	Modeling a surface	33
2.9	The VASP code	37
2.10	Nudged Elastic Band	40
2.11	Energy	41
2.12	Population analysis	42
2.13	Potential energy surface	47
2.14	Wiberg bond index	47
3.	Conversion of 1- and 2-Tetralone over HY Zeolites	51
3.1	Introduction	51
3.2	Experimental	53
3.3	Results and discussion	55
3.3.1	Thermal reactions of 1- and 2-tetralone (blank reactor)	55
3.3.2	Catalytic conversion of 1- and 2-tetralone reactions over the HY zeolites	57
3.4	Reaction pathways	64
3.5	Conclusions	68
4.	Conversion of 1-Tetralone over HY Zeolite: An Indicator of the Extent of Hydrogen Transfer	71

4.1	Introduction	71
4.2	Experimental	73
	4.2.1 Catalytic activity testing	73
	4.2.2 Computational methods	75
4.3	Results	77
	4.3.1 Catalytic reaction of pure compounds over HY zeolites	77
	4.3.2 Catalytic reaction of hydrocarbon with co-fed 1-tetralone over HY zeolites	79
	4.3.3 Effect of decalin concentration on the product distribution of 1-tetralone conversion over HY zeolites with varying acidity (Si/Al ratio 15 and 40)	84
	4.3.4 Proton affinity of naphthol from DFT calculation	88
	4.3.5 Hydrogen transfer ability of hydrocarbon species from DFT calculations	90
4.4	Discussion	92
4.5	Conclusions	95
5.	Catalytic Conversion of Anisole over HY and HZSM-5 Zeolites in the Presence of Different Hydrocarbon Mixtures	99
5.1	Introduction	99
5.2	Experimental	101
	5.2.1 Catalytic measurements	101
	5.2.2 Pulse experiment	102
	5.2.3 Catalyst characterization	104
	5.2.4 Computational details	105
5.3	Results and discussion	106
	5.3.1 Catalytic reactions of pure anisole over HY zeolites	106
	5.3.2 Effect of mixing anisole with different hydrocarbons over zeolites	110
	5.3.3 Coke formation during reaction of pure anisole and mixtures	116
	5.3.4 Recovery of anisole conversion by flushing the spent catalysts with tetralin	119
	5.3.5 Reaction pathways	121
5.4	Conclusions	133
6.	Anchoring Pd Nanoclusters onto Pristine and Functionalized Carbon Nanotubes	137
6.1	Introduction	137
6.2	Methods	138
	6.2.1 Experimental	138
	6.2.2 Models and computation	140

6.3	Results and discussion	143
7.3.1	Deposition of Pd on pristine and functionalized SWCNT	143
7.3.2	DFT calculation for Pd nanocluster adsorption on the pristine and functionalized SWCNT and MWCNT	147
6.4	Conclusions	153
7.	Comparative Study of Adsorption of Aldehydes on Pd(111) and PdCu(111) Surfaces	158
7.1	Introduction	158
7.2	Methodology	160
7.2.1	Experimental method	160
7.2.2	Computational method	161
7.3	Results and discussion	164
8.3.1	Periodic slab model	164
8.3.2	Cluster model	170
7.4	Conclusions	174
8	Examples of Combining Theoretical Calculations toward the Understanding of Experimental Results	178
8.1	Example 1: Catalyst deactivation by a strong adsorption of oxygenate aromatic compounds on acid catalysts	178
9.1.1	Experimental observation	178
9.1.2	Computational calculation	179
9.1.3	Results and Discussion	181
9.1.4	Conclusions	190
8.2	Example 2: Competitive adsorption of 1-pentene and isopropylamine (IPA) on cation-exchnaged zeolites	191
9.2.1	Experimental observation	191
9.2.2	Computational calculation	192
9.2.3	Results and Discussion	192
9.2.4	Conclusions	193
8.3	Example 3: Relation of adsorption energies and decarbonylation activities of different aldehydes on Pd(111)	195
9.3.1	Experimental observation	195
9.3.2	Computational calculation	196
9.3.3	Results and Discussion	197
9.3.4	Conclusions	200

APPENDICES

A	Mulliken Charges and Proton Affinity of Single-Ring Aromatic Compounds	203
B	Molecular Orbitals of Single-Ring Aromatic Compounds	205
C	Molecular Orbitals of Furanic Compounds	211
D	Potential Energy Surface (PES) of the Adsorbed Propylene on Zeolites	214
E	Proposed Reaction Path of Hydrodeoxygenation of Phenol on Zeolites	217
F	Relative Hydride Transfer Ability of Methylcyclohexene	219
G	Natural Bond Orbital (NBO) Analysis of Single-Ring Aromatic Compounds	220
H	Adsorption of Hydroxybenzaldehydes on Ru(0001) Surfaces	222
I	Adsorption of Furan on Pd and Ni Clusters	225
J	Adsorption of Acyl Species of Aldehydes on (111) Surfaces of Pt, Pd and Rh	228
K	Alkylation of Different Aromatic Compounds and Model Small Oxygenates in Bio-Oil Refining	229

LIST OF TABLES

Table 1.1	Properties of wood pyrolysis bio-oils and regular fuels.	7
Table 1.2	Main compositions in organic phase of bio-oil from <i>P. indicus</i> .	11
Table 3.1	Thermal reactions of 1- and 2-tetralone.	56
Table 3.2	Reactions of tetralin, tetralones and 1-naphthol catalyzed by HY zeolites.	63
Table 3.3	Reactions of 1-tetralol catalyzed by HY zeolites.	66
Table 4.1	Catalytic reaction of pure compounds over HY zeolites.	78
Table 4.2	Overall yields from catalytic reactions of mixture of hydrocarbons and 1-tetralone over HY zeolites.	80
Table 4.3	Conversion and selectivity from catalytic reactions of mixture of hydrocarbons and 1-tetralone over HY zeolites.	81
Table 4.4	Amount of coke on spent catalysts determined by an elemental analyzer.	82
Table 5.1	Product distributions from conversion of anisole and anisole-tetralin mixture (~50% tetralin) over HY zeolite. Reaction conditions: W/F = 0.42 h (wrt. anisole for co-feed reaction), T = 400 °C, P = 1 atm He.	107
Table 5.2	Comparison of amount of carbon deposited on spent catalysts from the reactions of different mixture feed over the HY zeolite. Reaction conditions: W/F = 0.42 h (wrt. anisole for co-feed reaction), T = 400 °C, P = 1 atm He. TOS = 3 h.	117
Table 5.3	Amounts of carbon formed on the spent over the HY zeolite. Reaction conditions: W/F = 0.42 h (wrt. anisole for co-feed reaction), T = 400 °C, P = 1 atm He. TOS = 3 h.	119
Table 5.4	Optimized geometrical parameters of adsorption complexes for anisole protonation step to form surface methoxide of dissociative pathway (distances in Å).	127

Table 5.5	Optimized geometrical parameters of adsorption complexes for propylene methylation step of dissociative pathway (distances in Å).	130
Table 5.6	Optimized geometrical parameters of adsorption complexes for associative phenol methylation with anisole (distances in Å).	133
Table 6.1	Pd–Pd, Pd–C and C–O bond lengths of a C _{2v} Pd ₄ cluster alone, and the adsorptions of Pd ₄ clusters on SWCNTs.	149
Table 7.1	Adsorption energies (kJ/mol) and optimized bond lengths (Å) of 2-methylpentanal on Pd(111) and PdCu(111) slabs (see Figure 8.2).	168
Table 7.2	Adsorption energies (kJ/mol) and optimized bond lengths (Å) of furfural on Pd(111) and PdCu(111) slabs (see Figure X.3).	168
Table 7.3	Adsorption energies (E _{ads}), and optimized distances of C1-O, C1-C2, C1-Metal and O-metal bonds for the systems illustrated in Figure 8.4.	172
Table A.1	Calculated values of Mulliken charge (q) of benzene, toluene, xylenes, phenol, and cresols.	203
Table B.1	Molecular orbital energies of different aromatic compounds.	207
Table G.1	Natural bond orbital (NBO) analysis of phenol, catechol, guaiacol, anisole and hydrogenated phenol.	220
Table H.1	Calculated heats of adsorption (eV) of <i>ortho</i> - and <i>para</i> -hydroxybenzaldehydes on Ru(0001) surfaces.	222
Table I.1	Calculated heats of adsorption and bond lengths of furan on different structures of Pd and Ni clusters.	226
Table I.2	Calculated bond index and natural bond orbital (NBO) analysis of furan on different structures of Pd and Ni clusters.	227

LIST OF FIGURES

Figure 1.1	Lignocellulose composition of wood.	3
Figure 3.1	Schematic diagram of the system.	54
Figure 3.2	Conversions of 1- and 2-tetralone as a function of temperature. Reaction conditions: 1 atm H ₂ , TOS 0.5 h, W/F = 1.723 h.	58
Figure 3.3	Product yields from the reaction of (a) 1-tetralone and (b) 2-tetralone as a function of temperature over HY zeolite. Reaction conditions: 1 atm H ₂ , TOS = 0.5 h, W/F = 1.723 h.	59
Figure 3.4	Product yields from the reaction of (a) 1-tetralone and (b) 2-tetralone as a function of space time (W/F) at 300 °C over HY. Reaction conditions: 1 atm H ₂ , TOS = 0.5 h.	61
Figure 3.5	Product yields from the reaction of 1-tetralone as a function of space time (W/F) at 500 °C over HY. Reaction conditions: 1 atm H ₂ , TOS = 0.5 h. The values at zero W/F correspond to those obtained in the blank reactor (thermal).	62
Figure 4.1	Effect of % co-fed decalin on (a) yield of naphthalene (NP); and (b) 2-naphthol to 1-naphthol ratio, and NP to naphthol ratio. Reaction conditions: 450 °C, 1 atm He, TOS = 0.5 h.	86
Figure 4.2	Effect of acidity on (a) yield of naphthalene (NP); and (b) 2-naphthol to 1-naphthol ratio, and NP to naphthol ratio. Reaction conditions: 450 °C, 1 atm He, TOS = 0.5 h.	87
Figure 4.3	Possible C ₁₀ H ₉ O ⁺ ions. Protonation of naphthol is compared for the keto-forms of 1-naphthol (1) and 2-naphthol (2) to form carbenium ions; the oxiranium cation (3); and the enol-forms of 1-naphthol (4,5) and 2-naphthol (6–7). The corresponding PAs in kJ/mol are shown in the parentheses.	89
Figure 4.4	Relative activation energy of hydride dissociation at different locations of the donor molecules. The calculated values relative to methane, and computed by DFT.	91

Figure 4.5	Relationships between the relative activation energy for hydride transfer reaction, and the bond index calculated from the NBO analysis.	92
Figure 5.1	Product composition at the reactor outlet as a function of time on stream during anisole conversion over the HY zeolite. Reaction conditions: W/F = 0.42 h , T = 400 °C, P = 1 atm He.	110
Figure 5.2	Anisole conversion over HY zeolite with different co-fed hydrocarbons as a function of time on stream. Pure anisole feed is indicated with a dashed line. Reaction conditions: W/F = 0.42 h (wrt. anisole for co-feed reactions), co-feed concentration = ~50%, T = 400 °C, P = 1 atm He.	112
Figure 5.3	Degree of phenol alkylation (i.e. (Cr+Xol)/Ph yield ratio) for pure anisole and mixture feed reactions over the HY zeolite. Reaction conditions: W/F = 0.42 h (wrt. anisole), T = 400 °C, P = 1 atm He, co-feed concentration = ~50%, TOS = 0.5 h.	114
Figure 5.4	Relationship between conversion of anisole and degree of phenol alkylation as a function of time on stream for a) pure anisole, b) anisole-tetralin mixture, c) anisole-benzene mixture, and d) anisole- <i>n</i> -decane mixture feeds. Reaction conditions: W/F = 0.42 h (wrt. anisole), T = 400 °C, P = 1 atm He, co-feed concentration = ~50%, TOS = 0.5 h.	115
Figure 5.5	Alkylnaphthalenes/naphthalene product ratio for pure tetralin and mixture feed reactions over the HY zeolite. Reaction conditions: W/F = 0.42 h (wrt. anisole), T = 400 °C, P = 1 atm He, TOS = 0.5 h.	116
Figure 5.6	Effect of co-fed tetralin on anisole conversion over the HY zeolite. Reaction conditions: W/F = 0.42 h (wrt. anisole for co-feed reaction), co-feed concentration = ~50%, T = 400 °C, P = 1 atm He.	120
Figure 5.7	Alkylnaphthalenes/naphthalene product ratio (at the 5 th pulse) for pure tetralin and mixture feeds over the HY and HZSM-5 zeolites in pulse experiment. Reaction conditions: T = 450 °C, P = 1 atm He. <u>pure Tet</u> : pure tetralin, catalyst/feed ratio = 70 (g/g); <u>An → Tet</u> : pulse tetralin right after anisole injection, catalyst/feed ratio = 70 (g/g tetralin) and 150 (g/g anisole); <u>An + Tet</u> : mixture of anisole and tetralin (30 wt% tetralin), catalyst/feed ratio = 70 (g/g tetralin).	123

Figure 5.8 Potential energy diagram for the surface methoxide formation step of the dissociative mechanism for anisole protonation. B3LYP/6-31G(d)+ZPE energies.	126
Figure 5.9 Potential energy diagram for the propylene methylation reaction step of the dissociative mechanism. B3LYP/6-31G(d)+ZPE energies.	129
Figure 5.10 Potential energy diagram for the associative phenol methylation with anisole reaction pathway. B3LYP/6-31G(d)+ZPE energies.	132
Figure 6.1 Front and side view of the optimized armchair (7, 7) SWCNT with a functionalized site represented by a $C_{265}O_{31}$ model tube.	140
Figure 6.2 The representative model for MWCNT, consisting of three layers of graphene sheets with an interlayer distance of ~ 3.4 Å.	142
Figure 6.3 Raman spectra of pristine and functionalized SWCNTs. Spectra are normalized with respect to the G-band and shifted vertically for clarity.	144
Figure 6.4 TEM images of (a) Pd nanoclusters dispersed on functionalized; and (b) pristine SWCNTs. The corresponding SWCNTs before Pd deposition are shown as reference in (c) and (d), respectively.	146
Figure 6.5 The structure models for (a) a Pd_4 cluster alone; (b) a perfect site (C_{13}); and (c) a functionalized site ($C_{12}O_3$) on the SWCNT. The corresponding adsorptions of Pd_4 on their sites are shown in boxes.	148
Figure 6.6 Frontier molecular orbitals of the Pd_4 adsorptions on different sites of SWCNTs: HOMOs (left) and LUMOs (right).	151
Figure 6.7 The models for Pd clusters adsorption on terrace sites (left); and steps sites (right) of MWCNT.	153
Figure 7.1 The periodic supercell representing a) Pd(111), and b) PdCu(111) surfaces.	162
Figure 7.2 DFT optimized structures of 2-methylpentanal (MPAL) in gas phase (a), and its adsorption on Pd(111) (b) and PdCu(111) (c-e) slabs. Red, gray, white, blue, and yellow spheres represent O, C, H, Pd and Cu atoms, respectively. The corresponding bond lengths are given in Table 8.1.	166

Figure 7.3	DFT optimized structures of furfural (FAL) in gas phase (a), and its adsorption on Pd(111) (b) and PdCu(111) (c-e) slabs. Red, gray, white, blue, and yellow spheres represent O, C, H, Pd and Cu atoms, respectively. The corresponding bond lengths are given in Table 8.2.	167
Figure 7.4	DFT optimized structures of 2-methylpentanal in gas phase (a), and its η^2 -(C-O) aldehyde adsorption on Pd ₁₀ (b) and Pd ₄ Cu ₆ (c) clusters. The corresponding adsorbed acyl species are shown in (d) and (e), respectively.	172
Figure 7.5	Conversion and yield of products from the reaction of furfural (a); and 2-methylpentanal (b) on Pd/SiO ₂ as a function of Cu loading. Reaction condition: W/F = 3 h, Temp = 125°C, H ₂ pressure = 1 atm, TOS = 15 min.	173
Figure 8.1	The simulated models of acid sites created by a) 2T, and b), 4T clusters models. Hydrogen, oxygen, silicon and aluminum are represented by white, red, gray and pink spheres, respectively.	180
Figure 8.2	Comparison of adsorption and HOMO energies of benzene, anisole, phenol and guaiacol on the 2T cluster models. Different adsorption locations on the molecules including at the ring, hydroxyl (-OH), and methoxyl (-O-CH ₃) groups were investigated.	183
Figure 8.3	The initial and optimized structures of benzene adsorption at the ring site in perpendicular (top) and parallel (bottom) manners on the 2T clusters.	184
Figure 8.4	The initial and optimized structures of anisole adsorption at the -O-CH ₃ (top) and the ring (bottom) sites on the 2T clusters.	185
Figure 8.5	The initial and optimized structures of phenol adsorption at the -OH (top) and the ring (bottom) sites on the 2T clusters.	186
Figure 8.6	The initial and optimized structures of guaiacol adsorption at the -OH (top) and the -O-CH ₃ (bottom) sites on the 2T clusters.	187
Figure 8.7	The initial and optimized structures of guaiacol adsorption at the ring site on the 2T clusters.	188
Figure 8.8	The Optimized structures of anisole on the Brønsted (a) and Lewis (b) acid sites; and guaiacol on the Brønsted (c), Lewis (d) and both Brønsted/Lewis acid sites (e) on the 4T clusters.	189

Figure 8.9 The initial and optimized structures of benzene adsorption on the 4T clusters.	190
Figure 8.10 Geometries of the adsorption complexes and the corresponding heats of adsorption of 1-pentene and IPA on the M-T3 model clusters.	194
Figure 8.11 Decarbonylation activities, activation energies and calculated adsorption heats of $\eta^1(\text{C})$ -acyl species of furfural, 2-methylpentenal, 2-methylpentanal and trimethylacetaldehyde on Pd(111) surfaces.	196
Figure 8.12 Geometries of isolated and optimized structures of $\eta^1(\text{C})$ -acyl species of a) furfural, b) 2-methylpentenal, c) 2-methylpentanal and d) trimethylacetaldehyde on Pd(111) surfaces.	199
Figure A.1 Calculated proton affinity (PA) and atomic charge at oxygens of toluene, methoxybenzenes (anisole), and methoxyphenols (guaiacols).	204
Figure B.1 Molecular orbital shapes of benzene, toluene and xylenes.	208
Figure B.2 Molecular orbital shapes of phenol and cresols.	209
Figure B.3 Molecular orbital shapes of anisole and guaiacol.	210
Figure C.1 Molecular orbital energies of different furanic compounds.	212
Figure C.2 Molecular orbital shapes of different furanic compounds.	213
Figure D.1 Plots of surface propoxide energy as functions of adsorption separation (C-O distance) and zeolite structure (Al-O-Si angle).	214
Figure D.2 Plots of LUMO energy of surface propoxide as functions of adsorption separation (C-O distance) and zeolite structure (Al-O-Si angle).	215
Figure E.1 The energetic profile of phenol hydrodeoxygenation on zeolites.	217
Figure F.1 Comparison of relative activation energy for hydride abstraction at different locations of methycyclohexene.	219

Figure H.1 Possible adsorption configurations of <i>o</i> -hydroxybenzaldehyde on Ru(0001) surfaces.	223
Figure H.2 Possible adsorption configurations of <i>p</i> -hydroxybenzaldehyde on Ru(0001) surfaces.	224
Figure I.1 Structures of M ₁₀ cluster (M = Pd and Ni).	225
Figure I.2 Optimized geometries of furan adsorption on Ni and Pd clusters.	226
Figure J.1 Heats of adsorption of acyl species of pentanal, methylbutanal and trimethylacetaldehyde on (111) surfaces of Pt, Pd and Rh.	228
Figure K.1 Alkylation of different feed over H-Beta at 200 °C. W/F = 1h. Carrier gas H ₂ 30ml/min.	231
Figure K.2 Calculated HOMO energies (eV) of benzene, toluene, and m-cresol.	233
Figure K.3 Calculated LUMO energy (eV) and total energy (Hartrees) of propoxide species (i.e. adsorbed propylene) at different separation distances.	233

ABSTRACT

Scientific research is mainly based upon observation and experiment, and accordingly, the purpose of theoretical study is to provide the conceptual framework for the prediction and explanation of observation. Consequently, the combination of experimental and theoretical studies could potentially bring about the versatility and advancement in research. In this regard, this concept was applied toward the research theme of bio-oil upgrading. Bio-oil is a complex mixture of oxygenates, and hence, the study of an efficient catalyst requires the use of model oxygenate compounds such as phenolic and furanic derivatives. In this contribution, examples of the combined experimental and theoretical approaches will be given for the understanding toward the observation and fundamental studies of those model compounds on different classes of catalysts including zeolites, metals and carbon nanotube-metal oxide catalysts. The scope of these studies cover in several aspects ranging from physical to electronic phenomenon, such as hydrogen transfer ability of hydrocarbons which have an effect on product distribution and catalyst stability, possible reaction paths of anisole conversion on zeolites, alkylation of different aromatics on zeolites, metal-support interaction of nanohybrid catalysts, stability of intermediate species on metal catalysts, etc.

CHAPTER 1

1. Introduction

The global economy is anticipated to grow four-fold by 2050. Particularly in fast developing countries like China and India, the growing rate may increase up to ten-fold.¹ This economy development will certainly be supplemented by an increase in energy demand.² Even though some part of the energy requirement is predicted to be substituted by electricity (i.e., produced from fuel cells, wind and solar),³ there are situations that the use of oil is more preferable and cannot be replaced.⁴ For instances, high intensity of energy can be stored and transported efficiently in oil, whereas a loss of electricity may be high up to 20% during a long distance transportation. In addition, oil is still the pillar of petrochemical industry, used for the production carbon-based chemicals and polymers. Due to these benefits, it is envisaged that the demand for oil consumption will be continuing for decades. Nevertheless, the availability of fossil fuels can be considerably influenced by economical and political turbulences. Moreover, the use of fossil fuels has severe outcome on the greenhouse gasses emission. It is foreseen that a 130 % rise in CO₂ emissions by 2050.¹

Therefore, a growing interest in energy research is directed towards renewable energy sources. Biomass is clean because it emits a negligible amount of SO_2 , NO_x , as well as zero net emission of CO_2 , in which the released CO_2 from biomass can be recycled back into the plants by the photosynthesis process. Liquid product yield (bio-oil) from the biomass fast pyrolysis liquefaction may be high up to 70-80%. Therefore, transformation of biomass, such as wood, into energy becomes a more critical area of research, and promising technology for renewable fuel sources in the future.⁵⁻⁷ However, bio-oil upgrading is needed to improve its properties and make it more fungible as a regular fuel from petroleum.

1.1 Chemical composition of wood

The structure of wood is built from different fiber-like structures namely cellulose, hemicellulose and lignin. (see Figure 1.1) These fiber-like constituents account for 95 to 97 wt. % of dried wood,⁸ whereas the remaining are resin and minerals. Cellulose is the main component of plant cell walls, while hemicelluloses and lignin are found to be less abundant and differs in hardwood (angiosperms) and softwood (gymnosperms). Roughly 40-50 % of the mass of both types of wood, based on their dry substance, consists of cellulose. Hardwood and softwood consist of 16-25 % and 23-33 % of lignin; and 20-30 % and 15-20 % of hemi-cellulose, respectively.⁹

The energy content of biomass is lower, as compared to that of conventional hydrocarbon fuel, due to the high oxygen content. The corresponding low heating value is 16-18 MJ/kg (dry basis). This value is lower than that of the regular fuels having the heating values range between 40-44 MJ/kg.¹⁰

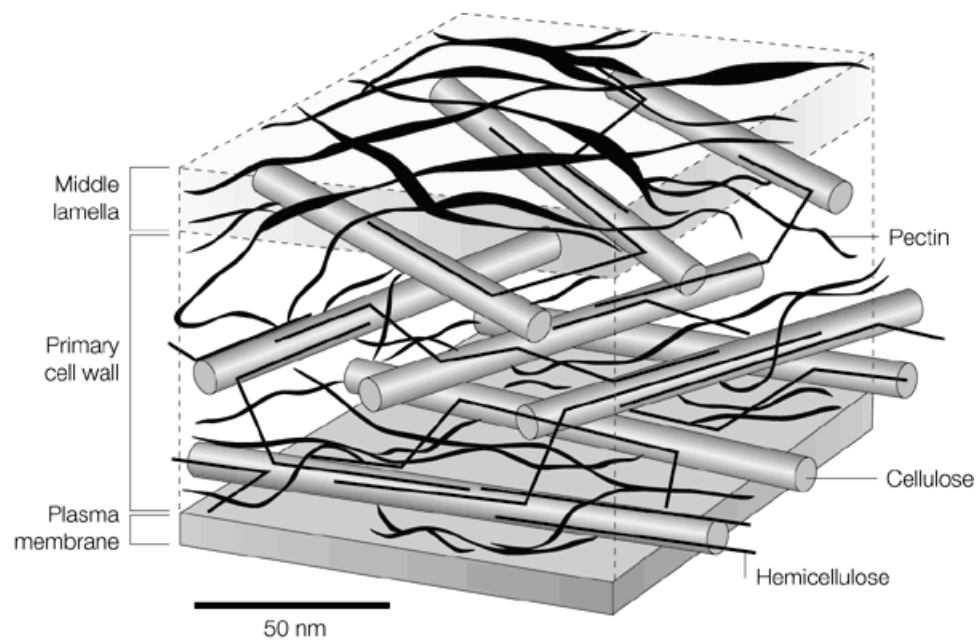


Figure 1.1 Lignocellulose composition of wood.¹¹

Cellulose

Polysaccharide, a so-called cellulose, is a backbone chain of D-glucose units linked by β -(1 \rightarrow 4) glucosidic bridge. Cellulose molecules contain 2,000 to

15,000 monomers of β -D-glucose, rotated by 180° with respect to each other. The cellulose polymers lie parallel to each other, and are held together by hydrogen bond. This leads to a band-like structure of cellulose polymers which possess diameters between 5-30 nm. Due to this high-strength structure, these molecules are extremely tough and durable.

Hemicelluloses

Hemicelluloses molecules are combined and branched polysaccharides. Major compositions are pentosanes and hexosanes. The former contains different pentose units, which are mainly D-xylose and L-arabinose; while the later are combination of hexoses, predominantly D-mannose, D-galactose, and D-glucose. Hemicelluloses are amorphous and contain a polymerization degree of about 200 monomers.

Lignin

Lignin is the second abundant fraction appearing in biomass. It contains numerous organic compounds, mainly containing carbonyl groups.¹²⁻¹⁴ Lignin is considered as a heterogeneous amorphous polymer, which consists of some extractives and inorganic materials. In contrast to cellulose and hemicellulose composed of 50/50 carbon and oxygen, lignin is formed of 60 wt. % carbon and

30 wt. % oxygen. Generally, lignin is synthesized from the polymerization of p-hydroxycinnamyl alcohol precursors,¹⁵ in which the corresponding basic constituent units of lignin are p-hydroxyphenylpropane, guaiacylpropane, and syringylpropane.

1.2 Pyrolysis of biomass

Since the past decade, there have been numerous studies dedicated for pyrolysis of biomass. It is conceivable that high heating rates and short reaction times in the pyrolysis process (i.e. so-called fast or flash pyrolysis) afford high yields of liquid products. Biomass is rapidly heated up to 500-600 °C in the absence of air/oxygen, which leads to decomposition of the biomass to a mixture of vapors and aerosols. And then the rapid cooling/condensation produce gases, char, and a dark viscous liquid, the bio-oil. Yields and properties of corresponding vapor, liquids, and solid products obtained from pyrolysis processes strongly depend upon various variables such as nature of the feedstock, heating rate, and reaction temperature. Generally, pyrolysis is a purely thermal process; however, some catalysts may be used during the conventional process.

Again, the amount of bio-oil, gas, and char produced from pyrolysis of wood depends on the chosen conditions.¹⁶ For examples, charcoal, CO₂ and water are predominant product for a pyrolysis at lower temperature (< 400 °C)

and heating rates (0.01-2 °C/s). This reaction path is shifted to liquid bio-oil production at higher temperature (400-800°C) and heating rate (10-1000 °C/s). As the pyrolysis temperature increased further, biomass can be cracked to mainly gaseous products such as CO, H₂ and CH₄.

1.3 Properties of bio-oils

As mentioned previously, physical and chemical properties of bio-oils strongly depend on the biomass feedstocks and on the pyrolysis conditions.¹⁷ Bio-oils are complex mixtures containing different class of molecules derived from degradation of cellulose, hemicellulose and lignin. Hence, the elemental constituents of bio-oil and conventional petroleum are different, and shown in Table 1.1.¹⁸

Generally, the bio-oils of oil plants have a higher heating value compared with those of wood, straw, or agricultural residues. For examples, bio-oils derived from safflower seed, rapeseed, and wood have heating values of 41.0, 36.4 and ~19 MJ/kg, respectively.^{19,20} The presence of water and oxygen content of bio-oils results in a less energy intensity. Density of bio-oils range from 1.19-1.28 g/cm³ and is comparatively higher than that of light oils.²¹

Table 1.1 Properties of wood pyrolysis bio-oils and regular fuels.

Properties	Bio-oil	Regular fuel
HHV (MJ/kg)	16–19	40
Density (g/cm ³)	1.19–1.28	0.85–0.94
pH	2.5–3.5	–
Flash point (°C)	53–76	45–70
Pour point (°C)	–12 to –33	–
Particulates (wt. %)	up to 3%	1
Viscosity (@ 50°C) (cP)	40–100	180
Water content (wt%)	15–30	0.1
Ash	0–0.2	0.1
Elemental analysis (wt%)		
C	54–58	85
H	5.5–7.0	11
O	35–40	1
N	0–0.2	0.3

A detectable pH obtained from bio-oils is around 2.5-3.5,²² substantially contributed from organic acids, particularly carboxylic acids such as acetic and formic acid. Again, the pH values are varied due to the type of feedstocks. For instances, the bio-oil of pine and hardwood have pH values of 2.6 and 2.8, respectively.²³ Drawbacks posed due to their acidity are corrosiveness and severity at elevated temperature, in which a special handling procedure is needed during the transportation and upgrading processes.

The flash point, which indicates the lowest temperature at which vapors above the liquid ignite when exposed to a flame, was reported to be between 53-76 °C, whereas the conventional diesel fuel flash points are known about 45-70 °C. Basically, flash points above 50 °C are determined to be safe. The pour point, indicating the lowest temperature that a liquid can be pumped,²⁴ is another important parameter for fuel applications. Pour points of bio-oils from hardwood and softwood are ranging from -12 to -33 °C, respectively.²⁵ Amount of small particulates may be varied due to different gas separation/filtration methods, and present up to 3 wt. % in bio-oils.²⁶⁻²⁸

Viscosity of bio-oils appears to depend on the age and water content of the bio-oil, therefore, a huge range of viscosity values can be expected. For examples, Bio-oils produced from rice straw, *Fraxinus mandshurica* and *Pterocarpus indicus* have a kinetic viscosity of 5-10, 10-70 and 70-350 mPa s, respectively.²⁹

Bio-oil contains a content of moisture up to 15-30 wt%. It is obtained from the original water in the feedstock as well as the product of dehydration during the process. The presence of water has both positive and negative effects on other bio-oils properties. For instances, the viscosity of bio-oils can be reduced (i.e., fluidity improved) by adding water, and at the same time, the heating value of bio-oils is lower. The presence of ash in bio-oils can cause an erosive/corrosive problem to the engines. Generally, minerals and alkali metals

such as sodium, potassium and vanadium and calcium, are responsible for those difficulties.

The oxygen content of bio-oils is typically high up to 35–40%.^{30,31} It is the major principal in deviating the bio-oil properties from the conventional fuel ones. The high content of oxygen results in the lower energy density of the bio-oils, and their immiscibility with hydrocarbon fuels. Bio-oils show a wide range of boiling point temperature due to their complex components. Moreover, the acidity of bio-oils makes them very reactive and unstable, in which polymerization can occur in the storage.

1.4 Compositions of bio-oils

Again, bio-oil is a complex mixture containing carbon, hydrogen and oxygen. It is composed of different species of oxygenated compounds including carboxylic acids, alcohols, aldehydes, esters, ketones, sugars, phenols, guaiacols, syringols, and furans.^{32,33} In addition to these organic compounds, the as-received bio-oil contains a lot of water, practically therefore, it can be divided into four fractions: namely aliphatic, aromatic, polar and non-volatile parts, by using solvent extraction and liquid chromatography techniques.³⁴ Identification revealed the high concentration of small polar components such as acetic acids and hydroxyacetones in the aqueous phase; and the highly oxygenated aromatic component in the oil phase.

Table 1.2 shows an example of the organic composition of bio-oil from the GC–MS analysis.²⁹ It is mainly composed of levoglucosan, furfural, phenols (with methyl, methoxy and/or propenyl groups), aldehydes (including benzaldehyde with methyl and/or hydroxyl) and vanillin, and also observed that these compositions are similar regardless the species of wood.^{29,35} In addition, it is noted that phenol and furan derivatives are the predominating compounds existing in the organic fraction of bio-oils.

Table 1.2 Main compositions in organic phase of bio-oil from *P. indicus*.

Compound	Relative composition (%)
Acetoxyacetone, 1-hydroxyl	1.21
<i>Furan derivatives</i>	(18.65)
Furfural	9.06
Furfural,5-methyl	1.82
Furanone, 5-methyl	0.49
2-Furanone	5.70
2-Cyclopentane-1-one, 3-methyl	1.58
<i>Phenol derivatives</i>	(54.39)
Phenol	2.55
Benzaldehyde, 2-hydroxyl	2.70
Phenol, 2-methyl	5.04
Phenol, 4-methyl	0.51
Phenol, 2-methoxyl	0.27
Phenol, 2,4-dimethyl	9.62
Phenol, 4-ethyl	2.18
Phenol, 2-methoxy-5-methyl	4.15
Phenol, 2-methoxy-4-methyl	0.55
Benzene, 1,2,4-trimethoxyl	3.80
Phenol, 2,6-dimethyl-4-(1-propenyl)	4.25
1,2-Benzenedicarboxylic acid, diisooctyl ester	1.80
Phenol, 2,6-dimethoxy-4-propenyl	3.14
Acetophenone, 1-(4-hydroxy-3-methoxy)	2.94
Benzaldehyde, 3,5-dimethyl-4-hydroxyl	4.54
Vanillin	6.35
Cinnamic aldehyde, 3,5-demethoxy-4-hydroxyl	2.19
Levoglucosan	6.75

1.5 Review of bio-oil upgrading

Direct utilization of bio-oil as the fossil fuel substitution presents a number of hindrances due to its poor properties such as high viscosity, thermal instability and corrosiveness. These problems are mainly contributed from the presence of oxygen content in the bio-oil. Hence, upgrading processes are required to remove the oxygen. Different approaches can be applied for the upgrading of bio-oils. Heterogeneous catalysts can be employed during the pyrolysis process in order to modify the vapor composition; otherwise, they can be used with bio-oils in order to modify the type and amount of functional groups in the oils. There are several techniques, both physical and chemical methods, have been studied.

Since the late 1980s, vapor phase catalytic reactions during the pyrolysis of biomass have been studied,³⁶⁻⁴³ in which zeolite materials were used as catalysts. In 1997, Katikaneri *et al.* combined catalytic approach into a fluidized bed reactor during the pyrolysis.⁴⁴ They used the solid catalyst (i.e., HZSM-5) as fluidizing material in the reactor. The liquid and gaseous products were separated and collected. In addition, they also studied the catalytic upgrading of pyrolysis oil produced from maple wood by the RTPTM process from ENSYN Technologies Inc.⁴⁵ Zeolites and silica-alumina catalysts were employed for these investigations. It is remarkable that the silica-alumina catalyst exhibited the highest selectivity for aliphatic hydrocarbons, whereas the HZSM-5 catalyst afforded the highest selectivity toward aromatic

hydrocarbons and the highest yield of organic liquid product. Another similar work on zeolites was reported by Williams *et al.*^{46,47} The objective was to investigate the effect of the presence of zeolites on formation of hazardous polycyclic aromatic hydrocarbons. It was noted that using zeolite catalyst for vapor phase upgrading during the pyrolysis resulted in an increased heavy aromatic compound production. And at the same time, the yield of pyrolysis oil decreased, while char and gaseous formation increased. Adjaye *et al.*^{48,49} exhibited that HZSM-5 was the most effective catalyst for producing the organic distillate fraction, overall hydrocarbons and aromatic hydrocarbons and the least coke formation. Reaction pathways were proposed that bio-oil conversion proceeded through the thermal decomposition and then followed by thermocatalytic conversion. The former step converted the bio-oil into light and heavy organics, as well as chars from polymerization of the bio-oil; while the later produced gas, water, coke, tar, and the desired organic fraction.

Oxygen existing in bio-oils can be removed catalytically as H₂O, CO₂, or CO. Nokkosmaki *et al.*⁵⁰ claimed that using ZnO catalyst in the pyrolysis vapor reaction can minimize the loss of liquid yields and improve the stability of the bio-oils. Adam *et al.*³⁵ showed the effects and catalytic properties of the mesopore structured MCM-41 based catalysts on bio-oil upgrading. It was found that the catalyst enhanced the production of acetic acid, furfural and furans, while the yields of phenolics compound reduced.

Another promising approach to obtain high quality bio oils is the hydrotreating processes. Generally, the reaction was performed by the catalysts of Co–Mo, Ni–Mo and their oxides on the Al₂O₃ supports under elevated pressure of hydrogen and/or CO. Oxygen is basically eliminated in the forms of H₂O and CO₂, in which the energy concentration of the bio-oils is enhanced. Pindoria *et al.*^{51,52} hydrotreated the vapor from fast pyrolysis and indicated that the catalyst deactivation resulted from the strong adsorption of the organic components themselves, which killed the acid sites, rather than the coke deposition. Elloit *et al.*⁵³ examined the effect of the flow directions on the conversion of bio-oils in a fixed bed reactor. They showed that the down-flow configuration bring about the higher conversion, as compared with the up-flow one. In addition, the two-fold conversion was observed over NiMo/ γ -Al₂O₃, in comparison of CoMo/spinel catalysts.

Moreover, the upgrading reaction by sulfided catalysts (i.e., sulfided Co–Mo–P/Al₂O₃) was investigated by Zhang *et al.*⁵⁴ This liquid phase reaction was operated at high pressure (2MPa) of hydrogen and temperature of 360 °C with the hydrogen donor solvent tetralin. It was marked that the oxygen content was reduced by 39%, and consequently the corresponding upgraded bio-oil was soluble in the hydrocarbon solvent. Boocock *et al.* studied the elimination of methoxy groups of phenol derivatives in bio-oils.⁵⁵ Sulfided and unsulfided forms of Mo_xO_y/Co_xO_y/ γ -Al₂O₃ and Mo_xO_y/Ni_xO_y/ γ -Al₂O₃ were used as catalysts. It was claimed that the sulfided cobalt oxide catalyst gave a higher loss of

methoxy groups in the bio-oils. A commercial Ru/ γ -Al₂O₃ catalyst and a copper chromite (CuCr₂O₄) catalyst were also tested by Gagnon *et al.*,⁵⁶ which suggested the optimum temperature for hydrodeoxygenation is as low as 80 °C.

1.6 Outline

The pillar of this thesis is the demonstration of the combined experimental and computational technique in research studies, in which the theme of bio-oil upgrading was emphasized. In this contribution, several useful theoretical techniques and analysis were incorporated toward the understanding of experimental results.

This chapter (Chapter 1) focuses on the introduction and background in bio-oils that involve in various aspects including research motivation, their production, compositions, properties, and upgrading. In the next chapter (Chapter 2), the basic principles regarding the quantum calculation are detailed. Some theoretical equations and concepts are presented. It is encouraged to be familiar with those meanings and definitions, particularly for a beginner, since they will constantly appear throughout the thesis.

After these introductory chapters, results will be given. In Chapter 3, the new method of H-transfer measurement was introduced. In this regard, 1-tetralone was used as the probe molecule, in which the degree of H-transfer

activity can be determined by the naphthalene-to-naphthol yield ratio. The H-transfer ability of different hydrocarbons, i.e. *n*-decane, decalin, tetralin and dimethyl tetralin, were tested and reported in Chapter 4. The effect of acid density of zeolites on the H-transfer rate was demonstrated. In addition, the -C-H bond strength of those H-donor molecules was calculated by the Wiberg bond index to compare with the H-transfer ability derived from the experiment.

Chapter 5 deals with the reaction of anisole on acidic zeolites. The reaction pathways and the effect of different hydrocarbon mixtures, such as tetralin, benzene, and *n*-decane, on the anisole conversion were discussed. Anchoring ability of Pd nanoclusters on carbon nanotubes was theoretically investigated in Chapter 6. Pristine and functionalized single- and multi-wall carbon nanotube models were used as platforms for the comparative study of the adsorption energies. Chapter 7 exhibits the comparison of the adsorption stability of aldehydes, i.e. furan and methyl pentanal, on pure Pd and bimetallic Pd-Cu. Both periodic slab and cluster models were used for the DFT calculation in this work.

The last chapter of this thesis (Chapter 8) presents a couple of examples demonstrating the benefit of combined experimental and theoretical technique. In this regards, the DFT calculations were performed in order to calculate heats of adsorption of different simulated systems, such as aromatics on acid sites, olefins and isopropylamine on cation-exchanged zeolites, and aldehydes on

Pd(111) surfaces. Moreover, some other small projects or uncategorized theoretical works were collected in the Appendices section.

References

-
- 1 International Energy Agency, Energy Technology Perspectives 2008. IEA Publications, Paris, **2008**.
 - 2 Shell energy scenarios to 2050. Shell international BV, **2008**.
 - 3 T.L Friedman *Hot, flat, and crowded*. Farrar, Straus and Giroux, New York, **2008**.
 - 4 M.J. Groeneveld *Inaugural Lecture*. University of Twente, Enchede, **2008**.
 - 5 S.R. Czernik, A.V. Bridgwater *Energy Fuels*. **2004**,18,590.
 - 6 D.S. Scott, J. Piskorz, D. Radlein *Ind Eng Chem Process Des Dev*. **1985**,24,581.
 - 7 A.V. Bridgwater, G.V.C. Peacocke *Sustain Renew Energy Rev*. **2000**,4,1.
 - 8 E. Sjöström *Wood Chemistry. Fundamentals and Applications*, Academic Press, New York, **1981**,208.
 - 9 W.E. Hillis, *In: Fundamentals of Thermochemical Biomass Conversion*, R.P. Overend, T.A. Milne, and L.K. Mudge (Eds.), Elsevier ASP, London, **1985**,14.
 - 10 M. Grabosky, R. Bain, *Properties of Biomass Relevant to Gasification, A Survey of Biomass Gasification. Volume II. -Principles of Gasification*, T.B. Reed, ed., Solar Energy Research Institute, Golden, CO, SERI/TR-33-329, **1979**.
 - 11 L.G. Smith *Nat Rev Mol Cell Bio*. **2001**,2,33.

-
- 12 P. Klason *Ber Dtsch Chem Ges.* **1920**,55,448.
- 13 E. Adler, K.J. Björkqvist, S. Häggroth *Acta Chem Scan.* **1948**,2,93.
- 14 E. Adler, L. Ellmer *Acta Chem Scan.* 1948,2,839.
- 15 W.G. Glasser *Lignin, In: Fundamentals of Thermochemical Biomass Conversion*, R.P. Overend, T.A. Milne, and L.K. Mudge (Eds.), Elsevier ASP, London, **1985**,61.
- 16 D. Radlein, J. Piskorz, D.S. Scott *J An App Pyrolysis* **1991**,19,41.
- 17 L. Fagernäs, *VTT Research Notes.* **1995**,1706.
- 18 A. Oasmaa, S. Czernik *Energy Fuels* **1999**,13,914.
- 19 S.H. Beis, O. Onay, O.M. Kockar *Renew Energy.* **2002**,26,21.
- 20 D. Ozcimen, F. Karaosmanoglu *Renew Energy.* **2004**,29,779.
- 21 R. Maggi, B. Delmon *Fuel.* **1994**,73,671.
- 22 D. Radlein, J. Piskorz, D.S. Scott *J An App Pyrolysis.* **1987**,12,51.
- 23 J.P. Diebold, NREL/SR-570-27613, **2000**.
- 24 G.V. Dyroff, 1993, 6. Ed., Philadelphia; ASTM; In: Oasmaa et al. *VTT Publication Nr. 306*, **1997**.
- 25 A. Oasmaa, E. Leppämäki, P. Koponen, J. Levander, E. Tapola *VTT Publication Nr. 306*, **1997**.
- 26 R. Maggi, B. Delmon, *In: Advance Thermochemical Biomass Conversion*, A.V. Bridgwater (Ed.), Blackie, **1994**,2,1086.
- 27 J.P. Diebold, S. Czernik, J.W. Scahill, S.D. Phillips, C.J. Feik, *Biomass Pyrolysis Oil Properties and Combustion Meeting*, Estes Park, Colorado, **1994**,90.
- 28 J.P. Diebold, J.W. Scahill, S. Czernik, S.D. Phillips, C.J. Feik, *Proceedings of the 2nd EU/Canada Workshop on Thermal Biomass Processing*, CPL Press, Newburry, U.K., **1996**,66.

-
- 29 Z.Y. Luo, S.R. Wang, Y.F. Liao, et al. *Biomass Bioenergy*. 2004,26,455.
- 30 B. Scholze, D. Meier *J Anal Appl Pyrol*. **2001**,60,41.
- 31 A. Oasmaa, S. Czernik *Energy Fuels*. **1999**,13,914.
- 32 Y. Guo, Y. Wang, F. Wei, et al. *Chem Ind Eng Progr*. **2001**,8,13.
- 33 W.M. Peng. Q.Y. Wu *New Energy Sour*. **2000**,22,39.
- 34 S.P. Zhang, Y.J. Yan, Z.W. Ren, et al. *J Chin Sci Technol*. **2001**,27,666.
- 35 J. Adam, M. Blazsó, E. Mészáros, et al. *Fuel*. **2005**,84,1494.
- 36 R. Maggi, E. Laurent, P. Grange, B. Delmon, *In: Biomass Energy, Ind. Environ*, G, Grassi, A. Collina, H. Zibetta (Eds.), Elsevier, London, **1992**,2,657.
- 37 M.C. Samolada, I.A. Vasalos, *In: Advance Thermochemical Biomass Conversion*, A.V. Bridgwater, (Ed.), Blackie, **1994**,2,859.
- 38 M.C. Samolada, E.D. Grigoriadou, I.A. Vasalos, *In: Biomass Energy, Ind. Environ*, G, Grassi, A. Collina, H. Zibetta (Eds.), Elsevier, London, **1992**,2,731.
- 39 A.V. Bridgwater, M.L. Cottam *Energy Biomass Wastes*. **1993**,16,689.
- 40 A.V. Bridgwater, M.L. Cottam *Energy Fuels*. **1992**,6,113.
- 41 D.S. Scott, J. Piskorz, M.A. Bergougnou, R. Graham, R.P. Overend *Ind Eng Chem Res*. **1988**,27,8.
- 42 D.S. Scott, S. Czernik, J. Piskorz, D. Radlein *Energy Biomass Wastes*. 1990,13,1349.
- 43 D.S. Scott, J. Piskorz, D. Radlein *Energy Biomass Wastes*. **1993**,16,797.
- 44 S.P.R. Katikaneni, J.D. Adjaye, R.O. Idem, N.N. Bakhshi, *In: Developments in Thermochemical Biomass Conversion*, Blackie Academic & Professional London, A.V. Bridgwater and D.G.B. Boocock (Eds.) **1997**,1,633.

-
- 45 S.P.R. Katikaneni, R.O. Idem, N.N. Bakhshi, *In: Biomass Gasification and Pyrolysis, State of the Art and Future Prospects*, M. Kaltschmitt and A.V. Bridgwater (Eds.), CPL Scientific, Newbury, **1997**,411.
- 46 P.T. Williams, P.A. Horne *J Anal Appl Pyrolysis*. **1995**,31,39.
- 47 P.T. Williams, N. Nugranad, P.A. Horne *In: Biomass Gasification and Pyrolysis, State of the Art and Future Prospects*, M. Kaltschmitt and A.V. Bridgwater (Eds.), CPL Scientific, Newbury, 1997,422.
- 48 J.D. Adjaye, N.N. Bakhshi *Fuel Process Technol*. **1995**,45,185.
- 49 J.D. Adjaye, N.N. Bakhshi *Fuel Process Technol*. **1995**,45,161.
- 50 M.I. Nokkosmaki, E.T. Kuoppala, E.A. Leppamaki, et al. *J Anal Appl Pyrol*. **2000**,55,119.
- 51 R.V. Pindoria, A. Megaritis, A.A. Herod, et al. *Fuel*. **1998**,77,1715.
- 52 R.V. Pindoria, J.-Y. Lim, J.E. Hawkes, et al. *Fuel*. **1997**,76,1013.
- 53 D.C. Elliott, G.G. Neuenschwander *Liquid fuel by low-severity hydrotreating of biocrude. Developments in thermochemical biomass conversion*. London: Blackie Academic and Professional, **1996**,611.
- 54 S.P. Zhang, Y. Yongjie, T. Li, et al. *Bioresour Technol*. **2005**,96,545.
- 55 D.G.B. Boocock, S.G. Allen, A. Chrowdhury, R. Fruchtl, *In: Pyrolysis Oils from Biomass, Producing, Analyzing, and Upgrading*; E.J. Soltes and T.A. Milne (Eds.), ACS Symposium Series #376, American Chemical Society, Washington, DC, **1988**,92.
- 56 J. Gagnon, S. Kaliaguine, *Ind Eng Chem Res*. **1988**,27,1783.

CHAPTER 2

2. Computational Background

2.1 Introduction to quantum mechanics Hamilton

The hydrogen atom containing one electron is the only system that an exact solution of the Schrödinger equation can be solved. For other non-ideal systems which contain more than one electron, only approximate solutions can be found. First principle quantum mechanical calculations are characterized by the fact that only natural constants such as Planck's constant, electron mass, electronic charge, and the exact masses of the atoms are used as initial data sources. In contrast, semi-empirical methods use approximations with regard to starting constants and operators. That is the calculation of some of integrals is neglected or some values are replaced by empirical data.

A tremendous amount of computational effort may be required for quantum mechanical calculations of a large system. Hence, approximations have been needed to simplify the calculation process. For examples, the assumption of separation of the electron motion from the nuclear due to the significant difference in mass between nucleus and electron can be made in the Born-

Oppenheimer approximation; or the calculations are simplified by limiting the number of basis functions to a restricted set.

2.2 Schrödinger equation and Born-Oppenheimer approximation

The time-independent non-relativistic Schrödinger equation¹ for a particle of mass m is given by

$$\left[-\frac{\hbar^2}{2m} \nabla^2 + V(r) \right] \psi(r) = E \psi(r),$$

where the term in brackets represents the Hamiltonian operator \hat{H} . For a random molecule with total wavefunction Φ and Hamilton operator \hat{H}_{tot} , the general Schrödinger equation can be written as:

$$\hat{H}_{tot}|\Phi\rangle = E|\Phi\rangle.$$

For a molecule with N electrons and M nuclei, the Hamiltonian becomes as a sum of five terms:

$$\begin{aligned} \hat{H}_{tot} &= \hat{T}_{el} + \hat{T}_{nucl} + \hat{V}_{nucl-el} + \hat{V}_{el-el} + \hat{V}_{nucl-nucl} \\ &= -\sum_{i=1}^N \frac{1}{2} \nabla_i^2 - \sum_{A=1}^M \frac{1}{2M_A} \nabla_A^2 - \sum_{i=1}^N \sum_{A=1}^M \frac{Z_A}{r_{iA}} + \sum_{i=1}^{N-1} \sum_{j>i}^N \frac{1}{r_{iA}} + \sum_{A=1}^{M-1} \sum_{B>A}^M \frac{Z_A Z_B}{R_{AB}}. \end{aligned}$$

The first term represents the kinetic energy of the electrons, followed by the kinetic energy of the nuclei, the electron-nucleus potential energy, the electron-electron potential energy, and the nucleus-nucleus potential energy.

The Born-Oppenheimer approximation is based on the idea that the mass difference between nucleus and electron is so large (e.g. H-Atom: $m_p/m_e = 1832$), so that their movements is independent from each other. The movement of the electrons is much faster in comparison of the nucleus. That is the nucleus is considered to be fixed, while the electron movement can be characterized by a separate Schrödinger equation. As a result, the nuclear kinetic energy term can be neglected, while the nucleus-nucleus potential energy term is considered to be constant and separated from the Hamilton operator. This minimizes the Hamilton operator to the following expression

$$\hat{H}_{elec} = - \sum_{i=1}^N \frac{1}{2} \nabla_i^2 - \sum_{i=1}^N \sum_{A=1}^M \frac{Z_A}{r_{iA}} + \sum_{i=1}^{N-1} \sum_{j>i}^N \frac{1}{r_{iA}}$$

and the Schrödinger equation can be simplified to

$$\hat{H}_{elec} |\psi_{elec}\rangle = E_{elec} |\psi_{elec}\rangle$$

where

$$\psi_{elec} = \psi_{elec}(\{\mathbf{r}_i\}; \{\mathbf{R}_A^0\})$$

The electronic wavefunction ψ_{elec} describes the motion of the electrons and is dependent on the coordinates of electrons $\{\mathbf{r}_i\}$ as variables. Here, $\{\mathbf{R}_A\}$ represents the set of coordinates for the fixed nuclei which is not considered as a variable in the calculation, but will influence the initial conditions of the Hamilton operator by potentially altering the electronic wavefunction itself. Another feature of the Born-Oppenheimer approximation is that it allows the total wavefunction to be estimated as a product of a nuclear wavefunction (χ_{nucl}) and an electronic wavefunction in which the nuclei have fixed coordinates (\mathbf{R}_A):

$$|\Phi\rangle_{BO}(\{\mathbf{r}_i\}; \{\mathbf{R}_A\}) \cong \psi_{\text{elec}}(\{\mathbf{r}_i\}; \{\mathbf{R}_A\}) \cdot \chi_{\text{nucl}}(\{\mathbf{R}_A\})$$

This relationship is also known as the adiabatic approximation.

2.3 Quantum mechanical methods

A wide range of first principle quantum mechanical calculation methods have been developed. However, most of calculations are carried out using only a particular sub class of methods also known as molecular orbital methods. The earliest and most extensively used molecular orbital method is the Hartree-Fock method.

Hartree-Fock method (HF)

Hartree-Fock calculation appears to be the oldest first principle approach, which is based on a few principles and do not employ any experimental data. The method works in principle by selecting one electron and estimating the interaction between itself and all other electrons by a mean value that is determined from their probability densities. This approach neglects the correlated movement of the electrons caused by their repulsion through equal electric charges. Despite this deficiency known as the “electron correlation error”, the Hartree-Fock method provides accurate results in many cases and is not limited to a specific class of chemical compounds. However, Hartree-Fock calculations require tremendous computer time.

Semi-Empirical methods

Semi-empirical calculations can be categorized somewhere in between first principle and molecular mechanics methods. Semi-empirical methods determine molecular orbitals within the Linear Combination of Atomic Orbitals (LCAO) model and are based on the variation principle in which most integrals along these calculations are approximated from experimental data. Hence, for chemical compounds that lie outside the classes of which these estimations are parametrized, results may be less accurate. However, semi-empirical calculations can be parametrized in detail for specific cases such as

spectroscopic properties. Most semi-empirical programs make use of the zero differential overlap (ZDO) approximation, which defines the overlap between different basis functions as zero. The various ZDO models can be lumped according to their approximations for one- and two-electron integrals.

Configuration Interaction (CI)

Together with the Møller-Plesset perturbation theory (MP) and Coupled Cluster (CC) methods, configuration interaction (CI) belongs to the class of post-Hartree Fock methods. Calculations of these types of calculation target at the approximation of the electron correlation based on the variation principle and MO-approach. The computational cost is rather expensive in which a lot of computer time and storage are required. Therefore, the major of application is subjected to small molecules. Moreover, they need a discrete choice of orbitals to be included which has to be manually performed.

Density Functional Theory (DFT)

Density Functional Theory (DFT) methods were developed by Kohn and Sham and are often considered as first principle methods for determining the molecular electronic structure, even if a lot of the most basic functionals use parameters derived from empirical data or from more complex calculations. In

DFT, the total energy is expressed in terms of the total electron density rather than the wave function, as in the HF method. In addition, there is an approximate Hamiltonian and an approximate expression for the total electron density, that is the DFT methods can be impressively accurate for less cost of computation. Nevertheless, unlike the pure first principle methods, there is no systematic way to improve the calculation by extending the form of the functional basis, since the electronic energy of the ground state of a system is totally described by the electron density. The energy itself is expressed as a functional which is practically a function of the electron density. Analogous to the wave function approach, the functional can be split into three terms:

$$E[\rho] = T[\rho] + E_{ne}[\rho] + E_{ee}[\rho]$$

where $T[\rho]$ is the kinetic energy of non-interacting electrons, $E_{ne}[\rho]$ describes the electron-nuclei interaction and the so-called Hartree term, $E_{ee}[\rho]$, is the electron-electron interaction, which can be split in a Coulomb part, $J_{ee}[\rho]$, and an exchange part, $E_{xc}[\rho]$.

Calculation of $T[\rho]$ and $E_{xc}[\rho]$ can be performed with the assumption of a homogeneous electron gas with non-interacting particles. Kohn and Sham presented the DFT for use in computational chemistry by the introduction of orbitals. $T[\rho]$ is split in an exactly computable term $T_s[\rho]$ and a small correction term. The calculation of $T_s[\rho]$ is carried out under the assumption of non-interacting particles, i.e. the orbital occupancy is expected to be 0 or 1,

resulting in an error since partially occupied orbitals are not valid in this approach.

2.4 Exchange-correlation functionals

To describe $E_{XC}[\rho]$, two approximations are generally used: the Local Density Approximation (LDA) and the Generalized Gradient Approximation (GGA). LDA is based on a model called uniform electron gas.² The assumption made for this approximation is that the charge density varies gradually throughout a molecule so that a localized region of the molecule behaves like a uniform electron gas,

$$E_{XC}^{LDA}[\rho(r)] = \int \rho(r) \varepsilon_{XC}[\rho(r)] dr$$

The energy functional describes local value of ρ at each point in space regardless at any other point. For GGA, an additional term is added to the LDA exchange-correlation energy. Gradient correlation are introduced to allow exchange correlation functional to vary (the density gradient is taken into account) and $E_{XC}[\rho]$ is expressed as

$$E_{XC}^{LDA}[\rho(r)] = \int f_{XC}(\rho(r), |\nabla\rho(r))\rho(r) dr$$

There are many exchange-correlation expressions in the literature, for example, Perdew (P86), Becke (B86, B88), Perdew-Wang (PW91), Laming-Termath-Handy (CAM) and Perdew-Burke-Enzerhof (PBE) deal with the exchange; while Perdew (P86), Lee-Yang-Parr (LYP), Perdew-Wang (PW91) and Perdew-Burke-Enzerhof (PBE) deal with the correlation.³⁻⁹

There is a third class of functionals in DFT which are called hybrid functionals, such as the popular B3LYP¹⁰ exchange-correlation functional. These include the exact exchange energy as a contribution from the exact exchange. This approach has extensively proven its accuracy for many systems, although they are much more time-demanding than the non-hybrid exchange-correlation functionals.

2.5 Basis functions

According to the LCAO principle, MOs (molecular orbitals) can be approximated by linear combination of AOs (atomic orbitals):

$$f(\vec{r}) = \sum_{i=1}^{\infty} a_i \psi_i(\vec{r})$$

AOs consist of wavefunctions ψ_i , and a complete set of functions would allow the exact description of any MO. Mathematically speaking, the complete basis sets, for example the Laguerre-functions, are used in the description of the

hydrogen atom. Generally, however, basis sets are always limited to a finite number of basis functions $\{\psi_i, i = 1, 2, \dots, k\}$, and the major errors in quantum mechanical MO calculations occur due to this limitation.

2.6 Basis sets

A basis set is a set of functions used to describe the orbital shapes existing in an atom. Molecular orbitals and entire wave functions are composed of the linear combinations of basis functions and angular functions. Most semi-empirical methods use in a predefined basis set. When first principle or density functional theory calculations are done, a basis set must be specified. Even though it is possible to create a basis set from scratch, most calculations are done using existing basis sets including minimal basis sets such as double zeta (DZ), triple zeta (TZ), split-valence basis sets, polarization functions and diffuse functions.

2.7 Quantum mechanical calculations

Single point calculations

This calculation is performed to obtain information regarding the energy, wave function and other interesting properties at a single fixed geometry. Single point calculations are usually carried out at the beginning of a study on a new molecule to gain an insight into the nature of the wave function. Nevertheless, they are also frequently done after a geometry optimization. In comparison of the geometry optimization, a larger basis set and a more superior method are required in the single point calculation. Therefore, the geometry optimization at a lower level and the energy calculation with a higher one are recommended for such a large system.

Geometry optimization calculations

This procedure calculates the wave function and energy at an initial geometry and then proceeds to a new geometry which presents a lower energy. This process is then iterated until a local minimum in the vicinity of the initial geometry has been found. In fact, this procedure determined the forces on the atoms by evaluating the gradient (first derivative) of the energy with respect to the atomic coordinates. In most of the cases, gradients may be calculated or

sophisticated algorithms may be used for choosing new geometries, resulting in a more rapid convergence towards the local minimum. However, it is marked that this procedure will not necessarily seek the lowest energy geometry, i.e. the global minimum.

Finding all local minima, and therefore the global minimum, for a particular set of atoms is not a simple job. The optimization sometimes eventually finds a saddle point which basically represents a transition state geometry. This will occur particularly if the symmetry and degrees of freedom are aimingly restricted. It is always a good idea to start a geometry optimization with a minimal basis set and method before proceeding to the more sophisticated ones for a particular problem. A geometry optimization can be initiated from geometries which were generated by a poorer approach.

Frequency calculations

Frequency calculations allow the prediction of IR and Raman spectra and their intensities through force constants while assuming the model of a harmonic oscillator. Vibrational frequencies are obtained by calculating the second derivatives of the energy with respect to the Cartesian coordinates of nuclei, and then transforming them to mass weighted coordinates. This transformation is only available at a stationary point. Frequencies calculated at an optimized local or global minimum have all real (positive) values. In

contrast, frequencies at a stationary point other than a minimum (e.g. saddle point) have one or more complex (negative) values, in which having one ‘imaginary frequency’ is used as an indicator for the existence of a transition structures.

By incorporating statistical thermodynamic concepts, frequency calculations also allow the calculation of thermodynamic quantities including zero-point energy (ZPE), Gibbs free energy, heat capacity, and entropy at a particular temperature. The computations are carried out by evaluating the vibrational, rotational, and translational partition functions at a specific temperature using standard expressions for an ideal gas.

2.8 Modeling a surface

The real catalysts in heterogeneous catalysis processes are typically subjected to different classes of solids such as metals and zeolites. Modeling this complex structure at the molecular level is impossible, but the simplified model. In fact, as an infinite number of atoms containing in real catalysts, this implies that the wave function has to be calculated for each of the infinite number of electrons and the basis set in which the wave function is expressed will be also infinite. Nevertheless, they can be modeled by two different approaches: the so-called cluster model approach,^{11,12} and the periodic slab model approach.^{11,13} In this thesis, the former is used to model zeolite catalysts; the latter is used to

model metal catalysts. In addition, the details of the periodic slab calculation are primarily focused in this present chapter.

The finite models have extensively proven their ability to describe local properties.¹⁴⁻¹⁶ The slab model is based on the band-structure theory. A bi-dimensional slab is formed by periodically repeating the geometry of the system on the x and y axes; whereas in the z axis, the periodicity is broken with a vacuum space to create the surface.

This periodic approach has some advantages compared to the cluster model. For example, it correctly describes materials with perfect faces are crystalline surfaces, making possible to study non local properties. Another advantage of supercell models is that they are well suited for studying the influence of adsorbates coverage on the surface. However, to study low coverage situations with slab models, a large supercell is needed, with a concomitant increase in computational costs.

Bloch's theorem and the plane-wave basis set

For a perfect metallic crystal, atoms are arranged in a pattern. The periodic units of the system are all equivalent and can be obtained by repeating a unit cell. The definition of a unit cell is not unique. It is possible to choose a unit cell with the smallest volume or the one having best symmetry properties.

Bloch's theorem applies the periodicity of the crystal to reduce the infinite number of one-electron wave functions to be computed to just a number of electrons. That is one can express the one-electron wave functions as the product of a cell periodic part and a wave-like part (Bloch functions).

$$\psi_{n,\vec{k}}(\vec{R}) = \exp i(\vec{k} \cdot \vec{R}) \phi_{nBAND,\vec{k}}(\vec{R})$$

where $\psi_{n,\vec{k}}(\vec{R})$ is the wave function of the periodic system, \vec{R} is the position in the crystal, \vec{k} is a vector in the crystal reciprocal space and $\phi_{nBAND,\vec{k}}(\vec{R})$ is a function associated with an energetic level for a periodical system (band) $nBAND$. The difficulty is then translated from the real to the reciprocal space. The infinite number of electrons is now mapped onto the problem of expressing the wave function in terms of an infinite number of reciprocal space vectors within the first Brillouin zone, \vec{k} . Unfortunately, one can not allocate an infinite number of \vec{k} . This problem can be resolved by sampling the Brillouin zone at special set of k-points in which be calculated by various methods. Among of those, the most popular ones are the Monkhorst-Pack method,¹⁷ the Cunningham method,¹⁸ and the Chadi-Cohen method.¹⁹ The total wave function at each k-point can be represented in terms of a discrete plane-wave basis set (3D-Fourrier series).

$$\psi_{n,\vec{k}}(\vec{R}) = \sum_g a_{nBAND,\vec{g},\vec{k}} \exp i(\vec{g} + \vec{k})\vec{R}$$

In principle, this set is infinite but one can consider it converged for large values of $|\vec{g} + \vec{k}|$. Introducing a plane-wave energy cut-off $|\vec{g} + \vec{k}| \leq E_{cut-off}$ reduces the basis set to a finite size. This energy cut-off value depends on energy system. Thus, it is crucial to test the convergence of the energy in order to take a correct value of the cut-off. In addition, the use of plane-waves forces to express the vacuum with the same accuracy as the regions of high electronic density. A large number of plane-waves are habitually needed. Using pseudopotentials reduces the $E_{cut-off}$ and, consequently, the size of the expansion.

The Projected Augmented Wave method

The computational cost can be tremendously increased particularly for such transition metals containing a large number of electrons. One way to handle this problem is to assume that the chemical bond does not depend on the core electrons. In fact, only the bonding energy is affected by the average electrostatic potential generated in the vicinity of the core. The plan is then to model the core electrons and their interaction with the other electrons. The concept of pseudopotential was introduced by Fermi and Hellmann who proposed to solve the Schrödinger equation for the valence electrons in the subspace orthogonal to the core electrons. This concept was extensively accepted and led to the development of pseudopotential methods such as norm-conserving pseudopotentials,²⁰ ultra-soft pseudopotentials (US-PP),²¹ and the

Projected Augmented Wave (PAW) method.²² The PAW method, introduced by Blöchl in 1994²² is built on projector functions that allow the complicated wave functions to be mapped onto “pseudo” wave functions, which are easier to be treated computationally. With this approach, one can model the core electrons taking the difference between the exact wave function and a pseudo-wave function obtained and neglecting the core electrons. The Schrödinger equation is then expressed as

$$\tau * H\tau\tilde{\Psi} = E\tau * \tau\tilde{\Psi}$$

Where $\tilde{\Psi}$ is pseudo wave function and τ is the operator of transformation that connected the exact wave function and the pseudo-wave function. In DFT, the Schrödinger equation is solved in order to determine the pseudo-wave function. Projectors then enable one to obtain the exact density, as long as the basis set expansion is complete. The PAW method has extensively proven its high performance for studying molecules, surfaces and solids.

2.9 The VASP code

The program VASP (Vienna *ab initio* Simulation Package), developed by G. Kresse, J. Furthmüller and J. Hafner,^{23,24} has been used widely to obtain a principal understanding in the surface catalysis. VASP applies DFT to periodical systems, using plane-waves and ultrasoft pseudopotentials (US-

PP).^{25,26} The US-PP reduces significantly the number of plane-waves needed by relaxing the norm conservation constraint on the pseudo wavefunction.

The Kohn-Sham equations are solved self-consistently with an iterative matrix diagonalization combined with a Broyden mixing method²⁷ for the charge density. The combination of these two methods makes the code very efficient, especially for transition metal systems presenting a complex band structure around the Fermi level. The forces acting on the atoms are calculated and can be used to relax the geometry of the system. Most of the algorithms implemented in VASP use an iterative matrix diagonalization scheme. They are based on the conjugate gradient scheme, or a residual minimization scheme - direct inversion in the iterative subspace (RMMDIIS). Those algorithms are working in a following way: it calculates the electronic ground state for given geometry, calculate forces, and then, based on the forces a new geometry is predicted and those steps are repeated until a criterion is reached. A special algorithm is the quasi-Newton, where the energy criterion is ignored and only the forces are minimized. Transition States structures and energies are also possible to find using a different technique implemented in the VASP code.

Plane waves are used as basis set and ultra soft pseudopotentials are replacing the core part of atoms. This allows a significant decrease of computational time. The Hamiltonian is easy to be determined in peaces in direct and reciprocal space. Fast Fourier Transformations (FFT) are used to

switch from direct to reciprocal space and opposite. This allows a decrease of number of plane-waves, which allows a partial diagonalization.

For the mixing of the charge density, an efficient Broyden/Pulay mixing scheme is used for convergence in a self-consistent density functional calculation. The linear mix of the two (or more) previous charge densities can be made; this can give significant benefits.^{23,28} It is often important to mix in a small amount of the input charge densities, as well as performing the mixing.

For partial occupancies, (techniques to improve the convergences with respect to k-points sampling) different methods are used: linear tetrahedron method (good for bulk calculation), smearing methods like finite temperature approaches (good for convergence of metallic surfaces), or improved functional form: Methfessel and Paxton method, finite methods, like gaussian or fermi smearing (good for accurate calculation required for DOS diagram, etc.)

The number of k-points sample in the irreducible part of the Brillouin zone is important for the accurate integration of the properties computed in reciprocal space. The k-points sample is often calculated by the program using the Monkhorst-Pack²⁹ method using a given mesh. Within the finite temperature approach, forces are defined as the derivative of the generalized free energy.

2.10 Nudged Elastic Band

The Nudged Elastic Band (NEB) Method developed by Jónsson *et al.*³⁰ is used to calculate the transition states. The major difference between NEB and elastic band (EB) method³¹ is that on NEB the perpendicular component of the spring force (on the reaction path) and the parallel component of the true force are projected out. Both are chain-of-states methods. Two points in the configuration space (hyperspace containing all the degrees of freedom) are required (initial and final state) and a linear interpolation can be made to produce the images along the elastic band. The program runs simultaneously each image and communicates (the forces) at the end of each ionic cycle in order to calculate the force acting on each image.

The term “nudged” indicates that the projection of the parallel component of true force acting on the images and the perpendicular component of the spring force are canceled. A smooth switching function is introduced and gradually turns on the perpendicular component of the spring force at large differences in the energies between images. The results obtained from the NEB are refined with a quasi-Newton algorithm²⁸ implemented in VASP. This implies that the atoms are moved to minimize their forces. However, the total energy is not taken into account for minimization. In this contribution, the program will be searching a stationary point.

2.11 Energy

The analysis of energetics can describe what molecular processes are likely to happen. All computational chemistry methods define a system with the lowest energy as the most stable structure. Thus, searching the shape of a molecule corresponds to searching the shape with the lowest energy. The amount of energy in a system can be divided into kinetic and potential energies. The kinetic energy may be further classified into vibrational, translational and rotational motion. A distinction is also made between the kinetic energy due to the motions of nuclei versus electrons. The potential energy may be described purely by the Coulomb's law, or broken down into energies of conformational energy, bond stretching and bending, hydrogen bonds, and so on.

Chemical processes, such as bond stretching or reactions, can be divided into adiabatic and diabatic processes. Adiabatic processes are those in which the system does not change state throughout the process, whereas diabatic, or nonadiabatic, processes are those in which a change in the electronic state is part of the process. Diabatic processes normally follow the lowest energy path, or may change state as necessary. In calculating a mathematical model of molecules, it is necessary to define a reference state that is defined as having zero energy. This zero of energy is different from one approximation to the other. For first principle or density functional theory (DFT) methods, which simulate all the electrons in a system, zero energy refers to having all nuclei and electrons at an infinite distance from one another. For some molecular

mechanics methods, the zero of energy is totally arbitrary. Even within a particular approximation, total energy values relative to the method of zero energy are often very inaccurate. That is almost always the result of systematic error. However, the most accurate values can be obtained by subtracting total energies from separate calculations. This is how the bond dissociation energies can be calculated accurately.

2.12 Population analysis

Population analysis is a mathematical approach of partitioning a wave function or electron density into charges on the nuclei, bond orders, and other related information. These are the most extensively used information that is not experimentally detectable because atomic charges do not correspond to any unique physical property. In fact, atoms have a positive nucleus surrounded by negative electrons, not partial charges on each atom. However, condensing nuclear charges and electron density down to partial charges on the nucleus results in an understanding of the electron density distribution. These are not integer formal charges, but rather fractions of an electron corresponding to the probability of an electron are near each nucleus or atom. Although this is an artificial assignment, it is very effective for predicting the sensitivity to nucleophilic or electrophilic attack and other aspects of molecular interaction. Only the most ionic compounds, such as alkali metal halides, will have nearly

whole number charges. Organometallics typically have charges on the order of ± 0.5 . Organic compounds often have charges around ± 0.2 or less.

Mulliken population analysis

One of the most extensively used population analysis methods is the Mulliken population analysis. The principal assumption used by the Mulliken scheme for partitioning the wave function is that the two overlapping orbitals are shared equally. This does not totally reflect the electronegativity of the individual elements. However, it does give a way for partitioning a wave function and has been found to be very effective for small basis sets. For large basis sets, results can be very unreasonable. This is due to diffuse functions describing adjacent atoms more than they describe the atom on which they are centered. In some cases, Mulliken analysis can assign an electron population to an orbital that is negative or more than two electrons. In addition, it tends to underestimate the charge separation in ionic bonded systems. Nevertheless, the Mulliken population is very popular since it is very easy to implement. That is why it is available in many software packages. This is a great benefit because population analysis is often used for the purpose of understanding chemistry rather than quantitatively predicting experimental results.

In Mulliken analysis, the integrals from a given orbital are not added. Instead, the contribution of a basis function in all orbitals is summed to give

the net population of that basis function. Likewise, the overlaps for a given pair of basis functions are summed for all orbitals in order to determine the overlap population for that pair of basis functions. The overlap populations can be zero by symmetry or negative, indicating anti-bonding interactions. Large positive overlaps between basis functions on different atoms are one indication of a chemical bond.

Gross populations are determined by starting with the net populations for a basis function, then adding half of every overlap population to which that basis function contributes. The Gross populations for all orbitals centered on a given atom can be summed in order to obtain the gross atomic population for that atom. The gross atomic population can be subtracted from the nuclear charge in order to obtain a net charge. Further analysis of overlap populations can yield bond orders.

Löwdin population analysis

The Löwdin population analysis was created to avoid some of the unreliable orbital populations predicted by the Mulliken analysis. The difference is that the atomic orbitals are first transformed into an orthogonal set, and then the molecular orbital coefficients are transformed to the representation of the wave function in the new basis. This type of analysis is less often used

because it requires more computational cost to complete the orthogonalization and has been incorporated into fewer software packages.

Natural bond order analysis

Natural bond order analysis (NBO) is the name of a whole set of analysis techniques. One of these is the natural population analysis (NPA) for obtaining occupancies (how many electrons are assigned to each atom) and charges. However, usage of the acronyms NBO and NPA might be interchangeable.

Rather than using the molecular orbitals directly, NBO uses the natural orbitals. Natural orbitals are the eigenfunctions of the first-order reduced density matrix. These are then localized and orthogonalized. The localization procedure allows orbitals to be defined as those centered on atoms and those encompassing pairs of atoms. These can be integrated to obtain charges on the atoms. Analysis of the basis function weights and nodal properties allows these transformed orbitals to be classified as bonding, antibonding, core, and Rydberg orbitals. There is also a procedure that searches for the π bonding patterns typical of a resonant system. This is not a rigorous assignment as there may be some electron occupancy of anti-bonding orbitals, which a simple Lewis model would predict to be unoccupied.

This results in a population analysis that is less basis set dependent than the Mulliken analysis. However, basis set effects are still readily apparent. This is also a popular technique because it is convenient to use a method that classifies the type of orbital.

Atom in molecules

A much less basis set dependent method is to analyze the total electron density. This is called the atoms in molecules (AIM) method. It is designed to examine the small effects due to bonding regardless of the electron density. This is done by examining the gradient and Laplacian of electron density. AIM analysis incorporates a number of graphic analysis techniques as well as population analysis. The first step in this process is to examine the total electron density to find the critical point in the middle of each bond. This is the point of minimum electron density along the line connecting the atoms. It reflects atomic sizes by being closer to the smaller atom. From the critical point, the gradient vector path (path of fastest electron density decrease) can be followed in all directions, which is nearly perpendicular to the line connecting atoms at the critical point. The gradient vector path defines surfaces in three-dimensional space, which will separate that space into regions around each nucleus. The number of electrons in this region can be integrated in order to find an electron population and thus an atomic charge. The bond order can be predicted, based on the magnitude of

the electron density at the bond critical point. The AIM analysis is also popular due to its reliability with large basis sets for which some others fail. Unfortunately, the numerical surface finding and integration involved in this analysis are not robust.

2.13 Potential energy surface

Once a Potential energy surface (PES) has been investigated, it can be analyzed to obtain information about the chemical system. The PES is the most comprehensive description of all the isomers, conformers, and energetically accessible motions of a chemical system. Minima on this surface correspond to optimized geometries. The lowest-energy minimum is called the global minimum. There can be many local minima, such as higher-energy conformers or isomers. The transition structure between the reactants and products of a reaction is a saddle point on this surface. A PES can be used to find both saddle points and reaction coordinates.

2.14 Wiberg bond index

In addition to the bond distance, the bond order analysis could be used to determine the bond strength. For quantum chemistry methods, this bond order distribution analysis is based on the Wiberg bond index³² which is defined

from atomic orbital interaction between two atoms. For each method where a basis set is attached to atoms it is possible to define the bond order, B_{AB} , between atom A and a neighboring atom B³³:

$$B_{AB} = \sum_{i \in A} \sum_{j \in B \neq A} (PS)_{ij}(PS)_{ji}$$

where P is a density matrix (obtained by $C^t C$ where C is the coefficient matrix of the molecular orbital on the basis set and $^t C$ is the transposed matrix of C and S the overlapping matrix. The subscripts i and j run only on the occupied eigenfunctions. For semi-empirical neglected differential overlapping quantum chemistry methods (S is diagonal), this approach leads to the Wiberg bond index $W^{32,33}$ of the bond A–B which is thus defined as:

$$W_{AB} = \sum_{i \in A} \sum_{j \in B \neq A} P_{ij}P_{ji}$$

The value of the Wiberg bond index is one for a perfect covalent single bond and zero for perfect ionic bond or no covalent bond. For example, $W=1$ for a single covalent bond (such as H–H), $W=2$ for a double covalent bond (such as C=C in ethylene $H_2C=CH_2$), $W=3$ for a triple covalent bond (like $C \equiv C$ in acetylene $HC \equiv CH$), independent of atom type. It may deviate more or less from the integer values as used by classical valence pictures.³³

References

-
- 1 E. Schrödinger *Phys Rev.* **1926**,28,1049.
 - 2 L.H. Thomas *Math Proc Cambridge Philos Soc.* **1927**, 23, 713.
 - 3 A. D. Becke *J Chem Phys.* **1986**,84,4525.
 - 4 A. D. Beck *Phys Rev A.* **1988**,38,3098.
 - 5 C.T. Lee, W.T. Yang, R.G. Parr *Phys Rev B.* **1988**,37,785.
 - 6 J.P. Perdew *Phys Rev B.* **1986**,34,7406.
 - 7 J.P. Perdew, W. Yue *Phys Rev B.* **1986**,33,8800.
 - 8 J.P. Perdew, *Phys Rev B.* **1986**,33,8822.
 - 9 J.P. Perdew, K. Burke, M. Ernzerhof *Phys Rev Lett.* **1996**,77,3865.
 - 10 A.D. Becke, *J Chem Phys.* **1993**,98,5648.
 - 11 F. Illas, J.M. Ricart, In *Química teórica y computacional*, **2001**.
 - 12 J. Sauer *Chem Rev.* **1989**,89,199.
 - 13 N.W. Ashcroft, N.D. Mermin, New York, **1976**.
 - 14 D. Curulla, A. Clotet, J.M. Ricart, F. Illas *J Phys Chem B* **1999**,103,5246.
 - 15 D. Curulla, R. Linke, A. Clotet, J.M. Ricart, J.W. Niemantsverdriet *Phys Chem Chem Phys.* **2002**,4,5372.
 - 16 A. Gil, A. Clotet, J.M. Ricart, G. Kresse, M. Gracia-Hernandez, N. Rosch, P. Sautet *Surf Sci.* **2003**,530,71.
 - 17 H.J. Monkhorst, J.D. Pack *Phys Rev B.* **1976**,13,5188.
 - 18 D.L. Cunningham *Phys Rev B.* **1974**,10,4988.
 - 19 D.J. Chadi, M.L. Cohen *Phys Rev B.* **1973**,8,5747.

-
- 20 D.R. Hamann, M. Schluter, C. Chiang *Phys Rev Lett.* **1979**,43,1494.
- 21 D. Vabderbilt *Phys Rev B.* **1990**,41,7892.
- 22 P.E. Blöchl *Phys Rev B.* **1994**,50,17953.
- 23 G. Kresse, J. Furthmüller *Comp Mat Sci.* **1996**,6,15.
- 24 G. Kresse, J. Furthmüller *Phys Rev B.* **1996**,54,169.
- 25 D. Vanderbilt *Phys Rev B.* **1990**,41,7892.
- 26 G. Kresse, J. Hafner *J Phys: Condens Matter.* **1994**,6,8245.
- 27 D.D. Jonsson *Phys Rev B.* **1980**,38,393.
- 28 P. Pulay *Chem Phys Lett.* **1980**,73,393.
- 29 H.J. Monkhorst, J.D. Pack *Phys Rev B.* **1976**,13,5188.
- 30 H. Jónsson, G. Mills, W. Jacobsen, Enrico Fermi Summer School (Lenci '97) proceedings, **1997**.
- 31 L.R. Pratt *J Chem Phys.* **1986**,85,5045.
- 32 K.A. Wiberg 1968 *Tetrahedron.* **1968**,24,1083.
- 33 I. Mayer *Chem. Phys. Lett.* **1983**,97,270.

CHAPTER 3

3. Conversion of 1- and 2-Tetralone over HY Zeolites

3.1 Introduction

The projected demand for transportation fuels exceeds the current capacity for light sweet crudes.¹ Security and sustainability concerns enhance the need for access to alternative domestic sources. Unconventional crude oils (heavy oil, bitumen, tar sands, shale oils, and coals) are abundant in North America and may reduce the consumption of imported feedstocks.² Therefore, these complex carbon resources are expected to contribute a growing fraction of transportation fuel production. Heavy crude oils have a density (specific gravity) approaching or even exceeding that of water. They usually are extremely viscous, with a consistency ranging from that of heavy molasses to a solid at room temperature. Conversion of heavy feedstocks to fuels via severe hydrotreating or cracking processes has been practiced for many years. However, these technologies present drawbacks related to the high consumption of hydrogen and demanding reaction conditions that they require. To convert complex carbon resources with typical H/C atomic ratios of about 1.1–1.2 to the range of transportation liquid fuels (H/C ~1.8 to 2.0) a very significant

amount of hydrogen is needed. At the same time, the high temperatures and pressures associated with these processes result in exceedingly high capital costs.

The use of heavy oil as a crude produces high aromaticity in the internal streams in the refinery (i.e. LCO) as well as a net increase in the volume of the heavier fractions (i.e. slurry oil) produced in the distillation units. One possible solution would be to recycle some of these heavier fractions through the catalytic cracking unit (FCC). However, it is well established that naphthalene, phenanthrene, and anthracene do not crack under typical FCC conditions, but instead they undergo condensation and form coke.³

Functionalization with heteroatoms, such as S, N, and O may greatly affect the reactivity of the aromatic rings and allow unzipping the stable structure of the heavy molecules under milder conditions than those used in hydrotreating. Such functionalization may create reactive centers in the molecule that would help selectively activating the molecule via H-transfer, ring-opening, etc. Hence, this work focused on reaction of tetralones (1 and 2), as the representative molecules of oxygenated aromatics on HY zeolites.

3.2 Experimental

A commercial HY zeolite from Zeolyst International (CBV 780, Si/Al ratio 40) was used as a catalyst. The reactions were conducted in a $\frac{1}{4}$ " stainless steel reactor at atmospheric pressure of hydrogen. The reactor temperature in the range 300–500 °C was controlled in a tube furnace. The feed reactants, tetralin, 1-tetralone, 1-tetralol, 1-naphthol, and 2-tetralone, were purchased from Sigma-Aldrich and used as received. The feed was introduced to the reaction system by bubbling hydrogen through a saturator adjusted at an appropriate temperature to obtain the desired vapor pressure of the specific reactant as shown in Figure 3.1. Space velocities were in the range 0.5–2.0 h⁻¹. Prior to each run, the feed was directed through a bypass until the concentration reached steady-state, and then it was switched to the reactor. Carbon mass balance closure was checked in every run by comparing the total mass determined from the analysis of the reactor outlet with that from the bypass.

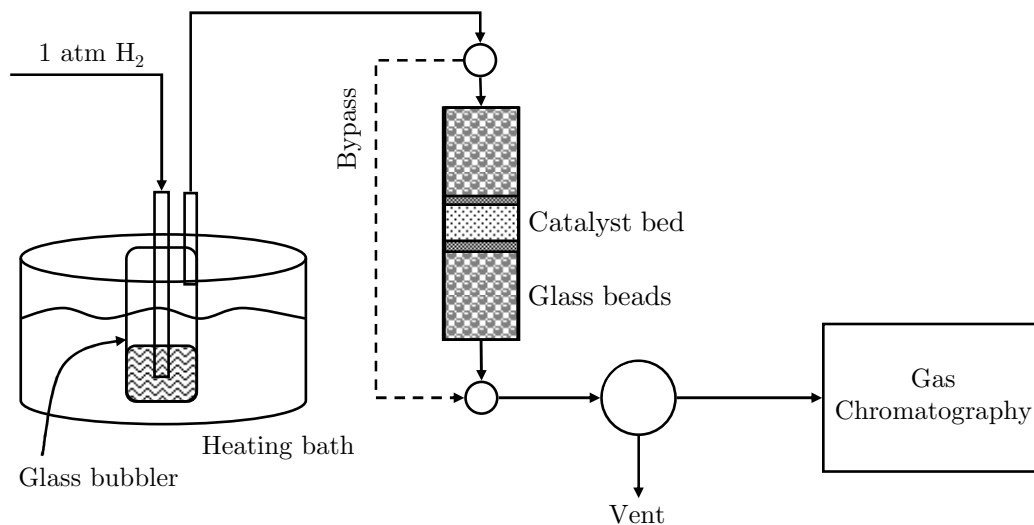


Figure 3.1 Schematic diagram of the system.

The amount of coke formation during reaction was determined in an elemental analyzer and found to be less than 1 wt% of the total weight of the spent catalyst, which indicates that the coke formation per pass is very small and does not affect the carbon balance or product distribution in a significant manner. Products were analyzed every 0.5 h after the beginning of the run with an on-line HP5890 gas chromatograph equipped with HP-5 column and an FID detector. To minimize the effect of catalyst deactivation in the analysis of initial reactivity, the values reported in this work are those obtained in the first measurement (i.e., after 0.5 h on stream). The temperature program started at 40 °C, linearly increased to 280 °C with a 15 °C/min heating ramp, and finally held for 8 min.

3.3 Results and discussion

3.3.1 Thermal reactions of 1- and 2-tetralone (blank reactor)

Before the catalytic measurements, runs without catalyst were conducted to determine the contribution of thermal reactions. The product yields obtained from 1- and 2-tetralone in a blank reactor filled with inert glass beads in the temperature range 300–500 °C are compared in Table 3.1. It is clear that the both compounds can be thermally decomposed and the conversion readily increases with temperature. Conversion of 2-tetralone is significantly higher than that of 1-tetralone at all temperatures. The higher reactivity of 2-tetralone is associated to its benzylic carbon that requires a relatively lower energy for C–H dissociation⁴ and hence it can be thermally activated more readily than 1-tetralone.⁵

Table 3.1 Thermal reactions of 1- and 2-tetralone.

Feed	1-Tetralone			2-Tetralone		
	300 °C	400 °C	500 °C	300 °C	400 °C	500 °C
Temperature						
Conversion (%)	5.6	11.0	42.4	15.0	22.6	56.0
Product yields (wt%)						
RO	0.0	0.3	1.7	0.0	0.0	0.0
RC	0.0	0.0	0.3	0.0	0.0	0.4
Tetralin	0.1	0.1	0.2	0.0	0.0	0.0
Dihydronaphthalene	0.6	0.8	1.8	0.0	0.0	0.0
Naphthalene	0.5	0.8	5.6	0.0	0.2	0.2
Tetralone	94.4	89.0	57.6	85.0	77.4	44.0
Tetralol	0.0	0.0	0.0	0.0	0.0	0.0
Naphthol	4.4	8.3	31.8	5.8	7.1	26.0
Heavies	0.0	0.7	1.0	9.2	15.4	29.3

Reaction conditions: 1 atm H₂, TOS 0.5 h.

For 1-tetralone conversion, naphthol is the main product. At 500 °C, production of naphthalene becomes significant. This suggests that at high temperatures hydrogen transfer may be occurring.⁶ By contrast, 2-tetralone produces heavy coupling compounds (i.e. 4-ring) as the major product with a lower selectivity toward the corresponding naphthol than 1-tetralone. At the same time, no naphthalene is obtained in the temperature range studied. Trace amounts of dihydronaphthalene, tetralin, ring-contraction (RO) and ring-opening (RO) products can be observed from 1-tetralone, while they do not appear from 2-tetralone conversion.

3.3.2 Catalytic conversion of 1- and 2-tetralone reactions over the HY zeolite

As shown in Figure 3.2, the presence of HY catalyst greatly enhances the conversion of both 1- and 2-tetralone compared to the runs in the blank reactor. As in the case of thermal conversion, 2-tetralone displays a much higher reactivity than 1-tetralone. Reactive adsorption of aromatic ketones on acid sites is well known.^{7,8} Our results show that the position of the carbonyl functionality not only has an effect on the reactivity toward thermal activation, but also toward catalytic activation.

Figure 3.3 shows the product distribution from 1- and 2-tetralone conversion over the HY zeolite as a function of temperature. It is seen that below 400 °C the acid-catalyzed reaction yields their corresponding naphthols as main products, suggesting an enhanced hydrogen transfer over the acid catalyst. Interestingly, as the temperature increases to 500 °C 2-naphthol was obtained from 1-tetralone and 1-naphthol from 2-tetralone, while the concentration of the corresponding naphthol decreased, suggesting that naphthol isomerization can take place over the acid HY zeolite at this high temperature.

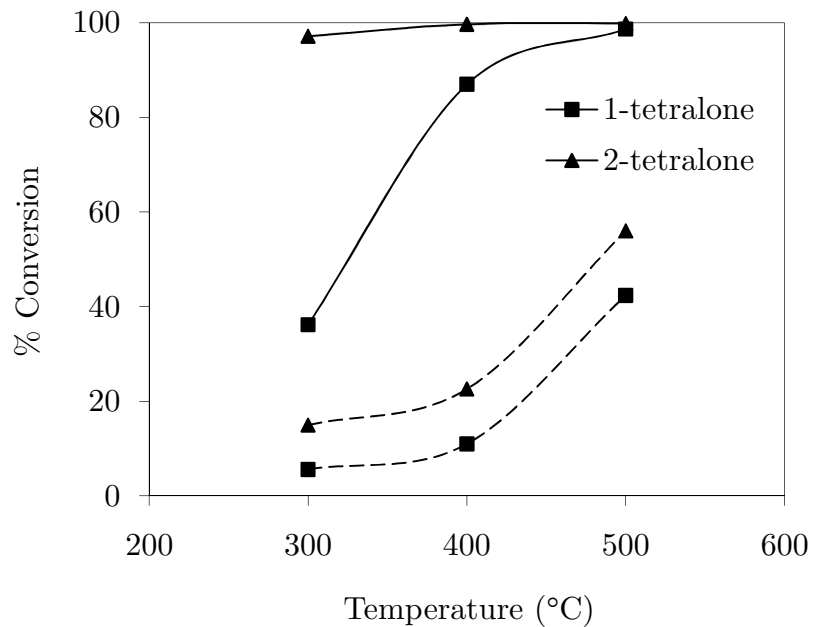


Figure 3.2 Conversions of 1- and 2-tetralone as a function of temperature. Reaction conditions: 1 atm H₂, TOS 0.5 h, W/F = 1.723 h. *Solid and dashed lines represent catalytic and thermal conversion, respectively.*

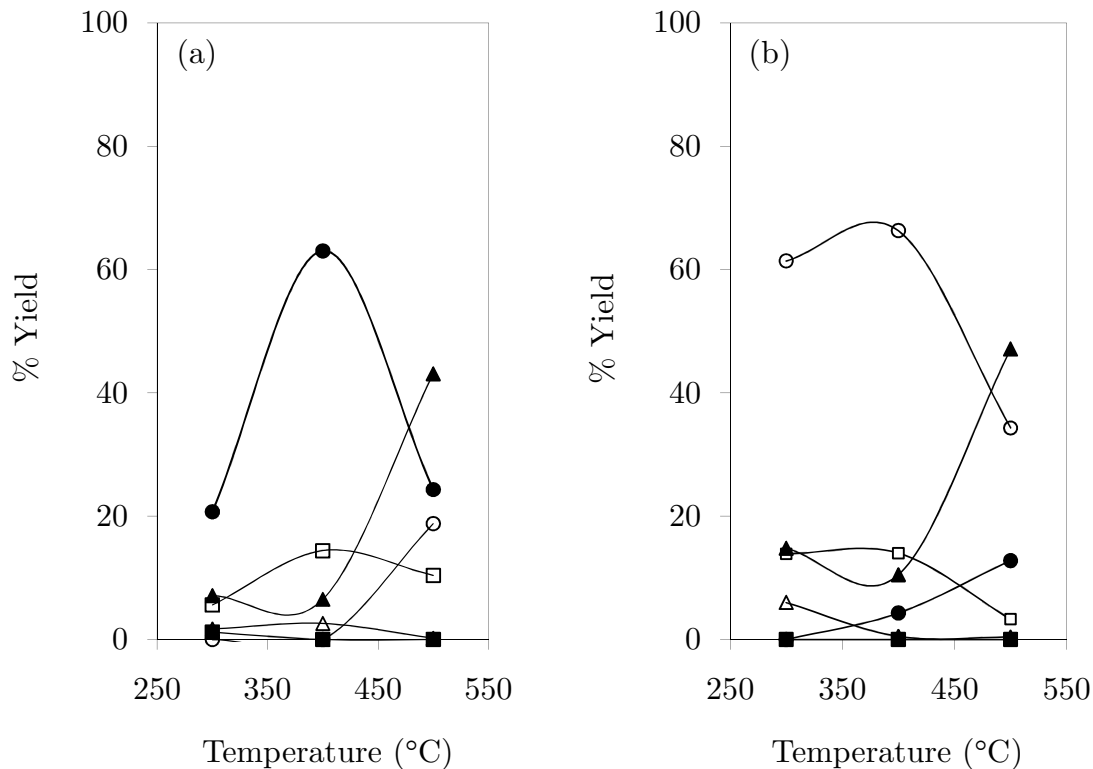


Figure 3.3 Product yields from the reaction of (a) 1-tetralone and (b) 2-tetralone as a function of temperature over HY zeolite. Reaction conditions: 1 atm H₂, TOS = 0.5 h, W/F = 1.723 h. *Tetralin* (open triangle), *dihydronaphthalene* (filled square), *naphthalene* (open square), *1-naphthol* (filled circle), *2-naphthol* (open circle) and *heavies* (filled triangle).

Also, coupling products, i.e. 4-ring compounds, were produced at high temperatures in significant amounts, suggesting the contribution of hydrogen transfer/coupling reactions, catalyzed by Brønsted sites.⁵

Production of naphthalene and tetralin was noticeably enhanced over the HY catalyst compared to the thermal reaction. This enhancement again suggests that hydrogen transfer is readily facilitated over acid sites,⁹⁻¹¹ so

deoxygenated products can be obtained. Only small amounts of ring-contraction and ring-opening products were found in this acid-catalyzed reaction.¹²

Figure 3.4 shows the evolution of product distribution and conversions of 1- and 2-tetralone with space time (W/F), over the HY zeolite at 300 °C. As described above, 2-tetralone is more reactive and sensitive to the presence of the acid catalyst than 1-tetralone. At this low temperature, the corresponding naphthols are the major products for both 1- and 2-tetralone, with no evidence of isomerization. Also, at low temperatures, deoxygenated products, naphthalene and tetralin only appear in relatively small amounts.

As shown in Figure 3.5, during the reaction of 1-tetralone over HY at 500 °C, while the overall conversion continuously increases with W/F, the yield of 1-naphthol goes through a maximum and then decreases at high W/F. This decrease in 1-naphthol is accompanied by a rapid increase in concentration of coupling products and 2-naphthol. While it is clear that secondary isomerization of 1-naphthol to 2-naphthol is an important reaction occurring at high temperature and W/F, formation of coupling products it also seems to be a secondary reaction. As shown in Figure 3.5, the first derivative of their concentration near zero W/F is approximately to zero. The experiment conducted with 1-naphthol as a feed (Table 3.2) indicates that this molecule can undergo coupling over HY.

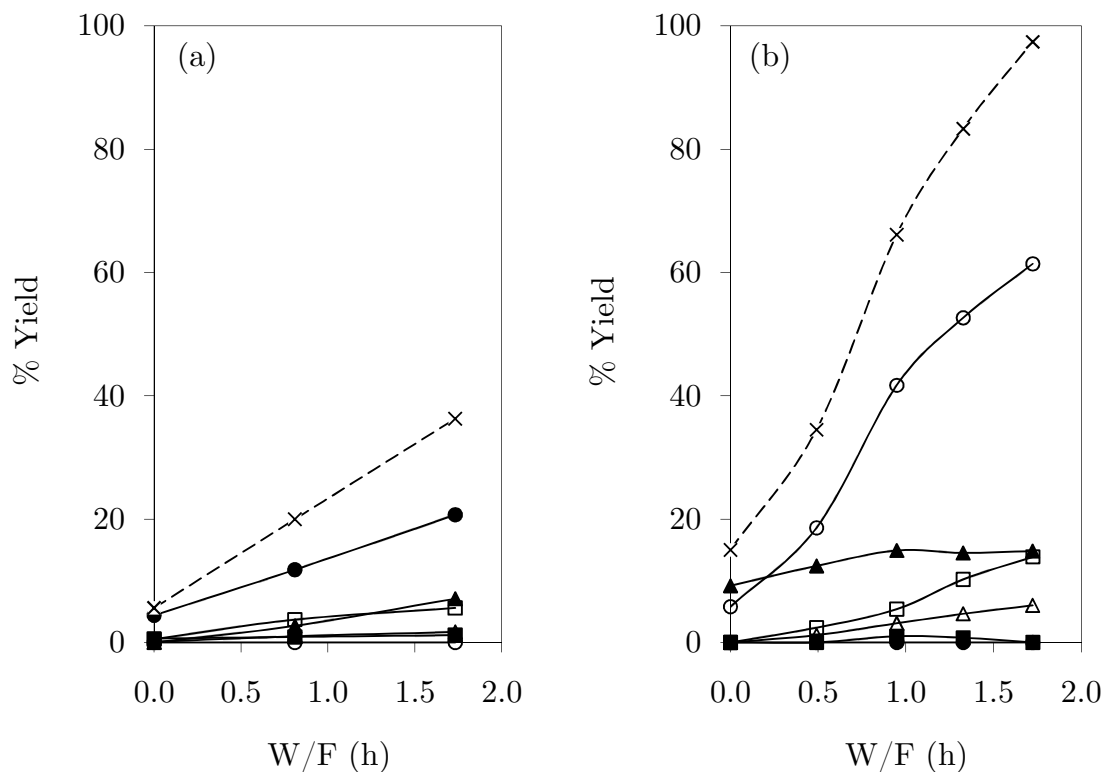


Figure 3.4 Product yields from the reaction of (a) 1-tetralone and (b) 2-tetralone as a function of space time (W/F) at 300 °C over HY. Reaction conditions: 1 atm H₂, TOS = 0.5 h. Tetralin (*open triangle*), dihydronaphthalene (*filled square*), naphthalene (*open square*), 1-naphthol (*filled circle*), 2-naphthol (*open circle*), heavies (*filled triangle*) and conversion (*times*)

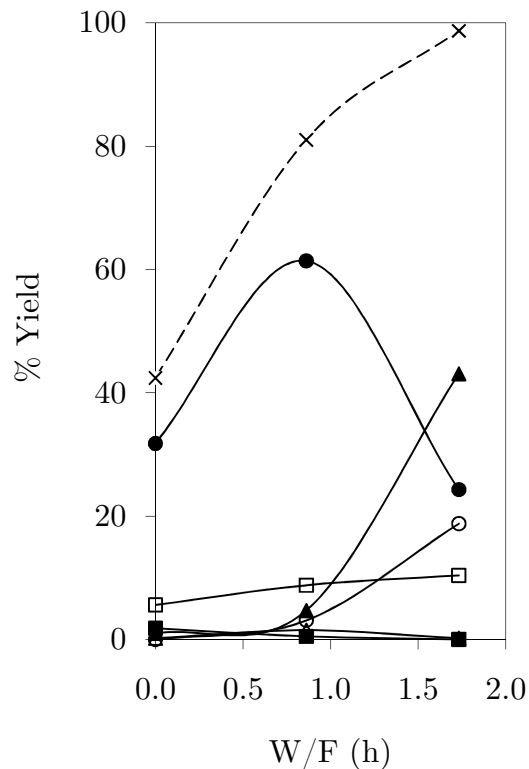


Figure 3.5 Product yields from the reaction of 1-tetralone as a function of space time (W/F) at 500 °C over HY. Reaction conditions: 1 atm H₂, TOS = 0.5 h. The values at zero W/F correspond to those obtained in the blank reactor (thermal). *Tetralin (open triangle), dihydronaphthalene (filled square), naphthalene (open square), 1-naphthol (filled circle), 2-naphthol (open circle), heavies (filled triangle) and conversion (times).*

Table 3.2 Reactions of tetralin, tetralones and 1-naphthol catalyzed by HY zeolite.

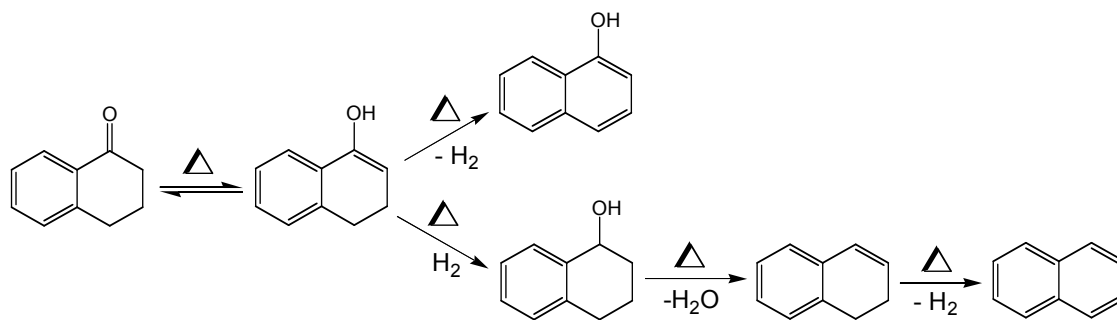
Feed	Tetralin	1-Tetralone	2-Tetralone	1-Naphthol	
Catalyst	HY	HY	HY	Blank	HY
Conversion (%)	11.5	98.7	99.9	0.0	36.4
Product yields (wt%)					
RO	0.0	0.8	0.5	0.0	0.0
RC	0.0	1.2	1.6	0.0	0.0
Tetralin	88.5	0.2	0.4	0.0	0.0
Dihydronaphthalene	0.0	0.0	0.0	0.0	0.0
Naphthalene	11.5	10.4	3.3	0.0	0.0
Tetralone	0.0	1.3	0.1	0.0	0.0
Tetralol	0.0	0.0	0.0	0.0	0.0
1-Naphthol	0.0	24.3	12.8	100.0	63.6
2-Naphthol	0.0	18.8	34.3	0.0	27.5
Heavies	0.0	43.1	47.1	0.0	8.9

Reaction conditions: 500 °C, 1 atm H₂, TOS 0.5 h.

3.4 Reaction pathways

The significant difference in reactivity of the two isomers can be explained from the higher stability of 1-tetralone due to the conjugation of the carbonyl group and the π system of the aromatic ring. In addition, the presence of a benzylic α -carbon (adjacent to both the C=O and the aromatic ring) in 2-tetralone leads to a more stable reaction intermediate,⁴ and consequently lower activation energy and higher rate for the thermal reaction. Conversely, 1-tetralone is expected to form a less stable intermediate with cross-conjugated double bonds. At the same time, a higher probability of formation of the free radical intermediate in 2-tetralone can explain the higher rate of formation of coupling products observed with 2-tetralone, but not with 1-tetralone, which does not have any benzylic α -carbon.

In parallel, dehydrogenation via C–H thermal cracking forming aromatic rings will be favored at high temperatures.¹³ This dehydrogenation would lead to the formation of the corresponding naphthols. As hydrogen would be produced in stoichiometric amounts during the dehydrogenation of 1-tetralone to 1-naphthol, a significant hydrogen transfer to fresh 1-tetralone can be expected. It is known that ketones are good hydrogen acceptors,¹⁴ leading to the formation of tetralol. This, in turn, can be readily dehydrated and subsequently dehydrogenated to produce stable naphthalene, as shown below.



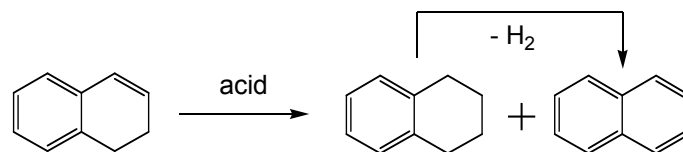
This reaction path is confirmed by the experiment done with 1-tetralol as a feed (see Table 3.3), which shows the production of dihydronaphthalene and naphthalene, as proposed. However, thermal conversion of tetralones favors dehydrogenation over deoxygenation (i.e. hydrogenation then dehydration). Consequently, the production of the corresponding naphthol is dominant over naphthalene (Table 3.1).

Table 3.3 Reactions of 1-tetralol catalyzed by HY zeolite.

Feed	1-Tetralol	
	Blank	HY
Catalyst		
Product yields (wt%)		
RO	0.0	0.0
RC	0.0	0.0
Tetralin	4.8	42.6
Dihydronaphthalene	59.5	0.0
Naphthalene	35.7	57.4
Tetralone	0.0	0.0
Tetralol	0.0	0.0
1-Naphthol	0.0	0.0
2-Naphthol	0.0	0.0
Heavies	0.0	0.0

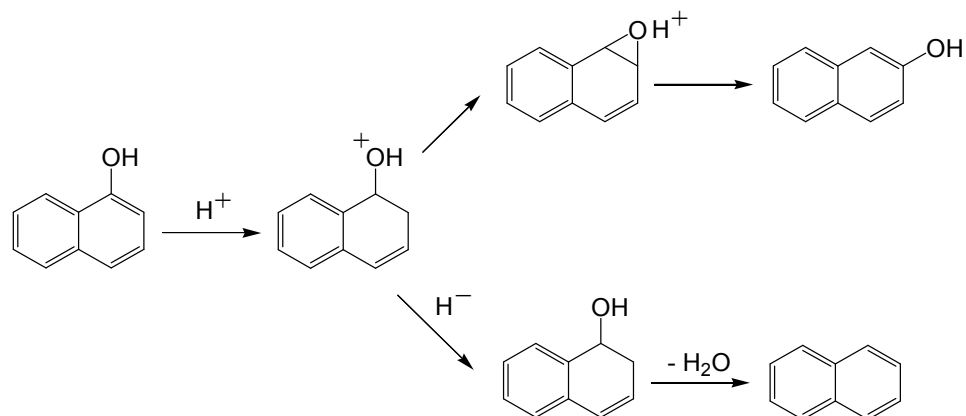
Reaction conditions: 300 °C, 1 atm H₂, TOS 0.5 h.

The situation is somewhat different in the presence of HY, in which conversion of the tetralones result from a combination of thermal and acid-catalyzed reactions. The presence of acid HY zeolite enhances the rate of the hydrogen transfer.⁹⁻¹¹ Hence, both the overall conversion and formation of naphthol are enhanced. However, the parallel reaction, i.e. hydrogen transfer to form tetralol that produces dihydronaphthalene and naphthalene, is greatly enhanced. Moreover, dihydronaphthalene is readily disproportionated (i.e. intermolecular hydride transfer) producing naphthalene and tetralin,^{15,16} as shown below.



As illustrated in Table 3.3, this disproportionation is largely observed in the acid-catalyzed reaction of 1-tetralol, but not in its thermal reaction. Naphthalene, at high temperatures, can also derive from tetralin dehydrogenation,^{17,18} which may explain the slight decrease in tetralin/naphthalene ratio observed at higher W/F. Thermal transformation of 1-naphthol to naphthalene could occur at high hydrogen pressures¹⁹ or high temperatures.²⁰ However, this reaction did not occur under the conditions of this study.

The observed isomerization and deoxygenation of 1-naphthol to 2-naphthol and naphthalene over HY zeolite at high temperatures can be explained as follows. Protonation of 1-naphthol by a Brønsted site of the HY zeolite leads to the formation of naphthalene-1,2-oxide intermediate.²¹⁻²³ Ring opening of this intermediate results in the formation of 2-naphthol. In a parallel path, acid-site assisted hydrogen transfer from carbon deposits or heavies can form a 1-hydroxy-1,2-dihydronaphthalene intermediate.^{21,24} This species can be readily dehydrated over the Brønsted sites to form naphthalene. The two parallel paths are illustrated in the following scheme.



Since heavy products derive mainly from thermal coupling of oxygenated aromatic intermediates,⁵ the formation of heavies would be suppressed under rapid hydrogen transfer. Accordingly, a similar product distribution was obtained from both 1- and 2-tetralone reactions over the acid catalyst despite the higher conversion obtained for 2-tetralone.

3.5 Conclusions

Among the two isomers, 2-tetralone is the most active for both thermal activation and acid-catalyzed reactions. The lower reactivity of 1-tetralone is due to the conjugation of the double bond of the carbonyl group with the aromatic ring, which makes the molecule more stable. Hydrogen transfer during the reaction pathway has a significant effect on product distribution. Dehydrogenation of each tetralone to its corresponding naphthol is the major

pathway. The hydrogen transfer promoted by the acid catalyst leads to the formation of deoxygenated products, namely naphthalene and trace amounts of dihydronaphthalene, which is an intermediate product. Heavy coupling products, formed by coupling of the intermediates, can be readily suppressed over acid-catalyzed reaction at relatively lower temperatures by hydrogen transfer.

References

- 1 International Energy Outlook, DOE report DOE/EIA-0484, **2009**.
- 2 World Energy Council, *Encyclopedia of energy*. World Energy Council, London, **2004**,731.
- 3 X. Dupain, E.D. Gamas, R. Madon, C.P. Kelkar, M. Makkee, J.A. Moulijn *Fuel*. **2003**,82,1559.
- 4 B. Bruckner *Adv Org Chem* 1. **2002**.
- 5 T. Kjærso, K. Daasbjerg, S.U. Pedersen *Electrochim Acta*. **2003**,48,1807.
- 6 F. Behar, R. Pelet *Energy Fuels*. **1988**,2,259.
- 7 C.P. Bezouhanova *Appl Catal A*. **2002**,229,127.
- 8 X. Lei, N.J. Turro *J Photochem Photobiol A*. **1992**,69,53.
- 9 G. Puente, U. Sedran *Chem Eng Sci*. **2000**,55,759.
- 10 J. Pajak, V. Krebs, J.F. Marêché, G. Furdin *Fuel Process Technol*. **1996**,48,73.
- 11 W. Suarez W-.C.Cheng, K. Rajagopalan, A.W. Peters *Chem Eng Sci*. **1990**,45,2581.

-
- 12 M. Santikunaporn, W.E. Alvarez, D.E. Resasco *Appl Catal A*. **2007**,325,175.
- 13 B. Xu, C. Sievers, S.B. Hong, R. Prins, J.A. van Bokhoven *J Catal*. **2006**,244,163.
- 14 A. Rattanasumrit, V. Ruangpornvisuti *J Mol Catal A*. **2005**,239,68.
- 15 A. Corma, V. Gonzalez-Alfaro, D.V. Orchilles *J Catal*. **2001**,200,34.
- 16 M. Santikunaporn, J.E. Herrera, S. Jongpatiwut, D.E. Resasco, W.E. Alvarez, E.L. Sughrue *J Catal*. **2004**,228,100.
- 17 A.T. Townsend, J. Abbot *Appl Catal A*. **1992**,90,97.
- 18 A.T. Townsend, J. Abbot *Appl Catal A*. **1993**,95,221.
- 19 E.H. Schlosberg, A. Kurs *J Org Chem*. **1984**,49,3032.
- 20 R. Cypres *Prepr Pap Am Chem Soc Div Fuel Chem*. **1981**,26.
- 21 P. Brandt, Z.S. Jia, A. Thibblin *J Org Chem*. **2002**,67,7676.
- 22 S.N. Rao, R.A. More O'Ferrall, S.C. Kelly, D.R. Boyd, R. Agarwal *J Am Chem Soc*. **1993**,115,5458.
- 23 G.J. Kasperek, T.C. Bruice *J Am Chem Soc*. **1972**,94,198.
- 24 N. Pirinccioglu, A. Thibblin *J Am Chem Soc*. **1998**,120,6512.

CHAPTER 4

4. Conversion of 1-Tetralone over HY Zeolite: An Indicator of the Extent of Hydrogen Transfer

4.1 Introduction

The extent of hydrogen transfer in fluid catalytic cracking (FCC) processes has an important effect on the product distribution and catalyst stability.¹⁻⁴ While hydrogen transfer has well known benefits, such as improved liquid yield and reduce coke formation, an excessive rate of hydrogen transfer may have negative effects. A major concern is the potential loss of olefinicity in the product by excessive hydrogen transfer, which has the undesired consequence of reducing octane number in the gasoline fractions.⁵⁻⁷

It is widely accepted that, in the transition state, the carbenium ions on the acid sites can accept hydride ions from hydrogen-donor molecules and that the extent of this transfer can be modified by the nature of the catalyst, e.g., density or proximity of acid sites, presence of rare earth, etc.^{8,9} However, hydrogen transfer is a bimolecular reaction; therefore, the nature of both the hydride donor and hydride acceptor can impact the hydrogen transfer process. Therefore, it is anticipated that varying the nature of the hydrogen donor, the

extent and rate of hydrogen transfer can be varied. In the majority of the previous studies about the extent of hydrogen transfer,^{8,9} the focus has been on the effect of different zeolite catalyst parameters, such as zeolite structure, number of Al per unit cell, and acidity strength, rather than the intrinsic properties of the different hydrocarbons that may act as H-donors. A simple method that can predict a-priori the ability of a given feed component or a mixture of components may have interesting applications in FCC technology. This is the focus of this contribution.

Being important components of typical FCC catalysts, HY, REY, and USHY zeolites have been the subject of many studies related to cracking and hydrogen transfer.¹⁰ In our previous study on 1-tetralone conversion on HY zeolites,¹¹ we showed that naphthol is a dominant product, which can further transform to naphthalene via hydride transfer-dehydration reactions. It was suggested that naphthalene formed predominantly in the presence of hydrogen donor molecules. In this study, we have investigated the reactivity of 1-tetralone in the presence of different hydrogen donor molecules, which typically exist in FCC feed stream such as paraffins, naphthenics, and aromatics. Using tetralone as an indicator is highly convenient since it only produces a small number of products, which facilitates the analysis and the quantification of the effects of the hydrogen donor. We have selected molecules with similar number of carbon atoms but with varying functionalities, which we anticipate that results in varying hydrogen transfer capacity.¹²⁻¹⁶ The relative rates of the

possible conversion paths of 1-tetralone were found to depend on the hydrogen-donation capacity of the hydrocarbons co-fed to the reactor. DFT calculations were used to provide a correlation between the energy of hydride dissociation and the extent of hydrogen transfer observed experimentally.

4.2 Experimental

4.2.1 Catalytic activity testing

The model hydrogen donors used in this study were *n*-decane, decalin, tetralin, and 1,5-dimethyl tetralin (DMT), while 1-tetralone was used as a hydrogen acceptor. These compounds are fairly heavy and their boiling points varied in a wide range. To avoid using a solvent that might interfere with the process of hydrogen transfer and minimize condensation in the system, the feed was introduced to the reactor using a vapor saturation vessel made of glass through which the carrier gas was bubbled. By adjusting the temperature of the saturator, the vapor pressure of the individual compounds can be readily controlled. When mixtures were co-fed into the reactor, each component was controlled independently in a separate saturator. The feed rate was regulated by the carrier gas flow, and an additional inert gas line was added to keep the total gas flow rate constant.

The reactions were conducted in a $\frac{1}{4}$ " stainless steel reactor. Commercial HY zeolite from Zeolyst International (Si/Al = 15 and 40) used as the catalyst was placed at the center of the reactor. Since the zeolites were purchased in the proton form, the only pretreatment needed was to heat them up in-situ under He flow at 450 °C for 1 h to remove adsorbed water or any other contaminants. The top and bottom parts of the packed bed were filled with 3 mm-diameter glass beads. The operating conditions were as follows: atmospheric pressure, 450 °C, He carrier gas, space-time, W/F = 1.6 h, with respect to the mass flow rate of 1-tetralone in both pure and mixed feeds. Prior to each run, the feed was sent through the by-pass line until the concentration stabilized. At this point, it was switched to enter the reactor. The carbon mass balance was checked for every run by the analysis of the by-pass and the reactor outlet. The reaction products were sampled every 0.5 h on stream and analyzed on-line using an HP5890 gas chromatograph, equipped with an HP-5 column and an FID detector. A carbon elemental analyzer was used to measure the amount of coke deposits on the catalysts. The acid properties of the various zeolites were characterized by temperature programmed desorption of ammonia (NH₃-TPD), conducted in a 0.25 in. o.d. quartz reactor. Before each experiment, the 50 mg of zeolite sample was pretreated for 0.5 h in flowing He (30 mL/min) at 600 °C to eliminate any adsorbed water. Then, the temperature was lowered to 100 °C, and the sample exposed to a 2% NH₃/He, 30 mL/min stream for 30 min to reach saturation. After exposure, pure He was passed for 0.5 h over the sample to remove any weakly adsorbed NH₃. To conduct the TPD, the temperature

was increased at a heating rate of 10 °C/min up to 650 °C. The evolution of desorbed species was continuously monitored by a Cirrus mass spectrometer (MKS) recording the signals $m/z = 17$ and 16 (corresponding to NH_3). The density of acid sites was quantified by calibrating the MS signals with the average of ten 5-mL-pulses of 2% NH_3/He .

4.2.2 Computational methods

To correlate the different extent of hydride transfer observed experimentally for the various compounds with their intrinsic molecular properties, density functional theory (DFT) calculations were carried out using the GAUSSIAN 03 suite of programs.¹⁷ Molecular geometries and zero-point energies (ZPE) for all species were optimized by the Berny analytical gradient method,¹⁸ and verified to be local minima by computing the Hessian matrix. DFT calculations for the doublet states of the radicals (i.e., protonated species) employed an unrestricted formalism. This study was computed at B3PW91 density functional with using the 6-31+G(d,p) basis set, which were claimed to provide a good estimation for hydrogen transfer reactions.¹⁹

Since, as discussed below, naphthol plays a central role in the hydride transfer mechanism,¹¹ it was important to determine which protonated intermediate is most likely to form. Using DFT, the proton affinity (PA) of

naphthol in different protonated structures was compared, according to the expression:^{20,21}

$$PA = - \{ H(C_{10}H_9O^+) - [H(C_{10}H_8O) + H(H^+)] \} \quad (1)$$

where $H(i)$ is the enthalpy of species i , being $C_{10}H_9O^+$ = the protonated naphthol in each specific structure; $C_{10}H_8O$ = naphthol; and H^+ = proton. That is, a large positive PA indicates a stable compound.

To compare the experimentally observed trends with the theoretical predictions, hydride dissociation energies of various donor molecules were calculated as follows:

$$E_{dis} = \{ [H(R^+) + H(\text{hydride})] - H(R-H) \} \quad (2)$$

where $R-H$ is the donor; and R^+ is a corresponding carbenium ion.

The relative activation energy of hydride dissociation (EA) can be expressed by a ratio of hydride dissociation energy (E_{dis}) for each donor molecule over that for the C-H breaking of methane (482.6 kJ/mol);

$$E_A(x) = \frac{E_{dis}(x)}{E_{dis}(CH_4)} \quad (3)$$

where x is a particular donor molecule. A lower EA value indicates a better hydrogen transfer ability. In this simplified analysis, proton affinity and relative activation energy values are taken as intrinsic properties of the individual

molecules and were determined in the gas phase basis, independent of their interaction with the solid catalyst. In addition, the natural bond orbital (NBO) theory²² was applied to analyze the nature of bonds to determine the Wiberg bond index, as theoretically described in Chapter 2.

4.3 Results

4.3.1 Catalytic reaction of pure compounds over HY zeolites

The total conversion and product distribution resulting from feeding the pure compounds (1-tetralone, *n*-decane, decalin, tetralin, and DMT) onto the HY (Si/Al = 15) zeolite are shown in Table 4.1. Observed cracking products are linear and branched alkenes/anes (C₁-C₆), cyclic olefins (C₆-C₁₀), and alkylbenzenes (e.g., ethylbenzene, toluene, and xylene). It is seen that DMT and 1-tetralone are significantly more reactive than the other compounds in the series. The crackability, i.e., conversion to lighter products, follows the order DMT > decalin > tetralin > *n*-decane. As expected, the presence of tertiary carbons in DMT and decalin increases the crackability of these molecules, as previously observed.²³⁻²⁵ Dehydrogenated products (i.e., alkylnaphthalenes) were obtained from DMT, but in a lower extent. Some naphthalene was also obtained from dehydrogenation of tetralin, but not from decalin.

Table 4.1 Catalytic reaction of pure compounds over HY zeolites.

Feed	1-Tetralone	<i>n</i> -Decane	Decalin	Tetralin	DMT
Conversion	97.7	9.4	19.3	26.3	100.0
Product yields (wt%)					
C ₁ -C ₆	0.0	9.4	10.7	3.5	32.1
Cyclic olefins (C ₆ -C ₁₀)	0.0	0.0	6.1	3.3	0.0
Alkylbenzenes	0.0	0.0	2.6	5.9	44.1
<i>n</i> -Decane	0.0	90.6	0.0	0.0	0.0
<i>trans</i> -Decalin	0.0	0.0	65.4	0.0	0.0
<i>cis</i> -Decalin	0.0	0.0	15.3	0.0	0.0
Tetralin	0.0	0.0	0.0	73.7	0.0
1,5-Dimethyltetralin	0.0	0.0	0.0	0.0	0.0
Alkyl-naphthalenes	0.0	0.0	0.0	0.0	23.8
Naphthalene	4.4	0.0	0.0	13.6	0.0
1-Tetralone	2.3	0.0	0.0	0.0	0.0
1-Naphthol	74.0	0.0	0.0	0.0	0.0
2-Naphthol	11.3	0.0	0.0	0.0	0.0
Coupling products	8.1	0.0	0.0	0.0	0.0

Reaction conditions: 450 °C, 1 atm He, HY (Si/Al = 15),
W/F = 1.6 h, TOS 0.5 h.

In contrast with the hydrocarbons, a major part of 1-tetralone conversion proceeded through dehydrogenation to form naphthols, without cracking. This is consistent with our previous study,¹¹ in which dehydrogenation of 1-tetralone to 1-naphthol was found to be the dominant reaction pathway, and isomerization of 1-naphthol toward 2-naphthol was observed only at high temperatures (i.e., >400 °C). Only a small amount of naphthalene can be produced from 1-tetralone when fed alone.

The extent of overall dehydrogenation follows the order 1-tetralone > DMT > tetralin. That is, it appears that the presence of the aromatic ring and substituted groups (e.g., methyl) on the naphthenic ring readily improves the hydrogen transfer ability of the molecule, leading to an increased degree of dehydrogenation.²⁶ It can be seen that coupling products (e.g., multi-ring oxygenates) are only produced from 1-tetralone.

4.3.2 Catalytic reaction of hydrocarbon with co-fed 1-tetralone over HY zeolites

In this experiment, 1-tetralone was co-fed with the hydrocarbons, i.e., *n*-decane, decalin, tetralin, and DMT. The overall yields from catalytic reactions of the mixture feeds are shown in Table 4.2. Significantly different conversions and product selectivities, as compared with those from the pure feeds, were observed for each corresponding hydrocarbon (Table 4.3). Although the conversion of 1-tetralone remained close to 100%, the product selectivity, particularly towards naphthalene, was very sensitive to the nature of the hydrocarbon co-fed in to the reactor. It appears that, in the presence of a hydrocarbon that may act as a hydrogen donor, the naphthols deriving from 1-tetralone behave as hydrogen acceptors and subsequently undergo dehydration to produce naphthalene, as previously proposed.¹¹ The extent of this transformation depends on the co-fed hydrocarbon. Therefore, the intrinsic

hydride transfer ability of a particular hydrocarbon species can be represented by the naphthalene-to-naphthol ratio derived from tetralone (Table 4.3).

Table 4.2 Overall yields from catalytic reactions of mixture of hydrocarbons and 1-tetralone over HY zeolites.

Feed	1-Tetralone	<i>n</i> -Decane	Decalin	Tetralin	DMT
Conversion	97.7	9.4	19.3	26.3	100.0
Product yields (wt%)					
C ₁ -C ₆	0.0	9.4	10.7	3.5	32.1
Cyclic olefins (C ₆ -C ₁₀)	0.0	0.0	6.1	3.3	0.0
Alkylbenzenes	0.0	0.0	2.6	5.9	44.1
<i>n</i> -Decane	0.0	90.6	0.0	0.0	0.0
<i>trans</i> -Decalin	0.0	0.0	65.4	0.0	0.0
<i>cis</i> -Decalin	0.0	0.0	15.3	0.0	0.0
Tetralin	0.0	0.0	0.0	73.7	0.0
1,5-Dimethyltetralin	0.0	0.0	0.0	0.0	0.0
Alkyl-naphthalenes	0.0	0.0	0.0	0.0	23.8
Naphthalene	4.4	0.0	0.0	13.6	0.0
1-Tetralone	2.3	0.0	0.0	0.0	0.0
1-Naphthol	74.0	0.0	0.0	0.0	0.0
2-Naphthol	11.3	0.0	0.0	0.0	0.0
Coupling products	8.1	0.0	0.0	0.0	0.0

Reaction conditions: % co-fed concentration = $50 \pm 5\%$, 450 °C, 1 atm He, HY (Si/Al = 15), W/F = 1.6 h, TOS 0.5 h.

Table 4.3 Conversion and selectivity from catalytic reactions of mixture of hydrocarbons and 1-tetralone over HY zeolites.

Feed	<i>n</i> -Decane	Decalin	Tetralin	DMT
Conversion of 1-tetralone	98.1	95.0	96.0	94.7
Conversion of hydrocarbon	4.4	14.7	57.3	98.4
Selectivity of 1-tetralone product (wt%)				
Naphthalene	10.7	59.7	60.3	82.1
1-Naphthol	65.4	27.4	25.3	13.4
2-Naphthol	18.8	3.9	8.3	1.6
Coupling products	5.1	9.0	6.0	2.9
Naphthalene/Naphthol ratio	0.1	1.9	1.8	5.5
Selectivity of hydrocarbon products (wt%)				
C ₁ -C ₆	100.0	22.3	4.9	9.8
Cyclic olefins (C ₆ -C ₁₀)	0.0	26.2	4.3	0.0
Alkylbenzenes	0.0	35.6	7.0	9.4
<i>n</i> -Decane	-	0.0	0.0	0.0
<i>trans</i> -Decalin	0.0	-	0.0	0.0
<i>cis</i> -Decalin	0.0	-	0.0	0.0
Tetralin	0.0	15.8	-	0.0
1,5-Dimethyltetralin	0.0	0.0	0.0	-
Alkyl-naphthalenes	0.0	0.0	0.0	80.8
Naphthalene	0.0	0.0	83.8	0.0

Reaction conditions: % co-fed concentration = $50 \pm 5\%$, 450 °C, 1 atm He, HY (Si/Al = 15), W/F = 1.6 h, TOS 0.5 h.

A clear trend is observed in this ratio, DMT > tetralin \approx decalin > *n*-decane. It is likely that a relatively rapid formation of coke occurred at the beginning of the run (i.e., ~first 10 min), whereas a quasi-plateau in activity was obtained later.²⁷ The integrated amounts of coke formed over 1 h on stream

are rather low (Table 4.4). Therefore, it can be expected that the contribution of hydrogen from coke to the total to hydrogen transfer is negligible compared to the significant changes observed in product distribution.

Table 4.4 Amount of coke on spent catalysts determined by an elemental analyzer.

Feed	Coke (%)
Tetralone	1.28
<i>n</i> -Decane	0.98
Decalin	1.16
Tetralin	1.77
DMT	1.59
<i>n</i> -Decane + Tetralone	1.96
Decalin + Tetralone	2.21
Tetralin + Tetralone	2.07
DMT + Tetralone	1.12

Reaction conditions: 450 °C, 1 atm He, HY (Si/Al = 15).

In parallel to the changes in 1-tetralone products as a consequence of the enhanced hydrogen transfer, changes in overall conversions and product distribution from the individual hydrocarbons were clearly observed. For example, in the conversion of DMT in the presence of tetralone, dehydrogenated products (i.e., alkylnaphthalenes) became dominant rather than cracking products, which dominated in the pure DMT feed reaction. Similar

behavior was observed with tetralin. In this case, the conversion significantly increased with a higher selectivity towards the dehydrogenated product, naphthalene. The dehydrogenation of DMT and tetralin can be ascribed to their intrinsic hydride donor ability, which is promoted in the presence of the hydride acceptor, 1-tetralone. In contrast to DMT and tetralin, no significant dehydrogenation products (i.e., tetralin or alkylbenzene) were obtained from decalin despite the high naphthalene/naphthol ratio observed in the parallel 1-tetralone reaction. In fact, this ratio was as high as that obtained when co-feeding tetralin. This suggests that the hydrogen transfer occurs from the cracking products, most of which end up as cycloalkenes and alkylbenzenes. Also, isomerization of (*cis*-, *trans*-) decalin, which involves hydrogen exchange but not net hydrogen donation may accelerate the hydrogen transfer process for the conversion of 1-tetralone into naphthalene and water. Therefore, a high yield of naphthalene was observed from 1-tetralone without a prominent change in the product distribution of decalin.

In the case of *n*-alkanes co-feed, their weaker hydrogen-donor ability had little effect in the naphthalene/naphthol product ratio of 1-tetralone (i.e., only a slight increase from about 0.05 for pure 1-tetralin alone to 0.13 for the mixed feed with added *n*-decane). It can be suggested a small amount of hydrogen transfer from *n*-decane can take place, essentially associated with cracking and coke formation. However, the cracking of both *n*-decane and decalin, lacking

aromatic structure, is significantly suppressed in the presence of tetralone, due to a competitive adsorption of the oxygenate.

At the same time, the yields of coupling products observed from all of the mixture feeds were significantly lower than that with pure 1-tetralone. This can be explained, again, by enhanced hydrogen transfer from the co-fed hydrocarbon, as well as by the dilution effect. The latter may be more important with the weaker hydrogen-donors (i.e., *n*-decane). However, a part of cracking products from decalin may participate in coupling formation, and result in a higher yield as compared to others.

4.3.3. Effect of decalin concentration on the product distribution of 1-tetralone conversion over HY zeolites with varying acidity (Si/Al ratio 15 and 40)

In addition to varying the nature of the hydrogen donor, we investigated the effect on hydrogen transfer of varying the concentration of the hydrocarbon as well as the acidity density of the catalyst. Increases in naphthalene yield were observed by increasing either the concentration of decalin (Figure 4.1a) or the acidity of the catalyst (Figure 4.2a). The contribution to naphthalene from decalin dehydrogenation is negligible under the reaction conditions investigated. Therefore, the enhanced concentration of naphthalene product can be solely ascribed to the tetralone conversion path, enhanced by hydrogen transfer. Since, in this path, hydrogen transfer enhances the conversion of naphthol to

naphthalene, a good indicator of the extent of hydrogen transfer is the naphthalene/naphthol ratio. This ratio clearly increases with either increasing concentration of the hydrogen donor (Figure 4.1b) or increasing acidity of the catalyst (Figure 4.2b). At the same time, since conversion of naphthol to naphthalene competes with isomerization, the 2-naphthol/1-naphthol ratio was found to decrease with increasing decalin concentration (Figure 4.1b). By contrast, when the acid density increases, both 1-naphthol isomerization and naphthalene production (i.e., hydrogen transfer) increase (Figure 4.2b) as expected.^{28,29}

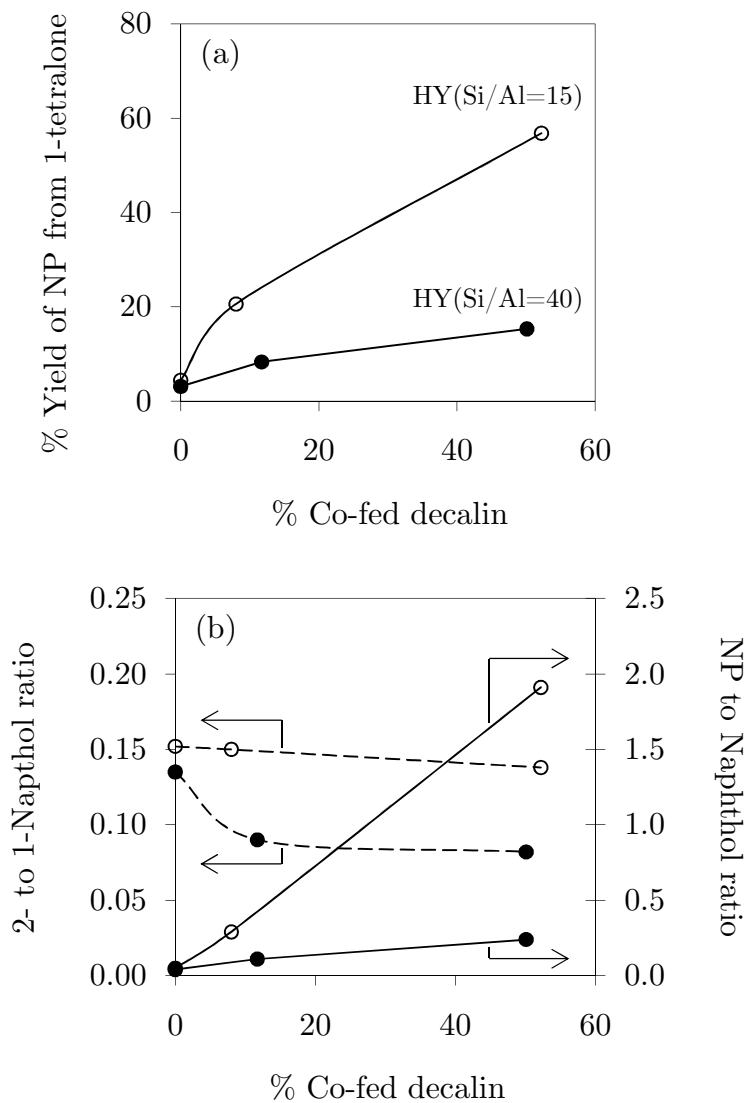


Figure 4.1 Effect of % co-fed decalin on (a) yield of naphthalene (NP); and (b) 2-naphthol to 1-naphthol ratio, and NP to naphthol ratio.

Reaction conditions: 450 °C, 1 atm He, TOS = 0.5 h.

HY(Si/Al = 15) (open circle), HY(Si/Al = 40) (filled circle).

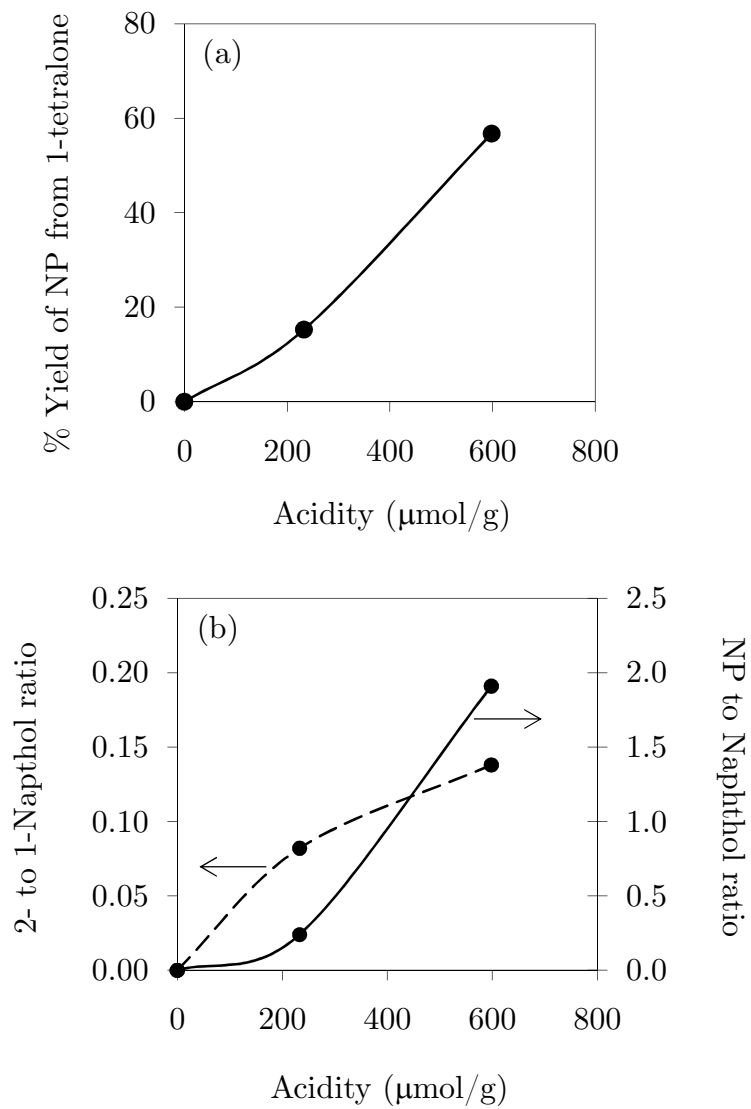


Figure 4.2 Effect of acidity on (a) yield of naphthalene (NP); and (b) 2-naphthol to 1-naphthol ratio, and NP to naphthol ratio. Reaction conditions: 450 °C, 1 atm He, TOS = 0.5 h.

4.3.4. Proton affinity of naphthol from DFT calculation

As mentioned above, naphthalene formation occurs via the acid-catalyzed dehydration of naphthol. Therefore, it is important to determine what kind of protonated naphthol species is the most probable structure. Figure 4.3 illustrates various possible protonated structures of naphthol and their corresponding proton affinity, which can be taken as a measure of their stability, i.e., the larger positive value the more stable. The various protonated species tested include the protonated keto-forms of 1-naphthol (**1**) and 2-naphthol (**2**) to form carbenium ions; the oxiranium cation (**3**); the protonated enol-forms of 1-naphthol (**4**, **5**) and 2-naphthol (**6**, **7**). The results of the calculations show that protonated keto-forms are the most favorable species (PA = 900 and 910 kJ/mol for **1**) and **2**), respectively). By contrast, the species protonated at C=C bond (enol-form of both 1- and 2-naphthol (**4**, **6**)), as well as that protonated at the oxygen atom (**5**, **7**) are less likely to be formed, i.e., they have low PA values. The favorable configuration of the protonated keto-forms difference could be ascribed to the direct conjugation of the positive charge on the oxygen atom with the π -system of the aromatic ring. Hence, the high electron density in the ring makes it favorable to shift towards the protonated site, enhancing stability of the oxonium ion species.^{20,21}

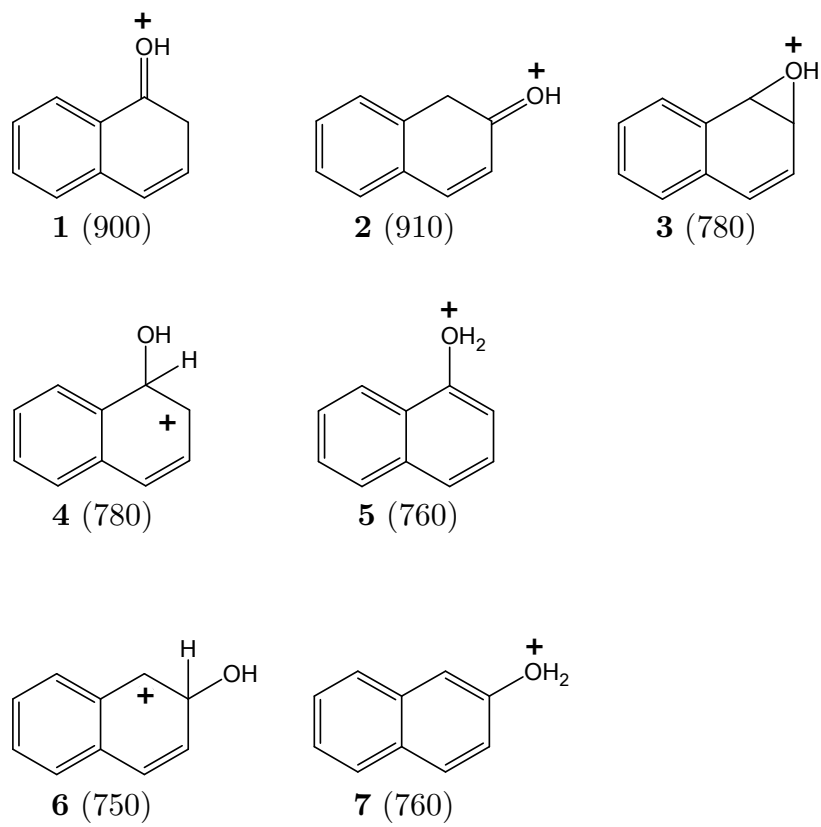


Figure 4.3 Possible $C_{10}H_9O^+$ ions. Protonation of naphthol is compared for the keto-forms of 1-naphthol (**1**) and 2-naphthol (**2**) to form carbenium ions; the oxiranium cation (**3**); and the enol-forms of 1-naphthol (**4,5**) and 2-naphthol (**6-7**). The corresponding PAs in kJ/mol are shown in the parentheses.

4.3.5. Hydrogen transfer ability of hydrocarbon species from DFT calculations

The hydride dissociation energies of various donor molecules calculated according to the Eqs. (2) and (3), relative to the C–H bond breaking in methane are shown in Figure 4.4 for different positions in each of the hydrogen donor molecule investigated. We can anticipate that the lower is the dissociation energy for a given molecular position, the more effective the hydrogen transfer should be. For a particular molecule, the energy required to dissociate the first hydride is lowest at the tertiary carbon, e.g., those in decalin and methyl tetralin, while the terminal carbon shows highest energy, e.g., those in *n*-decane, as expected.^{30,31} The dissociation from secondary carbons is relatively less probable as compared to that from tertiary carbons. Finally, the probability is particularly low (i.e., highest activation energy) for those from the aromatic ring, due to the higher electron density of carbons in the aromatic structure. The hydrogen on the aromatic ring is stabilized by sp² hybridization and least likely to be removed. By contrast, the hydrogen dissociation from the benzylic carbon is preferentially favorable since the positive charge formed can be stabilized by the delocalized π -electrons of the resonance structure. This effect is more pronounced by combining this effect with the presence of a tertiary carbon, as observed in methyl tetralin. According to the calculations, methyl tetralin should be the best hydrogen donor. Indeed, the trend of hydrogen transfer ability (DMT > tetralin \approx decalin > *n*-decane) predicted

according to the experimental naphthalene/naphthol ratios is consistent with the calculated relative activation energies for hydride dissociation.

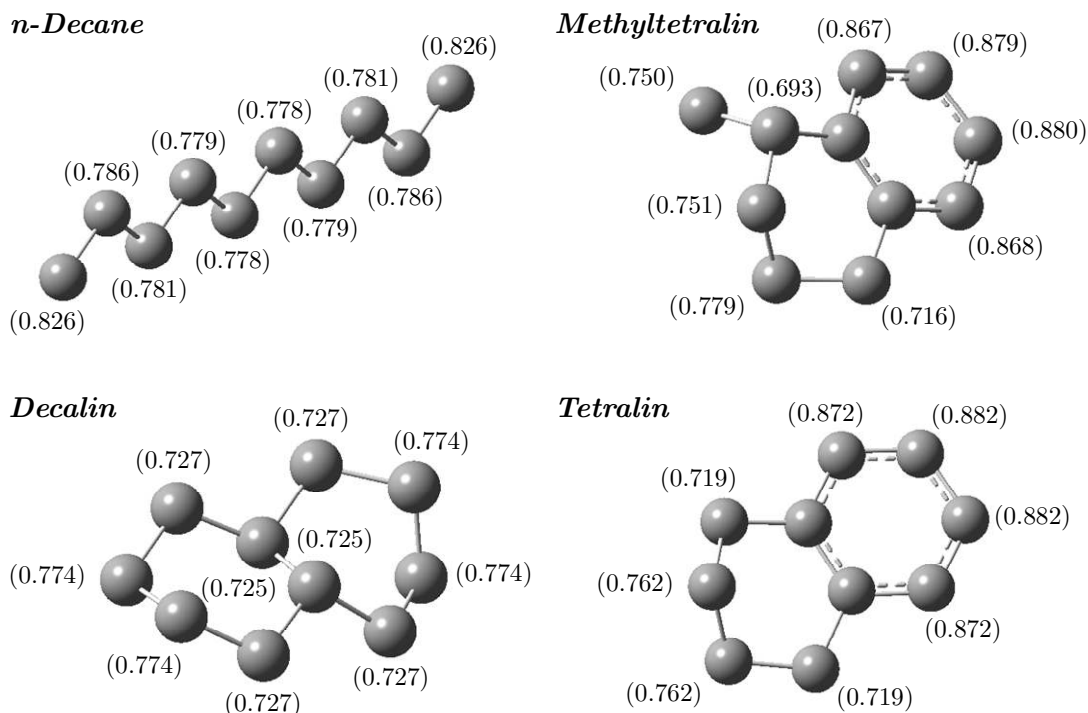


Figure 4.4 Relative activation energy of hydride dissociation at different locations of the donor molecules. The calculated values relative to methane, and computed by DFT.

Moreover, the hydride transfer ability can be semi-quantitatively determined from the strength of individual C-H bond in the naphthenic part of the molecules. As shown in Figure 4.5, a linear relationship can be found between the relative activation energy for hydride transfer reaction, as reported in Figure 4.4, and the Wiberg bond index calculated from the NBO analysis.

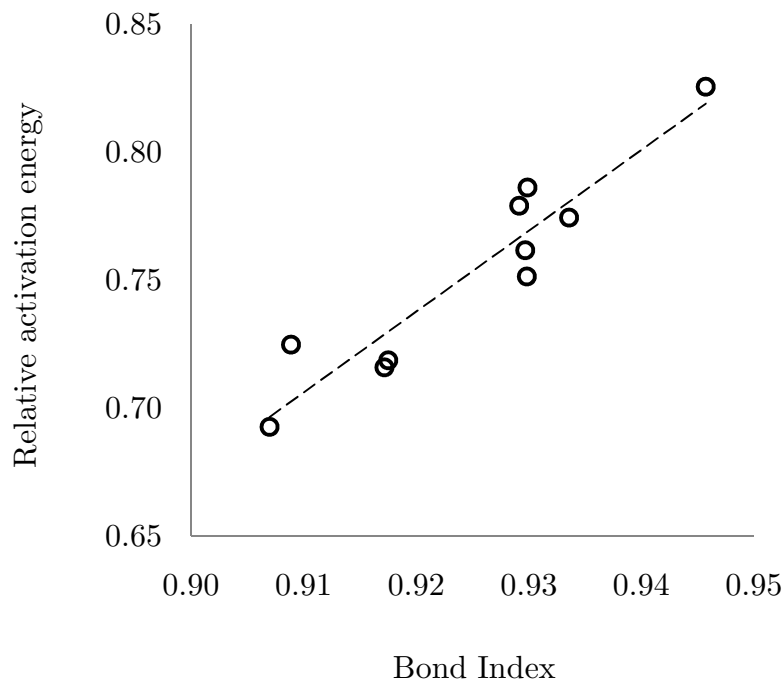


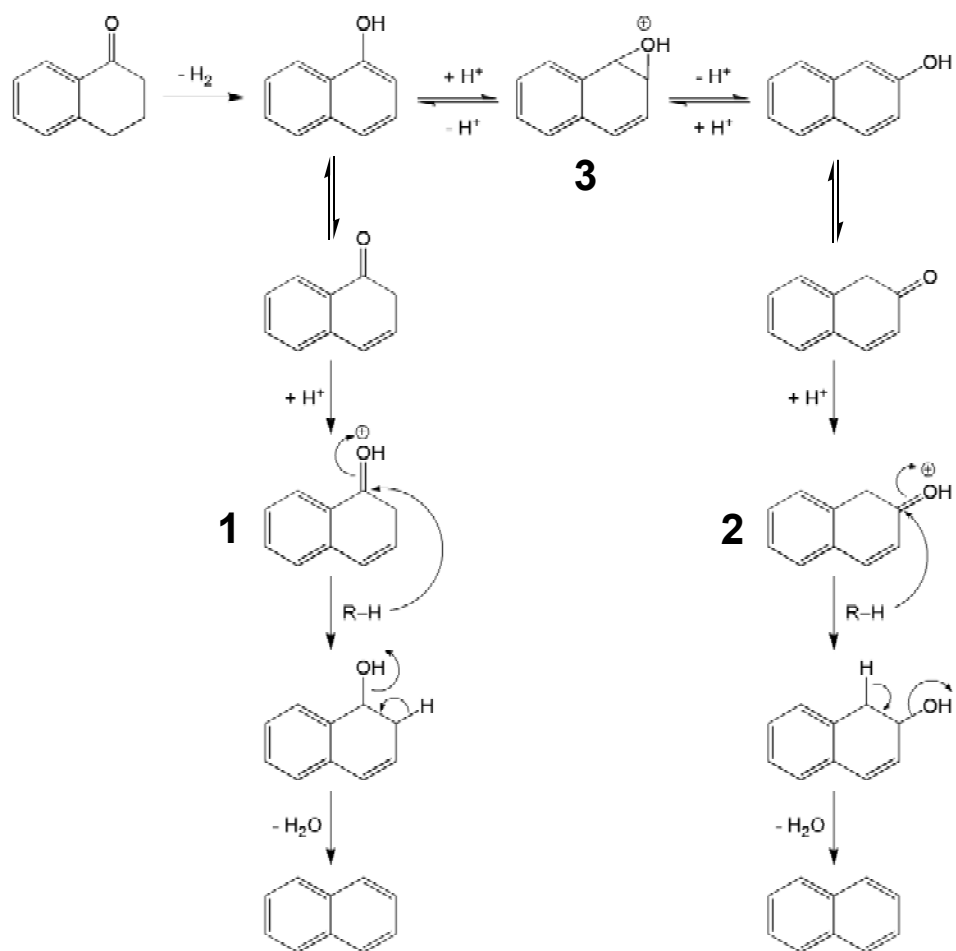
Figure 4.5 Relationships between the relative activation energy for hydride transfer reaction, and the bond index calculated from the NBO analysis.

4.4. Discussion

The catalytic conversion of 1-tetralone yields 1-naphthol as a primary product. Over strong acid sites, 1-naphthol can be isomerized to 2-naphthol, most probably via an oxiranium cation (**3**) as shown in the scheme below. At the same time, among all of the possible protonated naphthol species, the most stable structure is the most probable participant in the hydride transfer process. Therefore, the two keto-forms of naphthols (**1,2**) can be the protonated species that can act as hydride acceptors, leading to dehydrogenation and formation of naphthalene. Consequently, the rate of isomerization is low since the oxiranium

cation (**3**) is less stable and therefore less probable in the intermediate state than the keto-form species.

Depending on their hydrogen transfer ability, hydrocarbons can donate a hydride to the carbonyl carbon of the protonated keto-form of naphthol, generating the corresponding alcohol which can be rapidly dehydrated to produce naphthalene, as summarized in the scheme below. Since dehydration is relatively fast over acid catalysts,³² the rate at which naphthalene is produced can be determined by the rate of hydrogen transfer. The hydrocarbon acting as hydrogen donor is also converted according to their hydrogen transfer ability, giving rise to products that are also enhanced by the hydrogen transfer reaction, i.e., dehydrogenation and skeleton isomerization. From the applications point of view, the yield of naphthalene from 1-tetralone can be taken as a measure of the hydrogen transfer. So, the product distribution of 1-tetralone conversion can be used as an indicator of the hydrogen transfer ability of a particular hydrocarbon or mixture of hydrocarbons for a given catalyst. A simple method like this could give refiners a tool to select feeds or predict what changes in olefinicity and octane number one could expect when the feed is changed.



DMT performed as the best hydrogen donor since it contains hydrogen on a tertiary benzylic carbon, which shows low relative activation energy for hydride dissociation ($E_A \sim 0.693$, Figure 4.4). Likewise, tetralin exhibits a high rate of hydrogen transfer due to the presence of benzylic hydrogens ($E_A \sim 0.719$). Both DMT and tetralin convert mainly to their corresponding dehydrogenated product when co-fed with 1-tetralone. Due to the presence of tertiary carbons in its structure, decalin also possesses low relative activation energy for hydride dissociation ($E_A \sim 0.725$), but unlike the molecules containing one aromatic ring,

decalin facilitates hydrogen transfer via isomerization (*cis*- and *trans*-). The small increase in the production of alkylbenzene from decalin is also an indication of hydrogen transfer. When co-feeding weak hydrogen donors, such as *n*-decane, the effects are much less apparent. Moreover, the competitive adsorption of 1-tetralone and its products on the surface readily suppress the overall conversion of *n*-decane. This inhibition is due to strong adsorption of 1-tetralone and naphthol on the acid sites of the zeolite compared to a rather weak adsorption of the paraffin, lowering its reaction rate.

4.5. Conclusions

The acid-catalyzed reaction of 1-tetralone produces 1-naphthol as primary product, followed by secondary isomerization of 1-naphthol to 2-naphthol. The presence of hydrocarbons in the feed, which can act as a hydrogen donor, promotes hydrogen transfer reaction to the surface protonated naphthol, facilitating the dehydration of the corresponding alcohols to form naphthalene. Therefore, the yield of naphthalene from 1-tetralone can be taken as a measure of the hydrogen transfer. So, the product distribution of 1-tetralone conversion can be used as an indicator of the hydrogen transfer ability of a particular hydrocarbon or mixture of hydrocarbons. Both, the experimental naphthalene/naphthol ratios obtained experimentally and the DFT calculations show that the hydrogen transfer ability of hydrocarbon species follows the order

DMT > tetralin \approx decalin > *n*-decane. It has been shown that the hydrogen transfer reaction is also sensitive to acid site density (Si/Al ratio) and by a hydrogen donor concentration.

References

-
- 1 G.J. Kramer, R.A. Van Santen, C.A. Emeis, A.K. Nowak *Nature*. **1993**,363,529.
 - 2 M.C. Galiano, U.A. Sedran, *Ind Eng Chem Res*. **1997**,36,4207.
 - 3 D.M. Brouwer, H. Hogeveen *Prog Phys Org Chem*. **1972**,9,179.
 - 4 B.W. Wojciechowski, A. Corma *Catalytic Cracking: Catalysts, Chemistry and Kinetics*, Marcel Dekker, New York. **1986**.
 - 5 K.A. Cumming, B.W. Wojciechowski *Catal Rev*. **1996**,38,101.
 - 6 D. Wallenstein, R.H. Harding *Appl Catal A-Gen*. **2001**,214,11.
 - 7 D.S. Stratiev, I. Shishkova, P. Zeuthen, P. Vistisen *Ind Eng Chem Res*. **2007**,46,7691.
 - 8 A. Corma, A. Martinez, C. Martinez *J Catal*. **1994**,146,185.
 - 9 U.A. Sedran *Catal Rev*. **1994**,36,405.
 - 10 A. Feller, J.A. Lercher *Adv Catal*. **2004**,48,229.
 - 11 T. Prasomsri, R.E. Galiasso Tailleux, W.E. Alvarez, T. Sooknoi, D.E. Resasco *Catal Lett*. **2010**,135,226.
 - 12 J. Pajak, K.R. Brower *Energy Fuel* **1987**,1,363.
 - 13 J. Pajak, V. Krebs, J.F. Marêhé, G. Furdin *Fuel Proc. Technol*. **1996**,48,73.

-
- 14 T. Yao, Y. Kamiya *Bull Chem Soc Japan*. **1979**,52,492.
- 15 K. Chiba, H. Tagaya, T. Suzuki, S. Sato *Bull Chem Soc Japan* **1991**,64,1034.
- 16 R.W. Blue, C. Engle *J Ind Eng Chem* **1951**,43,494.
- 17 M.J. Frisch, G.W. Trucks, H.B. Schlegel, G.E. Scuseria, M.A. Robb, J.R. Cheeseman, J.A. Montgomery, Jr., T. Vreven, K.N. Kudin, J.C. Burant, J.M. Millam, S.S. Iyengar, J. Tomasi, V. Barone, B. Mennucci, M. Cossi, G. Scalmani, N. Rega, G. A. Petersson, H. Nakatsuji, M. Hada, M. Ehara, K. Toyota, R. Fukuda, J. Hasegawa, M. Ishida, T. Nakajima, Y. Honda, O. Kitao, H. Nakai, M. Klene, X. Li, J.E. Knox, H.P. Hratchian, J.B. Cross, V. Bakken, C. Adamo, J. Jaramillo, R. Gomperts, R.E. Stratmann, O. Yazyev, A.J. Austin, R. Cammi, C. Pomelli, J.W. Ochterski, P.Y. Ayala, K. Morokuma, G.A. Voth, P. Salvador, J.J. Dannenberg, V.G. Zakrzewski, S. Dapprich, A.D. Daniels, M.C. Strain, O. Farkas, D.K. Malick, A.D. Rabuck, K. Raghavachari, J.B. Foresman, J.V. Ortiz, Q. Cui, A.G. Baboul, S. Clifford, J. Cioslowski, B.B. Stefanov, G. Liu, A. Liashenko, P. Piskorz, I. Komaromi, R.L. Martin, D.J. Fox, T. Keith, M.A. Al-Laham, C.Y. Peng, A. Nanayakkara, M. Challacombe, P.M.W. Gill, B. Johnson, W. Chen, M.W. Wong, C. Gonzalez, J.A. Pople, Gaussian, Inc., Wallingford CT, **2004**.
- 18 H.B. Schlegel *J Comput Chem* **1982**,3,214.
- 19 M. Boronat, P. Viruela, A. Corma *J Phys Chem B*. **1997**,101,10069.
- 20 O. Tishchenko, N.-N. Pham-Tran, E.S. Kryachko, M.T. Nguyen, *J Phys Chem A*. **2001**,105,8709.
- 21 N. Solca, O. Dopfer *J Am Chem Soc*. **2004**,126,1716.
- 22 E. Reed, L.A. Curtiss, F. Weinhold *Chem Rev*. **1988**,88,899.
- 23 Z. Paál, P.G. Menon *Hydrogen Effects in Catalysis: Fundamentals and Practical Applications*, Marcel Dekker, New York, **1988**.
- 24 R.H. Mckee, A. Szayna *Ind Eng Chem*. **1930**,22,953.
- 25 G.M. Good, H.H. Voge, B.S. Greensfelder *Ind Eng Chem*. **1947**,39,1032.

-
- 26 D.C. Cronauer, D.M. Jewell, Y.T. Shah and R.J. Modi *Ind Eng Chem Fundam.* **1979**,18,153.
- 27 I. Graca, J.-D. Comparot, S. Laforge, P. Magnoux, J.M. Lopes, M.F. Ribeiro, F. Ramoa Ribeiro *Appl Catal A.* **2009**,353,123.
- 28 J. Meusinger, A. Corma *J Catal.* 1996,159,353.
- 29 X. Zhao, R.H. Harding *Ind Eng Chem Res.* **1999**,38,3854.
- 30 M.V. Frash, V.N. Solkan, V.B. Kazansky *J Chem Soc Faraday Trans.* **1997**,93,515.
- 31 C.J.A. Mota, D.L. Bhering, A. Ramírez-Solís *Int J Quantum Chem.* **2005**,105,174.
- 32 A.H. Keough, L.B. Sand *J Am Chem Soc.* **1961**,83,3536.

CHAPTER 5

5. Catalytic Conversion of Anisole over HY and HZSM-5 Zeolites in the Presence of Different Hydrocarbon Mixtures

5.1 Introduction

The unprecedented interest in renewable energy expressed in recent years by both government and industry has greatly accelerated research in this field.¹ As a result of these efforts, a significant increase in the role of renewable sources is expected for the near future.² In this regard, transportation is a crucial sector in which biomass-derived liquid fuels may have an important impact.^{3,4} Among the various approaches for production of biomass-derived liquids investigated during the last few decades, fast pyrolysis and catalytic pyrolysis appear as potential options.⁵ The products from these pyrolysis processes (so-called bio-oils) comprise different amounts of acids, esters, alcohols, furfural, aldehydes (including benzaldehyde with methyl and/or hydroxyl groups), and phenolics (phenol with methyl, methoxy and/or propenyl groups).⁶⁻⁹ Consequently, the oils directly obtained from fast pyrolysis (or even catalytic pyrolysis) processes cannot be directly used as transportation fuels without a prior upgrade. Their high oxygen and water contents cause chemical

instability, immiscibility with hydrocarbon fuels, high viscosity, high acidity, and low heating value.¹⁰

A major challenge in processing bio-oils in commercial scale is the massive production volume that will need to be handled. Therefore, it will be desirable to utilize existing refining infrastructure. For example, fluid catalytic cracking (FCC) represents a possible upgrading alternative since it is one of the largest refinery processes, it has flexibility for handling varying feedstocks, and does not require hydrogen, a valuable commodity. The primary function of the FCC process is to convert gas-oil streams containing high-boiling-point and high-molecular-weight hydrocarbons to more valuable products, such as high-octane gasoline and olefin-rich light gases, e.g. propylene. Co-processing bio-oils with conventional crude oil cuts in FCC units has been discussed in the literature.¹¹⁻¹⁴

Phenolics derived from lignin represent a significant fraction of bio-oil and are known to be much more refractory than other oxygenates in bio-oil.¹⁵⁻¹⁸ Moreover, they tend to accelerate catalyst deactivation due to enhanced coke formation and strong adsorption on acid sites.^{13,14} The objective of this contribution is to quantify this deactivating tendency on acidic zeolites, using anisole as a model phenolic compound and to explore the effects of the presence of some hydrocarbons representative of FCC components. We conducted most of our studies on HY zeolites, which are typical active components in FCC catalysts.¹⁹ For comparison, the behavior observed on an HZSM-5 zeolite was

also investigated. The influence of feed composition on the activity, product selectivity, and catalyst stability was investigated for various hydrocarbons in a continuous flow reactor. In addition, experiments were performed using a pulse reactor to elucidate the reaction pathway for the specific mixture of anisole and tetralin, which is an effective H-donor.

5.2 Experimental

5.2.1 Catalytic measurements

The catalytic measurements were conducted on a $\frac{1}{4}$ " stainless steel tubular reactor. Commercial zeolites (HY (Si/Al = 15 and 40) from Zeolyst International and HZSM-5 (Si/Al=45) from Süd-Chemie) were used as catalysts. Anisole, a phenolic model compound with a methoxy functionality, typically present in bio-oil phenolics, was used as the main feed. Various hydrocarbons including propylene ($C_3=$), benzene (Bz), *n*-decane (*n*- C_{10}) and tetralin (Tet), were used as co-feeds. In each run, the catalyst sample (50 mg, 40–60 mesh) was placed at the center of the reactor and held in place with plugs of clean glass wool. The top and bottom parts of the packed bed were filled with 3 mm-diameter glass beads. The thermocouple was affixed to the outside wall of the reactor, at the height corresponding to the center of the catalyst bed. The

operating conditions were as follows: atmospheric pressure, 400 °C, He carrier gas (40 mL/min), space-time (W/F) 0.42 h, with respect to the mass flow rate of anisole in both pure and mixed feeds. Prior to each run, the feed was sent through a by-pass until the concentration stabilized. At this point, the feed stream was switched to enter the reactor. The feed was introduced from a syringe pump at a liquid flow rate 0.12-0.24 mL/h and vaporized before entering the reactor. All pipelines were kept heated at 300 °C to avoid condensation of reactants. The products were analyzed on-line using an HP5890 gas chromatograph, equipped with an HP-5 column and a flame ionization detector (FID) detector. In parallel, the effluent was trapped in methanol, and analyzed by GC-MS (Shimadzu QP2010s) with the same HP-5 column, using reference standard compounds for identification. The space time (W/F), expressed in hours, is defined as the ratio between the mass of the catalyst and the mass flow rate of the feed.

It must be noted that the thermal conversion (i.e. blank run with an inert at the same reaction temperature) was negligible for all mixed feeds investigated.

5.2.2 Pulse experiment

The same reactor system was modified to operate in the pulse mode. In this case, two six-port valves were placed in a heating box, connected to the

reactor inlet, outlet and sample loop to switch the flow and inject the pulse of reactant. The reactor includes 2 parallel $\frac{1}{4}$ " stainless steel tubes, one for bypass, and the other for reaction, which are connected through 3-way valves, also placed inside the oven. The tubing was heated by heating tape to avoid condensation of the reactants.

The feed was injected from a syringe pump, evaporated in the injection port and carried by He gas flow (He #2) into the sampling valve to fill the loop. Then, by switching the six-port valve, another He gas stream (He #1) was used to push the mixture from the sample loop into the reactor and carry it directly into the GC column for analysis. The 30mg catalyst sample (HY, Si/Al=40 or HZSM-5, Si/Al=45) was mixed with 70mg Hisil silica used as diluents and packed in the reactor tube. The catalyst bed was placed between two sections of 1-mm glass beads and fixed in place with clean glass wool. Before starting the pulse reaction experiment over the catalyst, the mixture from the sample loop was sent repeated times through the bypass line until a stable pulse size was measured in the GC. Then, the 3-way valves were switch to reactor tube. The products leaving the reactor were analyzed by the same GC-FID system mentioned above. The operating conditions for the pulse experiments can be specified as follows. Pulse: 1.0-sec retention time, size: 0.0033 mmol tetralin and 0.0017 anisole mmol, atmospheric pressure, 450 °C.

5.2.3 Catalyst characterization

The coke deposited during reaction was analyzed by temperature programmed oxidation (TPO) of 30 mg samples of spent catalyst, under a gas flow of 2% O₂/He (30 mL/min). The heating ramp was 10 °C /min. The signals of H₂O (m/z = 18) and CO₂ (m/z = 44), were continuously monitored by a mass spectrometer (MKS). The total amount of coke deposits on the catalysts was quantified by a carbon elemental analyzer.

The acidic properties of the various zeolites were characterized by temperature programmed desorption of ammonia (NH₃-TPD), conducted in a 0.25 in. o.d. quartz reactor. Before each experiment, a 50 mg zeolite sample was pretreated for 0.5 h in flowing He (30 mL/min) at 600 °C to eliminate any adsorbed water. Then, the temperature was lowered to 100 °C, and the sample exposed to a 2% NH₃/He, 30 mL/min stream for 30 min to reach saturation. After exposure, pure He was passed for 0.5 h over the sample to remove any weakly adsorbed NH₃. To conduct the TPD, the temperature was increased at a heating rate of 10 °C/min up to 650 °C. The evolution of desorbed species was continuously monitored by a Cirrus mass spectrometer (MKS) recording the signals m/z = 17 and 16 (corresponding to NH₃) and 41 (corresponding to propylene). The density of acid sites was quantified by calibrating the MS signals with the average of ten 5-mL-pulses of 2% NH₃/He.

5.2.4 Computational details

The zeolite catalyst was simulated by an extensively used cluster model, which contains four tetrahedral atoms (4T) three silicon and one aluminum atom in order to generate the acidic site.²⁰ The silicon and oxygen atoms bonded to aluminum are saturated with hydrogen atoms, therefore creating a small surface of zeolite. According to the quite small size of the cluster, reacting molecules on the cluster were optimized with care to ensure that reactants and products were coordinated similarly to the cluster for all reactions, which leading to the reliable energy trends.

All calculations were performed by using GAUSSIAN 03 suite of programs.²¹ The B3LYP hybrid density functional combined with 6-31G(d) basis sets was utilized for all geometry optimizations. No geometric constraints were used in the optimizations.²²⁻²⁴ For all stationary points, vibrational spectra were calculated to ensure the correctness of calculations such as one imaginary frequency for transition states and zero for energy minima.

5.3. Results and discussion

5.3.1 Catalytic reactions of pure anisole over HY zeolite

The total conversion and product distribution obtained from feeding pure anisole (An) onto the HY zeolite are summarized in Table 5.1. The main products were phenol (Ph), cresol isomers (Cr), xylenol isomers (Xol), methylanisole isomers (MA), and trace amount of light gases (mainly methane for pure anisole feed and C₁-C₅ hydrocarbons for mixture feeds). In line with anisole conversion results previously observed on HZSM-5,²⁵⁻²⁷ we find here that transalkylation is the dominant reaction over HY. The transalkylation steps involved in the anisole conversion that account for the observed products, are as follows.²⁵

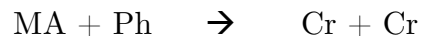
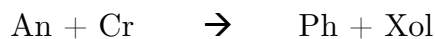
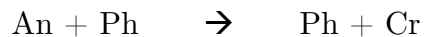
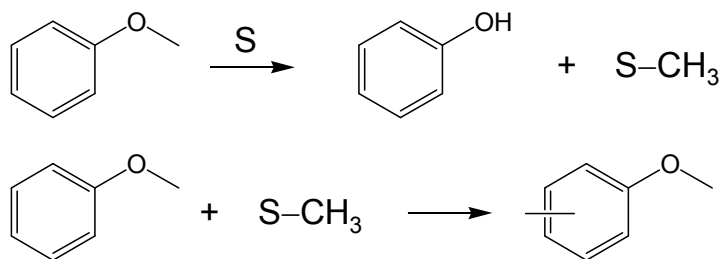


Table 5.1 Product distributions from conversion of anisole and anisole-tetralin mixture (~50% tetralin) over HY zeolite. Reaction conditions: W/F = 0.42 h (wrt. anisole for co-feed reaction), T = 400 °C, P = 1 atm He.

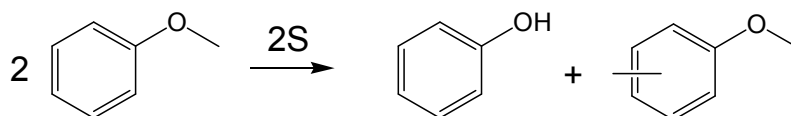
Feed	Anisole		Anisole + Tetralin	
	TOS 0.5 h	TOS 3.0 h	TOS 0.5 h	TOS 3.0 h
Conversion of anisole	83.6	13.9	100.0	100.0
Conversion of tetralin	-	-	98.4	96.6
Yield (wt%)				
C ₁ -C ₅	1.2	0.2	8.8	8.2
Anisole	16.4	86.1	0.0	0.0
Phenol	35.2	6.8	28.1	29.2
Methylanisoles	3.3	4.2	0.0	0.0
Cresols	26.4	1.4	12.5	13.1
Xylenols	17.5	1.3	2.8	2.8
Benzene	0.0	0.0	2.1	1.9
Toluene	0.0	0.0	3.5	3.0
Alkylbenzene	0.0	0.0	9.7	8.8
Tetralin	0.0	0.0	0.8	1.7
Naphthalene	0.0	0.0	20.0	19.9
Alkylnaphthalene	0.0	0.0	9.9	9.5
Heavies	0.0	0.0	1.8	1.9
Selectivity of anisole products (wt%)				
Methane	1.4	1.4	2.8	1.1
Phenol	42.1	48.9	63.7	64.0
Methylanisoles	3.9	30.2	0.0	0.0
Cresols	31.6	10.1	27.4	28.7
Xylenols	20.9	9.4	6.1	6.1

Scheme 1

Dissociative (sequential path)



Non-dissociative (bimolecular path)



It must be noted that these steps are not necessarily elementary and may involve intermediate steps.²⁵ Two possible reaction pathways can be considered for the transmethylation steps involved in these reactions (see scheme 1). The first one is a dissociative pathway, in which an anisole (An) molecule generates phenol (Ph) and a methyl group, which may remain on the catalyst site as a surface methoxy. In a second step, this methoxy group can be transferred to another aromatic molecule. This aromatic molecule could be An yielding MA (as shown in Scheme 1), but it also could be any of the molecules included in the secondary reactions shown above (Ph, Cr) or an aromatic molecule present in the feed, (e.g., tetralin). The second possible reaction pathway involves a non-dissociative bimolecular reaction. In this case, as shown in Scheme 1, two anisole molecules directly interact on the surface, producing Ph and MA. A similar non-dissociative bimolecular reaction could in principle

be operative for the other reactions mentioned above, including the reaction with tetralin, which is discussed below.

A rather fast catalyst deactivation was observed as a function of time on stream (TOS). That is, within 3 h of reaction, the anisole conversion dropped from more than 83% to less than 14%. Both, coke formation and strong adsorption of phenolic compounds (i.e. anisole and its derivatives) may be responsible for the rapid catalyst deactivation.^{13,14} An interesting trend in product distribution can be observed as the catalyst deactivates. Figure 5.1 shows the evolution of products (in yield %) as a function of TOS. It is first noted that phenol (Ph) is the most abundant product at all TOS. At the beginning of the run, the yield of cresol (Cr) and xylenol isomers (Xol) is higher than that of MA; however, this trend is reversed as the catalyst deactivates (i.e. at high TOS). A previous kinetic study²⁵ demonstrated that Ph and MA are the two primary products arising from anisole disproportionation. By contrast, Cr and Xol appear as secondary products derived from subsequent transalkylation steps.

The evolution of MA shows a maximum as a function of TOS. MA is only produced in the primary transalkylation while the subsequent steps only consume it. The catalyst deactivation causes an initial increase in MA due to a decreased consumption, but at long enough TOS the deactivation affects the primary step as well and the overall generation of products, including MA,

decreases. This maximum was not observed for Ph, which in secondary steps, is not only consumed but also produced.

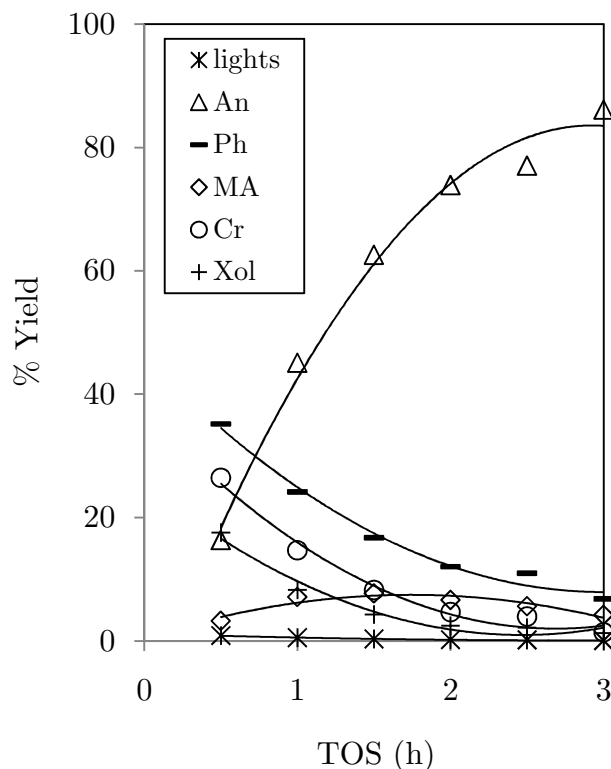


Figure 5.1 Product composition at the reactor outlet as a function of time on stream during anisole conversion over the HY zeolite.
 Reaction conditions: W/F = 0.42 h , T = 400 °C, P = 1 atm He.

5.3.2 Effect of mixing anisole with different hydrocarbons over zeolites

To compare the effect of co-feeding hydrocarbons on the reaction of anisole, reactions with mixed feeds were performed at the same $W/F(\text{An}) = 0.42$ h with respect to the mass rate of anisole ($F(\text{An})$). That is the total W/F

was in fact lower for the mixture because the total feed rate of the mixture (F) was higher than the feed rate of anisole alone ($F(\text{An})$), which was kept constant. As seen in Table 1, the anisole conversion of feed containing 50% tetralin was enhanced dramatically to $\sim 100\%$ (i.e. W/F became in excess) even though the total W/F was lower and the $W/F(\text{An})$ was the same as in the case of pure An.

In addition to the changes in activity and stability, significant changes in product distribution were observed with the mixed feed in comparison to the reaction with the pure anisole. For example, the amount of methylanisoles, cresols, and xylenols obtained with pure anisole were significantly higher than those obtained with the mixed feed. At the same time, no changes in product distribution were observed as a function of TOS during the reaction. As we have recently discussed,²⁸ tetralin is an effective H-donor in H-transfer reactions, and it is conceivable that a similar effect is responsible for the enhancement observed here.

A similar set of experiments was conducted with different co-fed hydrocarbons ($\sim 50\%$ hydrocarbon – 50% anisole). The effect of the presence of different hydrocarbons in the mixture is illustrated with the different deactivation profiles shown in Figure 5.2 together with the profile obtained with anisole alone (dashed line). The addition of tetralin greatly increased the anisole conversion on the HY zeolite. Since the conversion was 100% during the entire reaction time it is not possible to evaluate the deactivation, but it is clear that

the activity remained very high during the 3 h of the experiment. It is suggested that H-transfer from tetralin, a good H-donating compound²⁸ participates in this enhancement in conversion, which also results in minimization of coke deposition.

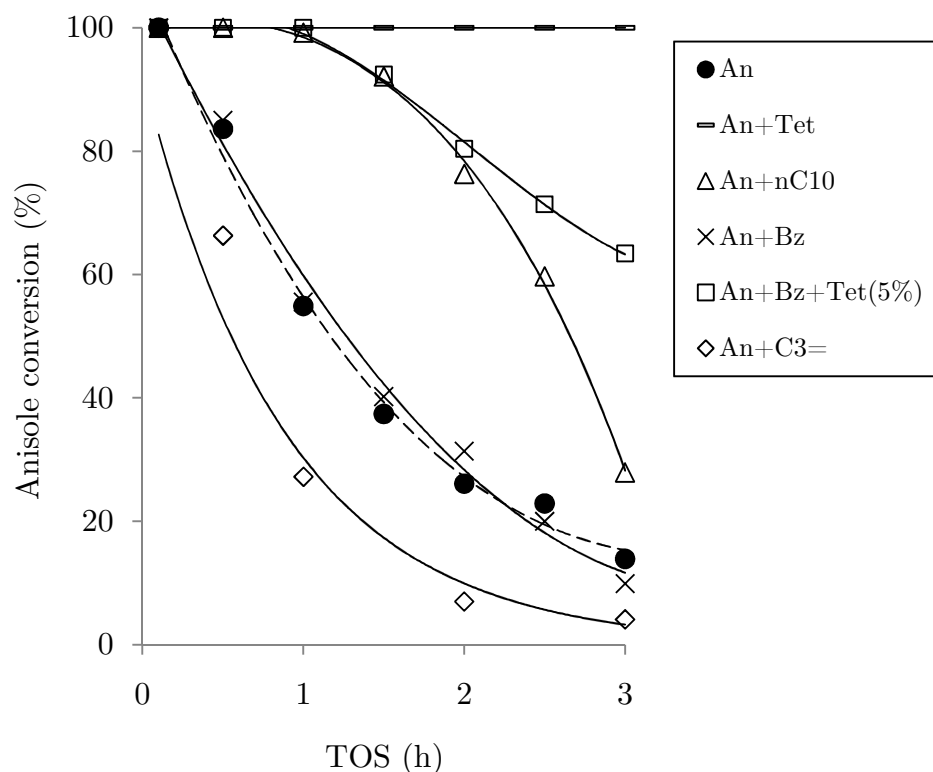


Figure 5.2 Anisole conversion over HY zeolite with different co-fed hydrocarbons as a function of time on stream. Pure anisole feed is indicated with a dashed line. Reaction conditions: W/F = 0.42 h (wrt. anisole for co-feed reactions), co-feed concentration = ~50%, T = 400 °C, P = 1 atm He.

In contrast, when benzene was used in the mixture instead of tetralin, the deactivation profile followed the same trend as that observed with pure

anisole. Benzene is not a H-donor molecule and therefore it is not surprising that it showed no enhancement in either anisole conversion or catalyst stability. Interestingly, as shown in Figure 5.2, adding only 5% of tetralin into the anisole/benzene mixture had a significant positive impact on anisole conversion. The addition of *n*-decane had a noticeable effect, although not as pronounced as that obtained with tetralin. Finally, co-feeding propylene had a negative effect on anisole conversion; it is evident that propylene itself can participate in coke formation^{29,30} and accelerates catalyst deactivation.

The presence of tetralin not only enhanced anisole conversion, but also influenced product distribution, as shown in Figure 5.3. For instance, the degree of the secondary reaction of phenol alkylation can be measured by the ratio (Cr+Xol)/Ph. For the pure anisole feed, this ratio was about 1.2 at the start of the reaction and decreased to about 1.0 as the catalyst deactivated, since the contribution of the secondary reactions became less prominent (Figure 5.4a). Similar behavior is observed when the anisole feed was mixed with propylene, *n*-decane or benzene than for pure anisole (Figures 5.4 c and d). By contrast, the ratio was less than about 0.5 for the anisole/tetralin mixture and it remained unchanged as a function of TOS (Figure 5.4b). The reduced phenol alkylation in the presence of tetralin was compensated by an increase in the alkylation of tetralin. In fact, the alkylnaphthalenes/naphthalene ratio gradually increases with the concentration of anisole in the feed as compared with that of pure tetralin (Figure 5.5). This trend demonstrates that anisole can

transfer its methyl group from the methoxyl group to naphthalene, which is a product of tetralin dehydrogenation.

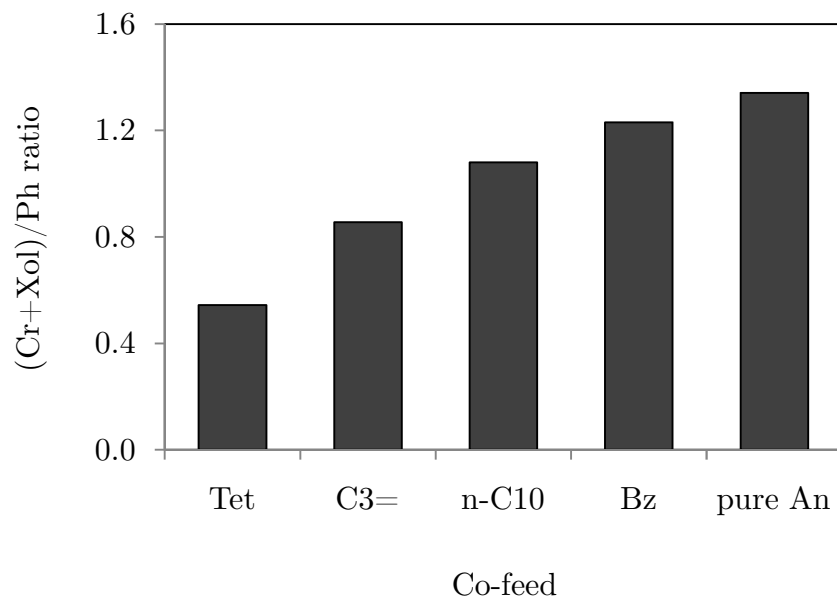


Figure 5.3 Degree of phenol alkylation (i.e. (Cr+Xol)/Ph yield ratio) for pure anisole and mixture feed reactions over the HY zeolite. Reaction conditions: W/F = 0.42 h (wrt. anisole), T = 400 °C, P = 1 atm He, co-feed concentration = ~50%, TOS = 0.5 h.

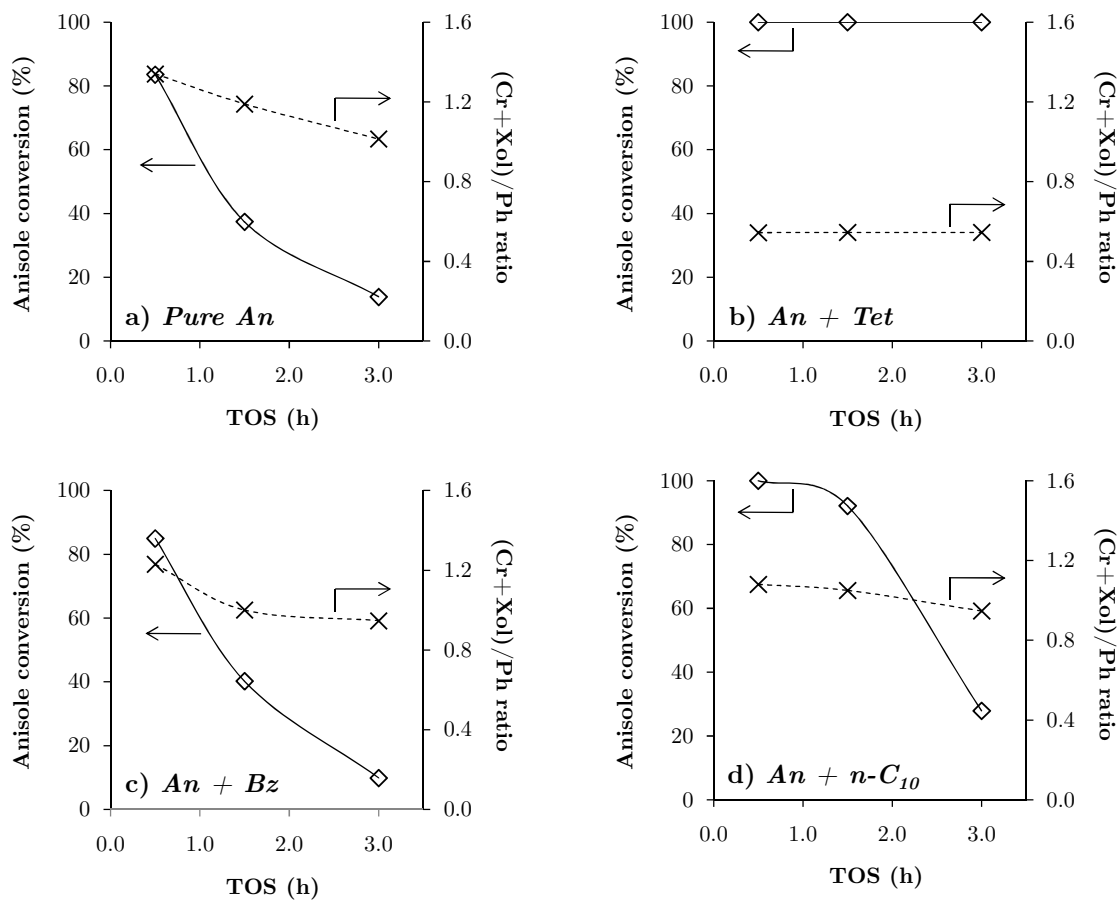


Figure 5.4 Relationship between conversion of anisole and degree of phenol alkylation as a function of time on stream for a) pure anisole, b) anisole-tetralin mixture, c) anisole-benzene mixture, and d) anisole-*n*-decane mixture feeds. Reaction conditions: W/F = 0.42 h (wrt. anisole), T = 400 °C, P = 1 atm He, co-feed concentration = ~50%, TOS = 0.5 h.

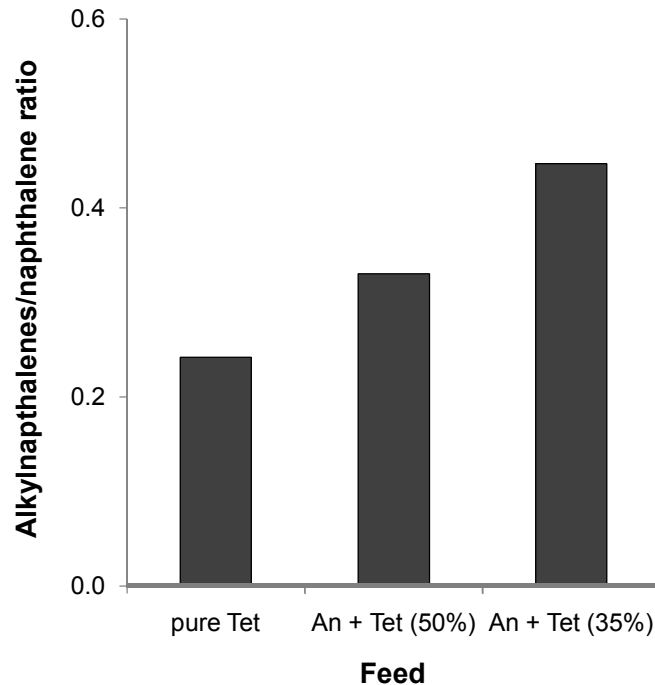


Figure 5.5 Alkylnaphthalenes/naphthalene product ratio for pure tetralin and mixture feed reactions over the HY zeolite. Reaction conditions: W/F = 0.42 h (wrt. anisole), T = 400 °C, P = 1 atm He, TOS = 0.5 h.

5.3.3 Coke formation during reaction of pure anisole and mixtures

Table 5.2 compares the amount of C (wt%) deposited on the HY zeolite during 3-h TOS from the different feed mixtures. The amounts deposited during this period from pure anisole and pure tetralin feeds are 11.8 and 3.0 wt% C, respectively. Interestingly, the addition of tetralin to anisole results in a reduction in C deposits. The extent of this reduction depends on the concentration of cofed tetralin. That is, the amount of C deposits dropped from 11.8 to 8.8 and 6.0 wt% C as the concentration of tetralin increased from 0 % to 35% and 50%, respectively. It must be noted that, as shown in Table 5.2, the

same trend is observed whether the amount of C deposits is compared to either the total amount of anisole or the total amount of feed passed over the catalyst.

Table 5.2 Comparison of amount of carbon deposited on spent catalysts from the reactions of different mixture feed over the HY zeolite.
Reaction conditions: W/F = 0.42 h (wrt. anisole for co-feed reaction),
T = 400 °C, P = 1 atm He. TOS = 3 h.

Feed	C (wt %)	mg _{carbon} /g _{anisole}	mg _{carbon} /g _{total feed}
Pure An	11.8	16.5	16.5
Pure Tet	3.0	-	4.1
An + Tet (50%)	6.0	8.4	4.2
An + Tet (35%)	8.8	12.3	8.0
An + <i>n</i> -C ₁₀	10.6	14.8	7.4
An + Bz	11.6	16.2	8.1
An + C ₃ =	15.9	22.3	11.1

We rationalize the reduction in C deposits by an enhanced H-transfer, which as previously shown,³¹ inhibits coke formation that results in catalyst deactivation, in line with the higher stability shown in Figure 5.2 when tetralin is added to the feed.

This concept is further supported by the almost insignificant effect on coke formation observed when other hydrocarbons with lower H-transfer capacity are used as co-feed. In fact, the amount of C deposited when incorporating *n*-decane and benzene to the anisole feed was about the same as

that deposited when anisole was used as a pure feed. Moreover, when a coke-forming molecule such as propylene was used, the C deposits increased to 15.9 wt% C. That is, the trends in coke formation are consistent with the observed deactivation patterns (Figure 5.2).

To gain further insight about the nature of the coke deposits, the evolution of H₂O and CO₂ during the TPO of the coked catalysts was monitored and quantified in a mass spectrometer. The integrated intensity ratios between the H₂O and CO₂ signals are reported in Table 5.3. It is apparent that the reaction under pure anisole produced a coke richer in H compared to that obtained under either pure tetralin or the anisole/tetralin mixture. This difference suggests that, in the absence of tetralin, anisole adsorbs strongly on the HY zeolite and forms carbonaceous deposits with a much lower extent of dehydrogenation.^{13,14} So, the deactivation due to anisole can be described as a molecular condensation process on the active surface, rather than the typical formation of polyaromatic coke. By contrast, in the presence of tetralin, elimination of anisole and its surface derivatives from the surface is assisted via H-transfer from tetralin. The coke thus formed is primarily arising from tetralin and from those species which cannot be eliminated from the surface via H-transfer. They become more dehydrogenated than the adsorbed anisole species, as suggested by the low H₂O/CO₂ ratio observed during TPO (Table 5.3).

Table 5.3 Amounts of carbon formed on the spent over the HY zeolite.
 Reaction conditions: W/F = 0.42 h (wrt. anisole for co-feed reaction),
 T = 400 °C, P = 1 atm He. TOS = 3 h.

Feed	C (wt %)	mg _{carbon} /g _{total feed}	A _{H₂O} /A _{CO₂}
Pure Tet	3.0	4.1	0.26
An + Tet (50%)	6.0	4.2	0.28
Pure An	11.8	16.5	0.56

5.3.4 Recovery of anisole conversion by flushing the spent catalysts with tetralin

Two additional experiments were conducted to shed further light on the role of tetralin in inhibiting deactivation by anisole (Figure 5.6). In the first experiment, a flow of pure anisole in He carrier was continuously fed for 2 h into the reactor at a W/F = 0.42 h and T = 400 °C. After stopping the flow of anisole (in He), pure tetralin (in He) was injected at the same W/F during 1 h. Finally, the feed of pure anisole (in He) was restarted at the same initial conditions. It is observed that during the first 2 h of reaction, the conversion of anisole dropped from ~80% to ~20%. However, after passing pure tetralin (in He) for 1 h, the anisole conversion was observed to recover to about 40%. After re-injection of the pure anisole feed, the catalyst started deactivating again. The partial recovery of the catalyst activity by passing tetralin suggests that at least some of the catalyst sites deactivated by anisole (or its derivatives) can be regenerated in the presence of tetralin. That is, unlike the typical deactivation

by coke, the strong adsorption of phenolic compounds (e.g. anisole and phenol) can be partially reversible by H-transfer from tetralin.

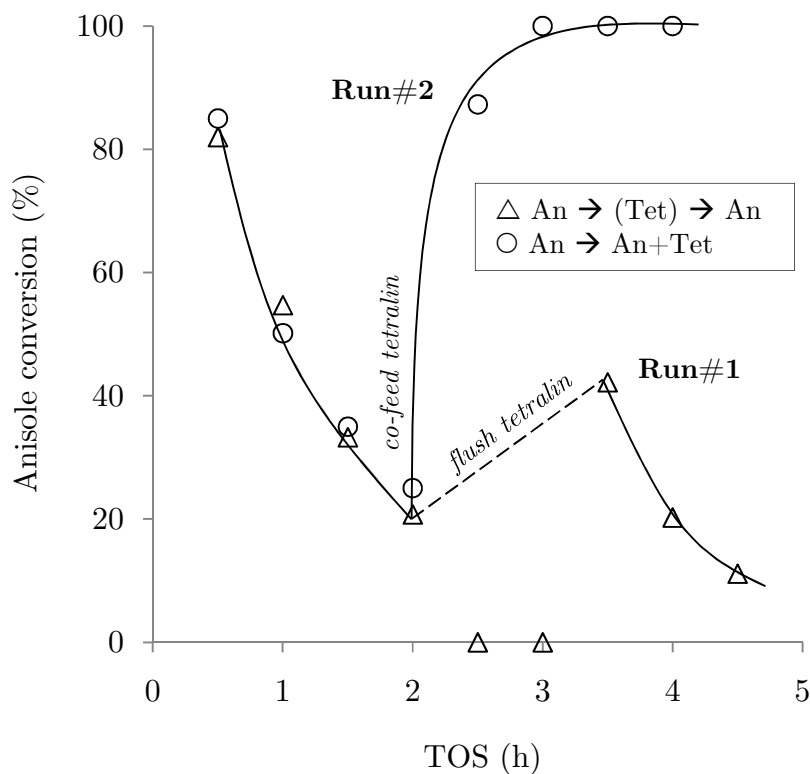


Figure 5.6 Effect of co-fed tetralin on anisole conversion over the HY zeolite. Reaction conditions: W/F = 0.42 h (wrt. anisole for co-feed reaction), co-feed concentration = ~50%, T = 400 °C, P = 1 atm He.

In the second experiment in this series, pure anisole (in He) was fed into the reactor for 2 h, under the same conditions as in the other sequence. However, in this case, after the first anisole reaction period, a 50/50 tetralin/anisole mixture was co-fed while the anisole conversion was being measured. As shown in Figure 5.6, a remarkable increase in anisole conversion

that went from ~20% to ~100% was observed as a function of time on stream, exceeding even the initial conversion observed under pure anisole. In this case, the role of tetralin is not only helping remove fragments that deactivate the surface, but also starting the non-dissociative bimolecular transalkylation, which is very significant on the open structure of HY zeolite.

5.3.5 Reaction pathways

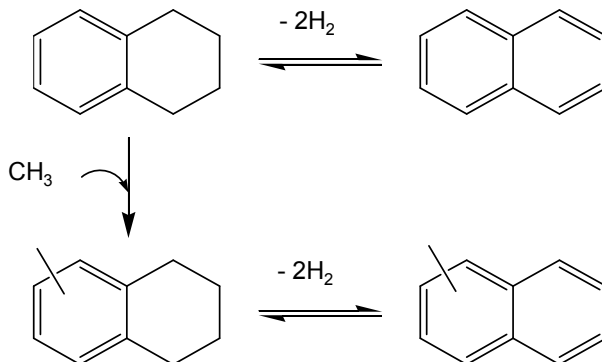
As mentioned above two possibilities can be considered for the transmethylation of aromatic molecules containing a methoxy group, a dissociative sequential pathway and a non-dissociative bimolecular pathway.

To check whether these paths occur to a significant extent the following experiment was devised. After stabilizing the reactor and the detector, a pulse of anisole was first fed to the reactor followed by a pulse of tetralin sent 4-5 s later. Since the two reactants are not simultaneously present on the catalyst, it is anticipated that only if the dissociative (sequential) pathway is operative transmethylation will be observed. That is, the anisole from the first pulse, can dissociate and leave a methyl group on the surface, this group can subsequently react with tetralin sent in the subsequent pulse.

Methylation preferentially occurs on activated aromatic rings. The aromatic ring in tetralin is highly activated and therefore it has the tendency to

accept a methyl group. At the same time, tetralin is a hydrogen donor and can easily dehydrogenate to naphthalene. Since the hydrogenation/dehydrogenation reactions can be equilibrated at the high temperature of the experiments, while alkylation involves tetralin, only alkylnaphthalene and naphthalene are observed in the products, as illustrated in Scheme 2.

Scheme 2



Accordingly, the ratio of methylnaphthalene-to-naphthalene represents the degree of transalkylation of tetralin. As shown in Figure 5.7, this ratio greatly increased with the addition of anisole since with pure tetralin, alkylation can only occur from cracking fragments. The significant increase observed during the sequential pulses (An \rightarrow Tet) compared to pure tetralin supports the concept of the dissociative mechanism. It is conceivable that, while the separation time between the anisole and tetralin pulses was very short (4 sec.), a significant fraction of the methyl group may leave the surface under the

continuous flow of He; therefore, the degree of tetralin alkylation in the sequential pulse experiment (i.e. An→Tet) is always lower than that for the mixed pulses (i.e. An+Tet), in which the surface methyl groups can be consumed immediately, as also shown in Figure 5.7 (grey bars).

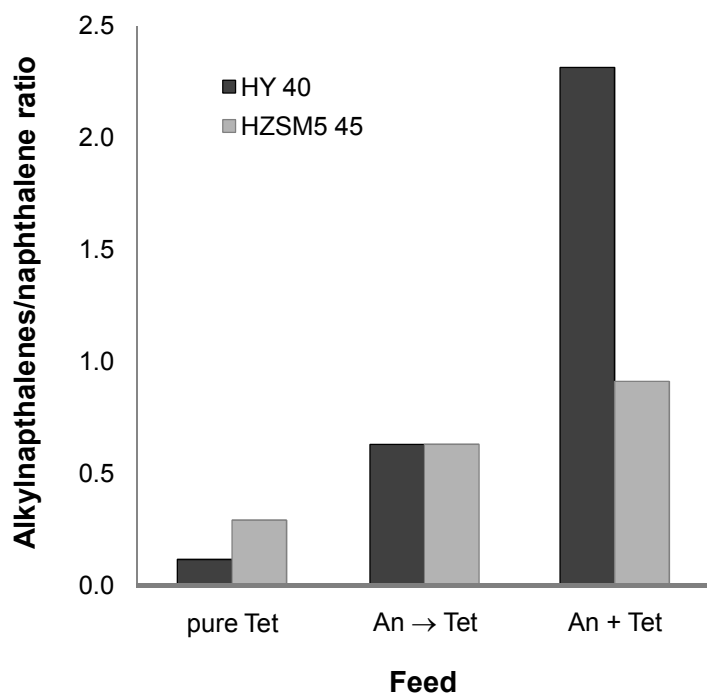


Figure 5.7 Alkylnaphthalenes/naphthalene product ratio (at the 5th pulse) for pure tetralin and mixture feeds over the HY and HZSM5 zeolites in pulse experiment. Reaction conditions: T = 450 °C, P = 1 atm He.

pure Tet: pure tetralin, catalyst/feed ratio = 70 (g/g); An → Tet: pulse tetralin right after anisole injection, catalyst/feed ratio = 70 (g/g tetralin) and 150 (g/g anisole); An + Tet: mixture of anisole and tetralin (30 wt% tetralin), catalyst/feed ratio = 70 (g/g tetralin).

Interesting differences are observed when the results obtained on HY are compared to those obtained over an HZSM-5 zeolite of similar Si/Al ratio.

When the sequential anisole/tetralin pulses were sent over the catalysts, the degree of tetralin alkylation (as measured by the alkylnaphthalene/naphthalene ratio) was almost identical for both HZSM-5 and HY. As discussed above, only the dissociative reaction pathway is operative in this case since anisole and tetralin are not simultaneously present over the catalysts. This reaction mode shows no significant differences between the two zeolites, with comparable number of acid sites. In contrast, in the mixed feed pulse experiments the extent of alkylation was much lower for HZSM-5 than for HY. Certainly, the differences in structure show a greater effect for the bimolecular path. The HZSM-5 zeolite has 10-membered ring aperture channels, with the diameter of 5.6 Å, whereas HY has 12-membered ring aperture channels with the diameter of 7.4 Å and much larger void spaces in the supercages.³² The more open structure of HY is favorable for the bimolecular re-arrangements required for the non-dissociative path, which results in an extra contribution towards the alkylation rate via the non-dissociative bimolecular path. By contrast, it has been long recognized that the much more restrictive pores in HZSM-5 inhibit bimolecular encounters.³³ More recent molecular dynamics studies of aromatics in MFI structures support this concept.³⁴ Similarly, one can predict that tetralin and anisole can diffuse with significant hindrance into the small channel of HZSM-5 and, as a result, the bimolecular reactions would be inhibited, making the dissociative reaction pathway dominant.

Furthermore, the two proposed mechanisms, dissociative and non-dissociative, were theoretically investigated by the model described above. For dissociative reaction pathway, migration of the methyl group of anisole (i.e. R-O-CH₃) occurs via the zeolite surface. If we consider now the corresponding surface methoxide formation from anisole, the reaction starts with the adsorption of anisole on the Brønsted acid active site of a zeolite, as the end-on adsorption complex. The potential energy diagram for this reaction is shown in Figure 5.8 and selected geometrical parameters are listed in Table 5.4. The anisole adsorbs on the acidic site through the H-bonding interaction between its oxygen (O3) and the surface proton (H1). The H1-O1 distance, therefore, increases from 0.96 to 1.02 Å (Ads_An). At the same time, C1-O3 is weakening (i.e. lengthened by 0.05 Å) because the electron is transferred from O3 to H1 during H-bonding.³⁵ In the transition state, the proton (H1) is migrated to the oxygen of adsorb anisole (O3) to form the H1-O3 bond; thereby the C1-O3 bond of the adsorbed anisole is cleaved to form the leaving phenol molecule. Its oxygen atom O3, C1, and the surface oxygen atom, O2, are aligned in a linear way. The breaking C1-O3 bond is elongated from 1.47 to 1.69 Å, and the C1-O2 distance decreases to 2.27 Å. The activation energy for the protonation step is 48.9 kcal/mol, which is slightly higher than the protonation of dimethyl ether (42.9 kcal/mol).³⁵ Next, the surface methoxide species and a methanol molecule are generated on the zeolite framework. The surface C1-O2 distance in the surface methoxide species is 1.46 Å (Z-OCH₃). The calculated adsorption energy of the methoxide-phenol complex calculated is 7.9 kcal/mol.

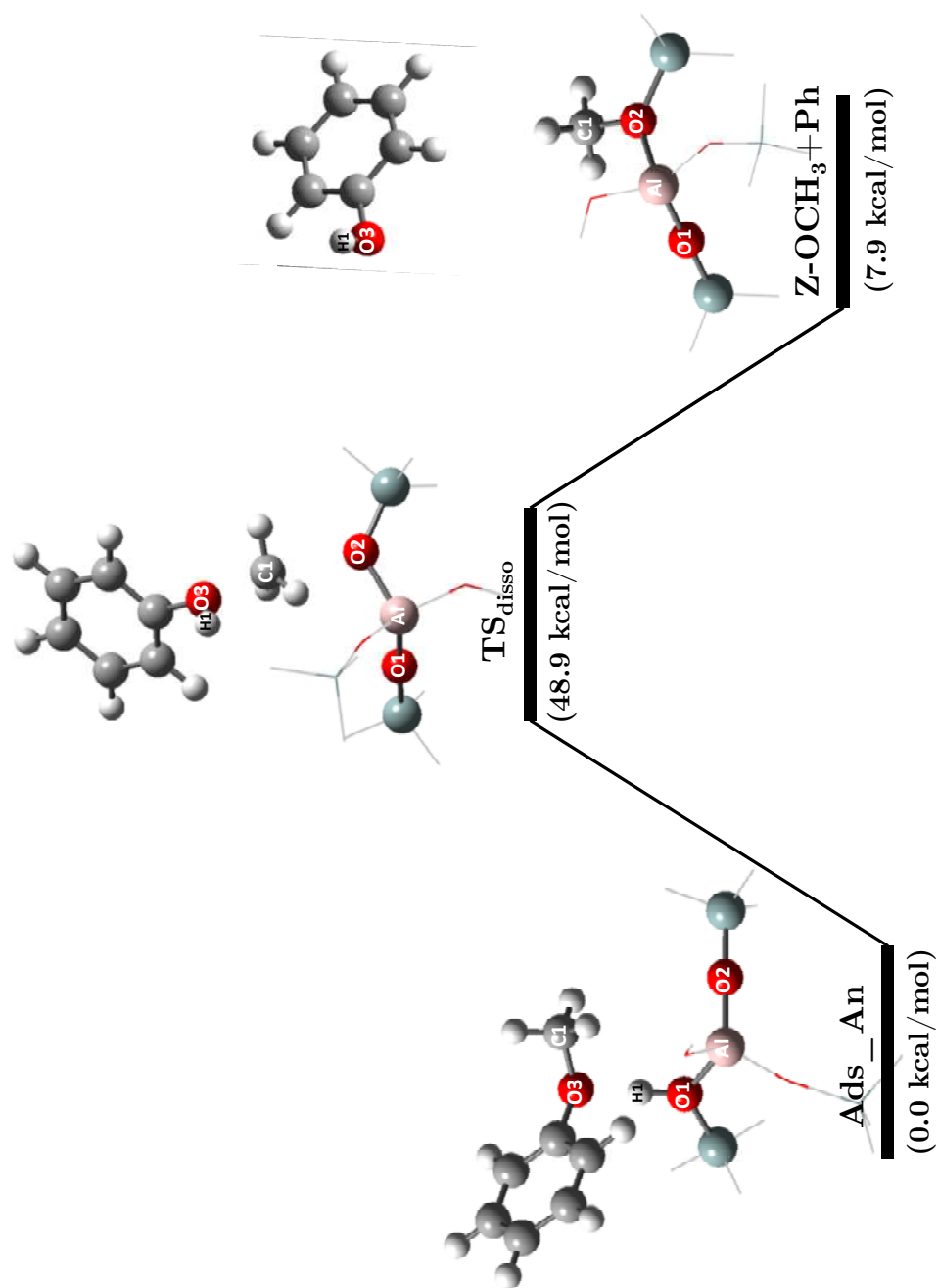


Figure 5.8 Potential energy diagram for the surface methoxide formation step of the dissociative mechanism for anisole protonation. B3LYP/6-31G(d)+ZPE energies.

Table 5.4 Optimized geometrical parameters of adsorption complexes for anisole protonation step to form surface methoxide of dissociative pathway (distances in Å).

Parameter	Isolated		Anisole adsorption (Ads_An)	Transition state (TS _{disso})	Surface methoxide (Z-OCH ₃)
	Anisole	Zeolite			
Distances					
O1-H1	-	0.96	1.02	3.56	-
H1-O3	-	-	1.51	0.97	-
C1-O2	-	-	3.98	2.27	1.46
C1-O3	1.42	-	1.47	1.69	-

Subsequently, the surface methoxide species on the zeolite surface acts as a methylating agent for an unsaturated molecule e.g. ethylene, propylene, phenol, and anisole. Propylene is used as an example for demonstration in this study. The corresponding calculated energy profile is shown in Figure 5.9, and geometric parameters are listed in Table 5.5. Propylene adsorbed on the surface methoxide and formed coadsorption complex ($C_3=Z-OCH_3$) as an initial step. Next, the reaction proceeds via the transition state (TS_{methyl}) that involves the concerted bond breaking of the C1-O2 bond and the formation of the C1-C2 bond. The C1-O2 distance increases from 1.46 to 2.29 Å, while the length of the C1-C2 distance decrease to 2.03 Å. At the same time C=C double bond of propylene (C2-C3) is weakening and the bond distance is slightly increased by 0.02 Å. This step of propylene methylation shows the calculated activation energy 36.8 kcal/mol. The corresponding butoxide intermediate ($Z-OC_4$) was produced and covalently bond to the O1 oxygen bridging atom of the zeolite framework. The adsorption energy of the butoxide intermediate is -14.6 kcal/mol. Then butene product can be formed via deprotonation reaction as the final step. In addition to propylene as a methyl acceptor, a similar study reported the energy barrier for methylation of ethylene 21.4 kcal/mol.³⁵ The activation energies for methylation are lower thane that of the methoxide formation. Therefore, it can be assumed that the anisole protonation to form the surface methoxide species is the limiting step of dissociative reaction pathway.

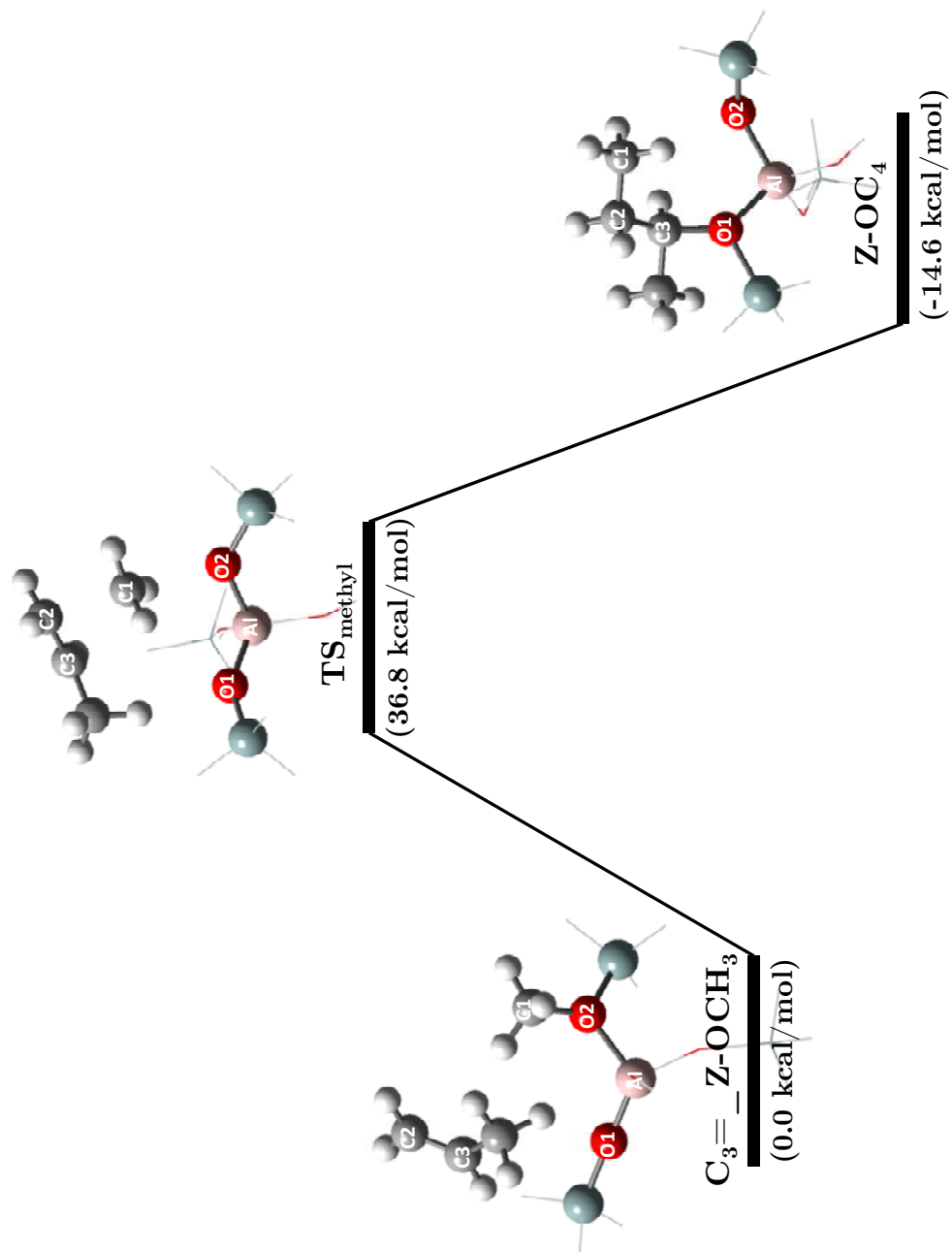


Figure 5.9 Potential energy diagram for the propylene methylation reaction step of the dissociative mechanism. B3LYP/6-31G(d)+ZPE energies.

Table 5.5 Optimized geometrical parameters of adsorption complexes for propylene methylation step of dissociative pathway (distances in Å).

Parameter	Isolated		Coadsorption complex (C ₃ =_Z-OCH ₃)	Transition state (TS _{methyl})	Butoxide (Z-OC ₄)
	Propylene	Methoxide			
Distances					
C1-O2	-	1.46	1.46	2.29	3.69
C1-C2	-	-	4.09	2.03	1.54
C1-C3	-	-	3.87	2.32	2.49
C2-C3	1.33	-	1.34	1.36	1.53
C3-O1	-	-	3.92	3.73	1.48

An alternative possible pathway is associative mechanism which has been assumed, where initially both reactants are loosely bound (physisorbed) to the cluster. Carbon-carbon bond formation then occurs in a single-step fashion and does not involve a methoxide intermediate. The energy profile for phenol methylation with anisole is shown in Figure 5.10, and selected geometrical parameters are listed in Table 5.6. This reaction is also initialized by adsorbed anisole and phenol over the Brønsted acid site (Ads_An+Ph). Then, phenol is methylated directly by anisole without the formation of the methoxide intermediate. Anisole is adsorbed on the acidic proton (H1) in the end-on formation via H-bonds. The neighboring phenol molecule is adsorbed weakly. The O1-H1 distance increases from 0.96 to 1.01 Å upon absorption, and the C1-O3 bond distance increases by approximately 0.03 Å. In the transition state (TS_{asso}) of this step, the adsorbed anisole is protonated at the O3 atom by the proton (H1) of zeolite. This methyl group undergoes an S_N2 type umbrella inversion and transferred to react with the C2 of the phenol molecule leading to the formation of the alkoxide species (Z-OR). The O1-H1 bond and C1-O3 distances are elongated to 1.60 and 4.46 Å, respectively, while the O3-H1 distance is shortened to 1.00 Å. The corresponding calculated energy barrier is 51.1 kcal/mol. Next, the alkoxide complex (Z-OR) is formed with a C3-O2 bond length of 1.51 Å and adsorption energy of 10.3 kcal/mol. A lower activation energy for alkoxide desorption is expected,^{35,36} thereby the direct methylation is considered as the limit step for associative reaction pathway which is slightly higher than the barrier for dissociative reaction pathway (48.9 kcal/mol).

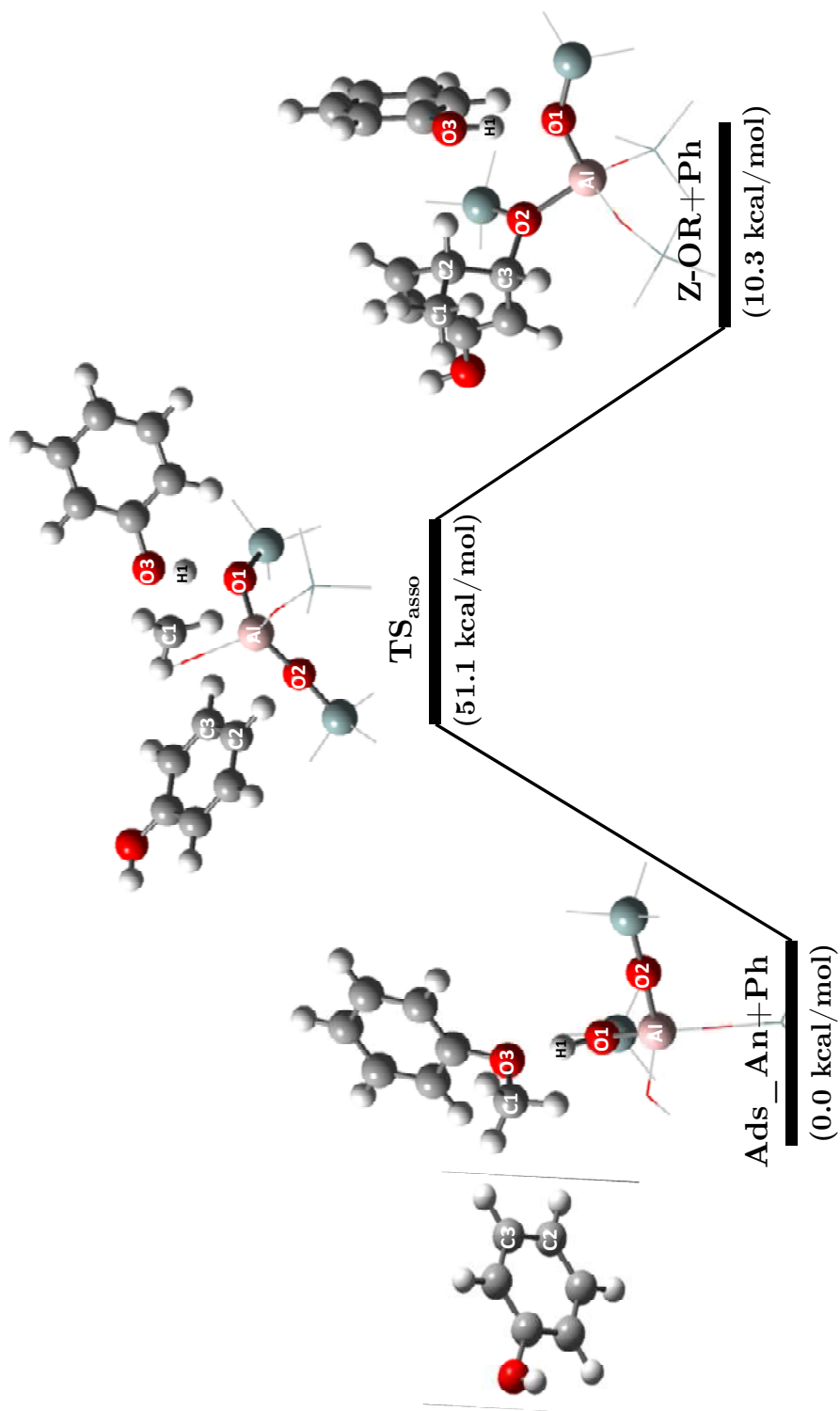


Figure 5.10 Potential energy diagram for the associative phenol methylation with anisole reaction pathway. B3LYP/6-31G(d)+ZPE energies.

Table 5.6 Optimized geometrical parameters of adsorption complexes for associative phenol methylation with anisole (distances in Å).

Parameter	Isolated		Coadsorption complex (Ads_An+Ph)	Transition state (TS _{asso})	Alkoxide complex (Z-OR+Ph)
	An / Ph	Zeolite			
Distances					
O1-H1	-	0.96	1.01	1.47	1.6
H1-O3	-	-	1.52	1.04	1.00
C1-O3	1.42	-	1.47	2.13	4.46
C1-C2	-	-	3.86	2.82	1.55
C1-C3	-	-	4.26	2.76	2.51
C2-C3	1.38	-	1.38	1.39	1.53
C3-O2	-	-	5.82	3.57	1.51

5.4. Conclusions

The conversion of anisole on HY zeolite produces phenol, cresols, xylenols and methylanisoles as main products during several transalkylation steps. Catalyst deactivation is significant under the reaction conditions and it is caused by strong adsorption of phenolic compounds and coke formation. The latter is an irreversible process, whereas the former is reversible and can be minimized by incorporation of molecules such as tetralin with high H-transfer capacity. Co-feeding tetralin or other H-donors has a beneficial effect on anisole conversion and reduces coke formation. Other hydrocarbons with a weaker H-transfer capacity have lower (e.g., *n*-decane), negligible (e.g., benzene) or even detrimental effect on activity (e.g., propylene).

References

- 1 D. L. Klass, in Biomass for Renewable Energy, Fuels, and Chemicals, Academic Press, S. Diego, **1998**.
- 2 B.J.M. de Vries, D.P. van Vuuren, M.M. Hoogwijk *Energy Policy*. **2007**,35,2590.
- 3 F. McGowan *Energy Policy*. **1991**,19,111.
- 4 J.T. Houghton, Y. Ding, D.J. Griggs, M. Noguer, P.J. van der Linden, X. Dai *Climate change 2001*, Cambridge University Press, Cambridge, **2001**.
- 5 E. Antonakou, A. Lappas, M.H. Nilsen, A. Bouzga, M. Stocker *Fuel*. **2006**,85,2202.
- 6 A. Oasmaa, S. Czernik *Energy Fuels*. **1999**,13,914.
- 7 A.V. Bridgwater *Chem Eng J*. **2003**,91,87.
- 8 S. Czernik, A.V. Bridgwater *Energy Fuels*. **2004**,18,590.
- 9 G.W. Huber, S. Iborra, A. Corma *Chem Rev*. **2009**,106,4044.
- 10 S. Czernik, R. Maggi, G.V.C. Peacocke In: A.V. Bridgwater, Editor, Review of Methods for Upgrading Biomass-Derived Fast Pyrolysis Oils, in Fast Pyrolysis of Biomass: A Handbook, vol. 2, CPL Press, Newbury, UK, **2002**. (Chapter 8)
- 11 V. Bui, G. Toussaint, D. Laurenti, C. Mirodatos, C. Geantet *Catal Today*. **2009**,143,172.
- 12 I. Graca, F. Ramoa Ribeiro, H.S. Cerqueira, Y.L. Lam, M.B.B. de Almeida *Appl Catal B*. **2009**,90,556.
- 13 I. Graca, J.-D. Comparot, S. Laforge, P. Magnoux, J.M. Lopes, M.F. Ribeiro, F. Ramoa Ribeiro *Energy & Fuels*. **2009**,23,4224.
- 14 I. Graca, J.-D. Comparot, S. Laforge, P. Magnoux, J.M. Lopes, M.F. Ribeiro, F. Ramoa Ribeiro *Appl Cat A*. **2009**,353,123.

-
- 15 A.G. Gayubo, A.T. Aguayo, A. Atutxa, R. Aguado, M. Olazar, J. Bilbao *Ind Eng Chem Res.* **2004**,43,2619.
- 16 A.G. Gayubo, A.T. Aguayo, A. Atutxa, R. Aguado, J. Bilbao *Ind Eng Chem Res.* 2004,43,2610.
- 17 J.D. Adjaye, N.N. Bakhshi *Fuel Process Technol.* **1995**,45,161.
- 18 J.D. Adjaye, N.N. Bakhshi *Biomass Bioenergy.* **1995**,8,131.
- 19 A. Corma *J Catal.* **2003**,216,298.
- 20 B. Arstad, S. Kolboe, O. Swang *J Phys Chem B.* **2002**,106,12722.
- 21 M. J. Frisch, et al. Gaussian, Inc., Wallingford CT, **2004**.
- 22 S. Svelle, B. Arstad, S. Kolboe, O. Swang *J Phys Chem B.* **2003**,107,9281.
- 23 S. Svelle, S. Kolboe, O. Swang *J Phys Chem B.* **2003**,108,2953.
- 24 B. Arstad, S. Kolboe, O. Swang *J Phys Chem B.* **2004**,108,2300.
- 25 X. Zhu, R.G. Mallinson, D.E. Resasco *Appl Catal A.* **2010**,379,172.
- 26 P.D. Chantal, S. Kaliaguine, J.L. Grandmaison *Appl Catal.* **1985**,18,133.
- 27 P.A. Horne, P.T. Williams *Renew Energy.* **1996**,7,131.
- 28 T. Prasomsri, R.E. Galiasso Tailleur, W.E. Alvarez, T. Sooknoi, D.E. Resasco *Appl Catal A.* **2010**,389,140.
- 29 B.E. Langner *Ind Eng Chem Proc DD.* **1981**,20,326.
- 30 G.F. Froment, J. De Meyer, E.G. Derouane *J Catal.* **1990**,124,391.
- 31 K.A. Cumming, B.W. Wojciechowski *Catal Rev– Sci & Eng.* **1996**,38,101.
- 32 R.T. Yang, *Adsorbents – Fundamentals and applications*, John Wiley & Sons Inc. **2003**,168.
- 33 J. Karger, M. Petzold, H. Pfeifer, S. Ernst, J. Weitkamp *J Catal.* **1992**,136,283.

-
- 34 R. Rungsisirakun, T. Nanok, M. Probst, J. Limtrakul *J Mol Graph & Mod.* **2006**,24,373.
- 35 T. Maihom, B. Boekfa, J. Sirijaraensre, T. Nanok, M. Probst, J. Limtrakul *J Phys Chem C.* **2009**,113,6654.
- 36 S. Svelle, S. Kolboe, O. Swang, U. Olsbye *J Phys Chem B.* **2005**,109,12874.

CHAPTER 6

6. Anchoring Pd Nanoclusters onto Pristine and Functionalized Carbon Nanotubes

6.1 Introduction

Carbon nanotubes are being widely used as a support material for supporting metallic nanoparticles for applications in heterogeneous catalysis,¹ fuel cells^{2,3} and sensors.^{4,6} Both multi- and single-wall carbon nanotubes (MWCNT and SWCNT) have been found to be effective in stabilizing small metal clusters. Recently, we have developed a novel carbon nanotube–transition metal oxide hybrid (i.e. SWCNT/silica) that simultaneously stabilizes water/oil emulsions and catalyzes reactions at the interface.⁷ This nanohybrid behaves as a solid surfactant (half hydrophilic/half hydrophobic) and can selectively catalyze reactions at each side of the interface in biphasic liquid system such as bio-oils. The two-faced catalytic nanohybrid, so called ‘Janus catalyst’⁸ can be synthesized in such a way that a catalytic function is placed on the hydrophobic side and a different catalytic function on the hydrophilic side. For example, base-catalyzed condensation reactions can occur in the aqueous phase

and metal-catalyzed hydrogenation on the organic phase. This combination is particularly relevant in the upgrading of bio-oils to biofuels.

It is therefore desirable to tailor the metal-anchoring ability of carbon nanotubes to maximize the dispersion and stability of nanoclusters on the surface of SWCNT by tuning the interaction between the metal clusters and the hydrophobic carbon support. It has been proposed that defect sites or functional groups on carbon nanotubes result in stronger metal-support interactions and consequently higher metal dispersion.⁹ For instance, surface chemical modifications of MWCNTs by wet-chemical synthesis methods have been found to be the crucial in depositing Pt particles on MWCNTs.¹⁰ Likewise, oxygen functionalized sites can be created by acid^{11,12} and plasma^{9,13} treatments. In this contribution, we combine density functional theory (DFT) calculations and experimental preparations to compare the extent of Pd-nanotube interaction on pristine and oxidized SWCNT and MWCNT.

6.2 Methods

6.2.1 Experimental

The SWCNT used in the experimental preparations were synthesized by the CoMoCAT technique,¹⁴ and used in the purified form (pristine) or oxygen-

functionalized.¹⁵ The functional groups were introduced by treating the SWCNT with HNO₃ 3 M in reflux for 3 h. Following this treatment, the nanotubes were filtered through a vacuum filtration system and washed with an extensive amount of distilled water. The SWCNT collected on the filter paper were finally dried in a vacuum oven overnight at 80 °C.

For the deposition of Pd nanoclusters, the pristine and functionalized SWCNT were dispersed on two separate dishes, which were then placed together inside a sputtering coater chamber (Hummer VI Triode Sputter Coater). The samples were coated by sputtering at a current of 5 mA for 1 min.

The pristine and functionalized SWCNT were characterized by Raman spectroscopy, by using a Jobin Yvon LabRam 600 single-grating spectrometer with a CCD detector instrument and excitation laser wavelength of 633 nm. For transmission electron microscopy (TEM) characterization, the samples were dispersed in isopropanol and sonicated by a horn sonicator (Cole-Parmer), operating at an amplitude of 25% for 10 min before deposition onto the TEM grids. Images were obtained on a JEOL 2000 system operating at an accelerating voltage of 200 kV.

6.2.2 Models and computation

A hybrid quantum mechanics/molecular mechanics (QM/MM) method was used to calculate the optimized structures and energies of the Pd nanoclusters on the pristine and functionalized single-wall carbon nanotubes (SWCNT). This technique has been extensively applied in previous SWCNT studies.¹⁶⁻²⁰ Two different structures, based on a 265-atom armchair (7, 7) SWCNT, were investigated. In both cases, each C-dangling bond at the edges was terminated with an O atom. In the structure containing a wall defect, the dangling bonds in the defect were also terminated with an O atom, as depicted in Figure 6.1.

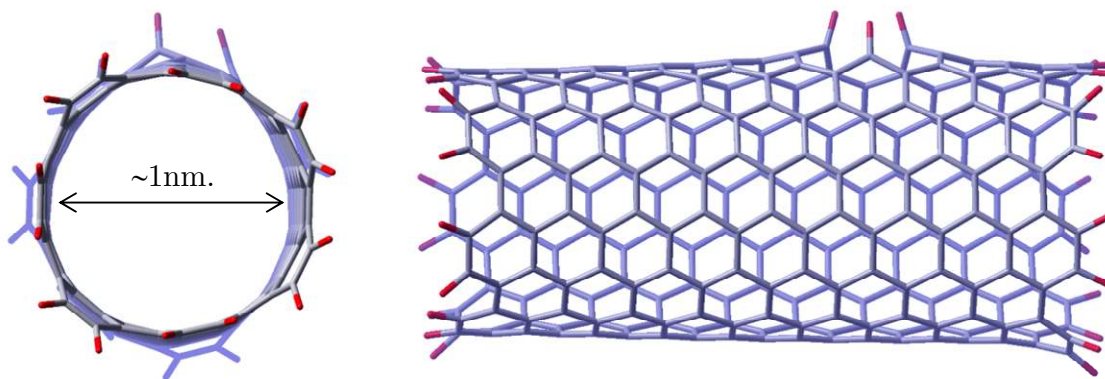


Figure 6.1 Front and side view of the optimized armchair (7, 7) SWCNT with a functionalized site represented by a $C_{265}O_{31}$ model tube.

The Pd/SWCNT structures were described at two levels of detail. The Pd₄ cluster and the nanotube sites of interest (C_{13} for a perfect site; and

C₁₂O₃ for a functionalized site) were treated at a higher level. The exchange–correlation hybrid functional B3LYP (Becke, three-parameter, Lee–Yang–Parr)^{21–23} with the LANL2DZ (Los Alamos effective core potential)^{24,25} was employed to describe the Pd₄ cluster. The 3-21+G(d) basis set^{22,23,26} was applied in the case of SWCNT sites. The remaining part of the SWCNT was defined as the lower layer and treated by the universal force field (UFF).^{27,28} The position of atoms in this layer was kept frozen, while the Pd₄ clusters were left free to move to the energetically most favored position.²⁹ All calculations for the SWCNT model were performed by using the GAUSSIAN-03 program suit.³⁰

In addition, the adsorption of Pd nanoclusters on MWCNTs was also investigated in this work. Three layers of graphene sheets were used as a representative for MWCNT surface as shown in Figure 6.2. The interlayer distance and a typical C–C bond length are ~3.4 Å and 1.41 Å, respectively.³¹ Each C-dangling bond at the edges of the steps sites was terminated with –COOH functional group. Adsorption energies of Pd Nanoclusters on terrace sites and step sites were examined to elucidate a role of defects containing the functional group. The spin-polarized periodic DFT calculations were performed using the Vienna ab initio simulation package (VASP)^{32–36}, in which the Kohn-Sham equations are solved by self-consistent algorithms. The dimensions of the unit cells are: $a = 9.769 \text{ \AA}$, $b = 29.160 \text{ \AA}$, $c = 30.00 \text{ \AA}$, and $\alpha = \beta = \gamma = 90^\circ$. A cutoff energy of 300 eV was used. Brillouin zone sampling was restricted to the Γ -point. Pd nanoclusters were freely optimized and a quasi-Newton forces-

minimization algorithm was employed for the forces-minimization algorithm. Convergence was assumed to be achieved when forces were below 0.05 eV/Å.

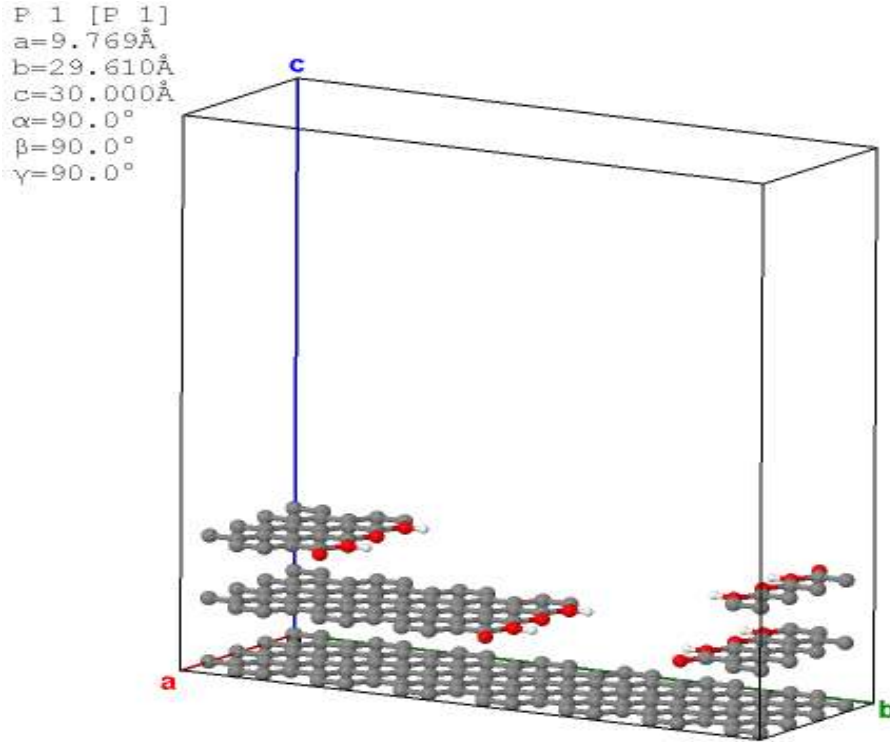


Figure 6.2 The representative model for MWCNT, consisting of three layers of graphene sheets with an interlayer distance of ~ 3.4 Å.

The binding energies between the Pd₄ cluster and CNT (i.e., SWCNT and MWCNT) were computed using the expression:

$$E_b = E_T(\text{Pd/CNT}) - E_T(\text{Pd}) - E_T(\text{CNT}) \quad (1)$$

where E_T (Pd) and E_T (CNT) are total energies of a free standing Pd cluster and a bare CNT, respectively; and E_T (Pd/CNT) is the total energy for the optimized configuration with Pd cluster adsorbed on the nanotube.

6.3 Results and discussion

6.3.1 Deposition of Pd on pristine and functionalized SWCNT

Oxidization by nitric acid has proven to be a convenient way for grafting oxygenated functional groups, without causing a significant structural damage to the nanotubes.^{15,37,38} As seen in the Raman spectra (Figure 6.3), the sample treated in nitric acid showed a D band at $\sim 1300\text{ cm}^{-1}$, which is somewhat broader and more intense than that of the pristine sample, which indicates an increase in the amount of functionalized sites on SWCNT,³⁹ but not large enough to compromise the nature of the nanotubes. In addition, it is observed that the Raman peaks of the functionalized SWCNT have been up-shifted in comparison to the pristine sample. These shifts have been previously attributed to lattice strains incorporated in the nanotube by the presence of the functional groups.³⁹

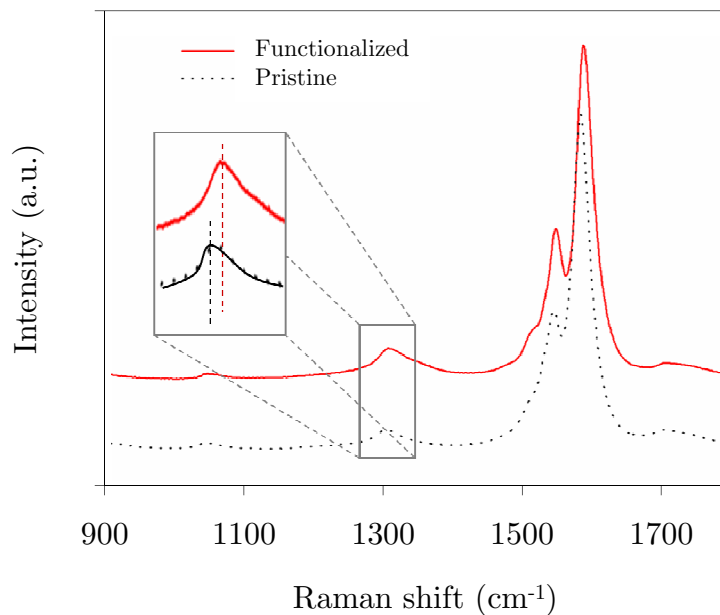


Figure 6.3 Raman spectra of pristine (*dashed line*) and functionalized (*solid line*) SWCNTs. Spectra are normalized with respect to the G-band and shifted vertically for clarity.

The extent of deposition of Pd on the pristine and functionalized nanotubes was measured by treating the two types of substrates under identical Pd vapor exposure conditions (identical sputtering time, position, and current). If different metal distributions are observed, they can only be due to different degrees of Pd–SWCNT interactions. An effective anchoring of Pd atoms from the vapor phase onto the surface would result in a higher concentration of clusters on the surface. By contrast, a weak interaction would not generate nucleation sites for condensation and the deposition would not occur in a selective manner. Indeed, a dramatic difference was observed in the degree of Pd deposition on the two nanotube samples. The effect of the functional groups

is evident in the TEM images of Figure 6.4, with the functionalized SWCNT (Figure 6.4a) and the pristine SWCNT (Figure 6.4b), which can be compared to the corresponding nanotubes before addition of Pd (Figures 6.4c and 6.4d, respectively).

The strength of the Pd–SWCNT interaction can also be illustrated by the resistance to the mechanical sonication that both samples are subject before the TEM measurement. Since both samples were sonicated at the same power and for the same amount of time, only those clusters that are effectively attached to the surface remain, while clusters only loosely deposited are ‘shaken off’ during sonication and left in the solvent.

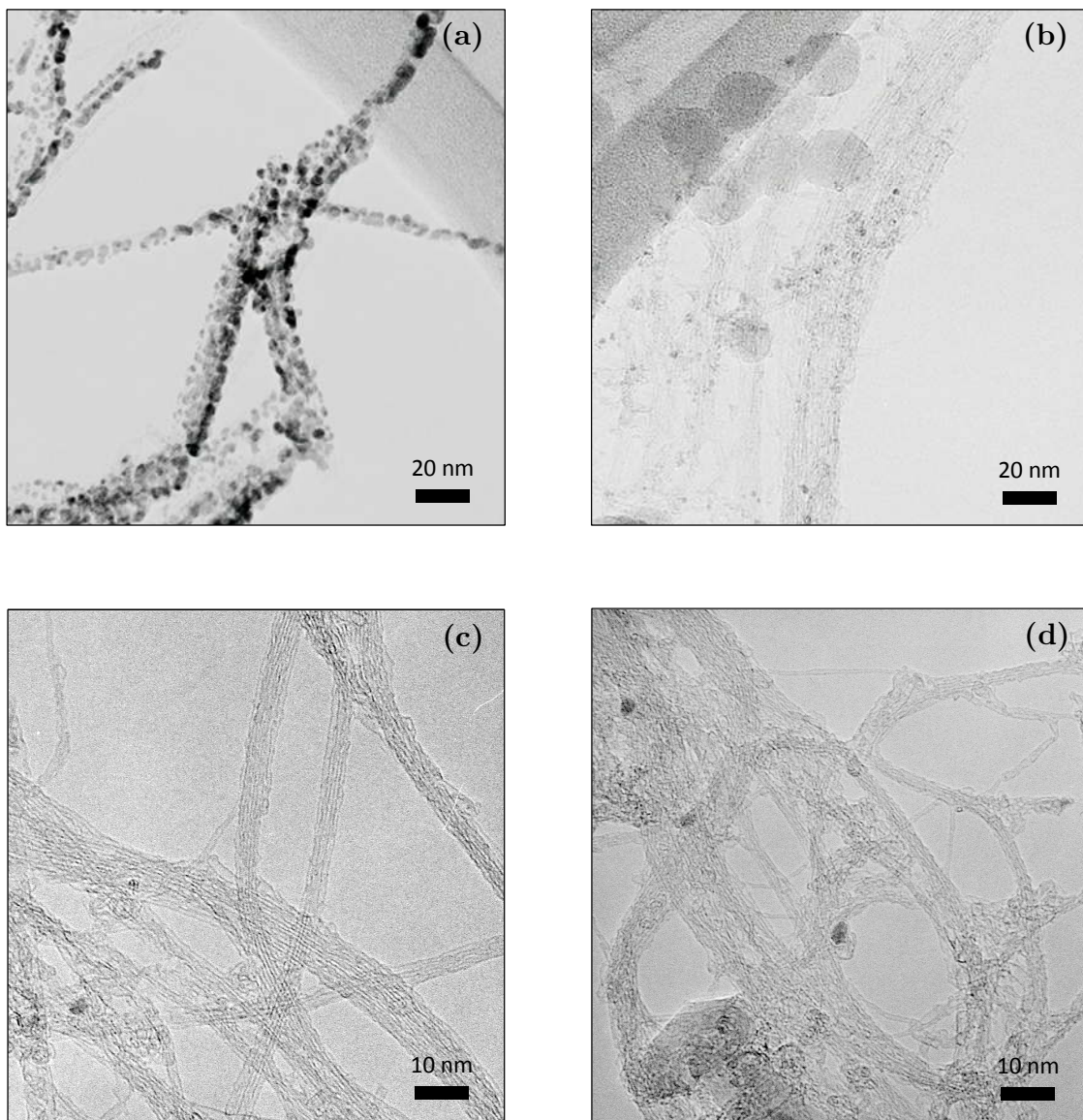


Figure 6.4 TEM images of (a) Pd nanoclusters dispersed on functionalized; and (b) pristine SWCNTs. The corresponding SWCNTs before Pd deposition are shown as reference in (c) and (d), respectively.

6.3.2 DFT calculation for Pd nanocluster adsorption on the pristine and functionalized SWCNT and MWCNT

To simulate the adsorption of a metallic Pd cluster on a SWCNT, a Pd₄ model with envelope-like C_{2v} symmetry was chosen as the representative cluster in this study, as shown in Figure 6.5. First, the isolated Pd₄ cluster was energetically optimized at triplet spin multiplicity, since the most stable cluster is obtained for the d8 electronic configuration of the metal valence electrons.^{18,40,41} Then, the combined Pd₄/SWCNT systems were calculated, but unlike the calculation of the isolated Pd₄ cluster, the Pd₄/SWCNT systems were optimized at the lowest possible multiplicity.^{17,18} The SWCNT with the functionalized site that acted as the anchoring place for adsorption was optimized from an initial structure, which had a typical C–C bond length ~1.41 Å and a nanotube diameter of 1 nm (see Figure 6.1). In the optimized structure we observed a slight extension of the C–C bonds (i.e. 1.42–1.44 Å) around the functionalized site, due to the presence of O atoms.

The adsorption models of Pd₄ clusters on the pristine and functionalized SWCNT were investigated over the perfect and the oxidized defective sites, respectively. The corresponding optimized geometries are shown in Table 6.1. It is worth noting that the structure of the two resulting Pd₄ clusters is distorted due to the interaction with the support. More specifically, this distortion results from the hybridization of the d orbital of the Pd atoms with the s and p orbitals of the adjacent C atoms,^{41,42} as seen in Figure 6.6. The final Pd–C bond

distance is $\sim 1.94\text{--}2.11 \text{ \AA}$, which is slightly shorter than that reported for a larger cluster (Pd_9) deposited on a nanotube.¹⁸

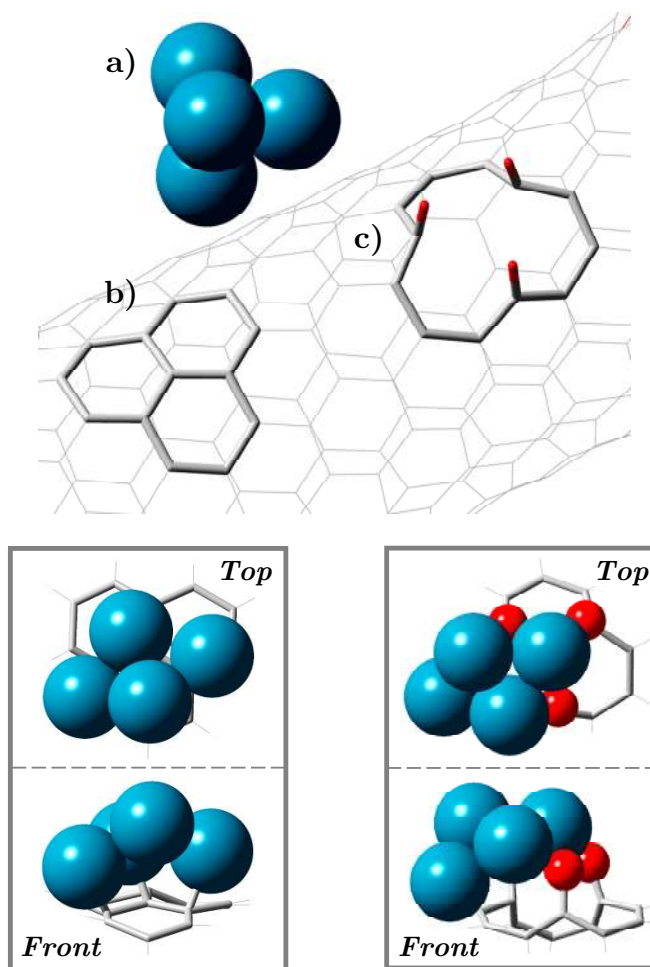
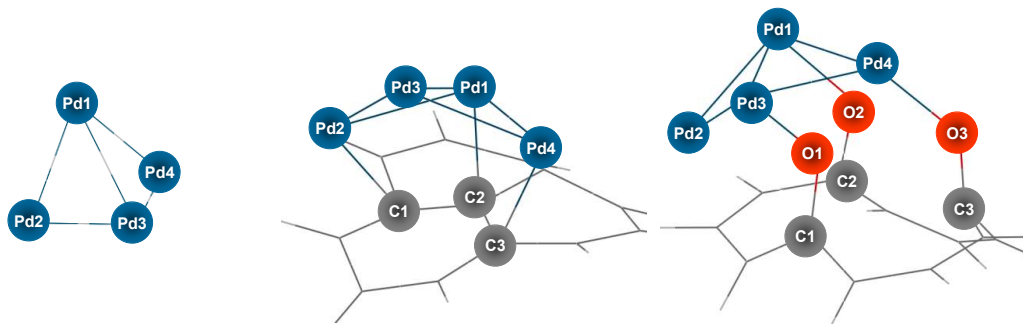


Figure 6.5 The structure models for (a) a Pd_4 cluster alone; (b) a perfect site (C_{13}); and (c) a functionalized site (C_{12}O_3) on the SWCNT. The corresponding adsorptions of Pd_4 on their sites are shown in boxes.

Table 6.1 Pd–Pd, Pd–C and C–O bond lengths of a C_{2v} Pd₄ cluster alone, and the adsorptions of Pd₄ clusters on SWCNTs.



Isolated Pd ₄		Pd ₄ /SWCNT _{perfect}		Pd ₄ /SWCNT _{func.}	
Bond	Length (Å)	Bond	Length (Å)	Bond	Length (Å)
Pd1 - Pd2	2.58	Pd1 - Pd2	2.80	Pd1 - Pd2	2.73
Pd1 - Pd3	2.84	Pd1 - Pd3	2.65	Pd1 - Pd3	2.70
Pd1 - Pd4	2.58	Pd1 - Pd4	2.80	Pd1 - Pd4	2.63
Pd2 - Pd3	2.58	Pd2 - Pd3	2.86	Pd2 - Pd3	2.71
Pd3 - Pd4	2.58	Pd3 - Pd4	2.90	Pd3 - Pd4	2.80
		Pd2 - C1	2.10	Pd3 - O1	1.95
		Pd1 - C2	2.11	Pd1 - O2	2.12
		Pd4 - C3	1.94	Pd4 - O3	2.06
				C1 - O1	1.42
				C2 - O2	1.42
				C3 - O3	1.37

The results on the functionalized SWCNT show some interesting differences. Unlike the pure covalent bonding obtained for the Pd₄/SWCNT_{pristine} system, deposition of Pd on the functionalized site (Pd₄/SWCNT_{func.}) involves a stronger type of interaction. The calculated Pd–O bond length is in the range 1.95–2.12 Å, which agree well with the results from X-ray diffraction (XRD) and extended X-ray absorption fine structure

(EXAFS) measurements.^{43,44} Formation of oxidized Pd species has been suggested from an X-ray photoelectron spectroscopy (XPS) study of Pd nanoparticles supported on oxygen plasma-treated MWCNT.⁹

The calculated energies for the adsorption of Pd₄ on the pristine and functionalized sites are also remarkably different and in line with the type of interactions just described. The binding energy of 2.56 eV for Pd adsorption on the pristine site is similar to that previously calculated.²⁸ However, the adsorption on the functionalized site increases by more than 70%, to 4.62 eV. This remarkable enhancement in adsorption energy can be ascribed to the modification of the electronic structures of the resulting cluster.

For instance, the energy difference between the highest occupied molecular orbital (HOMO) and the lowest unoccupied molecular orbital (LUMO) can be taken as a good indicator of changes in electronic properties and chemical reactivity.⁴⁵ We have calculated the HOMO–LUMO energy gap for the pristine and functionalized sites before the adsorption of Pd. A significant difference was observed between the two cases. The energy gap for the pristine structure is 1.14 eV, which is consistent with previous results.^{46,47} It is well known that the energy gap depends on diameter, chirality and even length of the nanotubes.⁴⁸⁻⁵¹ For instance, no HOMO–LUMO gaps can be expected from metallic nanotubes of infinite-length. However, in this case, we have only compared the changes in energy gaps caused by the presence of the oxygen atoms in the defect, keeping the other structural parameters constant.

These calculations indicate that the presence of oxygen atoms at the functionalized site reduce the HOMO–LUMO gap to 0.82 eV.

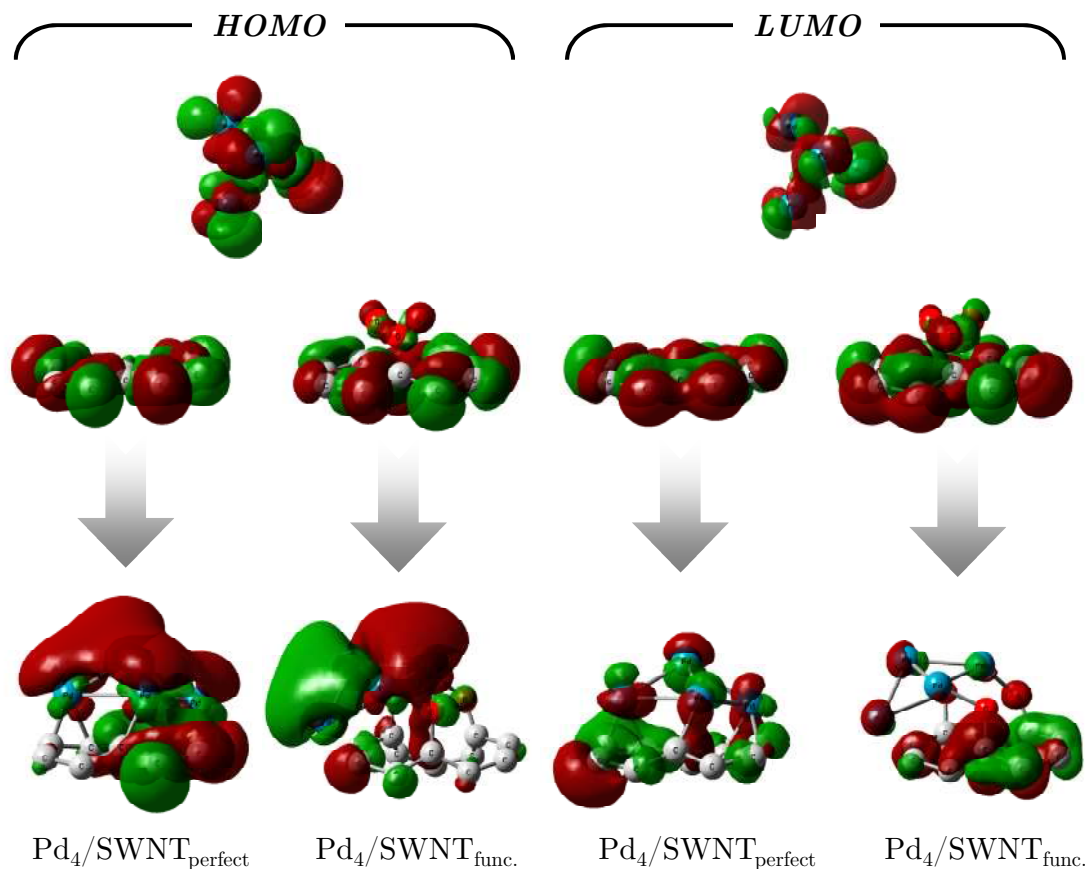


Figure 6.6 Frontier molecular orbitals of the Pd4 adsorptions on different sites of SWCNTs: HOMOs (left) and LUMOs (right).

This reduction can be explained by the higher density of states near the Fermi level, arising from the overlap of the 2p electrons of the O atoms and the π electron system of the nanotube. This phenomenon does not happen in the case of a pristine carbon nanotube, which does not contain functional

groups.^{52,53} A smaller HOMO–LUMO gap should result in an easier excitation of electrons from the low-lying occupied levels to the upper empty level, which in turn enhances the chemical reactivity towards an adsorbate. That is, the functionalized site with the HOMO–LUMO gap modified by oxygen atom (i.e. a smaller gap) may be responsible for a stronger Pd₄/SWCNT_{func.} interaction.

Moreover, the HOMO–LUMO gaps of both types of sites decreased upon the adsorption of the Pd cluster (i.e. it was reduced to 0.92 and 0.54 eV for Pd₄/SWCNT_{pristine} and Pd₄/SWCNT_{func.}, respectively). A similar extent of partial charge transfer, about 0.57–0.60 eV, was observed in both cases, which can be ascribed to the electronic reorganization caused by the interaction of the SWCNT and a high work function metal such as Pd.^{54, 55} That is, the presence of the 4d electrons of Pd in the antibonding orbitals of the nanotube leads to an enhancement of the electron density in the nanotube, and, consequently, a smaller energy gap.⁵⁶

Furthermore, the similar calculation was performed to understand the ability of wall defects in stabilizing Pd nanoclusters on the MWCNT model, as illustrated in Figure 6.7. The periodic slab model representing a 3-layer graphene was used as a platform for the adsorption of Pd nanoclusters. Based on the calculation, the binding energy on the step sites is 1.36 eV higher than that on the terrace sites of MWCNTs. This demonstrates the preferential adsorption of Pd nanoclusters on oxidized defects of MWCNTs, which is consistent with the previous study on SWCNTs and the experimental results of this study.⁵⁷

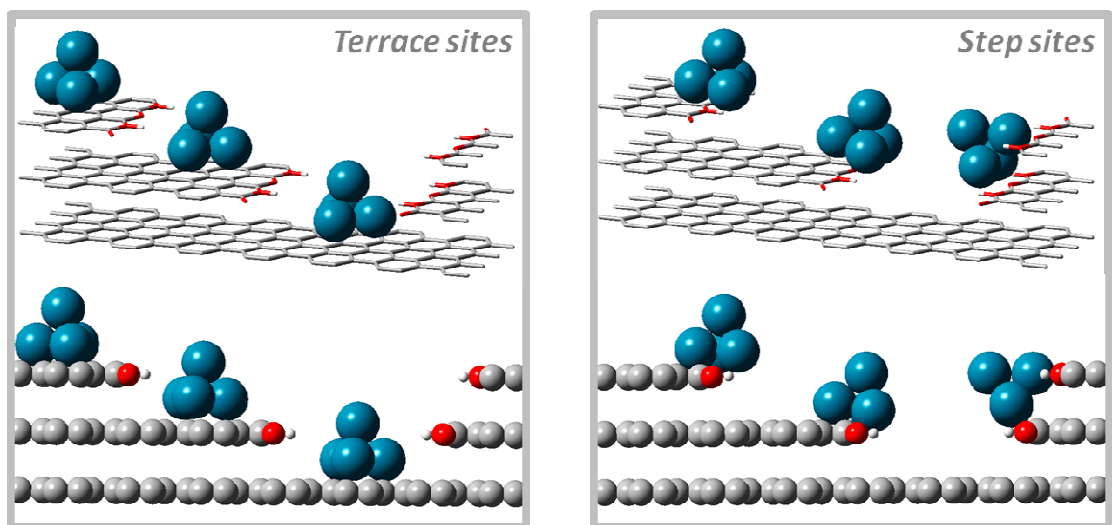


Figure 6.7 The models for Pd clusters adsorption on terrace sites (left); and steps sites (right) of MWCNT.

6.4. Conclusions

The combination of experimental measurements and DFT calculations of binding energies suggests that the Pd nanoclusters are much more effectively anchored on functionalized than on the pristine carbon nanotubes (both SWCNT and MWCNT). The modification of the electronic structure caused by the presence of oxygen atoms is responsible for the enhanced adsorption energy, leads to the formation of Pd–O bonds on the functionalized carbon nanotubes.

References

-
- 1 P. Serp, M. Corrias, P. Kalck *Appl Catal A-Gen.* **2003**,253,337.
 - 2 J.S. Ye, H.F. Cui, Y. Wen, W.D. Zhang, G.Q. Xu, F.S. Sheu *Microchim Acta.* **2006**,152,267.
 - 3 G.P. Jin, Y.F. Ding, P.P. Zheng *J Power Sources.* **2007**,166,80.
 - 4 Z. Siwy, L. Trofin, P. Kohli, L.A. Baker, C. Trautmann, C.R. Martin, *J Am Chem Soc.* **2005**,127,5000.
 - 5 J. Kong, M. Chapline, H. Dai *Adv Mater.* **2001**,13,1384.
 - 6 S. Yu, U. Welp, L.Z. Hua, A. Rydh, W.K. Kwok, H. Hau Wang *Chem Mater.* **2005**,17,3445.
 - 7 S. Crossley, J. Faria, M. Shen, D.E. Resasco *Science.* **2010**,327,68.
 - 8 D.J. Cole-Hamilton *Science.* **2010**,324,41.
 - 9 A. Felten, et al. *Micron.* **2009**,40,74.
 - 10 W. Li, C. Liang, W. Zhou, J. Qiu, Z. Zhou, G. Sun, Q. Xin, *J Phys Chem B.* **2003**,107,6292.
 - 11 J.P. Singh, X.G. Zhang, Hu-lin Li, A. Singh, R.N. Singh, *Int J Electrochem Sci.* **2008**,3,416.
 - 12 B.C. Satishkumary, E.M. Voglz, A. Govindarajx, C.N.R. Raoyzx, *J Phys D: Appl Phys.* **2009**,29,3173.
 - 13 C. Bittencourt et al. *Surf Sci.* **2007**,601,2800.
 - 14 D.E. Resasco, W.E. Alvarez, F. Pompeo, L. Balzano, J.E. Herrera, B. Kitiyanan, A. Borgna *J Nanoparticle Res.* **2002**,4,131.
 - 15 M.N. Tchoul, W.T. Ford, G. Lolli, D.E. Resasco, S. Arepalli, *Chem Mater.* **2007**,19,5765.
 - 16 V. D'Anna, D. Duca, F. Ferrante, G. La Manna *Phys Chem Chem Phys.* **2009**,11,4077.

-
- 17 V. D'Anna, D. Duca, F. Ferrante, G. La Manna *Phys Chem Chem Phys.* **2010**,12,1323.
- 18 D. Duca, F. Ferrante, G. La Manna *J Phys Chem C.* **2007**,111,5402.
- 19 S. Dapprich, I. Komáromi, K.S. Byun, K. Morokuma, M.J. Frisch *J Mol Struct Theochem.* **1999**,461-462, 1.
- 20 M. Svensson, S. Humbel, R.D.J. Froese, T. Matsubara, S. Sieber, K. Morokuma *J Phys Chem.* **1996**,100,19357.
- 21 A.D. Becke *J Chem Phys.* **1993**,98,1372.
- 22 P.J. Stephens, J.F. Devlin, C.F. Chabalowsky, M.J. Frisch *J Phys Chem.* **1994**,98,11623.
- 23 C. Lee, W. Yang, R.G. Parr *Phys Rev B.* **1988**,37,785.
- 24 P.J. Hay, W.R. Wadt *J Chem Phys.* **1985**,82,270.
- 25 P.J. Hay, W.R. Wadt *J Chem Phys.* **1985**,82,299.
- 26 A.D.J. Becke *Chem Phys.* **1993**,98,5648.
- 27 A.K. Rappè, C.J. Casewit, K.S. Colwell, W.A. Goddard, W.M. Skiff *J Am Chem Soc.* **1992**,114,10024.
- 28 A.K. Rappè, K.S. Colwell, C.J. Casewit *Inorg Chem.* **1993**,32,3428.
- 29 N. Armata, et al. *Top Catal.* **2009**,52,444.
- 30 M. J. Frisch, et al. Gaussian, Inc., Wallingford CT, **2004**.
- 31 L. Guan, K. Suenaga, S. Iijima *Nano Lett.* **2008**,8,459.
- 32 G. Kresse, J. Furthmueller *Phys Rev B.* **1996**,54,11169.
- 33 G. Kresse, J. Hafner *Phys Rev B.* **1994**,49,14251.
- 34 G. Kresse, J. Hafner *Phys Rev B.* **1993**,48,13115.
- 35 G. Kresse, J. Hafner *Phys Rev B.* **1993**,47,558.

-
- 36 G. Kresse, J. Furthmueller *Comp Mater Sci.* **1996**,6,15.
- 37 J. Chen, M.A. Hamon, H. Hu, Y. Chen, A.M. Rao, P.C. Eklund, R.C. Haddon *Science.* **1998**,282,95.
- 38 K.A. Worsley, I. Kalinina, E. Bekyarova, R.C. Haddon *J Am Chem Soc.* **2009**,131,18153.
- 39 U.J. Kim, C.A. Furtado, X. Liu, G. Chen, P.C. Eklund *J Am Chem Soc.* **2005**,127,15437.
- 40 C.D. Zeinalipour-Yazdi, A.L. Cooksy, A.M. Efstathiou *Surf Sci.* **2008**,602,1858.
- 41 A. Maiti, A. Ricca *Chem Phys Lett.* **2004**, 394,7.
- 42 D.H. Chi, et al. *Chem Phys Lett.* **2006**,432,213.
- 43 S.-J. Kim, S. Lemaux, G. Demazeau, J.-Y. Kim, J.-H. Choy *J Am Chem Soc.* **2001**,123,10413.
- 44 W.B. Li. et al. *Phys Scr.* **2005**,T115,749.
- 45 K. Fukui *Science.* **1982**,218,747.
- 46 M. Baldoni, A. Sgamellotti, F. Mercuri *Org Lett.* **2007**,9,4267.
- 47 F. Buonocore, F. Trani, D. Ninno, A. Di Matteo, G. Cantele, G. Iadonisi *Nanotechnology.* **2008**,19,025711.
- 48 B. Shan, K. Cho *Phys Rev Lett.* **2005**,94,236602.
- 49 C.W. Chen, M.H. Lee *Nanotechnology.* **2004**,15,480.
- 50 W.S. Su, T.C. Leung, B. Li, C.T. Chan *Appl Phys Lett.* **2007**,90,163103.
- 51 B.K. Agrawal, S. Agrawal, R. Srivastava *J Phys: Condens Matter.* **2003**,15,6931.
- 52 G. Zhang, W. Duan, G. Zhou, B. Gu *Solid State Commun.* **2002**,122,121.
- 53 H. Zheng, W. Duley *Phys Rev B.* **2008**,78,045421.

-
- 54 M. Penza, R. Rossi, M. Alvisi, G. Cassano, M.A. Signore, E. Serra, R. Giorgi *Sensor Actuat B-Chem.* **2008**,135,289.
- 55 P. Pannopard, P. Khongpracha, M. Probst, J. Limtrakul *J Mol Graph Model.* **2008**,28,62.
- 56 P. Tarakeshwar, D.M. Kim *J Phys Chem B.* **2005**,109,7601.
- 57 T. Prasomsri, D. Shi, D. E. Resasco *Chem Phys Lett.* **2010**,497,103.

CHAPTER 7

7. Comparative Study of Adsorption of Aldehydes on Pd(111) and PdCu(111) Surfaces

7.1 Introduction

As mentioned in Chapter 1, fast pyrolysis¹⁻⁶ shows an attractive method for lignocellulosic biomass conversion.⁷⁻¹¹ However, the bio-oil obtained has a relatively low heating value and typically contains a complex mixture of highly oxygenate compounds.¹² Moreover, the low chemical/thermal instability, corrosiveness, and high viscosity limit the storability and processability of these oils.¹³ Catalytic upgrading is, therefore, needed to stabilize bio-oils and make them fungible with conventional petroleum fuels.¹⁴ Among the different oxygenate compounds existing in bio-oils; aldehydes exhibit the high reactivity and are undesirable as fuel components.

Aldehyde hydrogenation to alcohols has been extensively studied over different metal catalysts.¹⁵⁻²³ For instances on Cu, hydrogenation of furfural to furfuryl alcohol is the predominating path, whereas decarbonylation appears only at high temperatures and with high metal loadings.^{24,25} In contrast to Pd, the higher activity for decarbonylation was observed.²⁶⁻³¹ The significant

difference between Cu and Pd is that, upon aldehyde adsorption, the former only leads to formation of -C=O-M (top, $\eta^1\text{-(O)}$) surface species, while the latter can stabilize both di-coordinated $\eta^2\text{-(C,O)}$ and acyl $\eta^1\text{-(C)}$ intermediates that lead to decarbonylation.

In this chapter, DFT calculations were performed. In particular, we compare here the adsorption of two different aldehydes, furfural and 2-methyl pentanal. This would help to understand how the molecule interacts with the surface, and mechanistic reaction paths. It is not only exhibit interesting differences in their chemical behavior, but represents that aldehydes are of importance in the upgrading of renewable fuels. Furfural (FAL) is produced both during pyrolysis of cellulose and in the dehydration of sugars.^{32,33} 2-Methylpentanal (MPAL) is formed upon aldol condensation and hydrogenation of propanal, which also can be obtained from glycerol, a biodiesel by-product.³⁴ It is important to state that the contribution of this chapter is mainly focused on the DFT calculation. Therefore, the supplemented experimental results reported were taken from Sitthisa *et al.*³⁵

7.2. Methodology

7.2.1 Experimental method³⁵

Pd/SiO₂ and Pd-Cu/SiO₂ catalysts were prepared by incipient wetness co-impregnation with aqueous solutions of the corresponding metal precursors (Pd(NO₃)₂ and Cu(NO₃)₂·H₂O, Sigma Aldrich). Precipitated silica (HiSil 210, PPG Co.) having a BET surface area of 124 m²/g was employed as support. A liquid/silica ratio of 1.26 ml/g was used to achieve incipient wetness for all samples. The loading of Pd metals were 5.0 and 0.5 wt.% for the conversion of 2-methylpentanal and furfural, respectively. After impregnation and drying in air at room temperature, the samples were further dried overnight at 110°C and calcined under 100 ml/min flow of air at 400°C for 4 h.

The reactions of the two aldehydes (FAL and MPAL) were carried out in a tubular flow reactor. The pelletized and sieved catalyst (size 250-425 µm) was placed at the center of a quartz tube reactor, between two layers of glass bead and quartz wool, installed vertically inside an electric furnace. Prior to the reaction, the catalyst was pre-reduced under flow of H₂ (60 ml/min, Airgas 99.99%) for 1 h at 250°C. The hydrogen partial pressure was controlled at the molar ratios H₂:FAL and H₂:MPAL at 25:1 and 12:1, respectively. After reduction, the catalyst was cooled down to the reaction temperature and the feed introduced continuously via a syringe pump (Cole Palmer). To keep all the

compounds in the vapor phase all lines before and after the reactor were kept heated at 220°C using heating tapes. The products were analyzed online on a gas chromatograph (Agilent model 6890) using HP-5 capillary column and FID detector.

7.2.2 Computational method

Density functional theory (DFT) calculations were performed to investigate optimized structures and the adsorption energies (E_{ads}) of molecular adsorption of 2-methyl pentanal (MPAL) and furfural (FAL) on Pd and Pd-Cu surfaces. Spin-polarized periodic DFT calculations were performed using the Vienna *ab initio* simulation package (VASP),³⁶⁻⁴⁰ in which the Kohn-Sham equations are solved by self-consistent algorithms. The valence electrons were described by plane wave basis sets with a cutoff energy of 300 eV and the core electrons were replaced by the projector augmented wave (PAW) pseudo-potentials^{41,42} for improving the computational efficiency. The Brillouin zone was sampled with a 3×3×1 Monkhorst-Pack k-point mesh. The exchange-correlation functional was described within the generalized gradient approximation (GGA) proposed by Perdew, Burke and Ernzerhof (PBE).⁴³ The Methfessel-Paxon method was employed to determine electron occupancies with a smearing width of 0.2 eV. As illustrated in Figure 7.1, both Pd(111) and PdCu(111) slab models were constructed based on a 4×4 unit cell with lattice

constants of 3.950 and 3.757 Å, respectively.⁴⁴ The slab model consists of three metal layers with a ~18 Å vacuum gap in the direction perpendicular to the surface. Surface adsorption of molecules was modeled taking place on the topmost layer of the slab. All the atoms of the adsorbates were allowed to relax to their optimized positions, while those of the metal slab were kept frozen in the originally optimized position. The model was relaxed until the forces were convergent to 0.03 eV/Å.

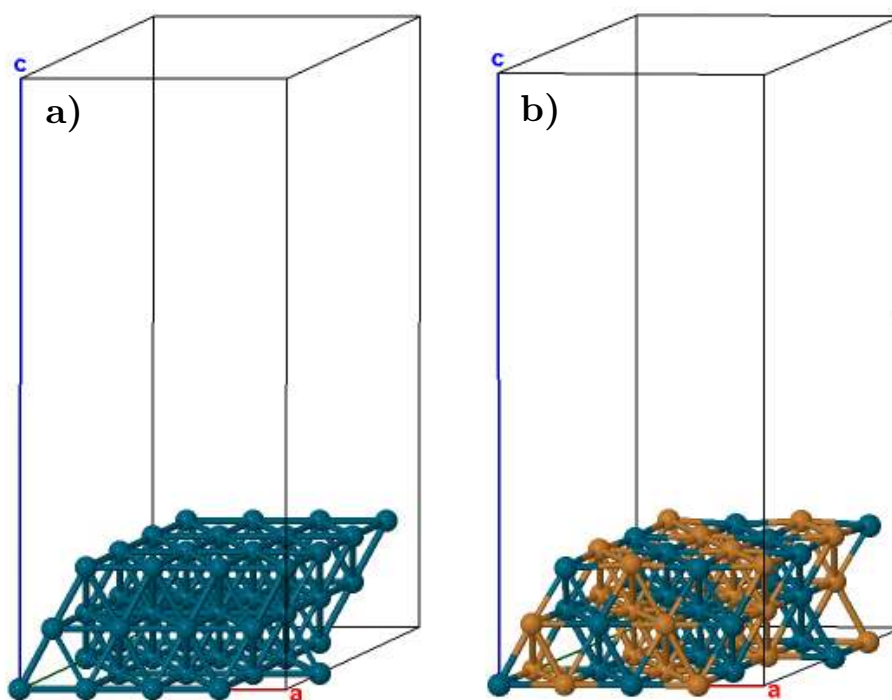


Figure 7.1 The periodic supercell representing a) Pd(111), and b) PdCu(111) surfaces.

In addition to the periodic slab model calculation, the cluster model was also theoretically investigated. Here, only MPAL was used, and the calculation was performed by the GAUSSIAN-03 program suit.⁴⁵ A monometallic Pd₁₀ cluster and a bimetallic Pd₄Cu₆ cluster were used as models. The exchange–correlation hybrid functional B3PW91 containing a combination of B3 exchange functional⁴⁶ and PW91 correlation functional^{47,48} with relativistic effective core potential basis set of double- ζ quality (LANL2DZ)⁴⁹ was used in this study. The isolated monometallic Pd₁₀ cluster was energetically optimized at triplet spin multiplicity since the most stable cluster is obtained for the d^8 electronic configuration of the metal valence electrons, whereas the most stable bimetallic Pd₄Cu₆ cluster has the lowest possible multiplicity in the ground state.⁵⁰ The simulated adsorption models were freely optimized to the energetically most favored position.

The adsorption energy, E_{ads} , was calculated from the equation,

$$E_{ads} = E_{slab/ads} - E_{slab} - E_{gas}$$

in which $E_{slab/ads}$ is the total energy of the slab with adsorbates, E_{slab} is the energy of the slab, and E_{gas} is the energy of each adsorbate in the gas phase.

7.3. Results and discussion

7.3.1 Periodic slab model

DFT calculations were performed to compare the adsorption energetic for MPAL and FAL on both Pd(111) and PdCu(111) slabs. Calculating the adsorption of such large molecules is complicated because the system exhibits numerous possibilities. We have selected the ones that we believe are most relevant for catalysis. To minimize the effect of adsorbate-adsorbate intermolecular interactions, we have chosen a low-coverage surface (1/16 ML) by setting a relatively large unit cell (4×4).

The optimized structures of MPAL in the gas phase and on the various surfaces are illustrated in Figure 7.2. The corresponding adsorption energies (E_{ads}) and bond lengths are summarized in Table 7.1. The calculations show that on Pd(111) the adsorption of the MPAL molecule occurs via the carbonyl group, interacting with the surface in a η^2 -(C,O) configuration, in which both C and O atoms of the carbonyl group are linked to the metal surface, while the aliphatic hydrocarbon part remains away from the surface. This theoretical result is consistent with the HEELS results obtained from Shekhar *et al.*,⁵¹ which have shown that the η^2 -(C,O) aldehyde is the dominant species observed on clean Pd surfaces, with some η^1 species only appearing at low temperatures. As summarized in Table 7.1, the adsorption energy for MPAL on Pd(111) is

27.0 kJ/mol. Also, it is worth noting that the C=O bond, d_1 , in the adsorbed state is 0.06 Å longer than that in the gas phase, which may be ascribed to the interaction of the carbonyl π^* bond with Pd(111) surface (i.e. electron back-donation). In contrast, the lengths for the other bonds d_2 , d_3 , d_4 , d_5 , and d_6 remain unchanged, indicating a low extent of interaction.

A similar calculation was conducted for furfural (FAL). The optimized structures of FAL in the gas phase and adsorbed on the different surfaces are illustrated in Figure 7.3. The corresponding adsorption energies (E_{ads}) and bond lengths are summarized in Table 7.2. On Pd(111), the presence of the aromatic ring in FAL plays a crucial role in promoting a flat adsorption on the surface. This results in a twofold increase in heat of adsorption of FAL (55.4 kJ/mol, Figure 7.2b) compared to MPAL (27.0 kJ/mol, Figure 7.1b). This result is consistent with DFT calculations of furan adsorption on Pd(111) made by Bradley *et al.*,⁵² who showed that preferred adsorption is with the ring essentially parallel to the surface. As opposed to Pd, our recent DFT calculations of FAL on Cu(111) surface⁵³ have shown a strong repulsion between the furan ring and the Cu(111) surface, due to the overlap of the 3d band of the surface Cu atoms and the aromatic furan ring. As a result, the adsorption of FAL on Cu(111) is weak and can only occur in the η^1 (O)-aldehyde configuration, via the carbonyl O atom.

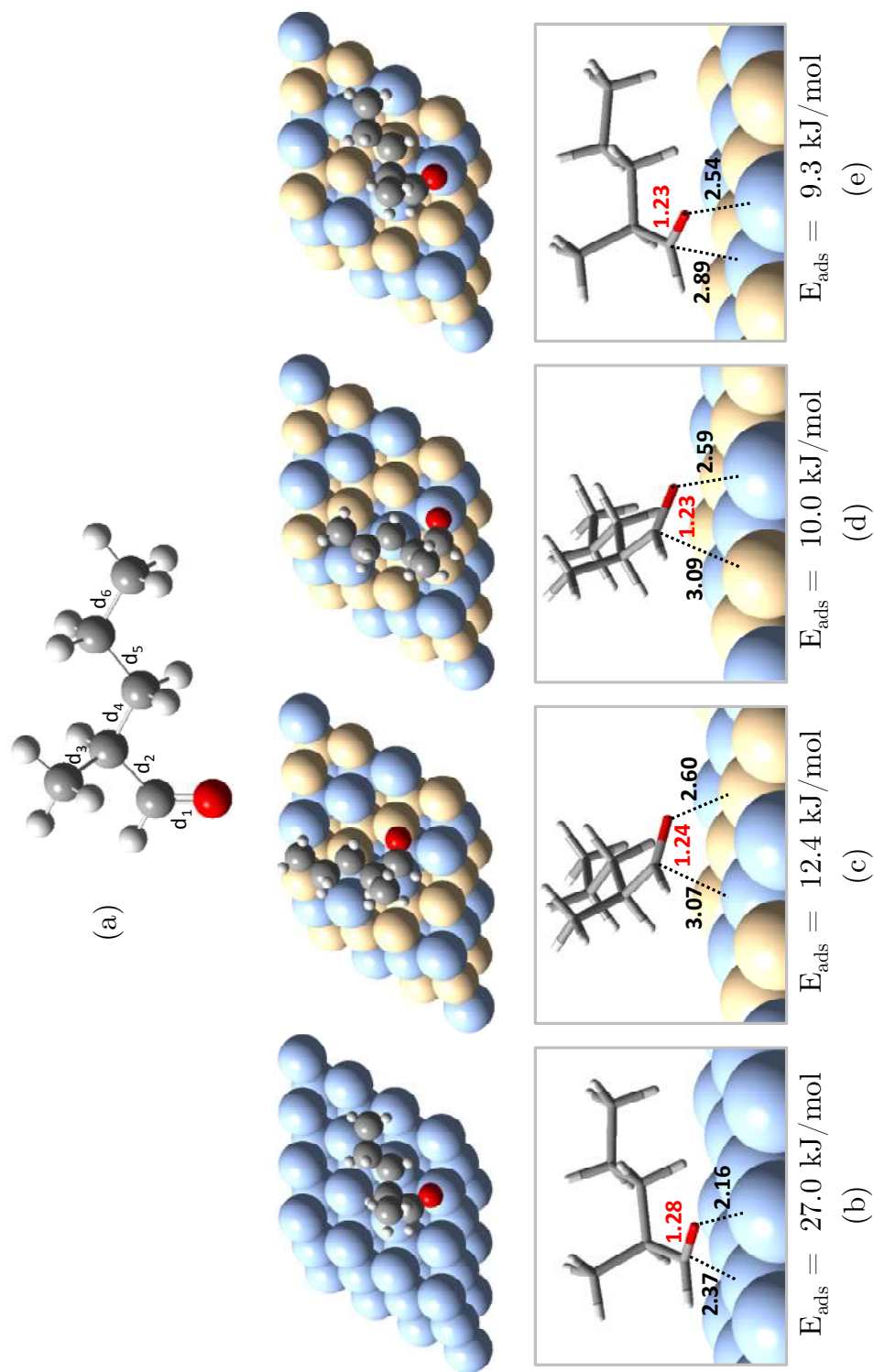


Figure 7.2 DFT optimized structures of 2-methylpentanal (MPAL) in gas phase (a), and its adsorption on Pd(111) (b) and PdCu(111) (c-e) slabs. Red, gray, white, blue, and yellow spheres represent O, C, H, Pd and Cu atoms, respectively. The corresponding bond lengths are given in Table 7.1.

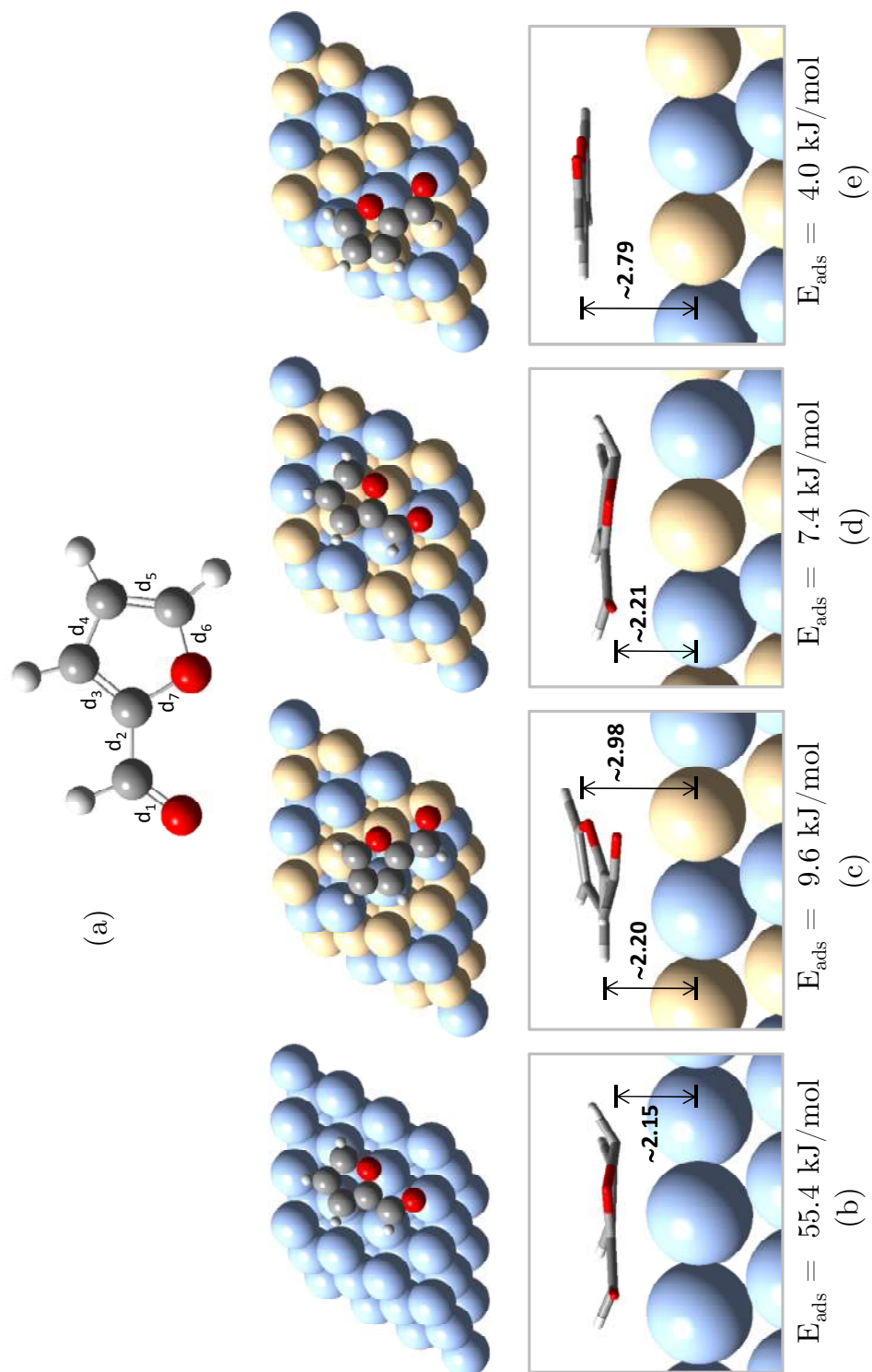


Figure 7.3 DFT optimized structures of furfural (FAL) in gas phase (a), and its adsorption on Pd(111) (b) and PdCu(111) (c-e) slabs. Red, gray, white, blue, and yellow spheres represent O, C, H, Pd and Cu atoms, respectively. The corresponding bond lengths are given in Table 7.2.

Table 7.1 Adsorption energies (kJ/mol) and optimized bond lengths (Å) of 2-methylpentanal on Pd(111) and PdCu(111) slabs (see Figure 7.2).

Model	MPAL	MPAL/Pd(111)	MPAL/PdCu(111)		
	(a)	(b)	(c)	(d)	(e)
E_{ads}	-	27.0	12.4	10.0	9.3
d_1	1.22	1.28	1.24	1.23	1.23
d_2	1.52	1.52	1.51	1.51	1.51
d_3	1.54	1.54	1.54	1.54	1.54
d_4	1.53	1.53	1.53	1.53	1.53
d_5	1.53	1.53	1.53	1.53	1.53
d_6	1.53	1.53	1.53	1.53	1.53

Table 7.2 Adsorption energies (kJ/mol) and optimized bond lengths (Å) of furfural on Pd(111) and PdCu(111) slabs (see Figure 7.3).

Model	FAL	FAL/Pd(111)	FAL/PdCu(111)		
	(a)	(b)	(c)	(d)	(e)
E_{ads}	-	55.4	9.6	7.4	4.0
d_1	1.23	1.31	1.30	1.28	1.23
d_2	1.46	1.47	1.47	1.45	1.46
d_3	1.39	1.44	1.42	1.41	1.39
d_4	1.43	1.44	1.44	1.42	1.43
d_5	1.38	1.45	1.37	1.44	1.38
d_6	1.37	1.40	1.39	1.40	1.37
d_7	1.39	1.40	1.39	1.40	1.39

A relevant comparison of the DFT results can be made for MPAL and FAL over the PdCu(111) surface. It is clearly seen that the presence of Cu significantly reduces the interaction of both aldehydes with the metal surface. Relative to those on the pure Pd, the heats of adsorption on the bimetallic surface are significantly reduced. That is, the adsorption strength of MPAL drops from 27.0 kJ/mol on Pd(111) to 12.4 kJ/mol on PdCu(111). Moreover, the heat of adsorption of FAL changes from 55.4 kJ/mol on Pd(111) to 9.6 kJ/mol on PdCu(111). This dramatic reduction in the strength of interaction can be ascribed to the effect of the aromatic ring, which has a strong affinity for Pd, but not for Cu.

Another aspect important to discuss is the significant changes in strength of interaction observed with respect to the place in which the molecule is adsorbed on PdCu(111). For instance, in the case of MPAL, the η^2 -(C-O) aldehyde adsorption with the C atom on top of Pd and the O atom on Cu (see Figure 7.2c) results in a higher adsorption energy (12.4 kJ/mol) than the other configurations (i.e. C/Cu-O/Pd or C/Pd-O/Pd). The preferential adsorption mode results in the higher elongation of the carbonyl bond, d_1 . Again, as in the case of pure Pd, the lengths of the other bonds (d_3 , d_4 , d_5 , and d_6) remain unmodified upon adsorption. In addition, the distances between C or O and the surface are significantly longer ~ 0.4 - 0.7 Å than those on Pd(111). This difference is in agreement with the trends in adsorption energy and the length

of the C=O bond. A weaker interaction results in longer adsorbate-surface distances and shorter/stronger carbonyl bonds.

The case of FAL is somewhat different due to the important role played by the furanic ring in the interaction with the surface. As mentioned above, on the pure Pd the presence of the ring greatly enhances the interaction. However, when Cu atoms are added, the stability of the adsorbed FAL is dramatically decreased. In the FAL adsorbed on Pd(111) all bonds are elongated, particularly the C=O and C=C bonds. To investigate this interaction, various FAL/PdCu(111) configurations were simulated.

It is interesting to see the different calculated energies and bond lengths as the molecule is placed on different places on the alloy surface. That is, while the heat of adsorption is much lower than on pure Pd, it is not as low when the O atoms in FAL are placed over Cu atom and the furanic ring over Pd atoms. By contrast, the adsorption energy is even lower when the ring is placed over Cu atoms. As shown on the side view of Figure 7.3d, the molecule even bends away from the Cu atom due to the apparent repulsion.

7.3.2 Cluster model

Furthermore, a similar trend of absorption behavior of MPAL was observed for the cluster modeled calculation implemented by GAUSSIAN03. The

absolute value of the heat of adsorption is quite different from that derived from the periodic slab calculation; however, this semi-quantitative analysis is good enough for the predictive mechanistic study. The optimized structures of MPAL in gas phase and adsorbed MPAL on the clusters are illustrated in Figure 7.4; and the corresponding adsorption energies (E_{ads}) and bond lengths are summarized in Table 7.3. The length of the C1-O bond increases with respect to that of the gas phase molecule upon formation of the η^2 -(C-O) aldehyde on the Pd₁₀ cluster, while the C1-C2 bond length remains unchanged, indicating a weakening of the carbonyl bond. The presence of Cu in the cluster has a significant effect on the energetics of the system. It is observed that when the η^2 -(C-O) aldehyde species is modeled with the C1 coordinated to Pd and O coordinated to Cu, the adsorption energy (E_{ads}) drops from 46.6 for pure Pd to 9.2 kJ/mol for the bimetallic cluster. The O-Cu bond length for MPAL/Pd₄Cu₆ is ~ 0.1 Å shorter than the O-Pd bond for MPAL/Pd₁₀. In contrast, the C1-Pd bond for MPAL/Pd₄Cu₆ is elongated from 2.14 Å on the pure Pd to 3.50 Å on the bimetallic cluster. That is, this configuration is more like an η^1 -(O) than an η^2 -(C-O) aldehyde. The carbonyl group is bonded to the surface mostly through the oxygen lone pair orbital. In the same manner, the stability of the acyl species was much higher on Pd than on the bimetallic cluster. In this case, even when in both cases the C1 atom was coordinated to a Pd atom, the adsorption energy on the pure Pd cluster (181.4 kJ/mol) was much higher than on the bimetallic cluster (136.5 kJ/mol). In agreement with this trend, a longer C1-Pd bond is observed on MPAL/Pd₄Cu₆ compared to MPAL/Pd₁₀.

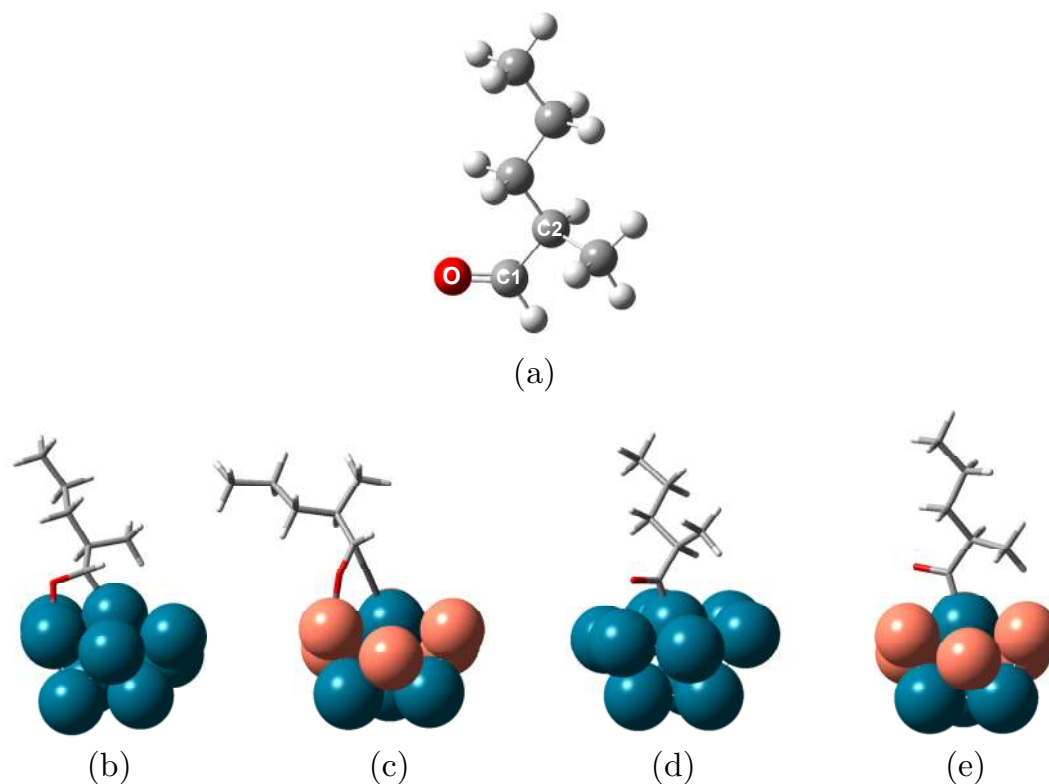


Figure 7.4 DFT optimized structures of 2-methylpentanal in gas phase (a), and its η^2 -(C-O) aldehyde adsorption on Pd₁₀ (b) and Pd₄Cu₆ (c) clusters. The corresponding adsorbed acyl species are shown in (d) and (e), respectively.

Table 7.3 Adsorption energies (E_{ads}), and optimized distances of C1-O, C1-C2, C1-Metal and O-metal bonds for the systems illustrated in Figure 7.4.

Structure	(a)	(b)	(c)	(d)	(e)
Species	Isolated	η^2 -(C-O)	η^2 -(C-O)	Acyl-(C)	Acyl-(C)
Cluster	-	Pd ₁₀	Pd ₄ Cu ₆	Pd ₁₀	Pd ₄ Cu ₆
E_{ads} (kJ/mol)	-	46.6	9.2	181.4	136.5
Bond length (Å)					
C1—O	1.24	1.34	1.25	1.25	1.26
C1—C2	1.52	1.53	1.50	1.53	1.54
C1—M	-	2.14	3.50	1.93	2.04
O—M	-	2.08	1.98	2.38	3.15

According to the DFT calculation, it can be suggested that addition of Cu leading to the formation of Pd-Cu alloy reduces the stability of the η^2 -(C-O) adsorption which is the precursor for decarbonylation reaction.³⁵ That is, in both cases, with FAL and MPAL feeds, the yield of the decarbonylation products, furan and pentane, respectively, was greatly reduced, while the yield of hydrogenated products (FOL and MPOL) significantly increased. This behavior is in an agreement with the experimental result showing the effect of Cu loading (see Figure 7.5).

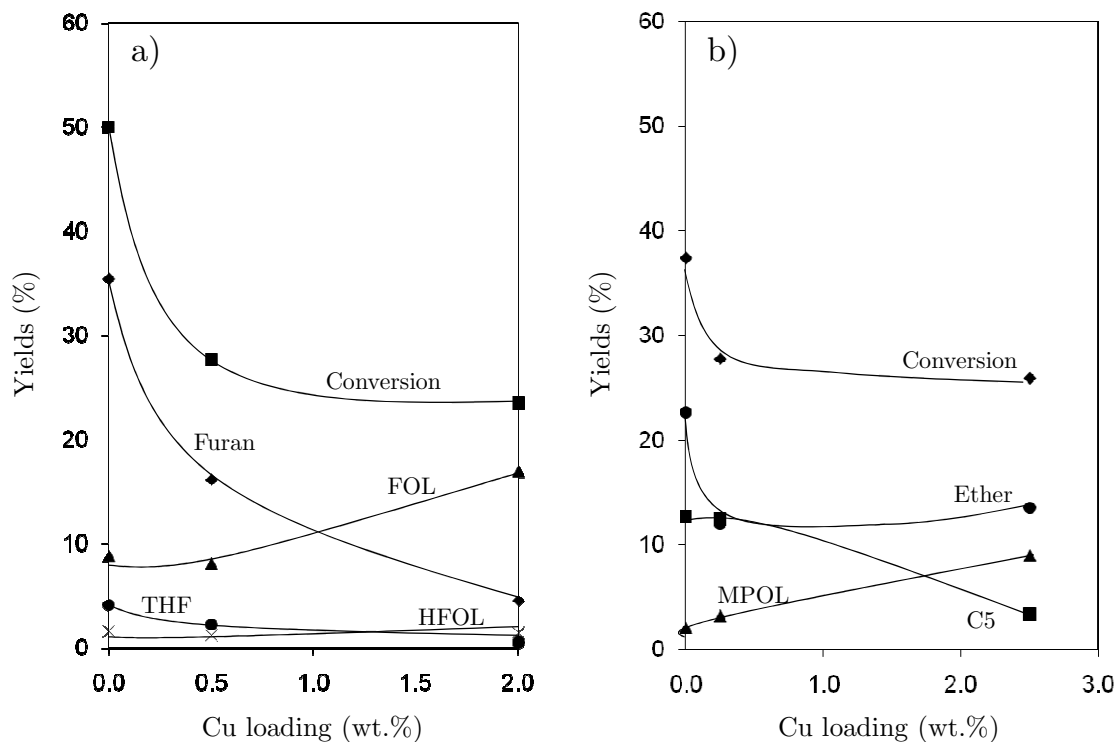


Figure 7.5 Conversion and yield of products from the reaction of furfural (a); and 2-methylpentanal (b) on Pd/SiO₂ as a function of Cu loading. Reaction condition: W/F = 3 h, Temp = 125°C, H₂ pressure = 1 atm, TOS = 15 min.³⁵

7.4. Conclusions

Pd-Cu alloy formation leads to an electronic structure different from that of pure Pd. This electronic perturbation results in a lower extent of electron back-donation to the π^* system of the aldehydes. As a result, the formation of the side-on η^2 -(C-O) aldehyde species is less stable on Pd-Cu than on pure Pd, which in turn makes the formation of the acyl intermediate less likely. Therefore, the decarbonylation rate is greatly reduced on Pd-Cu alloys, but the hydrogenation rate is increased.

References

-
- 1 A. Demirbas *Fuel Proc Technol.* **2007**,88,591.
 - 2 V.R. Wiggers, A. Wisniewski Jr., L.A.S. Madureira, A.A. Chivanga Barros, H.F. Meier *Fuel Proc Technol.* **2008**,88,2135.
 - 3 M.G. Perez, J. Shen, X. S. Wang, C.Z Li *Fuel Proc Technol.* **2010**,91,296.
 - 4 J. Lede, F. Broust, F.T. Ndiaye, M. Ferrer *Fuel.* **2007**,86,1800.
 - 5 M. Asadullah, M.A. Rahman, M.M. Ali, M.S. Rahman, M.A. Motin, M.B. Sultan, M.R. Alam *Fuel.* **2007**,86,2514.
 - 6 O. Onay, O.M. Kockar *Fuel.* **2006**,85,1921.
 - 7 A. Zabaniotou, O. Ioannidou, V. Skoulou *Fuel.* **2008**,87,1492.
 - 8 L.R. Lynd, J.H. Cushman, R.J. Nichols, C.E. Wyman *Science.* **1991**, 251,1318.
 - 9 G.W. Huber, S. Iborra, A. Corma *Chem Rev.* **2006**,106,4044.

-
- 10 G.W. Huber, A. Corma *Angew Chem, Int Ed.* **2007**,46,7184.
- 11 R.E.H. Sims, W. Mabee, J.N. Saddler, M. Taylor *Bioresour Technol.* **2010**,10,1570.
- 12 C. Amen-Chen, H. Pakdel, C. Roy *Biomass and Bioenergy.* **2001**,79,277.
- 13 Y.H.E. Sheu, R.G. Anthony, E.J. Soltes *Fuel Process Technol.* **1988**,19,31.
- 14 A.V. Bridgwater *Appl Catal A-Gen.* **1994**,116,5.
- 15 A. Ausavasukhi, T. Sooknoi, D.E. Resasco *J Catal.* **2009**,268,68.
- 16 M. Bejblova, P. Zamostny, L. Cervený, J. Cejka *Chem Com* **2003**,68,1969.
- 17 R. Abu-Reziq, D. Avnir, J. Blum *J Mol Catal A: Chem.* **2002**,187,277.
- 18 M. Bejblova, P. Zamostny, L. Cervený, J. Cejka *Appl Catal A: Gen.* **2005**,296,169.
- 19 M.A. Vannice, D. Poondi *J Catal.* **1997**,169,166.
- 20 Z. Ji-lu *J Anal Appl Pyrol.* **2007**,80,30.
- 21 P. Kluson, L. Cervený *J Mol Catal A: Chem.* **1996**,108,107.
- 22 F.H. Mahfud, F.Ghijsen, H.J. Heeres *J Mol Catal A: Chem.* **2007**,264,227.
- 23 A. Saadi, Z Rassoul, M.M. Bettahar *J Mol Catal A: Chem.* **2000**,164,205.
- 24 Y. Roman-Leshkov, C.J. Barrett, Z.Y. Liu, J.A. Dumesic *Nature Letters.* **2007**,447,982.
- 25 H.Y. Zheng, Y.L. Zhu, B.T. Teng, Z.Q. Bai, C.H. Zhang, H.W. Xiang, Y.W. Li *J Mol Catal A: Chem.* **2006**,246,18.
- 26 U.K. Singh, M.A. Vannice *J Catal.* **2000**,191,165.
- 27 U.K. Singh, M.A. Vannice *J Catal.* **2001**,199,73.

-
- 28 M.V. Arx, T. Mallat, A. Baiker *J Mol Catal A: Chem.* **1999**,48,275.
- 29 T.T. Pham, L.L. Lobban, D.E. Resasco, R.G. Mallinson *J Catal.* **2009**,266,9.
- 30 K.J. Jung, A. Gaset *Biomass.* **1988**,16,63.
- 31 R.D. Srivastava, A.K. Guha *J Catal.* **1985**,91,254.
- 32 J. Piskorza, D. Radlein, D.S. Scott *J Anal Appl Pyrol.* **1986**,9,121.
- 33 J.N. Chheda, Y. Román-Leshkov, J.A. Dumesic *Green Chem.* **2007**,9,342.
- 34 T.Q. Hoang, X. Zhu, T. Danuthai, L.L. Lobban, D.E. Resasco, R.G. Mallinson *Energy Fuels.* **2010**,24,3804.
- 35 S. Sitthisa, T. Pham, T. Prasomsri, T. Sooknoi, R.G. Mallinson, D.E. Resasco *J Catal.* **2010** – Submitted.
- 36 G. Kresse, J. Furthmueller *J Phys Rev B.* **1996**,54,11169.
- 37 G. Kresse, J. Hafner *J Phys Rev B.* **1994**,49,14251.
- 38 G. Kresse, J. Hafner *J Phys Rev B.* **1993**,48,13115.
- 39 G. Kresse, J. Hafner *J Phys Rev B.* **1993**,47,558.
- 40 G. Kresse, J. Furthmuller *Comput Mater Sci.* **1996**,6,15.
- 41 G. Kresse, D. Joubert *J Phys Rev B.* **1999**,59,1758.
- 42 P.E. Bloechl *J Phys Rev B.* **1994**,50,17953.
- 43 J.P. Perdew, K. Burke, M. Ernzerhof *Phys Rev Letters.* **1996**,77,3865.
- 44 F. Fouda-Onana, O. Savadogo *Electrochim Acta.* **2009**,54,1769.
- 45 M.J. Frisch, et al. Gaussian 03, Gaussian, Inc., Wallingford, CT, **2004**.
- 46 A.D. Becke *J Chem Phys.* **1993**,98,1372.

-
- 47 J.P. Perdew, J.A. Chevary, S.H. Vosko, K.A. Jackson, M.R. Pederson, D.J. Singh, C. Fiolhais *Phys Rev B*. **1992**,46,6671.
- 48 J.P. Perdew, Y. Wang *Phys Rev B*. **1992**,45,13244.
- 49 P.J. Hay, W.R. Wadt *J Chem Phys*. **1985**,82,299.
- 50 A. Maiti, A. Ricca *Chem Phys Lett*. **2004**,395,7.
- 51 R. Shekhar, R.V. Plank, J.M. Vohs, M.A. Barteau *J Phys Chem B*. **1997**,101,7939.
- 52 M.K. Bradley, J. bin Roson, D.P. Woodruff *Surf Sci*. **2010**,604,920.
- 53 S. Sitthisa, T. Sooknoi, Y. Ma, P.B. Balbuena, D.E. Resasco *J Catal*. **2011**,277,1.

CHAPTER 8

8. Examples of Combining Theoretical Calculations toward the Understanding of Experimental Results

8.1 Example 1: Catalyst deactivation by a strong adsorption of oxygenate aromatic compounds on acid catalysts

8.1.1 Experimental observation

One of the major problems in catalytic bio-oil upgrading is the catalyst deactivation. It is proposed that the deactivation is caused by not only coke formation, but also the strong adsorption of the oxygenate compounds on the surface of catalyst supports.^{1,2} It is noted that this effect is much more pronounced on the aluminosilicate-type of catalysts, which contain acid sites. Here, there are several supporting evidences observed during the experiments such as a mass loss per pass of the feed in the pulse/flow experiment, and a hydrogen-rich coke deposited on a spent catalyst.

The oxygen content presenting in bio-oil derived compounds, particularly phenolics, strongly interacts with acid sites of the catalysts. Among those

phenolic compounds in bio-oils, guaiacol exhibited highly competitive adsorption and rapid catalyst deactivation. As a result, one could assume a highest heat of adsorption of guaiacol.

Due to the fact that demethylation of guaiacol to produce catechol is fairly easy to take place on acid sites (see Appendix G), the experimental measurement of guaiacol adsorption heat with excluded effects from catechol by a calorimeter could be very complicated and tricky. In contrast, the DFT calculation provides a cleaner investigation and a better understanding of how the molecule interacts on the acid sites. Therefore, in this contribution, the adsorption of different molecules ranging from aromatic hydrocarbons to oxygenated aromatic compounds on Brønsted (B-acid) and Lewis acid (L-acid) sites was theoretically studied.

8.1.2 Computational calculation

The computational method performed in this example is similar to that discussed in Chapter 5. Two cluster models were used to represent the surface acid sites. As illustrated in Figure 8.1, the former, a so-called 2T cluster, represent only the Brønsted; while the later, a so-called 4T cluster, contains both Brønsted and Lewis acid sites. The Brønsted site is created by locating an acidic proton/hydrogen at the oxygen bridge between aluminum and silicon atoms, and the Lewis sites is modeled by the existence of the extraframework of

aluminum (EFAL), AlOH^{2+} , which coordinates with the oxygen next to the framework aluminum.³ To keep the cluster model neutral, as many framework aluminum atoms as necessary were used to compensate the positive charges of EFAL species.

Here, the selected aromatic compounds used in the study of adsorption heats are benzene (BZ), phenol (Ph), anisole (An) and guaiacol (Gua). No atom was constrained during the configuration optimizations of adsorption complex models. All the calculations in this study were performed using the GAUSSIAN 03 program package.⁴

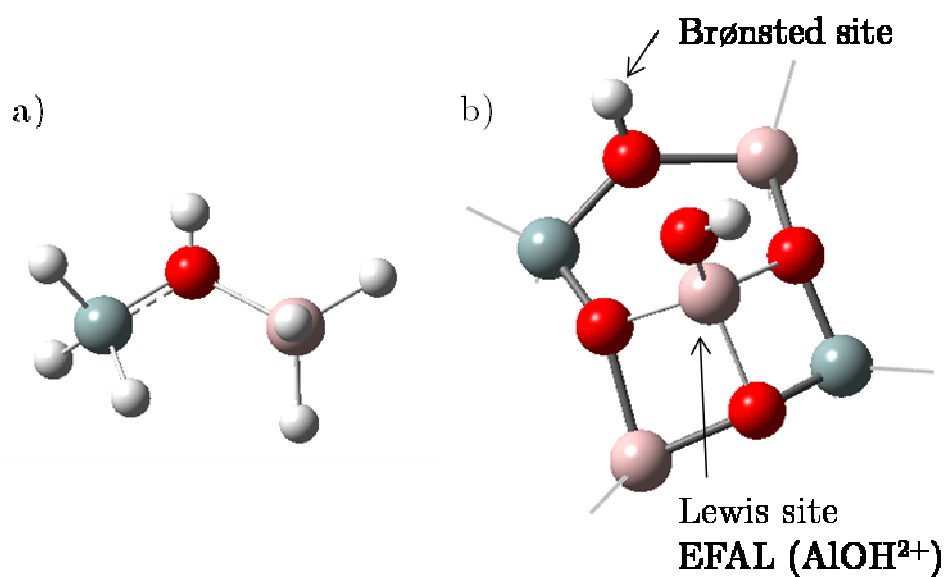


Figure 8.1 The simulated models of acid sites created by a) 2T, and b), 4T clusters models. Hydrogen, oxygen, silicon and aluminum are represented by white, red, gray and pink spheres, respectively.

8.1.3 Results and discussion

The comparison of adsorption heats of different studied molecules on the 2T cluster models which represent Brønsted acid sites is shown in Figure 8.2. Generally, the adsorption energy is highest for guaiacol (-16.4 kcal/mol) followed by phenol (-12.8 kcal/mol), anisole (-10.2 kcal/mol), and benzene exhibits the lowest adsorption heat (-5.6 kcal/mol). For oxygenate aromatics, there are two possible adsorption sites of the molecules, which are the oxygenate functional groups and the ring. The former shows a higher heat of adsorption than the later (see Figures 8.4 - 8.6). Interestingly, adsorption on the ring site of the oxygenate aromatics is also increase in the following order guaiacol > phenol > anisole. It can be suggested that the oxygenate functional groups themselves not only promote the interaction with the Brønsted acid site, but also affect on the adsorption at the ring site of the molecules. Along with the same analysis discussed in Appendix K, the presence of the substituents on the aromatic ring can modify the electronic structure of the molecules. The delocalized electrons at the aromatic ring of guaiacol, which contains two substituents (-OH and -O-CH₃), are destabilized more than that of phenol/anisole and benzene, which have single and none substituent, respectively. As a result, a higher HOMO energy of guaiacol leading to a better interaction with the acid site is expected.

According to Figure 8.3 illustrating the comparison of different initial adsorption structures of benzene on the acid site, it is interesting to see that the

optimized structures converge to exactly the same orientation in which the ring slightly tilts up – neither parallel or perpendicular to the surface. Another interesting case to see is the adsorption of guaiacol. As shown in Figure 8.6, the initial structures of guaiacol adsorption are oriented differently, whereas the optimized geometries converge to the same orientation, in which the hydroxyl ($-OH$) group aims toward the acidic proton. It is suggested that the adsorption by the $-OH$ is more preferential than the $-O-CH_3$. This concept can be successfully applied to the comparison between phenol and anisole, which phenol shows a higher heat of adsorption.

The similar calculations were performed on a bigger cluster, namely 4T cluster model, which had both Brønsted and Lewis. Firstly, it is important to mention that the absolute values adsorption energies from the DFT calculation strongly depend on the size of the cluster used. However, the semi-quantitative trend of heat of adsorption can be achieved for the purpose of comparison. As shown in Figure 8.8, guaiacol shows a higher adsorption energy than anisole. Interestingly, almost a twofold increase of heat of adsorption was seen when both of the oxygenated functional groups interact with the two acid sites (see Figure 8.8e). In addition, the coordination of guaiacol and the acid site through $-OH$ /Lewis acid and $-O-CH_3$ /Brønsted acid is recommended to be an appropriate orientation according to the charge and proton affinity analysis discussed in the Appendix A. Again, adsorption of benzene is relatively weaker

as compared with guaiacol and anisole, and it can only interact with Brønsted acid site (see Figure 8.9).

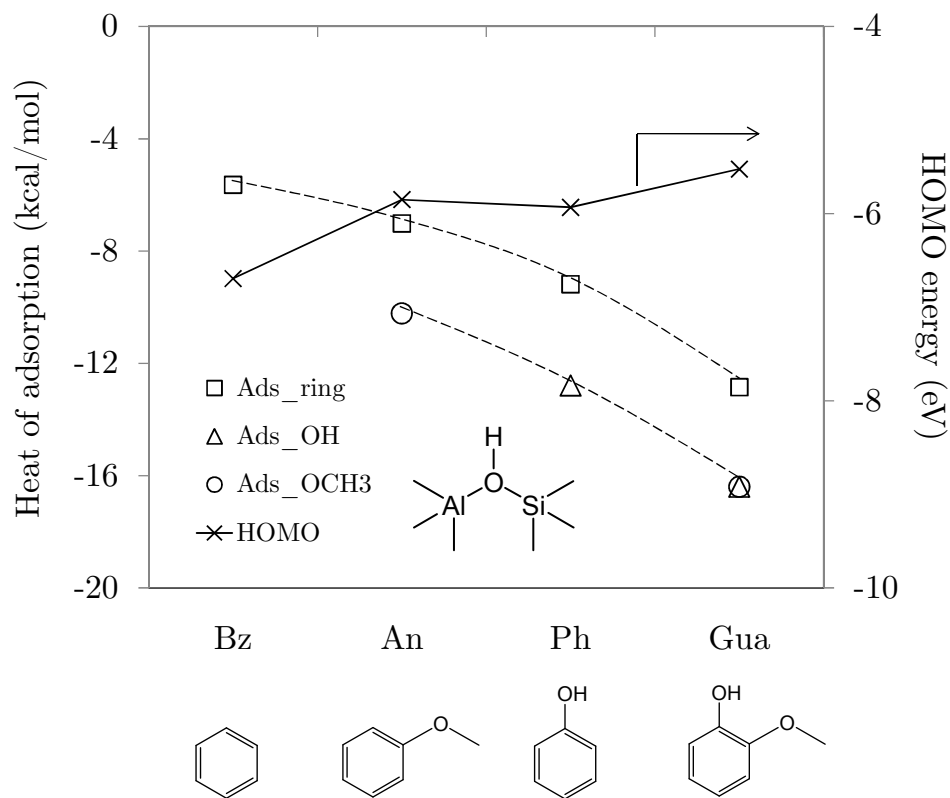


Figure 8.2 Comparison of adsorption and HOMO energies of benzene, anisole, phenol and guaiacol on the 2T cluster models. Different adsorption locations on the molecules including at the ring, hydroxyl (-OH), and methoxyl (-O-CH₃) groups were investigated.

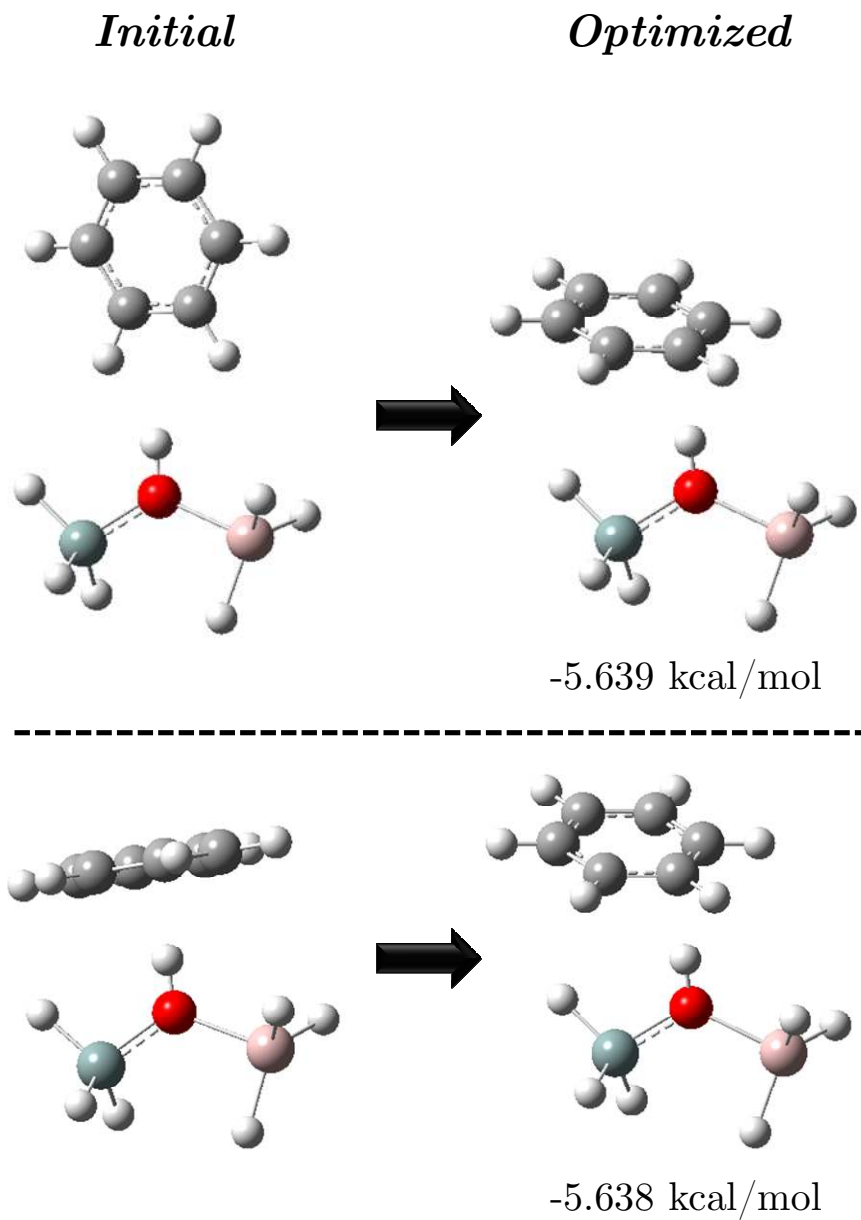


Figure 8.3 The initial and optimized structures of benzene adsorption at the ring site in perpendicular (top) and parallel (bottom) manners on the 2T clusters.

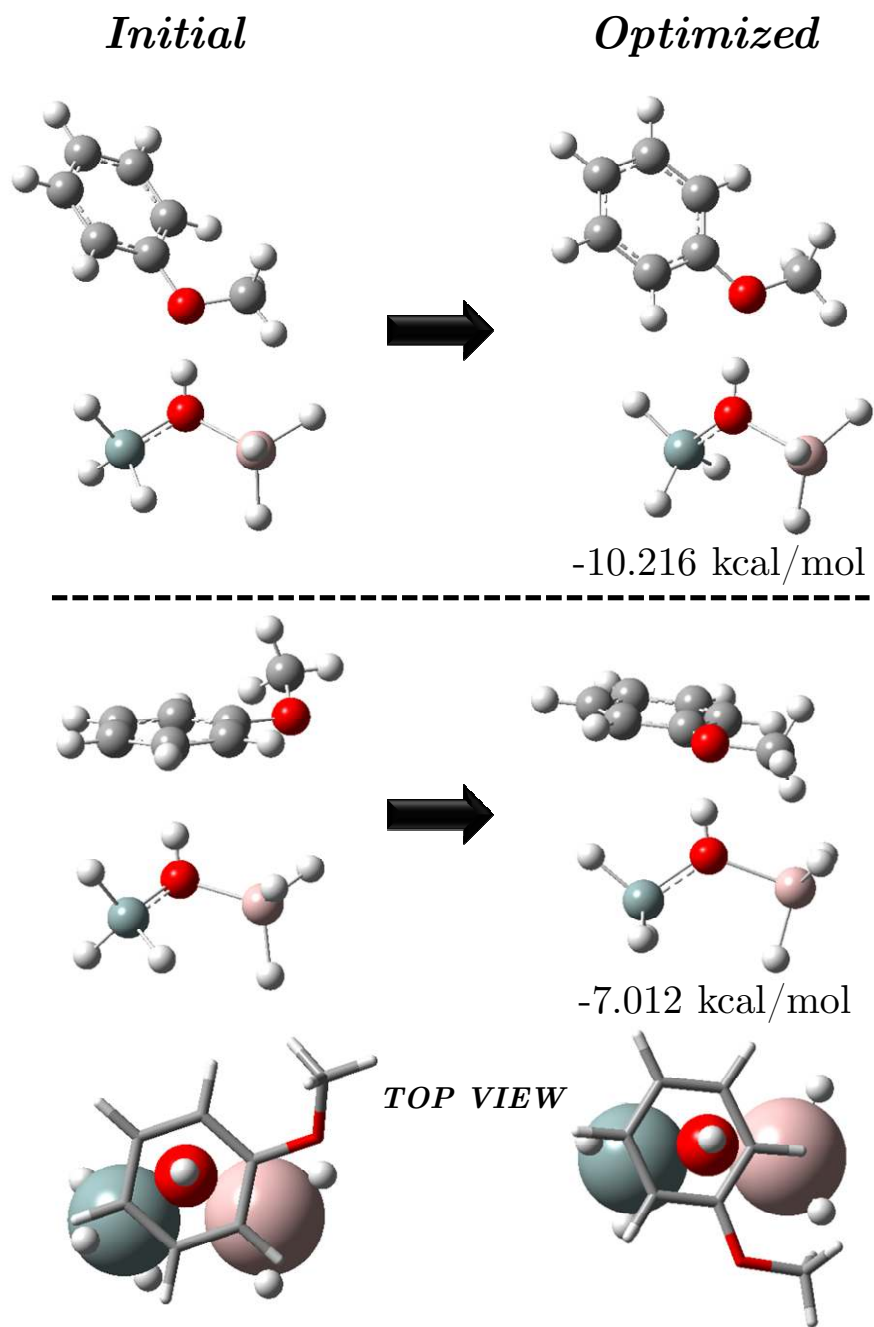


Figure 8.4 The initial and optimized structures of anisole adsorption at the $-O-CH_3$ (top) and the ring (bottom) sites on the 2T clusters.

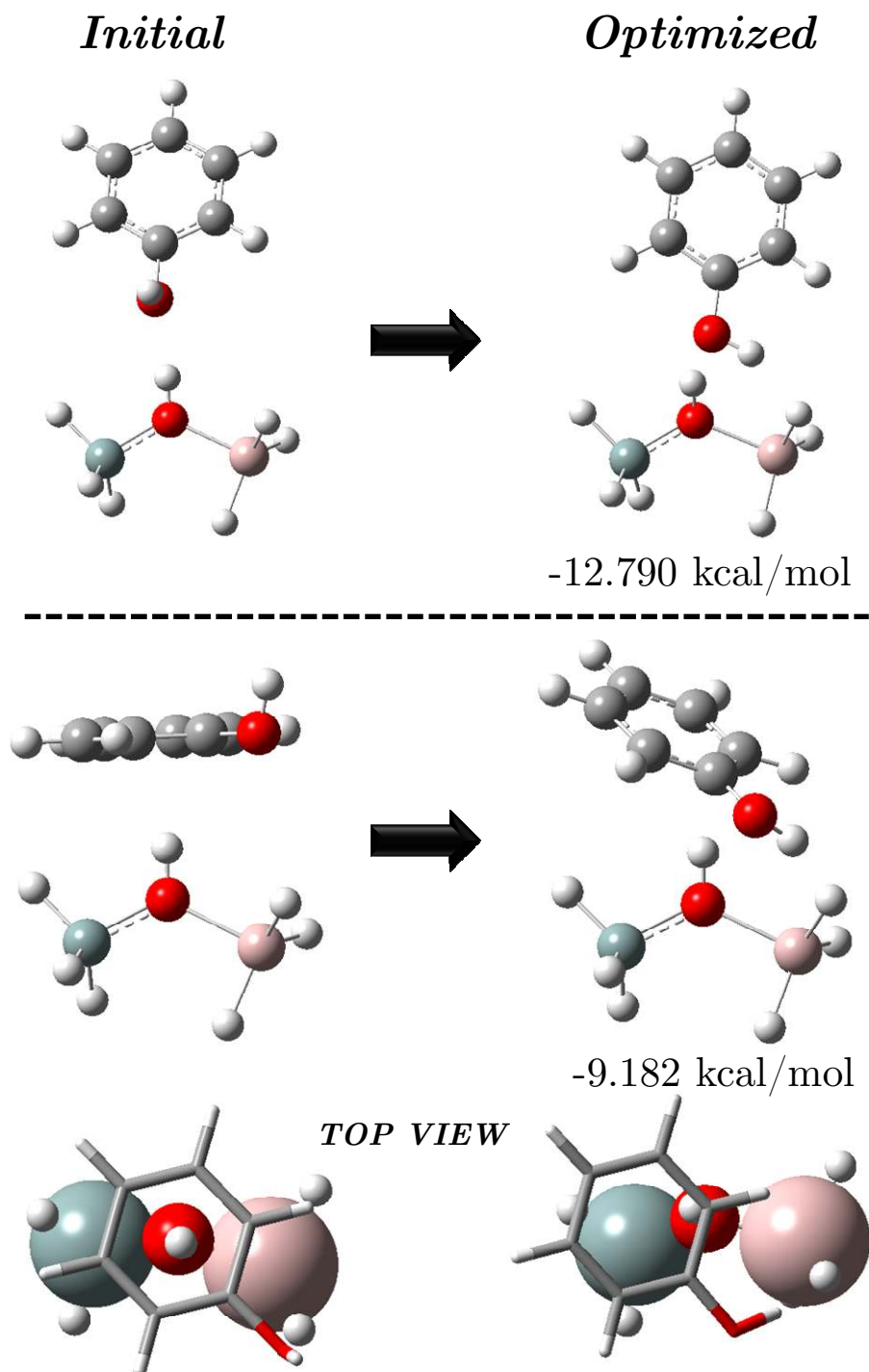


Figure 8.5 The initial and optimized structures of phenol adsorption at the -OH (top) and the ring (bottom) sites on the 2T clusters.

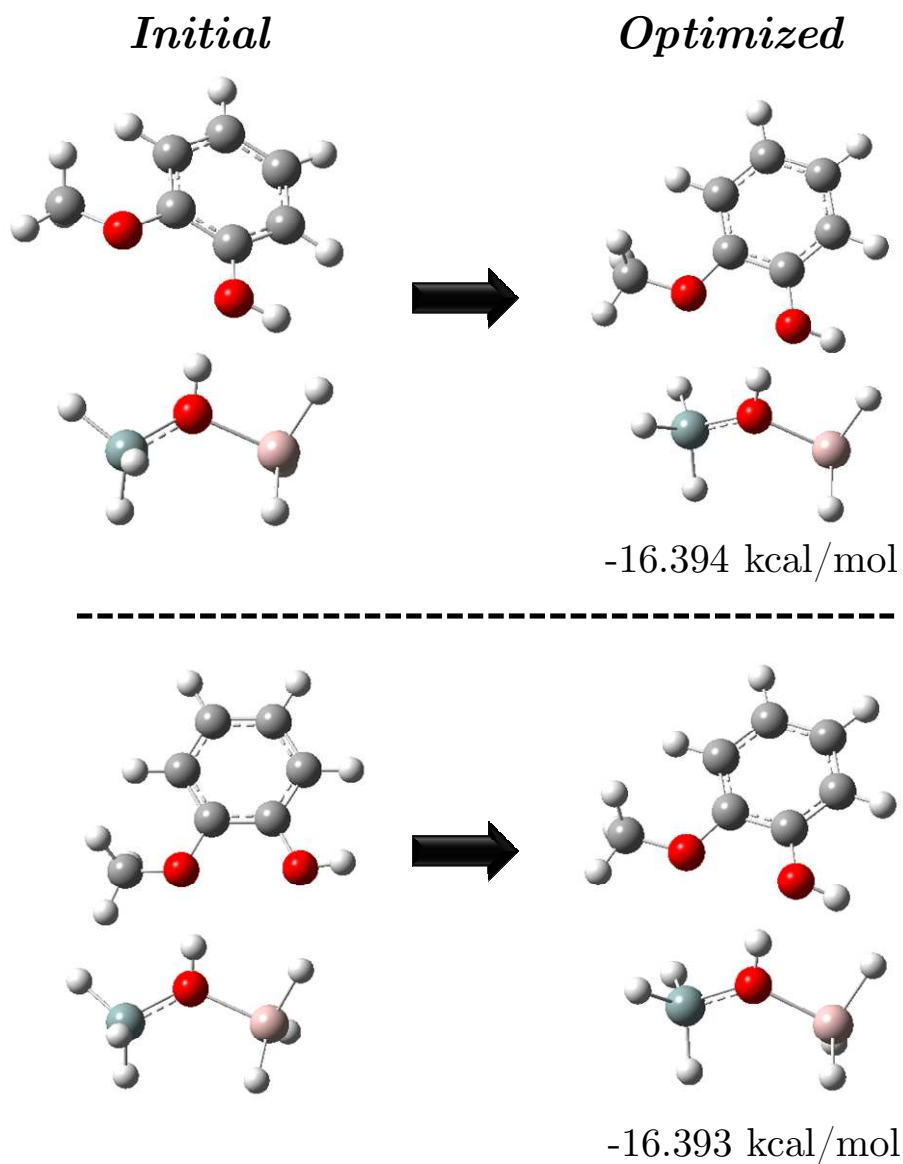


Figure 8.6 The initial and optimized structures of guaiacol adsorption at the -OH (top) and the -O-CH₃ (bottom) sites on the 2T clusters.

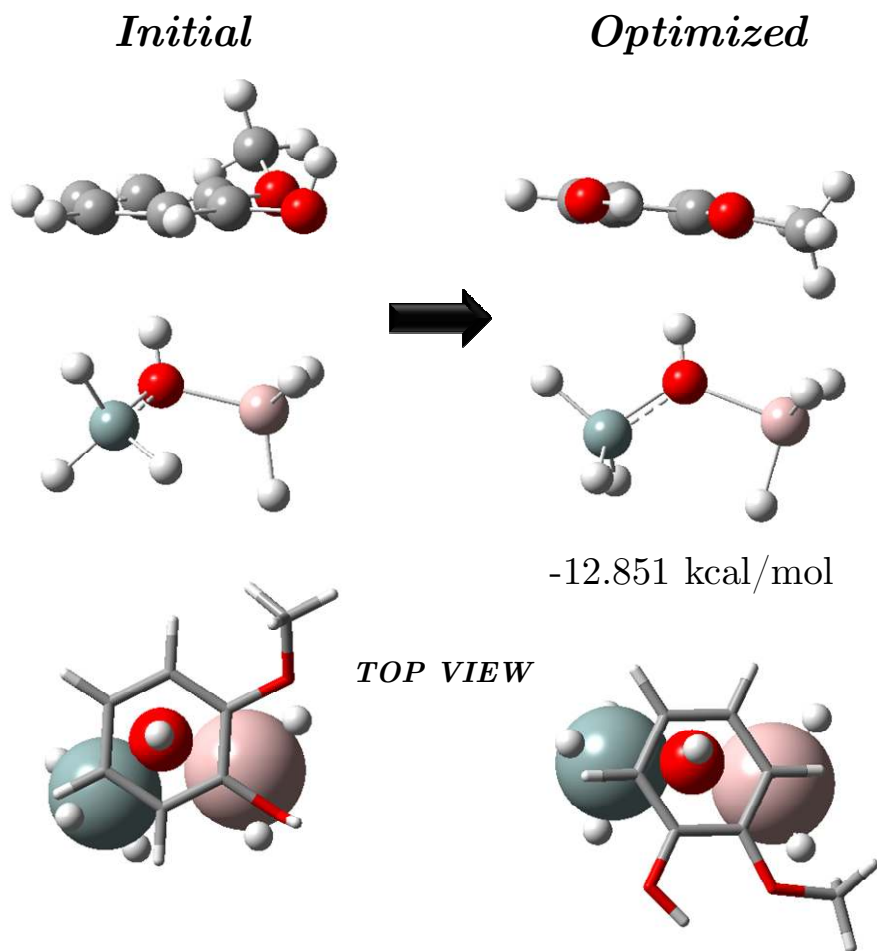


Figure 8.7 The initial and optimized structures of guaiacol adsorption at the ring site on the 2T clusters.

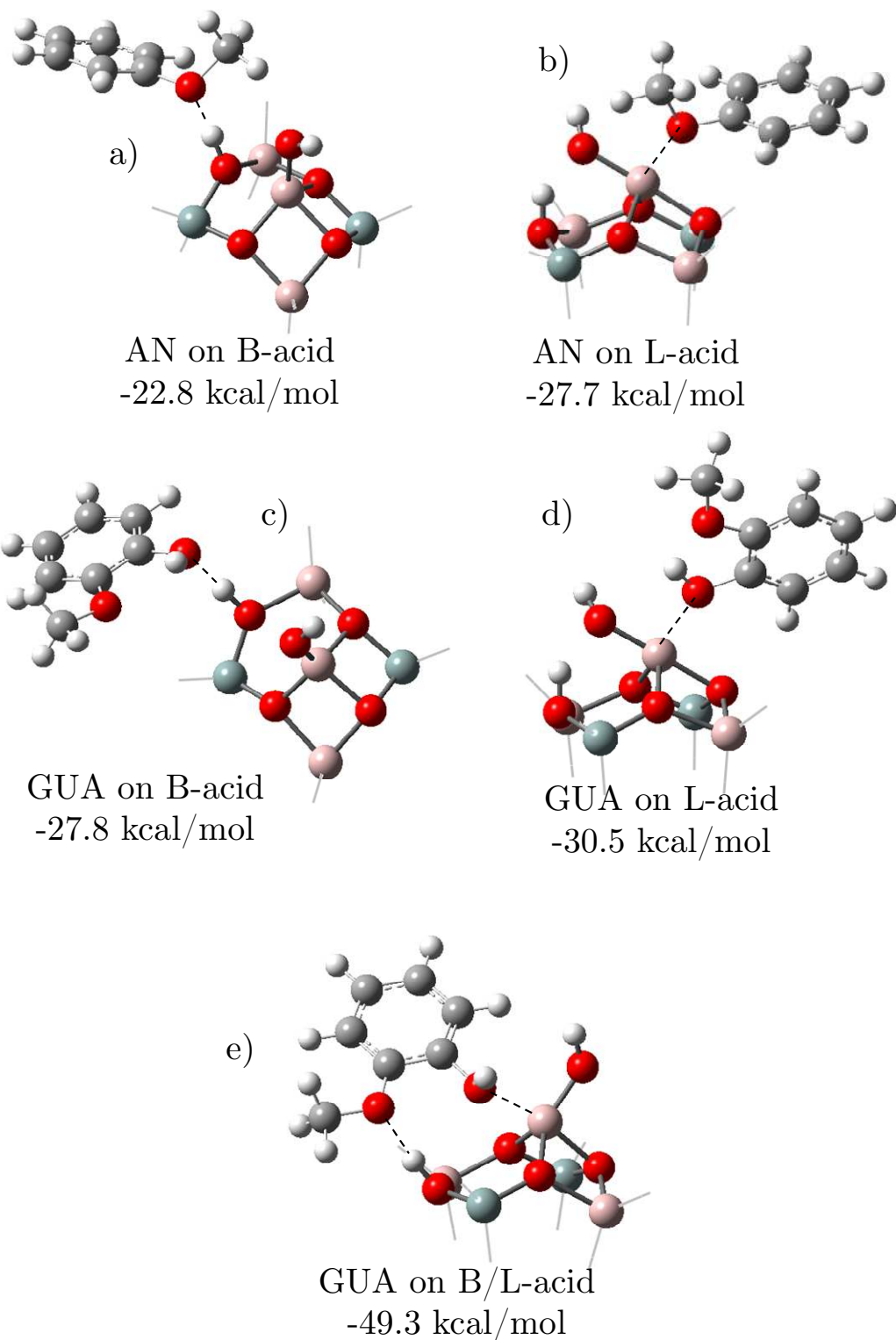


Figure 8.8 The Optimized structures of anisole on the Brønsted (a) and Lewis (b) acid sites; and guaiacol on the Brønsted (c), Lewis (d) and both Brønsted/Lewis acid sites (e) on the 4T clusters.

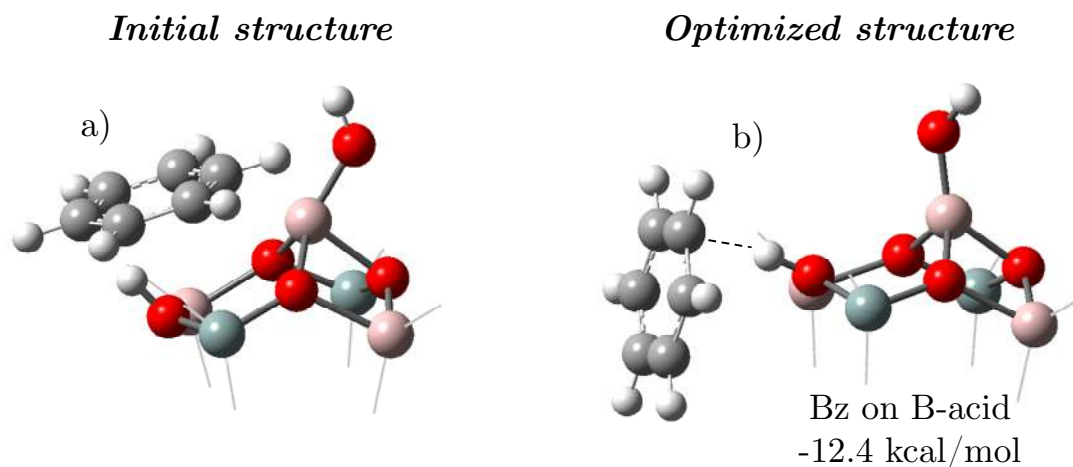


Figure 8.9 The initial and optimized structures of benzene adsorption on the 4T clusters.

8.1.4 Conclusions

Based on the DFT calculation, it can be said that oxygenate aromatic compounds existing in bio-oils, such as anisole and guaiacol, show a stronger adsorption than regular hydrocarbons i.e., benzene, on acid sites. That is an additional effect, in addition to the coke formation, for the rapid deactivation of the catalysts. The interaction is mainly contributed from the oxygen at the functional groups, in which the adsorption strength depends on the number of oxygen presenting in the molecule. The results from the DFT calculation are understandable and consistent well with the experimental investigation.

8.2 Example 2: Competitive adsorption of 1-pentene and isopropylamine (IPA) on cation-exchanged zeolites

8.2.1 Experimental observation

Small olefins produced from fluid catalytic cracking (FCC) processes in refineries are valueless in the sense of fuel production because they are too small and out of the fuels range. Therefore, the oligomerization of those small olefins is an important route to produce more desirable products such as motor fuels, plasticizers, medicines, dyes, resins, detergents, lubricants and additives.⁵ In this study, the objective is to maximize the production of linear hydrocarbons i.e., the diesel range fuels. Unfortunately, some branched hydrocarbons were produced from the undesirable isomerization/cracking. Cation-exchange zeolites were used as catalysts in the experiments, and it is possible that some Brønsted acid sites, which are responsible for the isomerization/cracking reaction, still remain on the catalysts. Interestingly, when isopropylamine (IPA) was pre-fed prior to the olefin feed, it was seen that the ratio of linear-to-branched hydrocarbon yield increase. This suggests the unwanted Brønsted acid sites were poisoned, in which the degree of isomerization/cracking is reduced. In this contribution, the DFT calculation of adsorption heats of 1-pentene and IPA was compared.

8.2.2 Computational calculation

Four different M -zeolite systems ($M = \text{H, Ni, Co and Fe}$) were studied to analyze the electronic properties of 1-pentene and IPA adsorbed on acidic proton and transition metals supported on a zeolite framework. A 3T model cluster $[\text{H}_3\text{SiOAl}(\text{OH})_2\text{OSiH}_3]$ was chosen as the model for the zeolite surface, with the atom M located on a bridge between two oxygen atoms. Similar model have been used successfully in the literature^{6,7} to represent one of the possible sites for the location of the metallic ion inside the zeolite framework.^{8,9} All calculations and geometry optimizations were performed by using the GAUSSIAN 03⁴ at a DFT level using Becke's three-parameter hybrid functional¹⁰ and Lee, Yang, and Parr's correlation functional¹¹ (B3LYP). The Lanl2dz basis set¹² were used for Ni, Co and Fe atoms, and 6-31+G(d, p) basis set for C, H, O, Al, and Si atoms were employed. The electronic charge distribution of the catalyst models was analyzed using the natural bond orbital (NBO) partition scheme.^{13,14} All atoms were relaxed during the optimization.

8.2.3 Results and discussion

The optimized structures of the adsorption complexes and their adsorption energies are shown in Figure 8.10. Based on this calculation, heat of adsorption of 1-pentene is highest on the Fe-T3 zeolite model (-52.2 kcal/mol), followed by Co-T3 (-40.3 kcal/mol) and Ni-T3 (-37.3 kcal/mol), whereas it

drops dramatically on the Brønsted acid site, H-T3, (-6.5 kcal/mol). The similar trend was seen for IPA adsorption on the transition metal atoms, and the corresponding adsorption heats of IPA are slightly lower than those of 1-pentene. In contrast, the heat of adsorption of IPA on the Brønsted acid site is considerably high (-50.1 kcal/mol) and consistent well with the experimental value.¹⁵ As a result, isomerization/cracking can be suppressed because the linear products have less chance to access the Brønsted acid sites. This implies that Brønsted acid sites can be effectively poisoned by IPA. At the same time, the competitive adsorption of 1-pentene and IPA is expected on the cation-exchanged zeolites.

8.2.4 Conclusions

Oligomerization of olefins, such as 1-pentene, takes place on the cationic transition metals exchanged in zeolites. These metals behave like a Lewis acid sites, in which two olefins can accommodate and react. However, the ion-exchange zeolite always contains a certain level of Brønsted acid sites, even it is incredibly small, and this could lead to the isomerization/cracking to produce branched products. From the experimental observation, pre-feeding of IPA onto the catalyst is capable to maximize the yield of linear products. This effect can be elucidated by the DFT calculation which shows that the heat of adsorption of IPA is significantly high on the acidic proton site, as compared to 1-pentene.

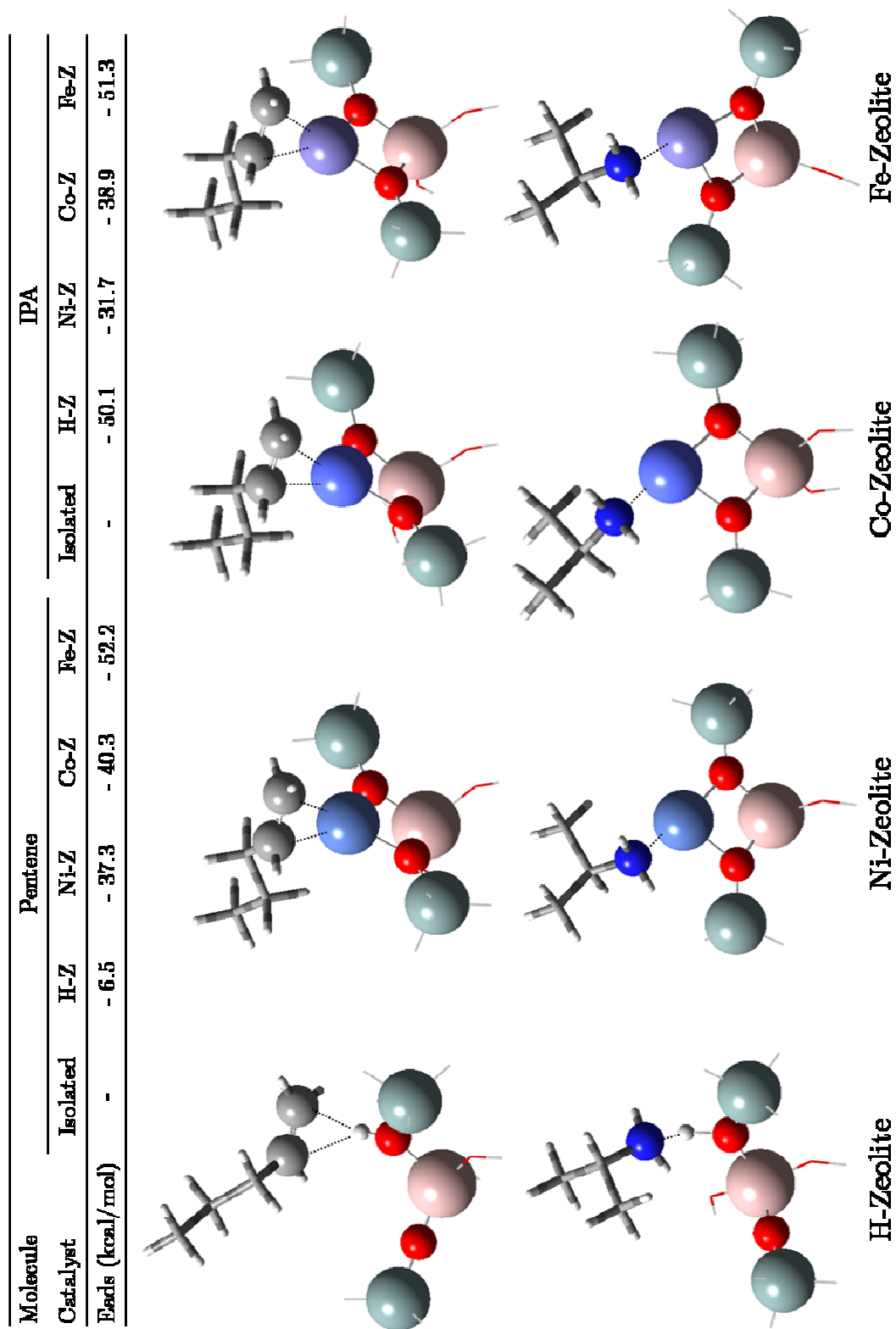


Figure 8.10 Geometries of the adsorption complexes and the corresponding heats of adsorption of 1-pentene and IPA on the M-T3 model clusters.

8.3 Example 3: Relation of adsorption energies and decarbonylation activities of different aldehydes on Pd(111)

8.3.1 Experimental observation

Motivation and justification of decarbonylation of aldehydes were already presented in Chapter 8. Among all transition metals, Pd is the most active one for decarbonylation reaction. Catalytic measurements of different aldehydes including furfural (FAL), 2-methylpentenal (MPEL), 2-methylpentanal (MPAL), and trimethylacetaldehyde (TMA) were conducted in gaseous phase fixed-bed reactor at a moderate temperature and atmospheric hydrogen pressure. The experimental decarbonylation activities and activation energies (E_a) are shown in Figure 8.11. It is important to mention that the experimental data were taken from the work by Sitthisa *et al.* The decarbonylation activity is in the following order $\text{MPEL} > \text{FAL} > \text{MPAL} > \text{TMA}$. This trend agrees well with the activation energy results. That is the most reactive MPAL shows the lowest barrier, while the most unreactive TMA shows the highest barrier. As discussed in Chapter 8, it is proposed that the stability of the adsorption intermediate plays a significant role on the catalytic activity. In this contribution, therefore, DFT calculation was performed in order to specifically investigate the adsorption of the $\eta^1(\text{C})$ -acyl species, which is a key intermediate for decarbonylation, on Pd(111) surfaces.

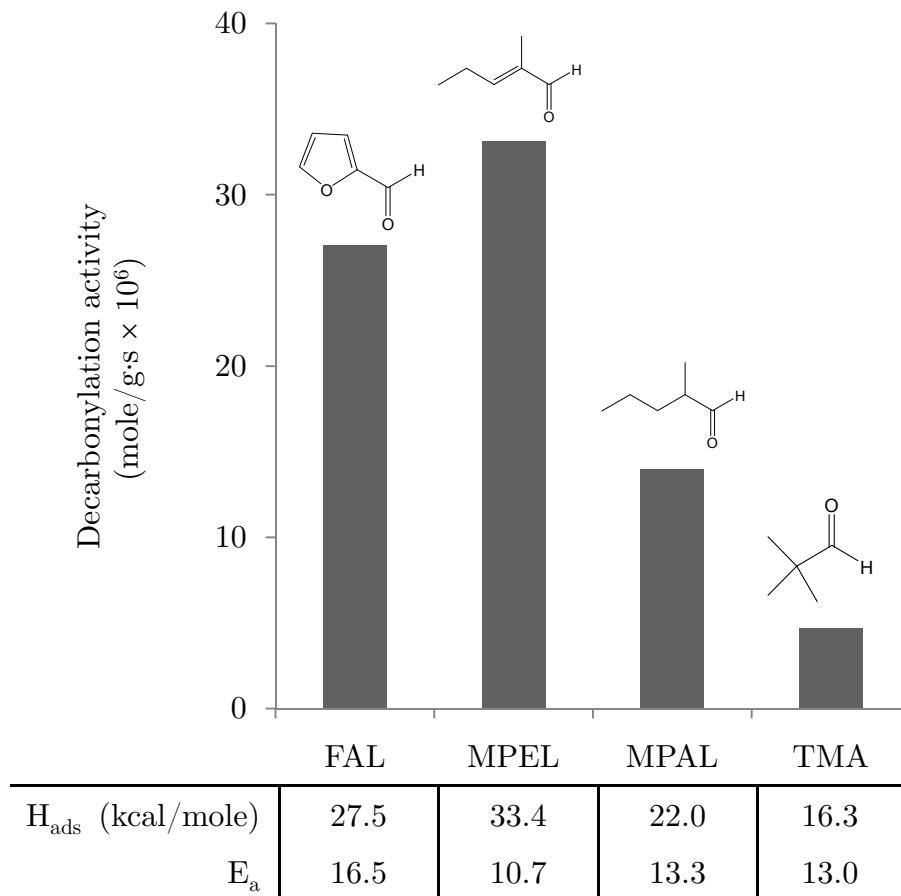


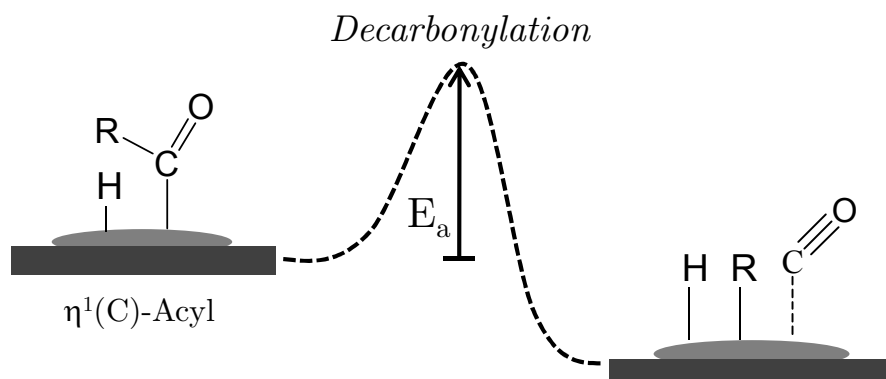
Figure 8.11 Decarbonylation activities, activation energies and calculated adsorption heats of $\eta^1(\text{C})$ -acyl species of furfural, 2-methylpentenal, 2-methylpentanal and trimethylacetaldehyde on Pd(111) surfaces. (The experimental data were taken from the work by Sitthisa *et al.*)

8.3.2 Computational calculation

Within this example, periodic DFT calculations were performed using the Vienna *ab initio* simulation package (VASP).¹⁶⁻²⁰ The slab model of Pd(111) surface and all other calculation details are the same as explained in Chapter 8.

8.3.3 Results and discussion

The electron energy loss spectroscopic signature (EELS) of surface species formed during the adsorption of aldehydes on different metals has been extensively investigated elsewhere. From the EELS results, it can be concluded that an η^2 -(C,O) aldehyde, in which both atoms (C and O) of the carbonyl group interact with the metal surface is the preferred species on clean Pd surfaces. In addition, they concluded that at high temperatures an acyl species (η^1 -(C)) can be formed via the C-H scission of η^2 -(C,O) intermediate. It is assumed that at the studied reaction temperature, most of the surface intermediates are the acyl species and it is a key element in the aldehyde decarbonylation, in which the rate and activity depends upon the stability and concentration on the surface. Moreover, it can be ascribed that the η^1 -(C) acyl species is determined as the precursor for decarbonylation reaction of aldehydes



The calculated heats of adsorption of the different aldehydes and the corresponding adsorption geometries are shown in Figure 8.11 and 8.12, respectively. In the case of MPEL, it is clearly seen that not only the carbonyl carbon bonds to the surface, but also the neighboring double bond can coordinate in a di- σ fashion to the Pd atoms. As a result, MPEL exhibits highest adsorption energy (33.4 kcal/mole). That double bond of MPEL is elongated ~ 1.3 Å as compared to that of the isolated molecule (see Figure 8.12b). In other words, the double bond loses its characteristic and become a single.

The similar behavior was observed on the adsorption of FAL (see Figure 8.12a). A part of the furan ring can coordinate to the surface as well; however, the interaction is less pronounced due to the double bond conjugation effect within the ring. That is the acyl adsorption energy of FAL (27.5 kcal/mole). In the case of the molecule containing no double bond such as MPAL and TMA, the molecule solely interacts with the surface through the carbonyl carbon. Therefore, a relative lower heat of adsorption is expected. Furthermore, the steric hindrance effect (e.g., three methyl groups in TMA) can makes the molecule even harder to adsorb, and results in a lower heat of adsorption. In this particular investigation, the acyl adsorption heats of MPAL and TMA are 22.0 and 16.3 kcal/mole, respectively.

Generally, levels of reaction rate and activity can be simply determined by the surface concentration, which directly connects to the ability to adsorb on

the surface i.e., the heat of adsorption. However, if the adsorption is too strong, the catalyst will be poisoned. In this example, the trend of the calculated adsorption energies is consistent well with the experimental decarbonylation activities, in which the molecule which has a higher heat of adsorption shows a better activity.

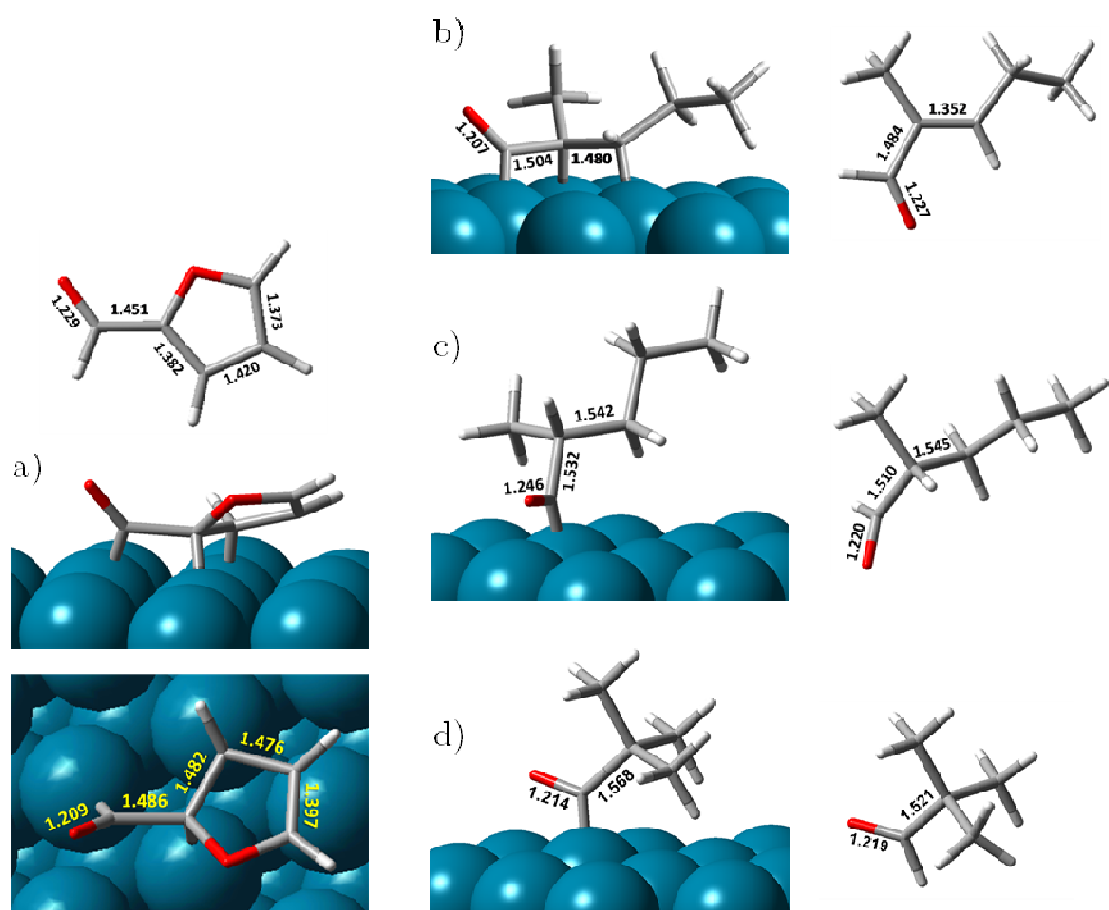


Figure 8.12 Geometries of isolated and optimized structures of $\eta^1(\text{C})$ -acyl species of a) furfural, b) 2-methylpentenal, c) 2-methylpentanal and d) trimethylacetaldehyde on Pd(111) surfaces.

In addition to the analysis of the surface concentration, a strong interaction of a molecule and a surface leads to the weakening of the bonds within a molecule. In this particular case, the modification of the C-C bond has an impact on the decarbonylation activity, in which the ability of the C-C bond breaking depends upon the bond strength.

8.3.4 Conclusions

On Pd catalysts, it is suggested that the surface $\eta^1\text{-C}$ acyl species is the main precursor for decarbonylation of aldehydes. The stability of this acyl intermediate strongly influences on the decarbonylation activity. Interpretation of the stability may be related to 1) the level of the surface concentration that affects to the reaction rate; and 2) the molecular bond weakening that leads to a lower energy needed to break the C-C bond. The calculated heats of adsorption from the DFT show a consistent trend as observed in the experimental results. That is the decarbonylation activity is in an order as follow: MPEL > FAL > MPAL > TMA.

References

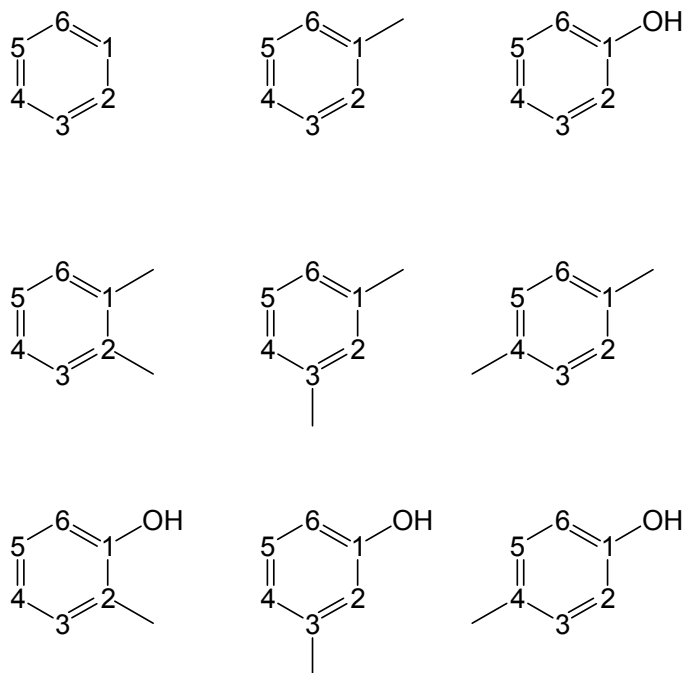
- 1 I. Graca, J.-D. Comparot, S. Laforge, P. Magnoux, J.M. Lopes, M.F. Ribeiro, F. Ramoa Ribeiro *Energy & Fuels*. **2009**,23,4224.
- 2 I. Graca, J.-D. Comparot, S. Laforge, P. Magnoux, J.M. Lopes, M.F. Ribeiro, F. Ramoa Ribeiro *Appl Cat A*. **2009**,353,123.
- 3 S. Li, A. Zheng, Y. Su, H. Zhang, L. Chen, J. Yang, C. Ye, F. Deng *J Am Chem Soc*. **2007**,129,11161.
- 4 M. J. Frisch et al. Gaussian03, revisionB.05; Gaussian, Inc.: Pittsburgh, PA, **2003**
- 5 C.T. O'Connor, M. Kojima *Catal Today*. **1990**,6,329.
- 6 L. Rodriguez-Santiago, M. Sierka, V. Branchadell, M. Sodupe, J. Sauer *J Am Chem Soc*. **1998**,120,1545.
- 7 X. Solans-Monfort, V. Branchadell, M. Sodupe *J Phys Chem A*. **2000**,104,3225.
- 8 P. Nachtigall, D. Nachtigallova, J. and Sauer *J Phys Chem B*. **2000**,104,1738.
- 9 A. Sierraalta, R. Anez, M.-R. Brussin *J Catal*. **2002**,205,107.
- 10 A.D. Becke *J Chem Phys*. **1993**,98,5648.
- 11 C. Lee, W. Yang, R.G. Parr *Phys Rev B*. **1988**,37,785.
- 12 P.J. Hay, W.R. Wadt *J Chem Phys*. **1985**,82,270.
- 13 E.D. Glendening, A.E. Reed, J.E. Carpenter, F. Weinhold NBO Version 3.1. Gaussian-94 Programs Package. Gaussian, Inc., Pittsburgh, PA, **1995**.
- 14 A.E. Reed, L.A. Curtiss, F. Weinhold *Chem Rev*. **1988**,88,899.
- 15 D.J. Parrillo, R.J. Gorte *Catal Lett*. **1992**,16,17.
- 16 G. Kresse, J. Furthmüller *J Phys Rev B*. **1996**,54,11169.
- 17 G. Kresse, J. Hafner *J Phys Rev B*. **1994**,49,14251.

-
- 18 G. Kresse, J. Hafner *J Phys Rev B*. **1993**,48,13115.
- 19 G. Kresse, J. Hafner *J Phys Rev B*. **1993**,47,558.
- 20 G. Kresse, J. Furthmuller *Comput Mater Sci*. **1996**,6,15.

APPENDIX A

Mulliken Charges and Proton Affinity of Single-Ring Aromatic Compounds

Table A.1 Calculated values of Mulliken charge (q) of benzene, toluene, xylenes, phenol, and cresols.



Compounds	q1	q2	q3	q4	q5	q6
benzene	-0.129	-0.129	-0.129	-0.129	-0.129	-0.129
toluene	0.177	-0.179	-0.127	-0.138	-0.127	-0.179
phenol	0.350	-0.195	-0.133	-0.135	-0.134	-0.158
xylene-o	0.131	0.131	-0.185	-0.128	-0.128	-0.185
xylene-m	0.183	-0.237	0.183	-0.184	-0.125	-0.184
xylene-p	0.175	-0.178	-0.178	0.175	-0.178	-0.178
cresol-o	0.272	0.155	-0.194	-0.130	-0.138	-0.156
cresol-m	0.357	-0.249	0.176	-0.189	-0.132	-0.162
cresol-p	0.346	-0.192	-0.189	0.177	-0.184	-0.156

BLUE: charge at -OH
 GREEN: charge at -OCH₃
 RED: PA in kcal/mol

$$PA = - \{ H(XH^+) - [H(X) + H(H^+)] \}$$

Where

$H(i)$ = enthalpy

X = neutral molecules

H⁺ = proton

XH⁺ = protonated species

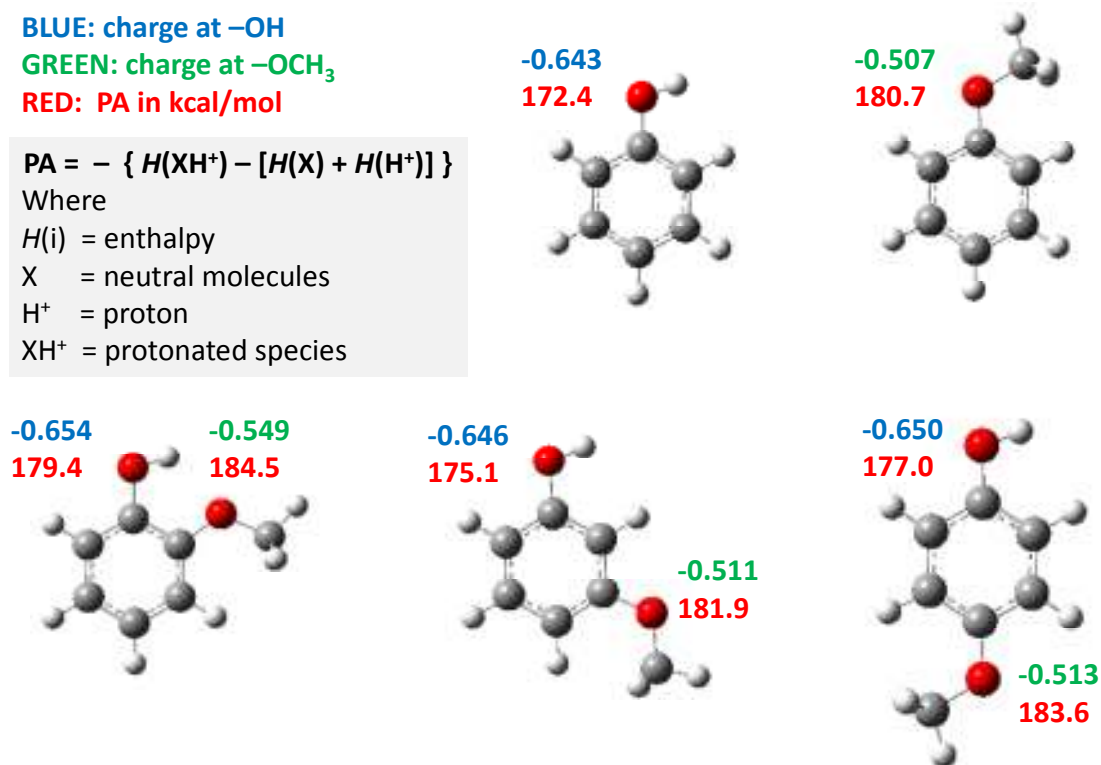


Figure A.1 Calculated proton affinity (PA) and atomic charge at oxygens of toluene, methoxybenzenes (anisole), and methoxyphenols (guaiacols).

Comments

- For electrophilic alkylation of aromatics, the alkylated products can be predicted by using DFT calculations. That is, an alkylating agent is likely to attack at the negatively charged atom in the aromatic ring (see Table A.1), in which the *ortho*- and *para*- positions are the preferential ones. However, this speculation might be altered due to the steric hindrance effect of highly substituent aromatics.
- As seen in Figure A.1, the hydroxyl group (-OH) shows a higher electron density, while the methoxyl group (-O-CH₃) shows a higher proton

affinity (PA). This suggests that the former ought to interact better with Lewis acid sites, and the later is easier to be protonated by Brønsted acid sites.

APPENDIX B

Molecular Orbitals of Single-Ring Aromatic Compounds

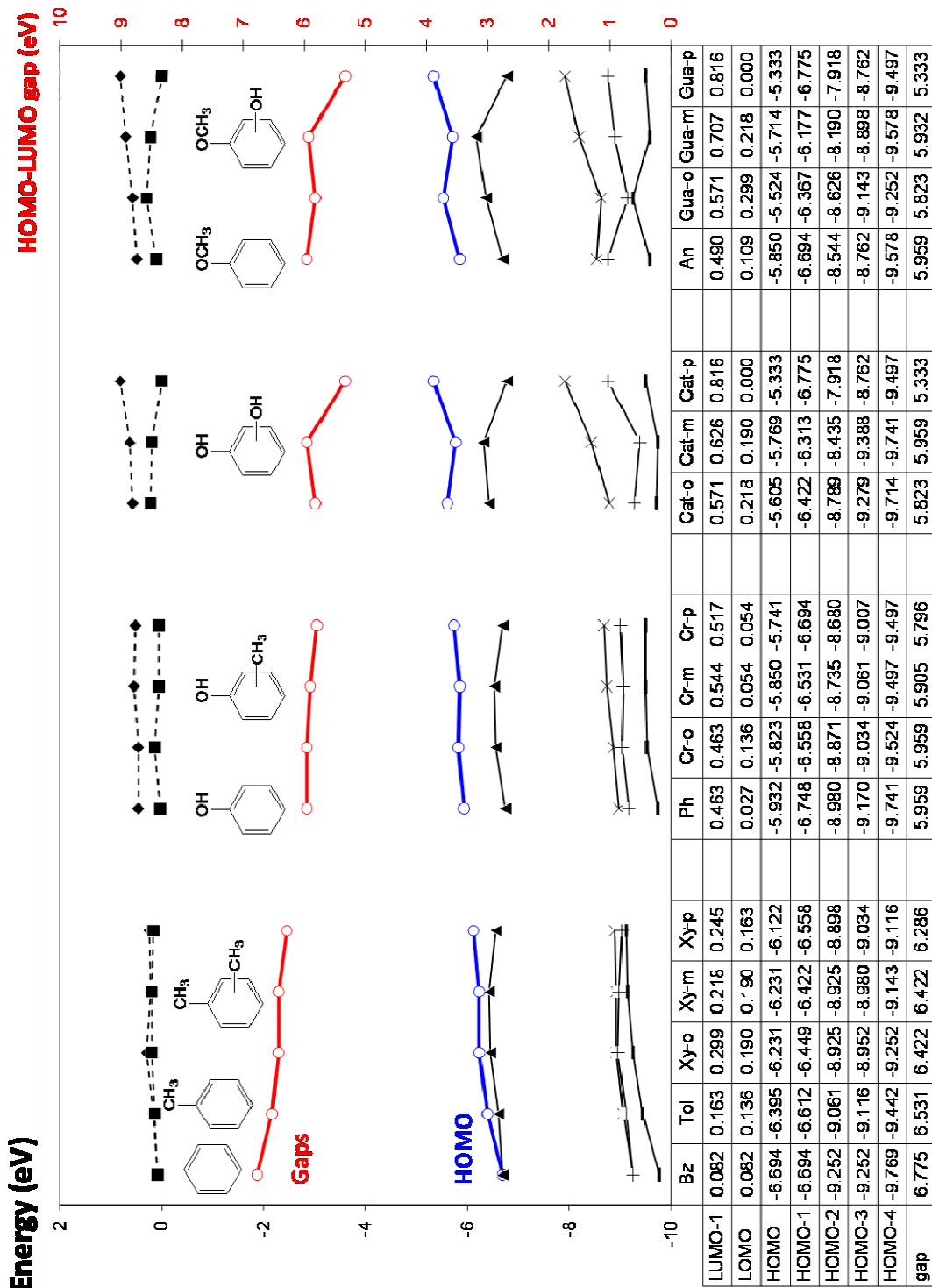
Nomenclatures

Bz	=	Benzene
Tol	=	Toluene (Methyl benzene)
Xy	=	Xylene (Dimethyl benzene)
Ph	=	Phenol (Hydroxybenzene)
Cr	=	Cresol (Methyl phenol)
Cat	=	Catechol (Benzenediol, Dihydroxybenzene)
An	=	Anisole (Methoxybenzene)
Gua	=	Guaiacol (Methoxyphenol)

Comments

- The presence of substituents can activate the benzene ring, as a result in a higher HOMO energy. The activation of the ring plays an important role in electrophilic alkylation of aromatics as discussed in Appendix K.
- In addition, the LUMO energy of substituent aromatics is lower than that of benzene. As a result, the HOMO-LUMO energy gap is smaller.

Table B.1 Molecular orbital energies of different aromatic compounds.



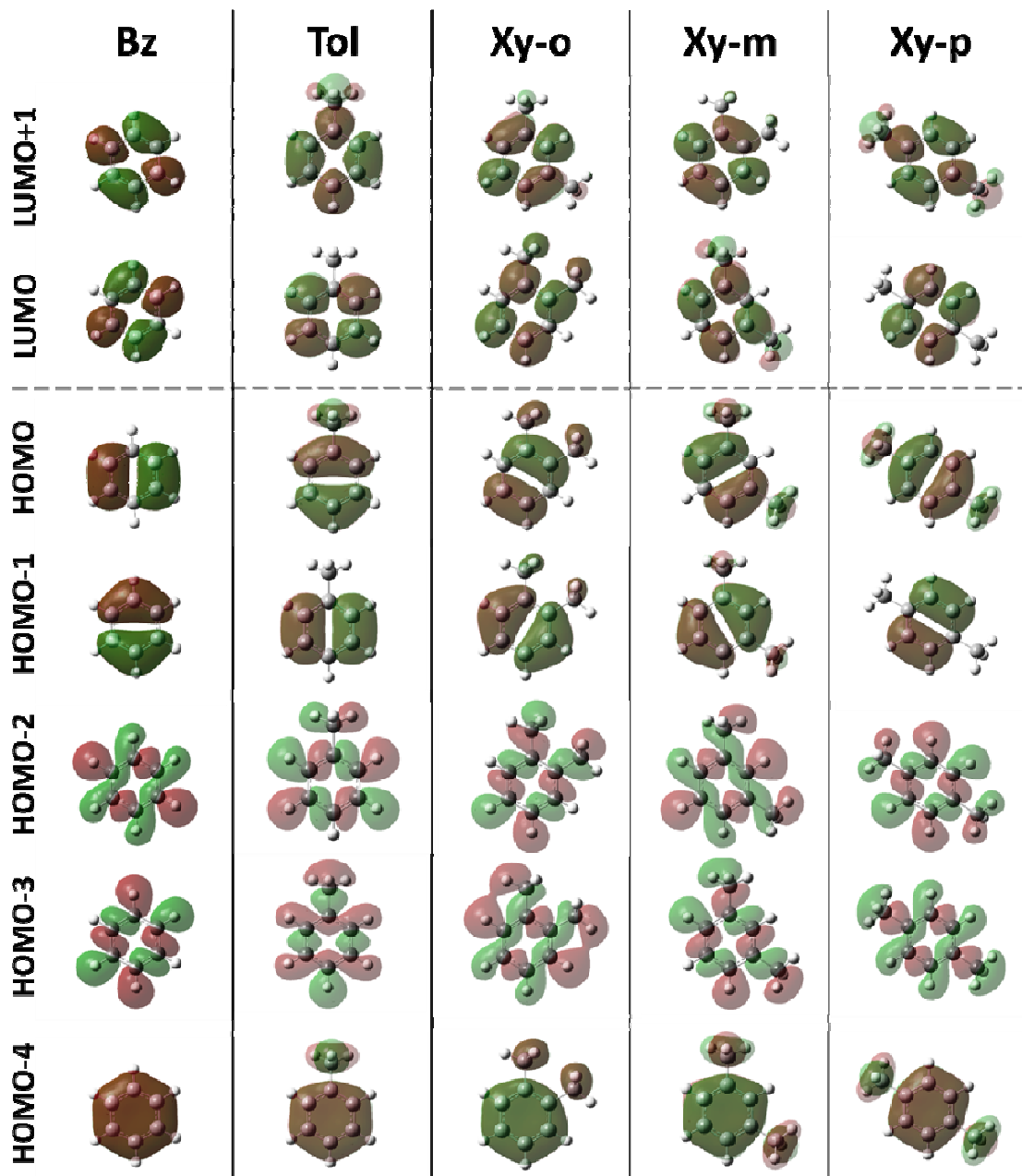


Figure B.1 Molecular orbital shapes of benzene, toluene and xylenes.

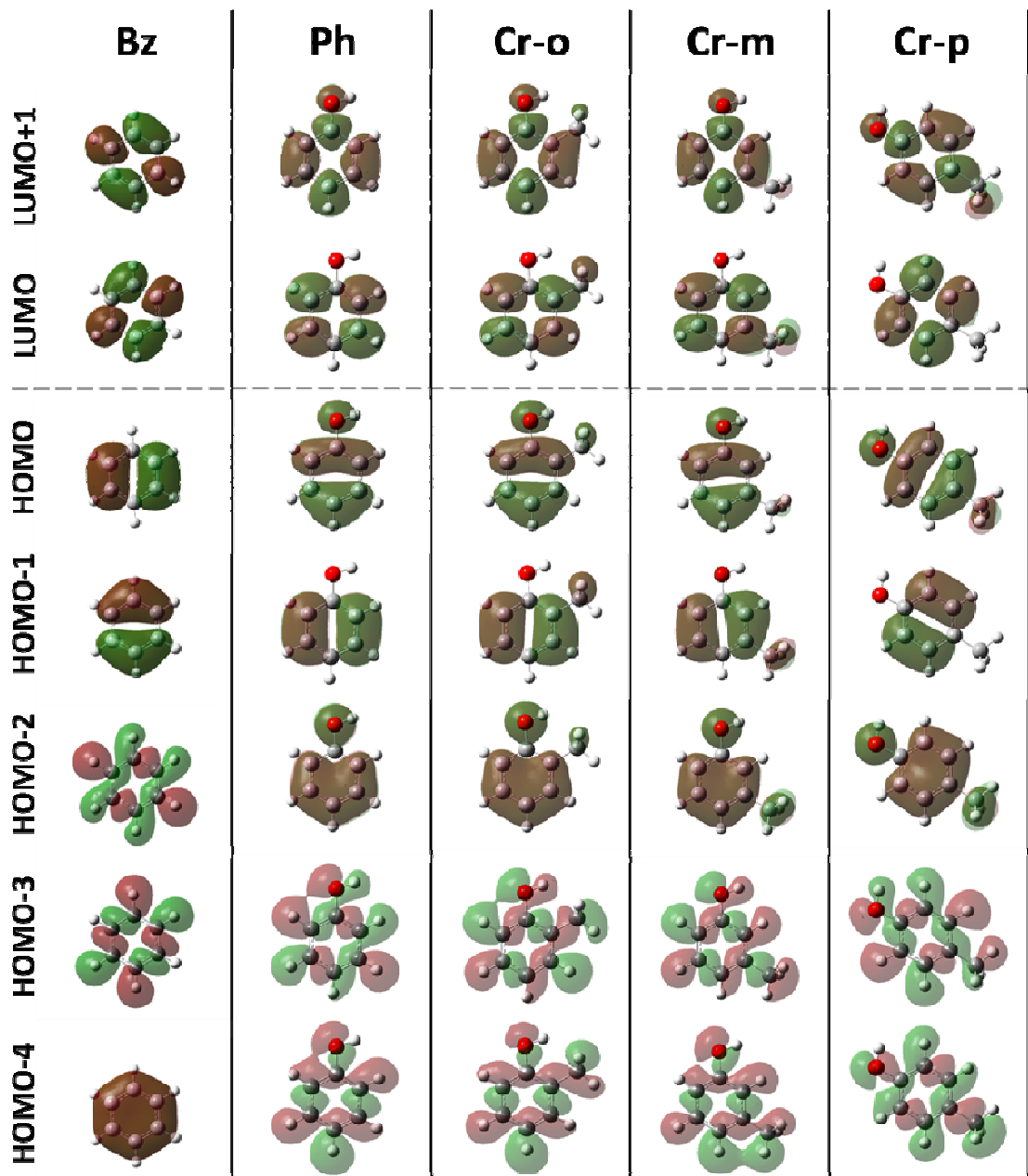


Figure B.2 Molecular orbital shapes of phenol and cresols.

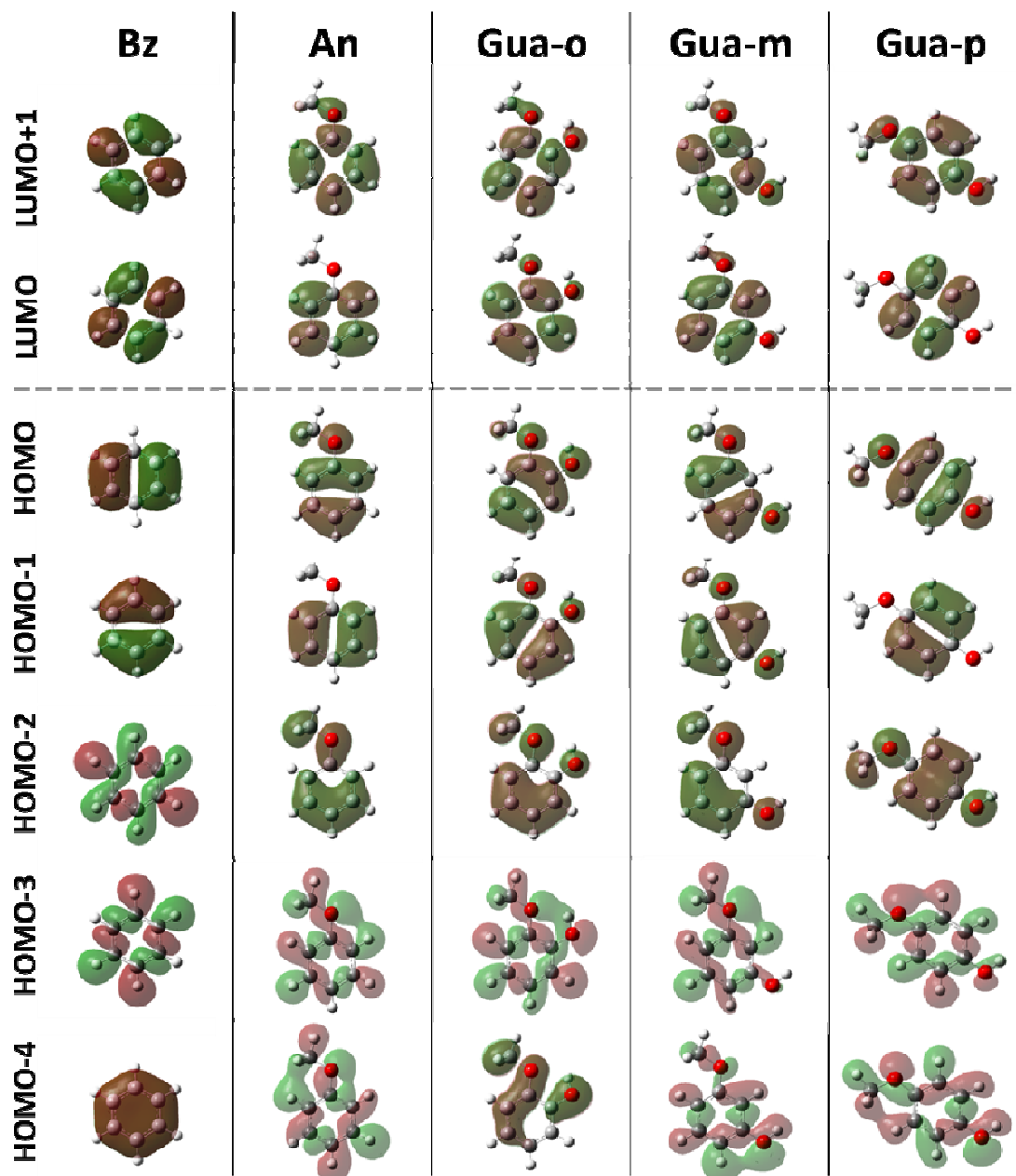


Figure B.3 Molecular orbital shapes of anisole and guaiacol.

APPENDIX C

Molecular Orbitals of Furanic Compounds

Nomenclatures

FAN	=	Furan
MFAN	=	Methyl furan
FOL	=	Furfuryl alcohol (2-Furanmethanol)
MFOL	=	5-Methyl furfuryl alcohol
FAL	=	Furfural (Furfuraldehyde)
MFAL	=	5-Methyl furfural

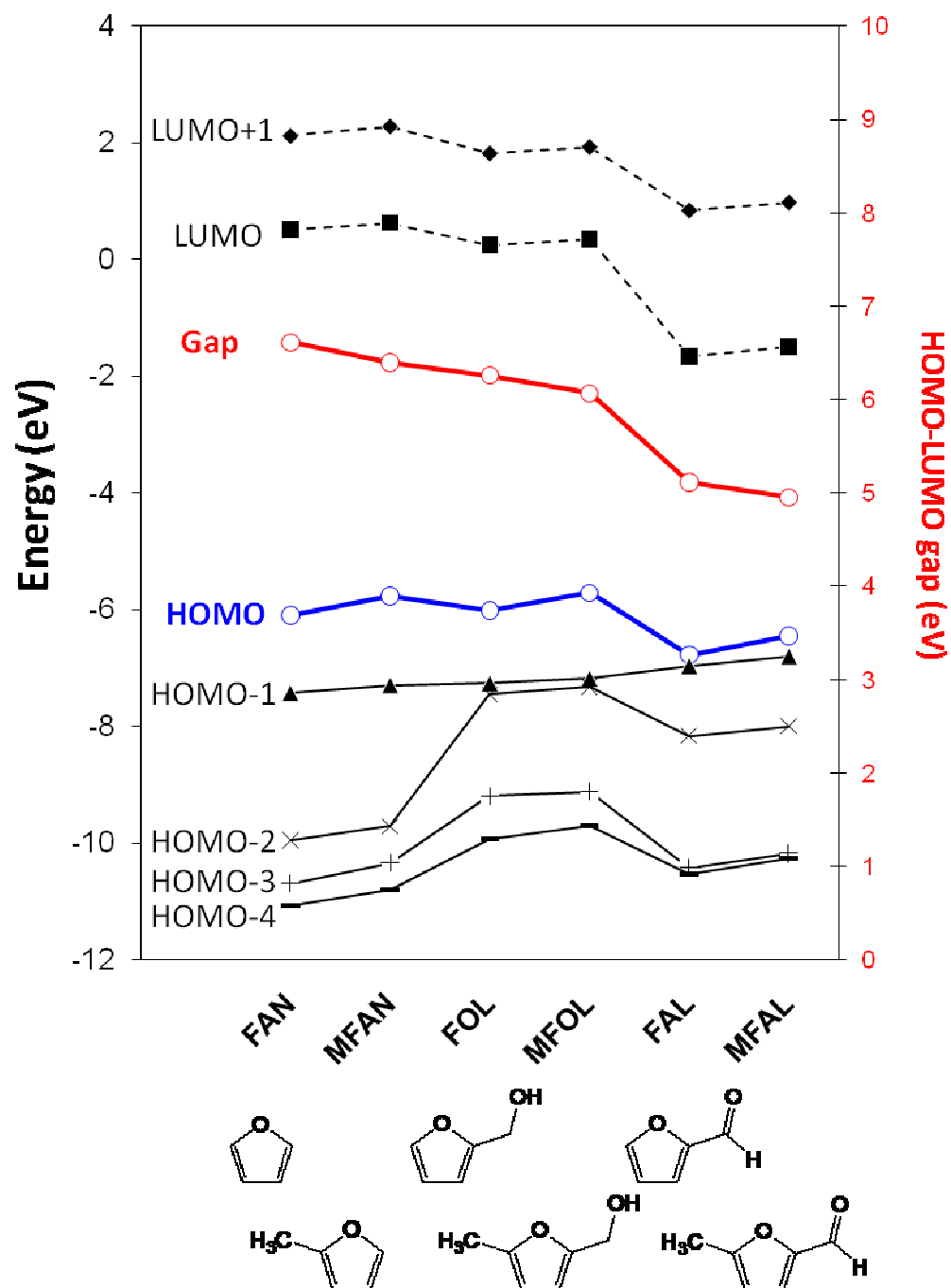


Figure C.1 Molecular orbital energies of different furanic compounds.

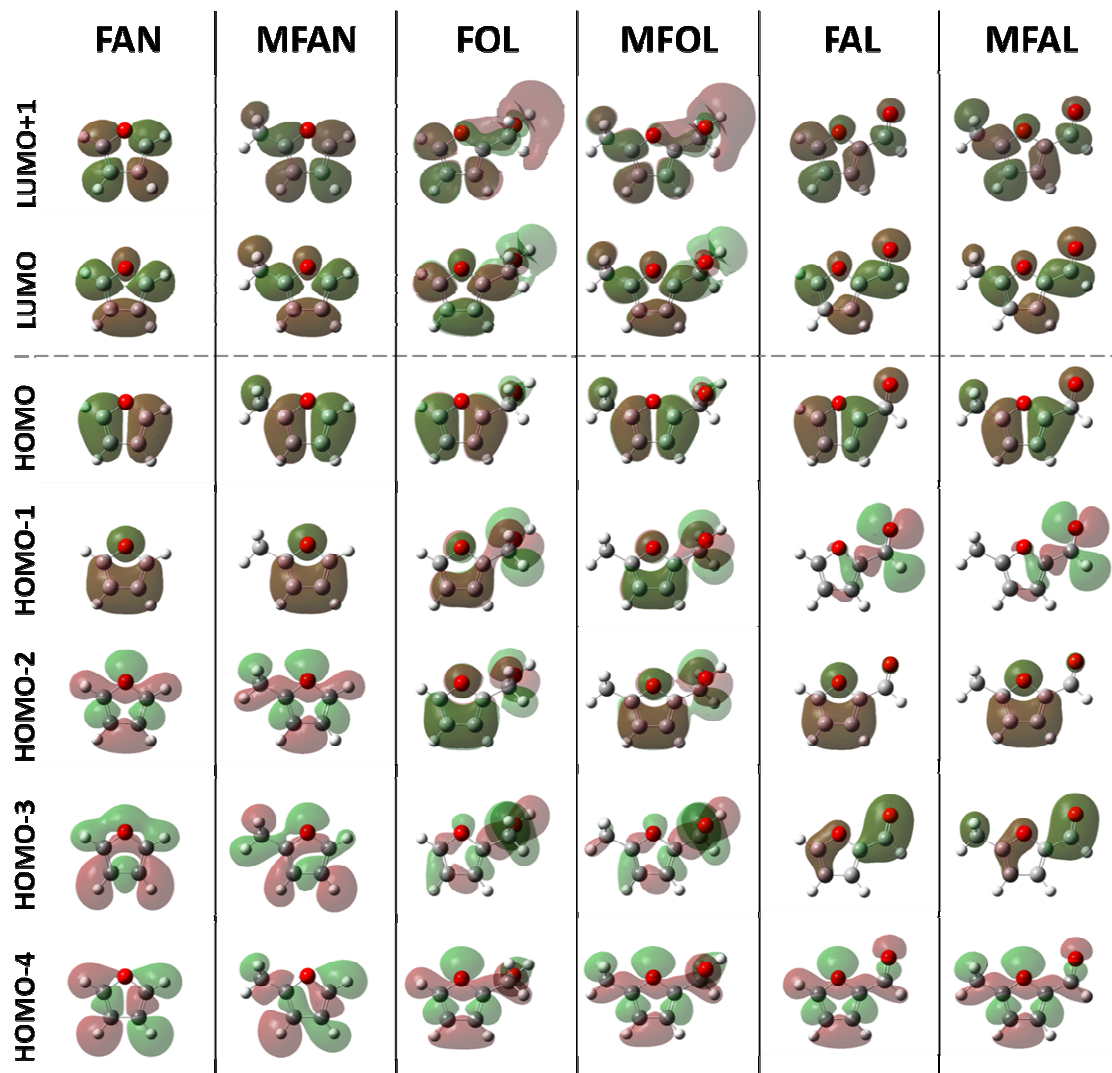


Figure C.2 Molecular orbital shapes of different furanic compounds.

APPENDIX D

Potential Energy Surface (PES) of the Adsorbed Propylene on Zeolites

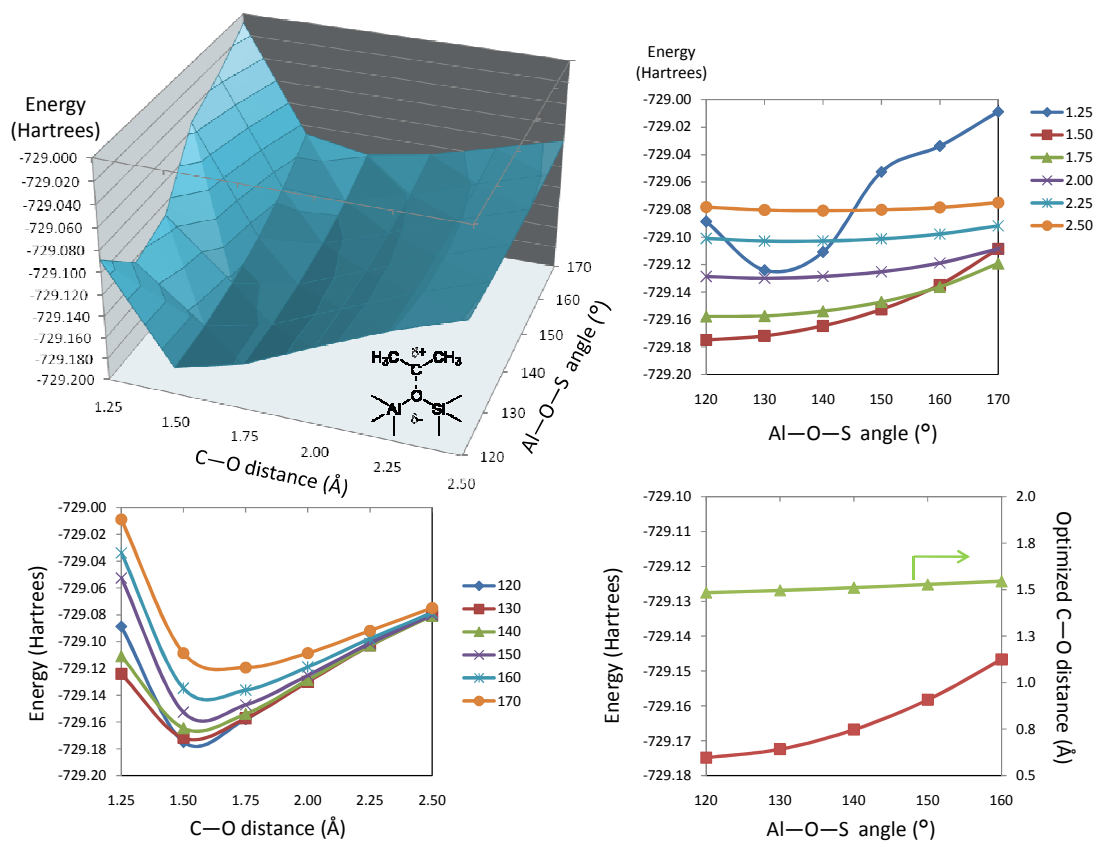


Figure D.1 Plots of surface propoxide energy as functions of adsorption separation (C-O distance) and zeolite structure (Al-O-Si angle).

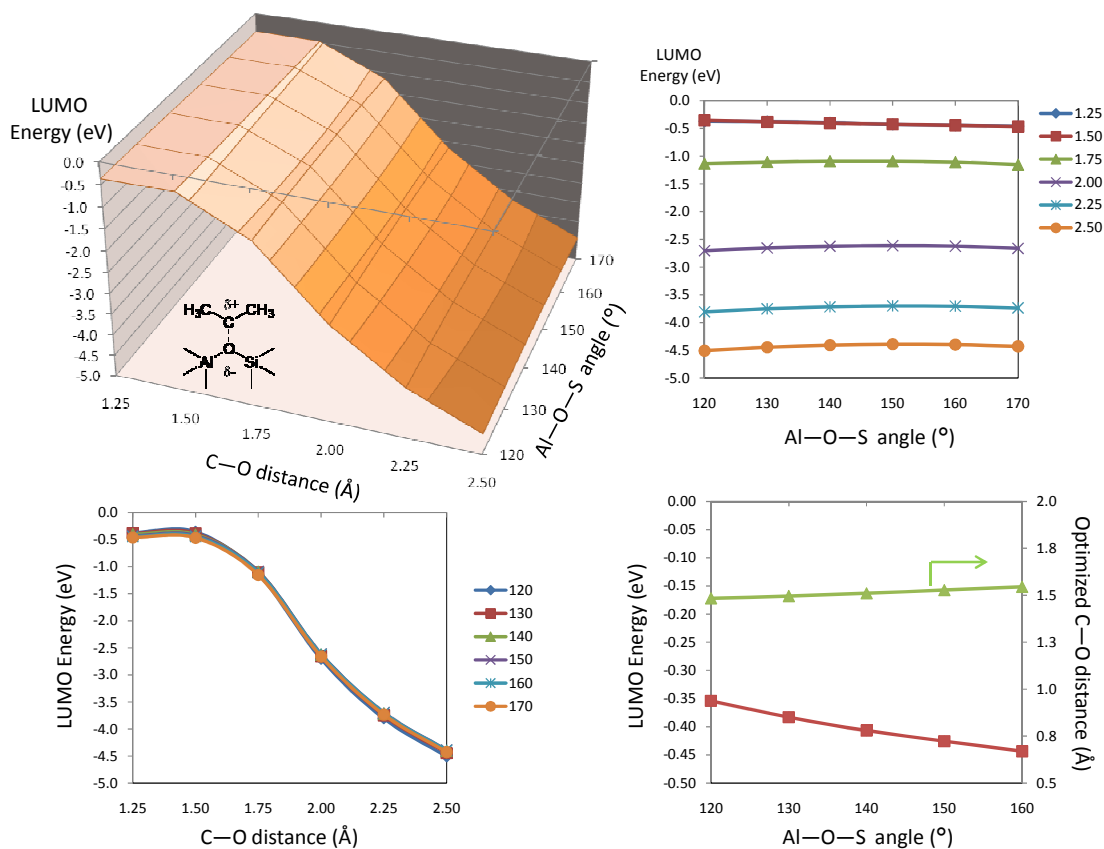


Figure D.2 Plots of LUMO energy of surface propoxide as functions of adsorption separation (C-O distance) and zeolite structure (Al-O-Si angle).

Comments

- The stability of adsorbed carbenium ions (i.e. surface propoxide) can be determined by the C-O distance. It shows that, in this particular case, the optimum distance is ~ 1.5 Å (Figure D.1).
- As the surface alkoxide is activated (i.e. the C-O distance increases), its energetic stability is reduced. At the same time, the LUMO energy decreases (Figure D.2). This surface alkoxide/carbenium ion can behave as an alkylating agent in the electrophilic alkylation of aromatics (as

discussed in Appendix K). Therefore, the modification of the LUMO will have an impact on the alkylation activity.

- The frontier molecular orbitals have not been modified much by varying zeolite structures, i.e. the Al-O-Si angle.
- It is exhibited that the surface propoxide species is less stable as the Al-O-Si angle increases.

APPENDIX E

Proposed Reaction Path of Hydrodeoxygenation of Phenol on Zeolites

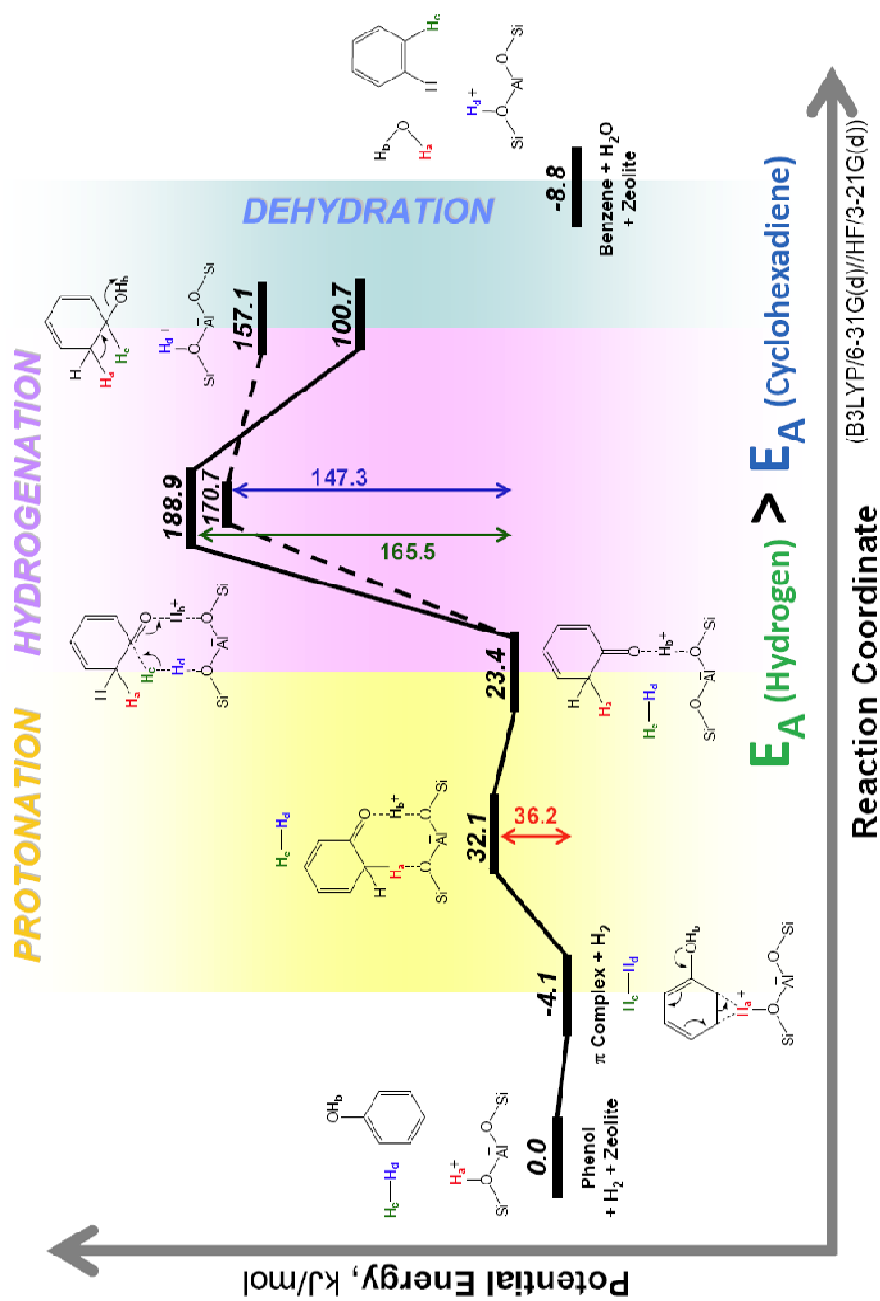


Figure E.1 The energetic profile of phenol hydrodeoxygenation on zeolites.

Comments

- The above figure depicts the proposed reaction path of hydrodeoxygenation of phenol on zeolites, which proceeds through protonation, partial hydrogenation of the ring, and dehydration.
- It is noted that the barrier of the hydrogenation step is significantly high, while protonation and dehydration is relatively easy to take place over acid sites.
- The H-transfer ability of the donor molecules (e.g. hydrogen and cyclohexadiene) has an impact on the activation energy for the hydrogenation step. As shown in this case, using cyclohexadiene as a H-source gives a lower barrier than using hydrogen,
- It might be expected that the presence of metal such as Pt can promote the ring hydrogenation, and leads to a moderate activation energy.

APPENDIX F

Relative Hydride Transfer Ability of Methylcyclohexene

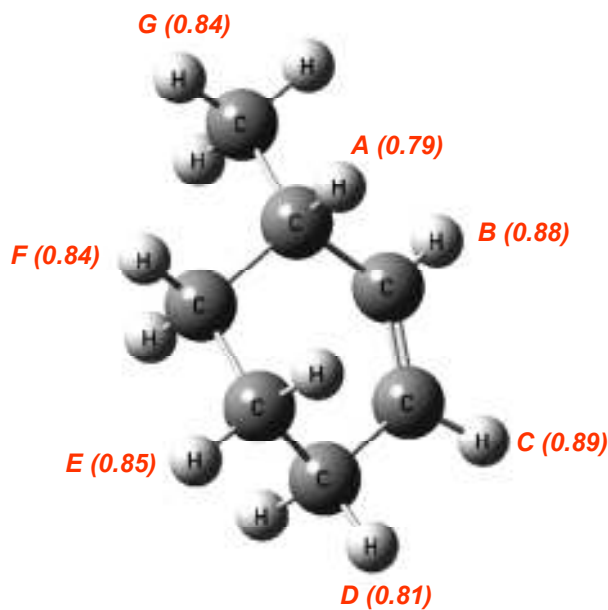


Figure F.1 Comparison of relative activation energy for hydride abstraction at different locations of methylcyclohexene.

Comments

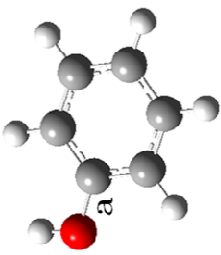
- It is hard to abstract a hydride at the carbon of C=C (**B** and **C**).
- The position next to the C=C (**A** and **D**) shows a lower activation energy than that of the further ones (**E** and **F**).
- The presence of alkyl group, resulting in a tertiary carbon, promotes the hydride transfer, i.e. hydride abstraction at **A** required less energy as compared to **F**.

APPENDIX G

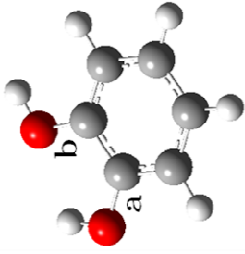
Natural Bond Orbital (NBO) Analysis of Single-Ring Aromatic Compounds

Table G.1 Natural bond orbital (NBO) analysis of phenol, catechol, guaiacol, anisole and hydrogenated phenol.

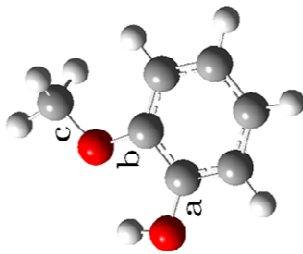
Molecule	Phenol		Catechol		Guaiacol		Anisole			HYD-Phenol	
	a	b	a	b	a	b	a	b	c	a	b
Length (Å)	1.37	1.38	1.36	1.38	1.36	1.37	1.42	1.37	1.42	1.44	1.44
Bond Index	1.02	0.99	1.03	0.99	1.03	0.97	0.90	1.00	0.91	0.29	0.29
BD*	0.34	0.32	0.35	0.32	0.36	0.34	0.27	0.36	0.29	0.27	0.27
BD	-0.92	-0.91	-0.91	-0.92	-0.91	-0.90	-0.84	-0.90	-0.83	-0.80	-0.80
BD-BD* gap	1.26	1.24	1.27	1.24	1.27	1.24	1.11	1.26	1.11	1.08	1.08
HOMO	-0.23	-0.22	-0.22	-0.22	-0.23	-0.23	-0.23	-0.22	-0.22	-0.21	-0.21
HOMO-BD* gap	0.58	0.54	0.58	0.54	0.59	0.57	0.51	0.58	0.51	0.51	0.51



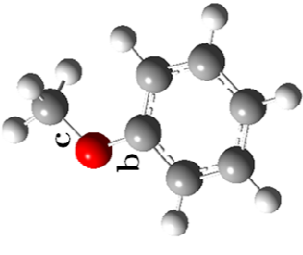
Phenol



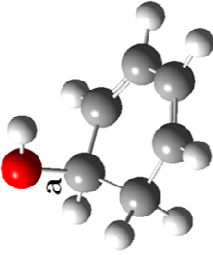
Catechol



Guaiacol



Anisole



Hydrogenated phenol

Note: - BD and BD* are energies of bonding and anti-bonding orbitals, respectively.
 at a particular C - O bond.
 - Energy in a.u.

Comments

- Here, it is proposed that the crackability of the C-O bond of molecules (i.e. deoxygenation) can be semi- determined by the energy gap between HOMO and C-O anti-bonding orbital.
- Based on this DFT calculation, demethylation is the easiest process since it shows the lowest energy gap. In addition, demethoxylation is easier than dehydroxylation.
- It is marked that both hydroxyl groups (-OH) of catechol are not intrinsically identical, in which one of them is weaker than the other. Hence, it is possible that guaiacol can be converted to catechol and further to phenol. However, C-O bond breaking of phenol is less likely due to its high energy gap.
- Interestingly, hydrogenated phenol (i.e. cyclohexanol) shows the lowest energy gap. As a result, the C-O bond breaking is expected to be very easy, and this is consistent to the proposal mentioned in appendix E. That is the hydrogenation/dehydration of phenol.

APPENDIX H

Adsorption of Hydroxybenzaldehydes on Ru(0001) Surfaces

Table H.1 Calculated heats of adsorption (eV) of *ortho*- and *para*-hydroxybenzaldehydes on Ru(0001) surfaces.

		Ortho-	Para-
parallel	1	-1.26	-1.21
	2	-1.19	-1.00
	3	-1.66	-1.57
	4	-1.70	-1.51
$\eta^1\text{-(O)}$	5	-0.35	-0.32
	6	-0.27	-0.26
$\eta^2\text{-(C-O)}$	7	-0.45	-0.42
	8	-0.54	-0.40

Comments

- For Ru, the crystal structure is hexagonal close-packed (hcp), which the top layer of the hcp(0001) is equivalent to that of the fcc(111) plane.
- Based on this DFT calculation, it exhibits that the interaction of the molecules on the surface is predominated by the aromatic ring. In addition, the carbonyl group is likely to adsorb the surface, while the hydroxyl group tilts up.
- Generally, *ortho*-hydroxybenzaldehyde gives a higher heat of adsorption than the *para*- one for a given orientation on the surface.

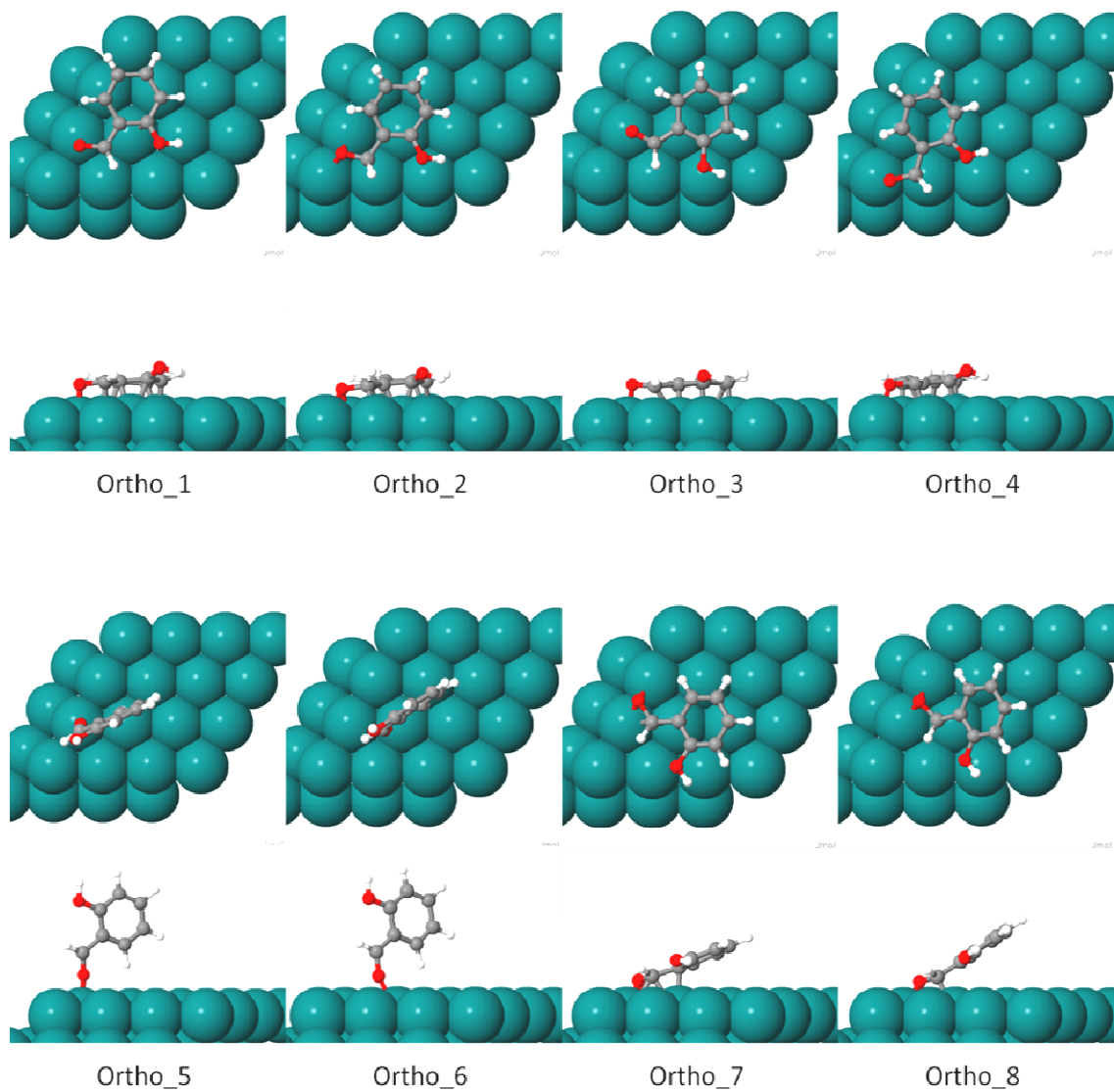


Figure H.1 Possible adsorption configurations of *o*-hydroxybenzaldehyde on Ru(0001) surfaces.

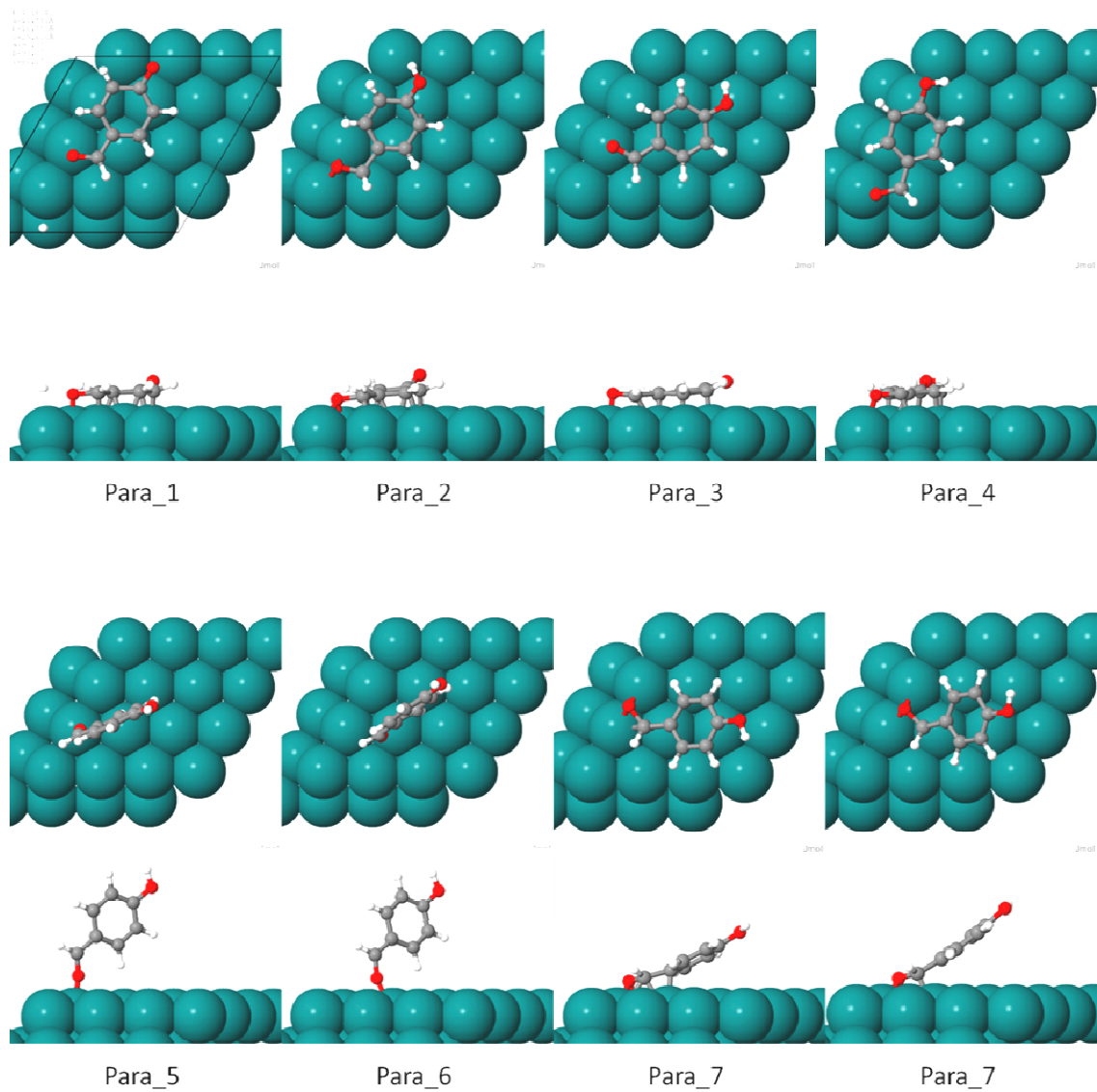


Figure H.2 Possible adsorption configurations of *p*-hydroxybenzaldehyde on Ru(0001) surfaces.

APPENDIX I

Adsorption of Furan on Pd and Ni Clusters

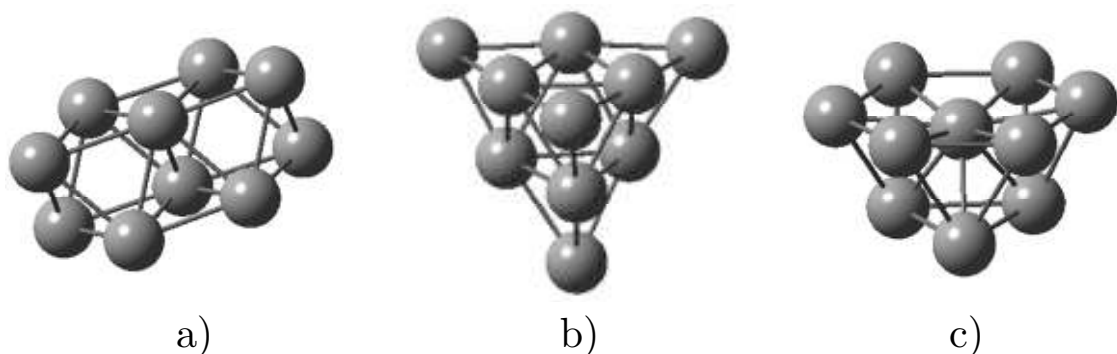
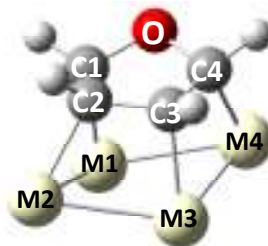


Figure I.1 Structures of M_{10} cluster ($M = \text{Pd}$ and Ni).

Comments

- For 10-metal clusters, It is reported that the structures **a** and **b** are the most stable geometries of Pd and Ni clusters, respectively.
- Adsorption energy of furan on Ni is higher than that on Pd. As a result, the bonds of the furan are weakened more on Ni (i.e. longer bond length, and lower bond index).
- It can be ascribed that hydrogenolysis, C-O bond breaking, is more likely on Ni, as compared to Pd.
- The trends, as mentioned above, of adsorption energies, bond lengths, and bond index are similar regardless the geometries of the cluster used in calculation (see Table I.1 and I.2).

Table I.1 Calculated heats of adsorption and bond lengths of furan on different structures of Pd and Ni clusters.



Molecule	THF		Furan	
	Isolated	Isolated	Pd _a (Pd _c)	Ni _b (Ni _c)
E _{ads} (eV)	-	-	1.12 (1.01)	1.25 (1.20)
kcal/mol)	-	-	25.5 (23.3)	28.8 (27.7)
Bond length (Å)				
O – C1	1.47	1.39	1.46 (1.44)	1.47 (1.46)
O – C4	1.47	1.39	1.44 (1.45)	1.46 (1.46)
C1 – C2	1.55	1.37	1.48 (1.49)	1.50 (1.49)
C2 – C3	1.55	1.45	1.48 (1.49)	1.50 (1.50)
C3 – C4	1.56	1.37	1.47 (1.48)	1.50 (1.48)

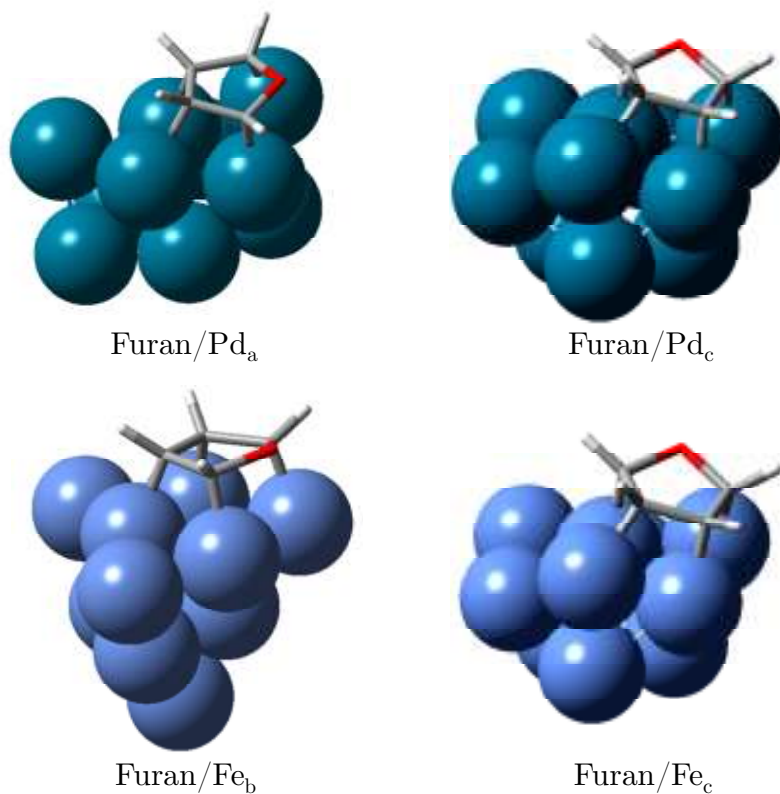
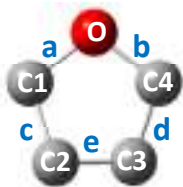


Figure I.2 Optimized geometries of furan adsorption on Ni and Pd clusters.

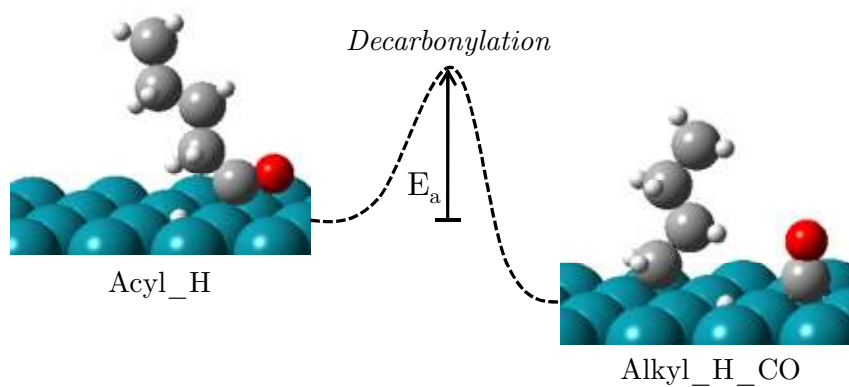
Table I.2 Calculated bond index and natural bond orbital (NBO) analysis of furan on different structures of Pd and Ni clusters.

Molecule	THF		Furan	
Cluster	Isolated	Isolated	Pd _a (Pd _c)	Ni _b (Ni _c)
Bond Index				
a	0.8989	1.0209	0.8960 (0.9251)	0.8995 (0.8918)
b	0.8989	1.0209	0.9564 (0.9175)	0.9043 (0.9093)
c	1.0169	1.6704	1.1938 (1.1506)	1.1150 (1.1523)
d	1.0169	1.6704	1.2374 (1.1866)	1.1362 (1.1624)
e	1.0130	1.2502	1.1929 (1.1570)	1.1233 (1.1216)
Bond Orbital Analysis				
a	O_sp3.00	O_sp2.42	O_sp2.89	O_sp2.97
	C1_sp4.00	C1_sp3.33	C1_sp3.97	C1_sp3.88
b	O_sp3.00	O_sp2.42	O_sp2.77	O_sp2.85
	C4_sp4.00	C4_sp3.34	C4_sp3.63	C4_sp3.89
c	C1_sp2.47	C1_sp1.46 +p	C1_sp1.83	C1_sp1.95
	C2_sp2.88	C2_sp1.96 +p	C2_sp2.10	C2_sp2.46
d	C4_sp2.47	C4_sp1.46 +p	C4_sp1.75	C4_sp1.90
	C3_sp2.88	C3_sp1.96 +p	C3_sp2.19	C3_sp2.40
e	C2_sp2.82	C2_sp1.07	C2_sp2.08	C2_sp2.28
	C3_sp2.82	C3_sp1.06	C3_sp2.12	C3_sp2.32



APPENDIX J

Adsorption of Acyl Species of Aldehydes on (111) Surfaces of Pt, Pd and Rh



Compounds	Metal	Adsorption energy (kcal/mol)	
		Acyl_H	Alkyl_H_CO
C5AL (pentanal)	Pt	-18.7	-23.8
	Pd	-25.0	-34.1
	Rh	-26.6	-42.0
MBAL (methyl butanal)	Pt	-14.4	-21.9
	Pd	-26.9	-29.7
	Rh	-31.9	-38.9
TMA (trimethyl acetaldehyde)	Pt	-8.7	-15.0
	Pd	-12.7	-29.1
	Rh	-30.0	-32.6

Figure J.1 Heats of adsorption of acyl species of pentanal, methylbutanal and trimethylacetaldehyde on (111) surfaces of Pt, Pd and Rh.

APPENDIX K

Alkylation of Different Aromatic Compounds and Model Small Oxygenates in Bio-Oil Refining

Computational method

The alkylation activity was investigated by the density functional theory (DFT) calculations. The concept of orbital control which relates to the interaction of molecular orbitals of two fragments, a donor and an acceptor, as applied to the analysis.^{1,2} In order to study the energy levels of molecular orbitals, the DFT calculations were performed using Becke's three parameters which employ the Lee-Yang-Parr correlation functional (B3LYP) and the 6-31G* basis set.^{3,4} The GAUSSIAN-03 program was employed to carry out all the DFT calculations.⁵ No symmetry constraints were placed on any of the gas-phase aromatic molecules (benzene, toluene and m-cresol) during optimizations to achieve the minimum-energy structures. The alkylating agent used in this study was simulated by the adsorbed iso-propoxide species on a simple zeolite cluster (see Figure K.3), in which the 'dangling' bonds are saturated by hydrogen atoms. Such a model has been extensively used to predict the properties of the zeolitic active sites.⁶ Again, optimizations of geometry were carried out when searching for the most stable configuration. Besides, the

activated alkoxide species were also investigated by fixing the C-O bond distance and relaxing the rest of the cluster.

Results and discussion

The results of alkylation of benzene, toluene and m-cresol with 1-propanol are shown in Figure K.1. It is noted that m-cresol give the highest alkylate yield, followed by toluene, and lowest for benzene. It is obviously seen that the presence of different substituents plays a significant role in the reactivity of the aromatic compounds. In this project, the DFT calculation is integrated in this analysis in order to explore the reactivity of the different aromatics. Corma *et al.* have studied the electrophilic alkylation of aromatic by utilizing the concept of molecular orbital control.⁷ Formation of a covalent bond requires an interaction of the main molecular orbitals (i.e. the more energetic) which are the highest occupied molecular orbital (HOMO) of aromatics and lowest unoccupied molecular orbital (LUMO) of alkylating agents, as the electron donor and acceptor fragments, respectively. Base on this analysis, the reaction activity/selectivity is somehow determined by the energy of HOMO-LUMO gap.

The substituents such as methyl (-CH₃) and hydroxyl (-OH) groups attaching to the aromatic rings can destabilized the electron in the (HOMO) as illustrated in Figure K.2. Therefore, m-cresol shows a highest HOMO energy, as

compared to toluene, whereas benzene shows the most stable HOMO electron. Assuming that the energy of the LUMO remains the same or at least the HOMO of the activated alkylating species cluster remains constant on the zeolite surface, therefore, the HOMO-LUMO energy gap is smallest for alkylation of m-cresol, higher for toluene and highest for benzene. This predicted trend of alkylation reactivity is consistent with the experiment results shown in Figure K.1.

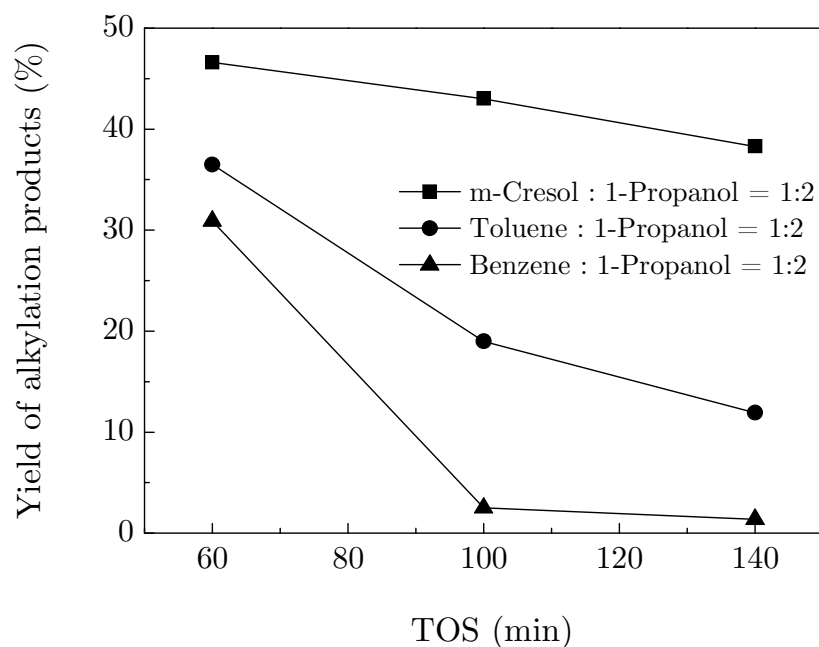


Figure K.1 Alkylation of different feed over H-Beta at 200 °C.
W/F = 1h. Carrier gas H₂ 30ml/min.

In addition to the theoretical investigation of the aromatic, it is worth to explore the electrophilic agent further. As using acid zeolites as catalysts, the alkylating agent can be considered as a complex oxide or an adsorbed carbenium ion. As generally known, 1-propanol is readily hydrogenated to propylene. Therefore, the simulated propoxide species or adsorbed propylene carbenium ion is used as the alkylating agent. According to stability of alkoxide species,⁸ the propoxide-zeolite complex may not react as an effective electrophile, and the geometry activation is needed (read more in Appendix D). As clearly shown in Figure K.3, the total energy of the propoxide is increased by elongation of the C—O bond, hence, significantly decrease of the LUMO energy can be achieved. This moment is likely to happen during the transition state. In addition, the position of the electrophilic attack can be predicted by considering the electron density on each potential position (see Appendix A), in which it is preferentially occur at *ortho*- and *para*- positions.

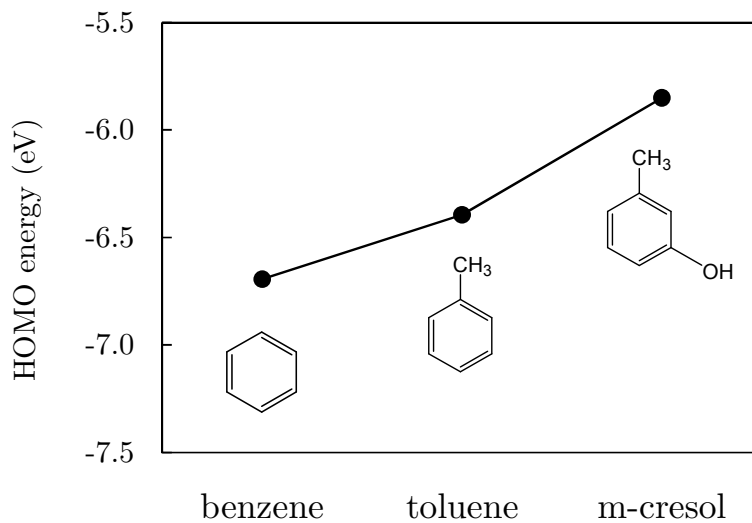


Figure K.2 Calculated HOMO energies (eV) of benzene, toluene, and m-cresol.

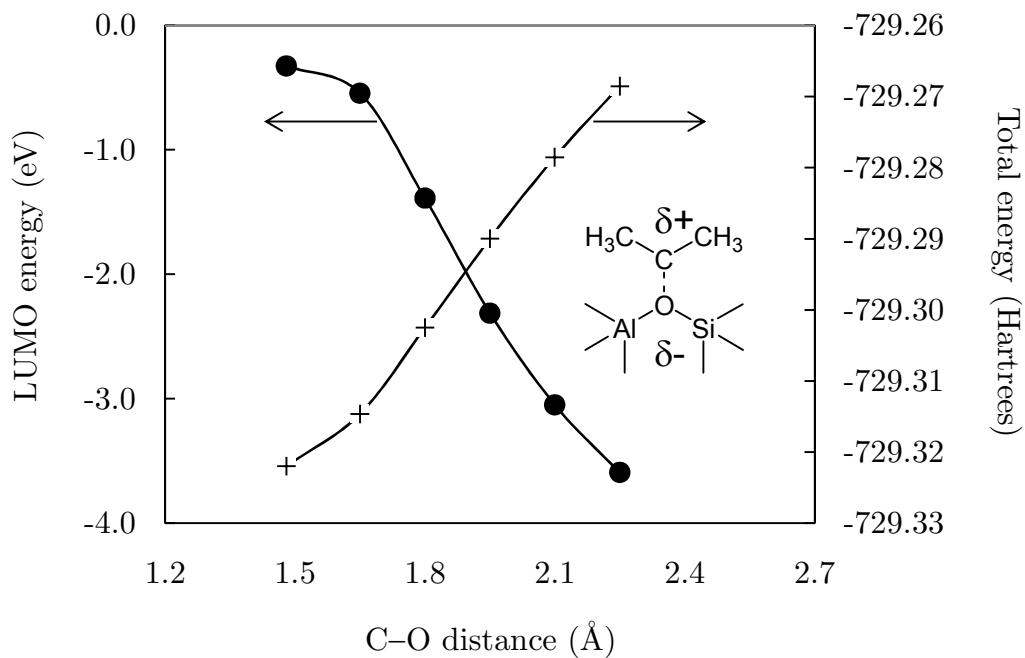


Figure K.3 Calculated LUMO energy (eV) and total energy (Hartrees) of propoxide species (i.e. adsorbed propylene) at different separation distances.

Conclusions

The activity of electrophilic aromatic alkylation can be semi-quantitatively determined by the mean of orbital control analysis. The formation of covalent bond between aromatics and an alkylating agent is contributed from the interaction of their frontier molecular orbitals, which are the HOMO of aromatics and the LUMO of the surface carbenium species complex. The presence of substituent destabilizes the aromaticity and leads to a higher HOMO energy. Consequently, the corresponding smaller HOMO-LUMO gap, referring to the activity indicator, is expected. That is, as the same alkylating agent is used, the alkylation activity is in the following order: m-cresol > toluene > benzene.

References

-
- 1 G. Klopman *J Am Chem SOC.* **1968**,90,223.
 - 2 L. Salem *J Am Chem SOC.* **1968**,90,543.
 - 3 A.D. Becke *J Chem Phys* **1993**,98,1372.
 - 4 C. Lee, W. Yang, R. G. Parr *Phys Rev B.* **1988**,37,785.
 - 5 M.J. Frisch *et al.* GAUSSIAN 03, Gaussian, Inc., Wallingford, CT, **2004**.
 - 6 J. Sauer *Chem Rev.* **1989**,89,199.
 - 7 A. Corma, C. Zicovich-Wilson P. Viruela *J Phys Org Chem.* **1994**,7,364.
 - 8 V.B. Kazansky *Acc Chem Res.* **1991**,24, 379.